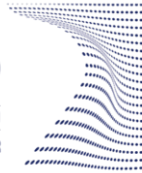




**ScuDo**  
Scuola di Dottorato ~ Doctoral School  
WHAT YOU ARE. TAKES YOU FAR



**KU LEUVEN**

ARENBERG DOCTORAL SCHOOL  
Faculty of Science, Department of Physics and Astronomy

Doctoral Dissertation  
Cotutelle Doctoral Program in:  
Metrology (Politecnico di Torino, 30<sup>th</sup> cycle) and Physics (KU Leuven)

# **Fabrication and characterization of reference nano and micro structures for 3D chemical analysis**

**Masoud Dialameh**

**Supervisors:**

Dr. Luca Boarino  
Dr. Natascia De Leo  
Prof. Wilfried Vandevorst

**Doctoral Examination Committee:**

Prof. Guido Mula, Università degli studi di Cagliari  
Dr. Jean Paul Barnes, CEA-Leti  
Dr. Gianbartolo Picotto, istituto nazionale di ricerca metrological (INRIM)  
Prof. Mariagrazia Graziano, politecnico di torino (Polito)  
Prof. Stefan De Gendt, Katholieke Universiteit Leuven (KUL)  
Prof. André Vantomme, Katholieke Universiteit Leuven (KUL)

Jun 2019



This thesis is licensed under a Creative Commons License, Attribution - Noncommercial - NoDerivative Works 4.0 International: see [www.creativecommons.org](http://www.creativecommons.org). The text may be reproduced for non-commercial purposes, provided that credit is given to the original author.

I hereby declare that, the contents and organisation of this dissertation constitute my own original work and does not compromise in any way the rights of third parties, including those relating to the security of personal data.

Masoud Dialameh  
Turin, Jun 12, 2019



# Summary

Industry is progressively moving towards complex 3D architectures and using advanced materials and heterogeneous systems, which includes both organic and inorganic materials. Obviously, the performance of such complex 3D systems is also determined by the 3D elemental distributions, e.g. dopant distributions, or chemical compositions at the nanometric scale. Thus, 3D metrology should provide an accurate elemental and chemical measurement solution with a 3D spatial resolution (both lateral and depth) down to the nanometric scale in accordance with the needs of the industry (e.g. down to sub nanometer scale for the semiconductor industry). In this content, time-of-flight secondary ion mass spectrometry (ToFSIMS), grazing incidence X-ray fluorescence (GIXRF) and atom probe tomography (APT) are among the potential enablers to resolve such a 3D spatial resolution. Despite the recent improvements to push ToFSIMS and GIXRF as the reliable 3D measurement techniques, the metrological assessment of such analyses has not been yet well evaluated. This is mainly due to the absence of the 3D reference materials and the calibration standards. On the other hand, APT is an inherent three-dimensional technique, which enables elemental identification and quantification at a near-atomic resolution. However, similar to the other aforementioned techniques, the metrological assessment of the APT analysis is also hampered due to the absence of the suitable reference materials.

In this project, we have developed several well-characterized organic-inorganic 3D microstructures as the potential reference material (RM) for 3D ToFSIMS. To prepare the 3D nanostructures with the characteristic dimensions below 20 nm as a test vehicle for GIXRF analysis, we exploited the self-assembly of di-block copolymers (DBC) as the lithography mask. We have also studied in detail the pattern transfer at sub 20 nm scale into the Si substrate.

In order to develop a potential reference material for APT, we have studied in detail the different aspects of the APT analysis, including ion trajectories, field-of-

view (FOV) and the calibration of the different reconstruction parameters. We have studied in detail the FOV for both hemispherical and the UV laser induced asymmetric tip shape. In addition, we suggested a new design for an APT specimen, which maximizes the FOV and allows to probe the entire specimen volume in APT (full tip imaging). We have proven the feasibility of full tip imaging both numerically (finite element analysis) and experimentally. To do so, a specimen preparation process was developed based on standard lithography and etching technique which allows to prepare multiple APT specimens in a repeatable fashion and with a minimized tip to tip variations in view of the tip radius and the shank angle. The developed full tip imaging feature can pave the way for the uncertainty assessment for all the reconstruction parameters and potentially enables a more reliable 3D data reconstruction in APT with the quantifiable uncertainties. In the absence of the certified reference material for APT, we have developed a well-characterized (i.e. traceable) B doped SiGe reference system (i.e. piece of wafer). Relying on this reference, the accuracy and the repeatability of APT analysis in view of Ge and B quantification over the specimen volume have been evaluated using UV and green lasers as well as in the different experimental conditions (electric field).

In addition, the feasibility of APT analysis of an organic-inorganic system based a polyaniline (Pani) - porous silicon (PSi) nanocomposite was evaluated in detail. We demonstrated that such a complex system could be analyzed by APT, whereby the 3D compositional distribution (lateral and depth distribution) was identified according to the distribution of monoatomic ions. The remained challenges for such an analysis were addressed and a potential solution was proposed.

# Acknowledgment

It gives me a great pleasure to acknowledge the many people who made this cotutelle PhD possible. I would like to gratefully thank my supervisors at INRIM, Dr. Luca Boarino and Dr. Natascia De Leo for your endless support, guidance and for funding my PhD. I would like to express my sincere gratitude to my supervisor at IMEC, Professor Wilfried Vandervorst for giving me the opportunity to conduct a part of my PhD research at IMEC. Your continuous support, patience and knowledge helped me during all stages of my research and writing of this thesis. I would like to thank my daily supervisor Dr. Claudia Fleischmann for encouraging my research and her advice. I am indebted to Dr. Federico Ferrarese Lupi for his tremendous guidance during my research at INRIM.

I would like to acknowledge the Materials and Components Analysis (MCA) group at IMEC and especially the Atom Probe Tomography team. I am thankful to Janusz Bogdanowicz for the fruitful discussions we had. I learned from him the fundamentals of APT. I am grateful to Ramya Cuduvally for her willingness to help me through the technical challenges I have faced. I would like to thank Richard Morris, Jonathan Op de Beek and Davit Melkonyan for the discussions and all the fun we have had during my research at IMEC. Valentina Spampinato was one of my closest friends and colleagues at IMEC. I have greatly enjoyed working with her and I would like to especially thank for the ToF-SIMS analysis she has done for this PhD project. I would like also to thank Paromita Kundu for the TEM analysis that she performed for my research. I want to acknowledge the other colleagues at MCA group who helped me during my research- Alexis Franquet, Hugo Bender, Chris Drijbooms and Patricia Van Marcke. Finally, I

would like to especially thank Thomas Hantschel and Paul van der Heide for supporting my research at IMEC.

I would like to sincerely acknowledge all my colleagues at INRIM who made this research possible. I am grateful to Matteo Fretto for training me on the processing techniques in the cleanroom. I would like to thank Emmanuelle Enrico and Roberto Rocii for their technical support in the laboratory and Nanofacility of Piemonte. Many thanks to Dario Imbruglio for the AFM measurements he performed for this project. I have greatly enjoyed working with Eleonora Cara and I want to thank her for involving me in her research. I would like to thank Dr. Gianbartolo Picotto and his group in the Length Metrology department at INRIM for the measurements that they performed for this project as well as the fruitful discussions we had.

I am very grateful for all the external collaborators we had during this work. Dr. Michele Perego, Dr. Gabriele Seguni and the rest of their research group at MDM IMM-CNR for the preparation of a part of the DBC samples in this project. Prof. Michele Laus and Prof. Katia Sparnacci from the University of Eastern Piedmont for their collaboration and supports. Prof. Guido Mula and Dr. Elisa Pinna from the University of Cagliari for specimen preparation. I would like to thank Trustech company for funding my research before starting this PhD and for the technical support during this work. Many thanks to Laura Maria Boschis, Erasmo Chessa and Niccolò Ciprianetti.

I would also like to express my gratitude to all partners of the EMPIR project 3D MetChemIT who support this PhD work. More specifically, I would like to thank Dr. Burkhard Beckhoff, Dr. Philipp Hönicke and Dr. Yves Kayser and the rest of their group at PTB in Berlin for their contribution in this PhD project as well as their support and hospitality during my visit as a guest researcher at their research center.

I have no words to express how grateful I am to my parents for all you have done for me during these years. I would like to especially thank my beloved fiancée Shamin who has unconditionally supported me during this mobility program and helped me to stay focused on this work.

# List of Abbreviations

1D	One-Dimensional
2D	Two-Dimensional
3D	Three-Dimensional
4PP	Four-Point Probe Resistive Measurement
AFM	Atomic Force Microscope
APT	Atom Probe Tomography
ARDE	Aspect Ratio Dependence Etch
BCP	Block Copolymer
CRM	Certified Reference Material
CSR	Charge State Ratio
DBC	Di-Block Copolymers
DC	Direct Current
DFT	Density Functional Theory
DLD	Delay Line Detectors
DRIE	Deep Reactive-Ion Etching
EBL	Electron Beam Lithography
EDS	Energy-Dispersive X-ray Spectroscopy
FEA	Finite Element Analysis
FEM	Finite Element Method
FET	Field-Effect Transistor
FIB	Focused Ion Beam
FIM	Field Ion Microscopy
FinFET	Fin Field-Effect Transistor
FOV	Field-of-View
GISAXS	Grazing-Incidence Small-Angle Scattering

GIXRF	Grazing Incidence X-ray Fluorescence
GO	Geometrical Optics
HAADF	High-Angle Annular Dark-Field
HRXRD	High Resolution X-ray Diffraction
IAD	Ion Angular Distribution
IF	Image Force
IR	Infrared
LA-AP	Laser-Assisted Atom Probe
LEAP	Local Electrode Atom Probe
LWATAP	Laser Assisted Wide Angle Tomographic Atom Probe
MCP	Micro Channel Plate
MEMS	Micro Electro-Mechanical Systems
MOSFET	Metal-Oxide-Semiconductor Field Effect Transistor
NMI	National Metrology Institute
NW	Nano Wire
Pani	Polyaniline
PMMA	Poly (Methyl Methacrylate)
PS	Polystyrene
PSi	Porous Silicon
RBS	Rutherford Backscattering Spectrometry
RCP	Random Copolymer
RIE	Reactive-Ion Etching
RM	Reference Material
RTP	Rapid Thermal Processing
SE	Spectroscopic Ellipsometry
SEM	Scanning Electron Microscope
SIMS	Secondary Ion Mass Spectrometry
SIS	Sequential Infiltration Synthesis
SPM	Scanning Probe Microscope
SSRM	Scanning Spreading Resistance Microscopy
STEM	Scanning Transmission Electron Microscopy
TEM	Transmission Electron Microscopy
ToF	Time-of-Flight
ToFSIMS	Time-of-Flight Secondary Ion Mass Spectrometry
TXRF	Total-Reflection X-ray Fluorescence
UV	Ultraviolet
XANES	X-ray Absorption Near-Edge Structure
XPS	X-ray Photoelectron Spectroscopy

XRD	X-Ray Diffraction
XRF	X-ray Fluorescence
XSW	X-ray Standing Wave



# Contents

1. Introduction.....	1
2. Preparation of 3D organic/inorganic micro and nano structures for 3D ToFSIMS and GIXRF.....	6
2.1 Preparation of reference 3D microstructures for 3D ToFSIMS .....	7
2.1.1 Fundamentals of 3D ToFSIMS.....	8
2.1.2 Design and fabrication .....	10
2.1.3 Traceable dimensional characterization.....	12
2.1.4 Preliminary 3D ToF-SIMS analysis .....	14
2.2 Preparation of 3D nanostructures for GIXRF.....	18
2.2.1 Fundamentals of GIXRF.....	18
2.2.2 3D structures with sub micrometer scale.....	22
2.2.3 3D nanostructures at sub 20 nm scale.....	23
Self-assembly of DBC .....	23
Pattern transfer at sub 20 nm scale .....	27
Realization of 3D heterogeneous nanostructures.....	36
2.2.4 Preliminary GIXRF analysis.....	36
2.3 Conclusion .....	38
3. Fundamentals of atom probe tomography .....	41
3.1 Theory of field evaporation .....	43
3.1.1 Image hump model (Müller model).....	44
3.1.2 Charge-exchange model (Gomer model).....	46
3.2 Post-ionization .....	48
3.3 Evaporation rate.....	49
3.4 Laser-tip interaction.....	52
3.4.1 Thermal pulsing .....	53

3.4.2	Photoionization .....	62
3.4.3	Optical pulsing .....	62
3.5	Field emitter apex shape .....	64
3.6	Specimen preparation .....	66
3.6.1	Focused Ion-Beam milling (FIB).....	67
3.6.2	Preparation of organic materials .....	71
3.7	Conclusion .....	72
4.	Field-of-view in atom probe tomography .....	74
4.1	Electric field.....	75
4.1.1	Electric field at the specimen surface .....	76
4.1.2	Electric field around the specimen.....	80
4.2	Ion trajectories .....	85
4.2.1	Point-Projection model .....	88
4.2.2	Radial projection with angular compression .....	92
4.3	Image magnification .....	93
4.4	3D data reconstruction .....	94
4.4.1	Bas reconstruction protocol .....	94
4.4.2	Calibration of reconstruction parameters.....	97
4.4.3	Common artefacts and lateral resolution .....	100
4.5	Field-of-view (FOV).....	105
4.5.1	Field-of-view for hemispherical tip shape .....	107
4.5.2	Field-of-view for UV-induced asymmetric tip shape .....	108
4.6	Full tip imaging.....	120
4.6.1	Design of specimen shape.....	122
4.6.2	Specimen preparation .....	138
4.6.3	Experimental proof of full tip imaging.....	142
4.7	Conclusion .....	151
5.	Atom probe tomography on blanket films .....	154
5.1	Reference material .....	155
5.2	APT specimen preparation.....	158
5.3	APT analysis .....	158
5.3.1	Laser absorption with UV laser light.....	160

5.3.2	Laser absorption with green laser light.....	165
5.4	Quantification of Ge and B in SiGe.....	171
5.5	Precision of APT quantification for Ge and B.....	179
5.6	APT analysis of multi-layer systems .....	182
5.7	Conclusion .....	186
6.	Atom probe tomography on organic/inorganic 3D nanostructures .....	189
6.1	APT analysis of organics .....	190
6.2	APT specimen preparation.....	192
6.3	APT analysis of PSi filled with Pani .....	193
6.3.1	APT 3D data reconstruction .....	194
6.3.2	Fragmentation of polyaniline.....	196
6.4	Conclusion .....	200
7.	Conclusion and Outline .....	201
7.1	Feature-dependent RIE etch as sub 20 nm.....	202
7.2	Field-of-view in APT.....	203
7.3	Accuracy and precision in APT analysis .....	205
7.4	Analysis of organics in APT.....	206
7.5	Outline for future developments in APT analysis .....	207
	Appendix A.....	209
	Appendix B.....	211
	References.....	214



# List of Tables

Table 1: Design for the inorganic template (Si microstructure) in three model-systems.....	11
Table 2: Traceable dimensional characterization of structured Si templates using a calibrated optical profilometer. ....	13
Table 3: Average relative depth, measured after the deposition of each organic layer (polystyrene and irganox). The measurements were carried out by the optical profilometer. ....	14
Table 4: Extraction of sputter yields from the planar reference organic layers. The measured crater depths were used to estimate the sputter yields with the reported standard deviations (S). The obtained results are in good agreement with the reported values in literature (see the last column). Measurement conditions were: 10keV Ar <sup>+</sup> <sub>5000</sub> sputter beam (0.4 nA). Reported by the ToFSIMS group of IMEC. ....	15
Table 5: Characteristic of DBC masks: DBC molar mass (M <sub>n</sub> ), polystyrene block molar mass (M <sub>n</sub> styrene), polystyrene volume fraction (f), polydispersity Index (PDI), average cylinder diameter (d), average center-to-center distance (L <sub>0</sub> ), DBC film thickness (h). The aspect ratio was calculated as h/d. ....	26
Table 6: Comparison between the nominal Cr mass deposition, calculated according to the Cr density and the structural morphology, and the quantified value obtained from the reference-free GIXRF analysis. ....	38
Table 7: Comparison between different currently available techniques for the determination of specimen radius along the specimen depth. Please note that for all the three techniques the specimen shape is assumed to remain a truncated cone terminated by a hemispherical cap throughout the analysis. ....	96
Table 8: Estimation of the local magnification in APT analysis for the measurement stopped at the interface between SiGe and bulk Si. The local magnification at each interface position has been calculated and reported together with average magnification on each side of local maximum of the apex height (shadow side and laser side). ....	120
Table 9: The coefficients used to fit the empirical correlation between $\xi$ and $k_f$ $\xi = a + b \times k_f^{13} + c$ for each data set shown in Figure 74.....	137

Table 10: Comparison between the number of atoms detected in APT and the actual number atoms expected from the NW within the reconstructed volume. The expected number of atoms were estimated from the SEM image. ....	145
Table 11: Comparison between the average atomic density obtained from APT 3D data reconstruction of a slice of NW shown in Figure 82a. The standard atomic density of the native oxide is assumed to be equal to thermally grown silicon dioxide ( $2.3 \times 10^{22}$ atoms/cm <sup>3</sup> ). The compression factor for the volume was calculated based on the ration between obtained average density and the standard atomic density multiplied by the detection efficiency. For the fixed number of atoms and the NW height, the compression factor for the diameter was calculated as the square root of that of volume. Finally, the dimension of a NW having the standard atomic density and the same number of detected atoms was estimated by multiplying the reconstructed values of diameter/thickness by the calculated compression factor.....	146
Table 12: Average Ge concentration, B content and SiGe film thickness measured on the 300 mm wafer shown in Figure 87. For in-line characterizations techniques (HRXRD, SE and 4PP), the measurements were carried out across the entire wafer. While for GIXRF, SIMS and RBS the measurements were performed on a piece of wafer (40 mm < x < 60 mm, 40 mm < y < 60 mm). Please note that the associated uncertainty was only available for GIXRF-XRR and RBS measurements. The reported B content by GIXRF is the preliminary result.....	157
Table 13: The experimental parameters used to study the quantification and depth profiling of B doped SiGe film in LAWATAP APT tool.....	159
Table 14: The Ge concentrations and their statistical uncertainties obtained from the APT measurements at a fixed experimental condition and a Si CSR > 0.95. The precision of the APT measurement was also evaluated in view of the average Ge concentration. Please note that the reported statistical uncertainty was calculated according to standard deviation (including the counting statistics) of different voxels using the 68.27 % confidence level. ....	181
Table 15: Experimental condition used during APT analysis of the porous silicon filled with polyaniline. The measurement was carried out in LAWATAP instrument, where the pulse rate is fixed to a value of about 100 kHz. ....	194
Table 16: Recipe of the Bosch process used to etch the Si templates with a target depth about 2.3 $\mu$ m. ....	209
Table 17: Recipe of Cryogenic etch process used to etch the Si substrate using DBC masks. ....	209
Table 18: Brief description of the process steps used for the preparation of the potential reference sample for APT. ....	212
Table 19: DRIE Bosch recipe for etching of micropost using Oxford 100 Cobra DRIE tool. ....	213
Table 20: RIE etch recipe for etching of nanowire using Oxford 100 RIE tool. ....	213

# List of Figures

Figure 1: Schematic representation of four operational modes in ToFSIMS: (a) Surface spectroscopy (b) Surface imaging (c) depth profiling (d) 3D analysis. Reproduced from [4].	8
Figure 2: Template design for the reference structures in three model-systems. The image at the bottom schematically represents the cross-section for one of the above square shape unit cells after the depositing of the organic layers	11
Figure 3: SEM micrographs of the microstructured Si templates prepared according to the designed model-systems (on top). The SEM cross-section image for one of the 3D microstructures (model 3), filled with polystyrene and irganox.	12
Figure 4: Morphological characterization of the 3D microstructures after the deposition of each organic layer (polystyrene and irganox). The measurements were carried out by the optical profilometer.	13
Figure 5: Depth profile for the reference planar organic layers. The molecular fragments of the irganox1010 ( $C_{15}H_{23}O^+$ , $C_{56}H_{83}O_9^+$ ) and polystyrene ( $C_7H_7^+$ , $C_{15}H_{13}^+$ ) are labeled in blue and green color respectively. The Si signal is shown in red color. Reported by the ToFSIMS group of IMEC.	15
Figure 6: Depth profile obtained from 3D microstructured organic-inorganics systems from model 3 ( $5 \times 5 \mu m^2$ ). The molecular fragments of the irganox1010 ( $C_{15}H_{23}O^+$ , $C_{56}H_{83}O_9^+$ ) and polystyrene ( $C_7H_7^+$ , $C_{15}H_{13}^+$ ) are labeled in blue and green color respectively. The Si signal is shown in red color. Reported by the ToFSIMS group of IMEC.	16
Figure 7: Chemical maps obtain from ToFSIMS (first row) at different analysis depth (see the main text). The molecular fragments of the irganox and polystyrene are indicated in blue and green color respectively, while the Si signal is shown in red color. The corresponding SPM images, topography (second row) and phase (third row) are also shown below the chemical images. Reported by the ToFSIMS group of IMEC.	17
Figure 8: The comparison between the estimated layer thickness obtained from ToFSIMS measurement according to the sputter yields (irganox and	

polystyrene) and the SEM cross-section image of the same specimen model 3 ( $5 \times 5 \mu\text{m}^2$ structures). Reported by the ToFSIMS group of IMEC.....	17
Figure 9: 3D reconstructed volume for the developed 3D structure in model 3 ( $5 \times 5 \mu\text{m}^2$ ), according to the combination of the chemical maps (from ToFSIMS) and the topography (from SPM). Reported by the ToFSIMS group of IMEC.....	18
Figure 10: SEM image of the 3D Cr and Al nanostructures: (a) Cr randomly distributed, (b) Cr array-like ordered, (c) Al array-like ordered.....	23
Figure 11: SEM images of the perpendicularly oriented cylinders (at bottom) and the distribution of pore diameter (on top) calculated for different PS-b-PMMA BCP on a large area. The BCPs have molar masses ranging from 39 to 205 kg/mol. The reported values for pore diameter (d) and center-to-center distance ( $L_0$ ) were rounded to the nearest integer. Reproduced from [43].....	24
Figure 12: Schematic representation of the experimental procedures used for the self-assembly of PS-b-PMMA DBCs in perpendicularly oriented cylinders on the Si substrate and its successive pattern transfer. (a) Substrate cleaning and functionalization. (b) Deposition and grafting of random copolymer (RCP). (c) Deposition of block copolymer (BCP). (d) Phase-separation and self-assembly of PMMA (in yellow color) in perpendicularly oriented cylinders. (e) Selective removal of the PMMA cylinders. (f) Removal of RCP from the bottom of the cylinders. (g) Pattern transfer into the Si substrate. (h) Removal of the residuals of PS mask.....	25
Figure 13: (a) SEM image of the self-assembled DBC (B82) before the selective removal of the PMMA cylinders. (b) AFM height map of the same sample after the removal of the PMMA cylinders and the RCP thin film.....	27
Figure 14: The measured etch depth as a function of RIE etch time ( $t_{\text{RIE}}$ ) for the bare Si substrates (a) and the nanostructured Si by the B82 DBC pattern (b). 29	
Figure 15: Surface morphology of nanostructured Si after the pattern transfer from B82 DBC mask: (a–d) AFM micrographs, (e–h) transversal AFM depth profiles. The measured area was $250 \times 250 \text{ [nm]}^2$ for all the samples. Note that the measured depth of pores by AFM cannot be used to extract the depth of etch, due to the limitation of the AFM tip to deeply penetrate inside the narrow pores.....	30
Figure 16: (a) Etch depth in Si as a function of RIE etch time ( $t_{\text{RIE}}$ ) for the DBC masks having different pore diameters. (b) The calculated etch rates for the different DBC masks as a function of their pore diameters. The etch rate for the bare Si is also indicated by a green dashed line.....	31
Figure 17: Evolution of the pore diameter in Si as a function of etch time for the three groups of DBC masks. The mask diameter for each DBC group is also indicated by a dashed line in the figure. The reported pore diameters were calculated from the SEM images. For $t_{\text{RIE}} < 50 \text{ s}$ , due to the insufficient contrast in the SEM images, the pore diameters were not reported. ....	32
Figure 18: SEM image of the nanopatterned Si structures after the pattern transfer of the DBC masks using different etch durations. Four operation windows were identified (see the main text for the criteria) as: (A) Incomplete pattern transfer. (B1) Good pattern transfer. (B2) Appearance of roughness surface. (C) Distorted zone. ....	33

Figure 19: Comparison between etch behavior of B54 DBC masks having different thicknesses: 30 nm and 40 nm. The horizontal axis shows the etch duration. ....	33
Figure 20: (a) Schematic representation of the prepared 3D heterogeneous nanostructures by the deposition of Al over the nanostructured Si, SiO <sub>2</sub> and the B67 DBC mask. (b) The SEM image of a self-assembled DBC mask (B67) before the deposition of Al. (c) The SEM image of the same mask after the deposition of Al. ....	36
Figure 21: (a) Experimental GIXRF curve for array-like ordered Cr nanostructures as a function of the incident angle for the different in-plane orientations indicated by $\varphi$ angle (see the inset). (b) The comparison between the experimental fluorescence signal with GIXRF (black) and calculated model (red). The green-dotted curve indicates the fraction of GIXRF signal by the XSW excitation. The blue-dotted curve describes the direct excitation at the sides of the structures. ....	37
Figure 22: Comparison among GIXRF angular fluorescence profiles (Al-K signal) for different nanostructures obtained from DBC masks (see the inset). ....	38
Figure 23: Schematic representation of APT measurement setup in laser mode using local electrode. ....	42
Figure 24: 1D potential energy diagram versus distance from the surface. (a) In the absence of electric field, atoms are bonded to the surface with cohesive energy $\Lambda$ , while ions are attracted to the surface by image force. The required energy to n-times ionize and remove an atom from the surface is $Q_{0,n}$ . (b) In the presence of electric field and by considering only the electrostatic repulsive force $eF$ (neglecting other intrinsic repulsive forces), an energy barrier $Q_b$ must be to overcome to n-times ionize and remove an atom from the surface. This diagram shows the classical description of barrier height in the original Müller model. (c) The quantum description of barrier height $Q_b$ which is known as charge-exchange model. In this model, the electrostatic Maxwell stress is also taken into account which can pull out the atom from the surface. The corresponding energy barrier $Q_b$ in this model is lower than the approximated value by Müller model (b). Reproduced from the reference [82]. ....	44
Figure 25: Kingham curve for Si. The vertical axis indicates the CSR of the Si Si <sub>2</sub> + /Si <sub>2</sub> + +Si <sub>1</sub> + $\times 100$ and the horizontal axis shows the intensity of electric field. Reproduced from the reference [94]. ....	49
Figure 26: Arrhenius plots for field evaporation of at three different electric fields ( $F_1 > F_2 > F_3$ ). The vertical axis shows the logarithmic scale of the evaporation rate in layer per second. The experimental data points are indicated by black dots on the figure. At each electric field, the data points were interpolated by two linear functions: Blue (tunneling regime) and red (Thermally activated regime). The corresponding barrier height $Q_b$ at each electric field ( $F_1$ , $F_2$ and $F_3$ ) is also reported in the figure. The transient between thermally activated regime and tunneling regime can be seen at low temperature ( $T < 40$ K) for $F_1$ and $F_2$ plots. Reproduced from the reference [100]. ....	50

Figure 27: Schematic representation of various combinations of electric field and temperature which can result in field evaporation at three different evaporation rates  $\Phi_1 > \Phi_2 > \Phi_3$ . The  $\Phi_2$  curve corresponds to a calibration curve of field and temperature for tungsten tip at fixed detection rate of 0.005 [104]. The schematic view of the pulsing modes at a constant base temperature (Voltage pulsing) or constant DC field (Thermal pulsing) is also depicted in blue. ....52

Figure 28: The absorption map of Al tip in the incident laser with axial polarization obtained by finite difference simulation in time domain. (a) laser wavelength equal to 355 nm (b) laser wavelength equal to 1200 nm. (c) Normalized absorption density profile along the tip axis for  $\lambda=360$  nm (blue),  $\lambda=515$  nm (green),  $\lambda=800$  nm (red), and  $\lambda=1200$  nm (brown). In the inset, the zoom of absorption profiles at the apex for  $\lambda=360$  nm (blue) and 515 nm (green) is shown. Reproduced from the reference [111]. ....55

Figure 29: Schematic representation of photon absorption in the silicon for three different wavelengths. Reproduced from [113]. ....56

Figure 30: Electron and lattice excitation and relaxation mechanism for a direct band-gap material, excited by the laser photons. (a) multiphoton absorption, (b) free-carrier absorption, (c) impact ionization, (d) carrier distribution, (e) carrier-carrier scattering, (f) carrier-phonon scattering, (g) radiative recombination, (h) Auger recombination, (i) diffusion of excited carriers, (j) thermal diffusion, (k) ablation and (l) resolidification or condensation. (m) The timescales for all the aforementioned processes involved. Reproduced from [114]. ....57

Figure 31: The absorption map computed by finite-difference time domain simulation for a silicon tip with apex radius of 35 nm and a shank angle of  $4^\circ$ , using three different wavelengths (a) IR at the wavelength of 1030 nm, (b) Green at the wavelength of 515 nm, (c) UV at the wavelength of 345 nm. The laser comes from top (vector  $k$ ) and it is polarized parallel to the tip axis (vector  $F_{opt}$ ). The unit for the colorbar is  $J/m^3$ . The insets show the zoom view of the first 450 nm (in Z direction) of the absorption maps. Reproduced from [113]. ....59

Figure 32: Schematic representation of the reduction in the band-gap under the presence of an intense electric field within the semiconductor bulk material. The dotted rectangles are the schematic of the new band structure, where the new band-gap ( $E_{gap}'$ ) is shown by a dotted red arrow. The required photon energy to be absorbed by the material in the presence and absence of the electric field is indicated by black and dotted red arrow. Reproduced from [82]. ....60

Figure 33: (a) Mass spectrum of  $Si282 +$  peak analyzed by APT at  $\lambda=650$  nm. The fast and delayed evaporation processes are indicated on the spectrum. (b) the conversion of the mass spectrum in time, where  $t=0$  corresponds to the maximum intensity of  $Si282 +$  peak. The fast evaporation mechanism (black dash line) is interpolated by a Gaussian function with a standard deviation of 150 ps. The delayed evaporation (black solid line) starts with a leading edge of about 1.5 ns and ends with a trailing edge which takes about 3 ns. The maximum of the

slower process has a delay of about 3 ns respect to the fast evaporation process. Reproduced from [82].....	63
Figure 34: SEM images of specimens after APT analysis using (a) UV laser and (c) Green laser. In (b) and (d) The numerically predicted absorption map for UV and green laser are shown respectively. The laser direction was from left to right for all the figures. Reproduced from reference [128].....	65
Figure 35: The standard specimen preparation using FIB based technique. (a) deposition of a Pt capping layer over the region of interest. (b) Ion milling around the side of the region of interest, which is covered by Pt cap, and the successive V shape milling and preparation of cantilever wedge (lamella). (c) Removal of the lamella by in-situ micromanipulator. (d) Fine positioning of the lift-out lamella on top of the career micropost. (e) Welding the one side of the lamella to the career post using Pt deposition and cut the rest of the lamella. (f) Welding the other side of V-shaped wedge. (g) Realigning the region of interested to start the tip sharpening step. (h) Annular milling the chunk of material into the cylindrical shape. (i) Further milling with the annular pattern while the diameter of the pattern is progressively reduced. (k) Final cleaning step with low energy beam (2 or 5 keV) without any pattern to reduce the tip diameter and remove the FIB induced damages. (m) low and (n) high magnification image of the final specimen for APT analysis. Reproduced from the reference [133].....	68
Figure 36: SEM images of a commercially available array of career microposts from Cameca (a) and single tungsten wire (b). .....	68
Figure 37: The comparison among the extent of Ga implantation in steel predicted by Monte Carlo simulation (dash lines) and measured by APT (solid lines) for two different milling conditions (30 kV in red and 5kV in black). Reported from reference [83]. .....	69
Figure 38: An example of APT mass sepctar for C60-doped P3HT polymer, obtained from an APT tip prepared by dip coating (a) and FIB lift-out technique (b). The molecular peaks for the polymers are absent in case of FIB lift-out sample prep. The spectra are reported from reference [136].....	70
Figure 39: Schematic representation of electric field direction (a) and the uniform charge density (b) at the surface of metallic sphere having a radius of R. Reproduced from reference [82].....	76
Figure 40: Local field enhancement and charge distribution for different Au (110) surfaces obtained from quantum calculations: (a) 1x1, (b) 1x2, and (c) 1x3 missing-row surface reconstruction. The positions of the ions are indicated by black dots and the positive and negative contours for charges are plotted in red and green respectively. Reproduced from reference [152].....	78
Figure 41: (a) Distribution of electric field in the vicinity of <001> terrace for a specimen having a simple cubic lattice structure. The inset shows the relative intensity of electric field above the first terrace as a function of the distance from the terrace center (indicated by r). The intensity of the electric field progressively increases toward the terrace edge. (b) The local field enhancement factor $\gamma$ , computed on the 3D apex surface of hemispheric metallic tip with FCC structure.	

The  $\gamma$  maximizes at the edge positions of crystalline terraces. Reproduced from reference [89]. ..... 79

Figure 42: Schematic representation of voltage drop along the APT specimen height for insulating material. At the presence of strong electric field, the band bending causes voltage drop in the vicinity of the apex. The ion emission (evaporation event) can cause carrier generation and the corresponding electric current  $I_{\text{evap}}$ . Under the laser illumination the charge density increases significantly which improve the conductivity in the specimen depth. The voltage drop along the specimen depth is shown: in the absence of ion emission and no laser illumination (dashed black line), in the presence of ion emission and no laser illumination (solid blue line), in the presence of ion emission and laser illumination (solid red line). Reproduced from reference [82]. ..... 80

Figure 43: Schematic representation of boundary condition problem and the system design for finite element analysis using COMSOL multi physics software package. To reduce the computational power, only a part of chamber volume ( $x = 100 \mu\text{m}$ ) is considered in our analysis, where the distribution of the electric field is unaffected from the choice of  $x$ . The defined boundary conditions are as the follows: zero-charge (in black), fixed applied potential (in red), equipotential (in blue) and internal axisymmetric boundary (in green). The specimen is assumed to be a tall cylinder having a small radius  $r$  and height of  $L$ . The actual dimension for the local electrode aperture and the specimen to detector distance in LEAP 5000 APT instrument has been considered in our study. Please note that the figure is not in scale. .... 82

Figure 44: Generated triangular mesh for the two-dimensional control volume described in Figure 43. A fine mesh size was employed in the vicinity of tip apex to capture the variation of the electric field close to the apex (inset). The tip diameter and height were fixed to 60 nm and 50  $\mu\text{m}$  respectively. .... 83

Figure 45: Finite element simulation of electric field around the APT specimen (diameter: 60 nm, height: 50  $\mu\text{m}$ ) at 1 kV applied potential. The color bar indicates the magnitude of the electric field in V/m. The magnitude of electric field drops significantly as the distance from tip apex increases e.g. it drops about an order of magnitude at 80 nm away from the tip apex. .... 83

Figure 46: Validity assessment of finite element analysis (FEA) of the electric field at the specimen apex. (a) the expected linear trend between the magnitude of electric field and applied potential ( $F = VkfR$ ) was investigated for six different tip heights having the same tip diameter of 60 nm. The slope of each line is determined by the  $1kfR$ . (b) The validity of our FEA has been compared and assessed by a numerical study by Loi S. T., et al. [151]. In particular field factor  $k_f$  has been calculated for different tip dimensions (different diameters and heights) as described in this reference. A good agreement between the simulated data and values of  $k_f$  reported in this reference has been obtained with average deviation below 1%. .... 84

Figure 47: Finite element analysis of ion trajectories and electric field lines for a 50  $\mu\text{m}$  long nanowire with a diameter of 60 nm. The apex was uniformly covered by 20 particles having the unit charge and mass of  $4.66 \times 10^{-24}$  g. After

the release of particles in the presence of the calculated electric field, their trajectories towards local electrode were tracked and reported in (a). The color bar indicates the magnitude of the ion velocity at each stage of the flight. The inset (b) shows the enlarged view of the particle trajectories in the vicinity of the tip apex with the same color code as the main plot (a). The electric field lines, generated from the tip apex are also reported in (c), where the color map shows the magnitude of the electric field at the applied potential of 1000 V. ....87

Figure 48: Schematic representation of point-projection model and the definition of image compression factor  $\xi$ . Reproduced from [83]......89

Figure 49: (a) Detector hit map (desorption image) for pure Al after collection of 300,000 events. The main poles are indexed by red color on the hit map. The schematic representation of the image compression factor ( $\xi$ ) as a function of the angle between the major crystallographic planes ( $\theta_{\text{crys}}$ ) and the corresponding angle between the indexed poles on the desorption image. The figure is reproduced from the references [83] and [163]. .....90

Figure 50: Relation between image compression factor ( $\xi$ ) and field factor ( $k_f$ ). (a) numerically obtained trend by finite element analysis of a hemispheric tip shape with different shank angles (1 to 30 degrees) and specimen-to-detector distances (0.03 to 1.8 m) [164]. (b) Experimental observation of the relation between  $\xi$  and  $k_f$ , extracted from different measurements on Al alloys (different colors codes) for a range of radius of curvatures. The expected power law is also indicated with a dashed line. Reproduced from reference [165]. .....91

Figure 51: Variation of the magnitude of electric field and image compression factor ( $\xi$ ) as a function of launch angle  $\theta$  (angular distance from the specimen axis). The analysis was obtained by finite element simulation of a truncated hemispheric cap with 60 nm tip radius and  $10^\circ$  shank angle. Reproduced from reference [151]. .....92

Figure 52: The accuracy of radial projection with angular compression model versus point-projection model to describe the projection of ions and formation of desorption map for pure Al. The distance between the poles on the desorption map (D) is plotted against the crystallographic angles on the specimen (planes direction) in degrees. The markers are the angular distances of the poles from the origin of the projection, while the radial projection with angular compression model is plotted in dash line and point-projection in solid line. Reproduced from reference [83]. .....93

Figure 53: Schematic representation of the correction factor to account for tip curvature instead of the tangent plane. Reported from reference [83]. .....96

Figure 54: Schematic representation of some common artefacts which degrade the lateral resolution of APT analysis. Reproduced from reference [82]. ..... 100

Figure 55: Evolution of tip shape for a metallic multi-layer system consisting of species with different evaporation field. (a) Schematic representation of the layers. (b) to (i) evolution of tip shape for different sequences of evaporation obtained by finite element simulation. (j) TEM image of the specimen apex shape after several sequences of evaporation. Different radii of curvature have been induced due to the differences in the field evaporation of the layers. (k) 3D

reconstructed volume from the simulated data, whereby a considerable distortion is predicted due to the induced artefacts by trajectory aberration. (l) 3D reconstructed volume obtained from the APT measurement, whereby similar to the predicted shape the trajectory aberration caused an artefact in the reconstructed volume. The inset shows atomic plains in the FeCo layer. Reproduced from reference [172]..... 102

Figure 56: (a), (b) Trajectory aberration and formation of zones with high and low density on the desorption map for the same multilayer system reported in the Figure 55. (a) The position of the dense ring on the desorption map, is assigned to the local dips on the tip shape. The TEM image of the tip shape is also reported. Each desorption map contains 10,000 events. Reproduced from reference [83]. ..... 102

Figure 57: Representation of field-of-view (FOV) in atom probe microscopy for Al (face centered cubic lattice). (a) Desorption image of the surface atoms measured in field ion microscopy. (b) 3D representation of surface atoms for FCC lattice of Al. FOV is depicted with orange dash line, crystallographic directions are indicated by green  $\langle 011 \rangle$  and blue  $\langle 002 \rangle$  arrays and finally zones axis are indicated by solid lines, following the color code of crystallographic directions. Reproduced from reference [82]..... 105

Figure 58: Schematic comparison between field-of-view (FOV) and solid-angle-of-detector for a hemispheric apex shape. The trajectory of the last ion within the FOV is schematically represented in red. The corresponding image compression factor ( $\xi$ ) is also depicted..... 106

Figure 59: TEM images of a prepared APT specimen according to the developed FIB based sharpening protocol, where as a the thick amorphized shell was induced by the FIB damage (Ga ions) around the crystalline core of the specimen. (a) schematic representation of the wafer used for the preparation of the APT specimen. (b) TEM image of the prepared specimen using the developed protocol. Each material on the image is labeled based on the image contrast. (c) zoom view of the interface between amorphized and crystalline interface in bulk Si. (d) and (e) the fast Fourier transform of a part of the TEM image shown in (c), corresponding to the amorphized and crystalline phase respectively. The periodic pattern in (e) clearly indicates the presence of ordered crystalline structure in the dark core region of the specimen image. .... 109

Figure 60: 3D reconstruction of APT measurement on a specimen prepared according to the developed specimen preparation protocol. (a) The 2D Ga atomic concentration and Si density maps for a slice of the specimen from height of 20 to 30 nm. The 2D Si CSR, Si density and Ga atomic concentration maps are plotted for the slice of specimen from a height of 80 to 96 nm (b) and 130 to 146 nm. (d) The 2D Ge atomic concentration and Si density maps are plotted at the interface between SiGe and bulk Si, corresponding to a slice of specimen with a height from 170 to 186 nm. The lateral position (in x direction) of the observed ring and its diameter are compared for different 2D maps by drawn dash line in (b) and (c). The APT measurement was carried out in LAWATAP tool using UV laser wavelength at a laser power corresponding to Si CSR of about 20 %. .... 110

Figure 61: Estimation of local apex curvature from the TEM image of the APT specimen, which its APT measurement was stopped at SiGe/Si interface. (a) Calculated tangent vector at each pixel P of the apex boundary by fitting a line to 81 pixels centered at the pixel P. (b) Identification of apex boundary on the TEM image of the specimen apex. (c) A zoom view of the apex border defined on the binary TEM image. A fitted line centered at the pixel P over 50 pixels is also shown in red. (d) High-angle annular dark-field scanning TEM (HAADF) image of the specimen shown in (b), where the remained SiGe at the interface is visible on the top most region of the specimen. .... 114

Figure 62: TEM images of the APT specimen at different radial orientations respect to specimen axis: (a) The laser illuminated side (b) The shadow side. The direction of laser illumination has been approximately shown on the figures. (c) The orientation of the captured TEM images are indicated by the dash lines on the APT 2D density map obtained from the last 3 M detected events. The APT measurement was carried out in UV laser mode (Si CSR ~ 20 %) and the measurement was stopped at the SiGe/bulk Si interface. .... 117

Figure 63: Correlation of the TEM image of the specimen after the APT measurement to the APT hit map in the corresponding direction, where the APT measurement was stopped at the interface between SiGe and bulk Si. (a) A central slice of APT hit map for the last 300,000 detected events, where the Si<sup>+</sup> ions are represented by red dots. (b) The same APT hit map shown in (a), while the Ge<sup>+</sup> ions are also shown in green dots. (c) Bright-field scanning TEM image of the specimen after APT measurement together with high-angle annular dark-field scanning TEM (HAADF) image in the inset. The identification of the tip axis, detector center line and the interfaces are discussed in the text. The interfaces are labeled as the following: Interface I: amorphized/crystalline SiGe, Interface II: SiGe and bulk Si and Interface III: amorphized/crystalline Si. The ion trajectories (Si in red and Ge in green) and the normal of the apex (in orange) are schematically represented at the apex for the ions evaporated from the interfaces and the top most part of the tip. .... 118

Figure 64: Schematic representation of a new APT specimen design consist of a nanowire prepared on top of a cylindrical micropost. Note that the design is not to scale. .... 123

Figure 65: Finite element simulation of the magnitude of the electric field for a nanowire tip shape prepared on top of a cylindrical micropost. (a) Variation of the magnitude of electric field in the vicinity of tip apex depending on the micropost diameter and height. The applied electric potential was 1kV for all the simulations. (b) Field factor  $k_f$  as a function of the micropost diameter and height (legend value). Note that the nanowire dimension was kept constant to a diameter of 80 nm and height of 800 nm for all the simulations. .... 124

Figure 66: Influence of the nanowire (NW) dimension on the field enhancement at the tip apex as investigated by finite element analysis. (a) Influence of the NW diameter on  $k_f$ , for a range of nanowire diameters from 40 to 160 nm and micropost dimensions (shown in the legend), while the NW height was kept constant to 600 nm. (b) Influence of the NW height on  $k_f$ , for a range of

nanowire heights (200 to 1200 nm) and micropost dimensions (shown in the legend), while the NW diameter was kept constant to 80 nm. In both figures, the calculated  $k_f$  for the given range of NW dimension (diameter or height) were normalized to the  $k_f$  obtained from the NW having (a) diameter equal to 80 nm with the same micropost dimension (b) NW having a height equal to 600 nm with the same micropost dimension..... 126

Figure 67: Compression of the electric field lines created at the tip apex for different designs of the APT specimen. (a) The influence of the micropost diameter on the compression of the electric field lines is shown for two different diameters ( $D_1=1$  and  $D_2=11 \mu\text{m}$ ), while the post height was kept constant to 50  $\mu\text{m}$ . (b) The influence of the micropost height on the compression of the electric field lines for two different heights ( $L_1=5$  and  $L_2=50\mu\text{m}$ ) at a fixed post diameter equal to 3  $\mu\text{m}$ . The nanowire height and diameter were identical for all the figures (diameter: 80 nm and height: 600 nm). The field lines were drawn uniformly from the tip apex and the magnitude of electric field is alternatively indicated by the color bar at 1 kV applied electric potential. .... 128

Figure 68: Compression of the electric field lines due to the presence of a flat area on top of the cylindrical micropost. (a) schematic representation of the electric field at the tip apex, nanowire sidewalls and on the flat area of micropost. Distribution of the electric field lines created from the tip apex, nanowire sidewalls and on the flat area of the micropost was plotted for a micropost having a height equal to 50  $\mu\text{m}$  and a diameter equal to 500 nm (a) and 11  $\mu\text{m}$  (b). The nanowire height and diameter were identical for both figures (diameter: 80 nm and height: 600 nm). Note that the electric field lines were drawn uniformly from the specimen surface and the magnitude of electric field is alternatively indicated by the color bar at 1 kV applied electric potential. .... 129

Figure 69: Ion trajectories in between the specimen apex and the local electrode for the standard APT specimen (top) and the proposed specimen design (NW prepared on top of cylindrical micropost). (a) The influence of micropost diameter on the compression of ion trajectories for two different micropost diameters ( $D_1=1$  and  $D_2=11 \mu\text{m}$ ), while the post height was kept constant to 50  $\mu\text{m}$ . (b) The influence of micropost height on the compression of ion trajectories for two different heights ( $L_1=5$  and  $L_2=50\mu\text{m}$ ) at a fixed post diameter equal to 3  $\mu\text{m}$ . Note that the nanowire dimension is identical for all the figures (diameter: 80 nm and height: 600 nm). The color bar shows the magnitude of ion velocity along the traveling path, which was calculated at 1kV applied electric potential. .... 130

Figure 70: Variation of field factor  $k_f$  (in black) and image compression factor  $\xi$  (in red) as a function of the angular distance from the specimen axis (launch angle). The analysis was carried out by finite element simulation for a nanowire (diameter: 80 nm and height: 600 nm) mounted on top of a cylindrical micropost having a diameter of 5  $\mu\text{m}$  and a height of 20  $\mu\text{m}$ . Note that the calculated  $\xi$  at zero angle had a relatively high error due to the propagation of the error caused in the calculation of the trajectory slope at the aperture position for such a straight flight path. .... 132

Figure 71: Image compression factor  $\xi$  calculated for different combinations of micropost diameter and height, which are indicated in the horizontal axis and the legend respectively.  $\xi$  was calculated for different micropost dimensions using finite element simulation of ion trajectories at 1 kV applied potential, while the nanowire diameter and height were kept at 80 and 600 nm respectively. .... 134

Figure 72: Relation between image compression factor ( $\xi$ ) and field factor ( $k_f$ ) for a nanowire tip shape prepared on cylindrical micropost.  $\xi$  and  $k_f$  were calculated for 36 different specimen dimensions by varying the micropost heights in a range: 5, 10, 20, 30, 40 and 50  $\mu\text{m}$  and micropost diameter in a range: 1, 3, 5, 7, 9 and 11  $\mu\text{m}$ . The nanowire diameter and height were kept constant to 80 and 600 nm respectively. The finite element simulation was carried out at 1 kV applied potential. .... 134

Figure 73: Correlation between image compression factor  $\xi$  and field factor  $k_f$  as a function of the applied potential  $V$  for a NW tip shape on top of cylindrical micropost. The applied voltage was varied from 1 to 5 and 10 kV and  $\xi$  was calculated at 12 field factors  $k_f$  corresponding to different micropost heights (5, 10, 30 and 50  $\mu\text{m}$ ) and diameters (2, 5, and 11  $\mu\text{m}$ ), while the nanowire diameter and height were kept constant to 80 and 600 nm respectively. .... 135

Figure 74: Influence of the nanowire dimensions on the image compression factor  $\xi$  plotted against the field factor  $k_f$ . (a) Influence of NW diameter on  $\xi$ . The NW diameter was varied in a range between 40 to 160 nm, while the NW height was kept constant to 600 nm. The finite element simulation of the ion trajectories and the calculation of  $\xi$  were repeated for four different microposts having a height of 50  $\mu\text{m}$  and diameters of 3, 5, 7 and 11  $\mu\text{m}$ , corresponding to post 1 to 4 in the legend. (b) Influence of the NW height on  $\xi$ . The NW height was varied in range between 200 to 1600 nm, while the NW diameter was kept constant to 80 nm. Note that only the NW height creating a  $k_f$  below 35, were reported in this figure. .... 137

Figure 75: Required dimensions of the cylindrical micropost, which can create enough field enhancement at the NW apex and maximize the field-of-view during APT analysis. This window was calculated for a NW having a diameter of 80 nm and height of 600 nm. The criteria for identifying the operation window were based on:  $2 < \text{field factor } k_f < 25$  and image compression factor  $\xi > 2$ . .... 138

Figure 76: (a) Schematic representation of the 4-inch wafer design consisting of 26 unit cells, shown by blue rectangles. The green rectangles are the alignment markers for the different lithography steps. (b) Schematic representation of a unit cell consisting of 8 different cells each having a fixed micropost diameter from 1 to 11  $\mu\text{m}$ . (c) The chip design consists of 16 micropost in four staggered rows. Each row ends to a single or double circular fiducial to facility the navigation among different microposts using the APT tool. .... 139

Figure 77: (a) SEM micrograph of a circular pattern of HSQ resist obtained by electron beam lithography (EBL). The target diameter for this pattern was 80 nm. (b) SEM micrograph of four different nanowires after the pattern transfer into the silicon (100) substrate by reactive ion etching technique. The target diameter for

each NW is reported on top the of the SEM image. All SEM images were taken at 52° tilt angle using 5 kV in the immersion mode..... 140

Figure 78: Preparation of a cylindrical micropost using optical lithography and deep reactive-ion etching (DRIE). (a) SEM micrograph of the patterned optical resist obtained from optical lithography process. The target diameter and the actual diameter of each pattern is shown in the figures. An etched micropost with the target diameter of 6  $\mu\text{m}$  (b) and 3  $\mu\text{m}$  (c) are shown. Note that due to the degradation of the resist at the edges of the pattern, a roughness on the micopost sidewalls develops and a slight reduction in the apparent micropost diameter was observed for tall microposts..... 141

Figure 79: A final APT specimen consisting of a nanowire prepared on top of a cylindrical micropost with the dimensions according to the FEA. (a) Image of the prepared chip in the form of micro coupon consisting of 16 microposts. The inset shows the SEM image from the edge of the prepared chip, where the three microposts can be seen. (b) SEM image of one micropost with the NW prepared on the top. The micropost had a diameter and a height of 5 and 35  $\mu\text{m}$  respectively. Since the edges of the micropost were smoothed by FIB, a reduction in the microspost diameter (to 3  $\mu\text{m}$ ) on the very top part of the post is observed. (c) Enlarged view of the NW prepared on the top of micropost with a design diameter of 80 nm and height of 600 nm. The NW was cleaned by FIB to ensure the complete removal of the oxide resist from the top region of the NW. This caused a tapered shape on the first 80 nm of the NW. All SEM images were taken at 52° tilt angle using 5 kV. .... 142

Figure 80: Laser and specimen alignment for the microcoupons with a nanowire tip on top of a cylindrical micropost. (a) Navigation from one micropost to another micropost following the standard procedure suggested by CAMECA for the standard micro coupons. Note that there were two missing microposts in the first row. (b) Alignment of 35  $\mu\text{m}$  long micropost in front of local electrode. The laser alignment was also carried according to the standard procedure. (c) Difficulty in the alignment of a short micropost (14  $\mu\text{m}$  long), where the local electrode became very close to the flat area of the micro coupon. .... 143

Figure 81: The 3D reconstruction of the APT data obtained from a NW tip prepared on top of cylindrical micropost having a diameter of about 5  $\mu\text{m}$  and height of 36  $\mu\text{m}$ . (a) SEM image of the NW before APT measurement. Three different regions are highlighted on the SEM image: Region I: the unreconstructed top part of NW corresponding to 1.7 M detected events before the auto laser alignment was completely achieved. The height of this region was calculated from the SEM image. Region II and II: tapered and zero degree-shank angle regions of the NW corresponding to 17.3 M detected ions. The height of these two regions were obtained from the APT reconstructed data. (b) 3D reconstruction of APT data, where  $\text{Si}^+$  and  $\text{Si}^{++}$  ions are represented by the blue dots and  $\text{O}^+$  and  $\text{SiO}^+$  ions by the red dots. (c) To visualize the core central region of the reconstructed tip, a section cut along the y plane (with  $y = 0$ ) is plotted. . 144

Figure 82: 2D density and concentration maps plotted for a slice of the NW from a height of 100 nm to 150 nm (a). (b) The 2D atomic density map for all

decomposed atoms: Si, O and C. The 2D atomic concentration maps were also plotted for Si in (c), O in (d) and C in (e). ..... 145

Figure 83: Estimated image compression factor ( $\xi$ ) as a function of angular distance from the specimen axis (launch angle) for two different NW heights corresponding to the initial and the end height of shank region in the 3D reconstructed APT data (height of 344 and 455 nm). The calculation of  $\xi$  was obtained by finite element simulation of ion trajectories. .... 147

Figure 84: Reconstruction artefact induced due to the differences between the field evaporation of Si (or Ge) and SiO<sub>2</sub>. (a) Cross-sectional dark-field scanning TEM image of the SiGe fin before APT specimen preparation. (b) SEM image of the APT specimen prepared from the SiGe fin. (c) 3D reconstructed APT data, where the Ge, Si and O atoms were represented by blue, red and green dots. The fin width in the reconstructed data is smaller than the actual value. (d) Estimated tip shape and electric field distribution by finite element simulation. (e) Ion trajectories evaporated from one atomic row above the calculated apex shape, where the ion trajectories from the SiO<sub>2</sub> and fin region are shown in green and blue respectively. The figure is reported from reference [13]. ..... 149

Figure 85: Applied potential during APT analysis. (a) Different regions of the NW heights were used to construct the schematic representation. The height of region I (not reconstructed part) was estimated from the SEM image of the tip, based on the number of ions detected before the complete laser alignment. While, the height of region II (tapered region) and III (null-shank angle) were extracted from the 3D reconstructed data. (b) The experimental voltage curve is plotted in blue and the predicted voltage curve by FEA in red. The trend was only calculated for shank region of the tip (region III) and the calculation was based on the simulated field factor ( $k_f$ ) for NWs having different heights (similar to different sequences of evaporation) and knowing the experimental voltage at the ion sequence of 5.5 M. .... 150

Figure 86: Increase in the background noise for mass spectrum/time-of-flight for ion sequences > 17 M. (a) The collected mass spectrum versus ion sequences. The major Si peaks are also identified on the figure. (b) Detection rate (in black) and background level for time-of-flight (in blue) are plotted versus ion sequence. The background level raised markedly for ion sequences > 17 M, while the detection rate remained unchanged. .... 151

Figure 87: (a) Schematic representation of 300 mm wafer used in our study, where the SiGe (100) and Si (100) have been epitaxially grown on a bulk Si (100) wafer. (b) Distribution of SiGe film thickness across the entire wafer area, measured by spectroscopic ellipsometry (SE). The color bar indicates the thickness values. The region demarcated by red lines was selected for APT, SIMS and RBS analysis (c) Distribution of active B concentration across the entire wafer area, measured by four point probe (4PP) resistive measurement technique. The measurements have been performed at 48 points, indicated by the black dots and the resistance were interpolated elsewhere. Please note that 4pp measurement was performed on the wafer without the Si cap layer. .... 156

Figure 88: (a) Schematic representation of the wafer used for the preparation of APT specimens. (b) SEM image of one of the prepared APT specimens using the standard FIB lift-out technique. The image was taken after the 5 keV cleaning step. The measured specimen diameters, from the SEM image, at the tip apex, initial of SiGe layer and at the end of SiGe layer are shown on the image. .... 158

Figure 89: Laser power and the measured Si CSR ( $\text{Si}^{2+}/(\text{Si}^{2+}+\text{Si}^+)$ ) for APT analysis in UV (left) and green (right) laser light. Each point on the figures corresponds to one APT specimen measured at a fixed laser power. The error bars have been computed according to the combination of counting statistics and the standard deviation of the Si CSR over a voxel of  $1 \times 1 \times 5 \text{ nm}^3$  in the 3D reconstructed volume. Please note that the measurements were carried out at a fixed detection flux ( $\sim 0.005 \text{ atom/pulse}$ )..... 159

Figure 90: The distribution of Si CSR ( $\text{Si}^{2+}/(\text{Si}^{2+}+\text{Si}^+)$ ) across a 50 nm thick section (in z direction) of the specimen in the SiGe region in the direction of UV laser illumination (a) 1D distribution of Si CSR across x direction (laser illumination) of the reconstructed data for the APT measurements carried out at different laser powers. The horizontal axis shows the normalized lateral positions with respect to the reconstructed tip radius for each measurement. (b) 2D Si CSR map for the same measurement reported in (a) at laser powers equal to 3, 8 and 12 mW. (c) The absorption map computed by finite-difference time domain simulation (reported from [128]) for a silicon tip having an apex radius of 35 nm and a shank angle of  $4^\circ$  illuminated by UV laser light. .... 161

Figure 91: Si CSR ( $\text{Si}^{2+}/(\text{Si}^{2+}+\text{Si}^+)$ ) along the analysis depth for different APT measurements carried out at several UV laser powers. Please note that there was a mass overlap between  $\text{Ni}^{2+}$  and  $\text{Si}^+$ , at the first stage of APT measurement, corresponding to the highlighted region in the gray color, this caused an error in the extraction of Si CSR. Hence this part of the profiles has been partially excluded from the plot. The depth profile of Si CSRs for the different measurements have been aligned based on the Ge depth profile (position of SiGe layer). The initial and end of SiGe interfaces are also indicated by black dash lines on the figure. .... 162

Figure 92: Schematic representation of the FOV for a hemispheric tip shape. Please note that the indicated launch angle corresponds to the last detected atom on the specimen apex within the FOV. .... 163

Figure 93: Si CSR ( $\text{Si}^{2+}/(\text{Si}^{2+}+\text{Si}^+)$ ) along the analysis depth for the APT measurement carried out with a green laser using different laser powers. The specimens measured at 55 and 100 mW laser power locally fractured within the SiGe layer, while the measurements were continued successfully after this local fracture. We reported the rest of the measurements, after the fracture events, by excluding about 400 k events from the fractured position. Please note that there was a mass overlap between  $\text{Ni}^{2+}$  and  $\text{Si}^+$ , at the first stage of APT measurement, corresponding to the highlighted region in the gray color, which caused an error in the extraction of the Si CSR. Hence this part of the profiles has been partially excluded from the plot. The Si CSR depth profiles for the different measurements

have been aligned based on the Ge depth profile. The initial and end of the SiGe interfaces are also indicated by the black dash lines in figure..... 166

Figure 94: (a) The predicted 3D absorption map computed by finite-difference time domain for a silicon tip having an apex radius of 25 nm and a shank angle of 6°. The image in the center shows the successive absorption maxima along the specimen depth at the laser illuminated side of the tip. The images on the top and the bottom show the laser absorption pattern in the tip cross-section at different positions along the specimen depth. The figure is reported from [192]. (b) The experimentally observed variation of Si CSR for APT measurement carried out at 55 mW green laser power on a SiGe/Si specimen having apex radius of about 30 nm and a shank angle of about 6°. The image in the center shows depth profile of Si<sup>2+</sup> and Si<sup>+</sup> along the analysis depth, where the marked region up to 19 nm in depth, belongs to SiGe layer and the rest corresponds to bulk Si. The images at the top and the bottom show the 2D Si CSR maps for the specimen cross-section having a 5 nm thin depth. The 2D Si density maps are also shown for two sections of the tip at 50 nm and 160 nm in depth. .... 168

Figure 95: 3D absorption maps computed for a silicon tip having a fixed shank angle of 4° at four different initial tip diameters (a) 20 nm, (b) 50 nm, (c) 100 nm and (d) 160 nm illuminated by green laser. The absorption maps were calculated by finite-difference time domain simulations Reproduced from [192]. .... 169

Figure 96: SEM images of APT specimens after analysis at different laser powers. .... 170

Figure 97: Average Ge concentration versus Si CSR (Si<sup>2+</sup>/ (Si<sup>2+</sup>+ Si<sup>+</sup>)), (~ electric field) for different specimens measured with UV (left) and green (right) laser light. Each point in the figure corresponds to one APT specimen measured at the fixed laser power. The error bars were calculated according to the counting statistics and the standard deviation of the voxel means (see Equation 5.11) by taking the voxel size as 1 × 1 × 5 nm<sup>3</sup>. The linear fit for each data set is also plotted. The dashed black line indicates the reference Ge concentration obtained from the GIXRF measurement. .... 173

Figure 98: The distribution of local Ge concentration across the specimen diameter for APT measurements carried out with a UV laser at different laser powers. A 50 nm thick section (in z direction) of the reconstructed tip in the SiGe film was used for this analysis. (a) Distribution of local Ge concentration versus lateral position on the specimen in x direction (laser direction). To compare different specimens having different diameters, each position was normalized to the tip radius. (b) Distribution of local Si CSR versus lateral position on the specimen in x direction. (c) Correlation between local Ge concentration and local Si CSR across the specimen diameters. This figure was obtained by combing the figures (a) and (b). The error bars were calculated according to the weighted standard deviation. .... 174

Figure 99: The depth profile of Ge concentration and Si CSR for different APT measurements carried out with UV laser. Each curve corresponds to one

specimen measured at a fixed laser power. The interfaces between Si cap/SiGe and SiGe/bulk are indicated by black dashed lines..... 175

Figure 100: The depth profile of Ge concentration and Si CSR for different APT measurements carried out in green laser. Each curve corresponds one specimen measured at a fixed laser power. The interfaces between Si cap/SiGe and SiGe/bulk are indicated by black dashed line. .... 176

Figure 101: Estimated additional Ge concentration by assigning all background counts to Ge as a function of Si CSR ( $\text{Si}^{2+}/(\text{Si}^{2+} + \text{Si}^+)$ ) for UV. The background level was estimated by ranging the entire non ranged mass-to-charges in the mass spectrum. Each marker corresponds to one specimen measured at a fixed laser power..... 177

Figure 102: Ge concentration versus electric field (Si CSR) for three different  $\text{Si}_x\text{Ge}_{1-x}$  compositions ( $x \sim 22, 50$  and  $72$ ). The APT measurements for  $\text{Si}_{28}\text{Ge}_{72}$  was carried out in LEAP 5000 XR, while the other measurements were carried out in LAWATAP. Please note that the markers reported for  $\text{Si}_{28}\text{Ge}_{72}$  and  $\text{Si}_{50}\text{Ge}_{50}$  are lateral slices of one and two specimens respectively, while each marker for  $\text{Si}_{78}\text{Ge}_{22}$  corresponds to one tip measured at a fixed laser power. The error bars have been calculated according to the standard deviations. .... 178

Figure 103: APT quantification of B content in  $\text{Si}_{78}\text{Ge}_{22}$  versus Si CSR (electric field) for measurements carried out at both UV and green laser in LAWATAP tool. The error bars were calculated according to the counting statistics and standard deviation of voxel means (see equation 5.11) for the reported parameters by taking the voxel size as  $1 \times 1 \times 5 \text{ nm}^3$ . .... 179

Figure 104: Repeatability of Ge quantification in SiGe by APT using UV (left) and green laser (right). Each marker corresponds on one APT tip measured at a fixed Si CSR  $> 95 \%$ . The error bars were calculated according to the counting statistics and the standard deviation of the voxel means (see equation 5.11) for a voxel size of  $1 \times 1 \times 5 \text{ nm}^3$ . .... 180

Figure 105: Repeatability of B quantification in SiGe by APT using UV (left) and green (right) laser light. Each marker corresponds on one APT tip measured at a fixed Si CSR  $> 95 \%$  with all the other experimental conditions kept constant during all the measurements. The error bars were calculated according to the counting statistics and standard deviation of voxel means (see equation 5.11) for the reported parameters over the reconstructed volume by taking the voxel size as  $1 \times 1 \times 5 \text{ nm}^3$ . .... 181

Figure 106: Lateral distribution of Ge (left) and B (right) concentration across the specimen diameter (2D concentration maps) measured at Si CSR $\sim 0.99$  in UV laser..... 182

Figure 107: Representation of the measurement flow for the developed combined STEM/EDS tomography-APT analysis. (a) The schematic representation of the SiGe multi-layer system and the TEM image of the prepared sharpened APT specimen by standard FIB lift-out technique. (b) The ortho slices obtained from STEM-EDS tomography on the sharpened APT tip. (c) The 3D reconstructed APT data obtained from the APT measurement on the same sharpened specimen after cleaning by oxygen plasma. .... 183

Figure 108: Comparison between the depth profiles obtained by APT measurements (using UV and green laser) and the EDS analysis. The depth profiles for the APT measurements were taken from the $7 \times 7 \text{ nm}^2$ core central region of the reconstructed data. ....	184
Figure 109: Gradual decrease in the electric field (Ge CSR) along the analysis depth for the APT measurements in UV and green laser (left). The TEM image of the APT specimen before the measurement in UV laser (right). ....	185
Figure 110: SEM top (a) and cross-section (b) images of porous silicon (PSi) as the inorganic template. (c) SEM cross-section image of PSi filled by polyaniline. The thickness of PSi layer was measured about $1 \mu\text{m}$ . The schematic representation of the monomer is also shown in the figure. Please note that SEM image shown in (b) were taken from a similar system with a thicker PSi layer. .	190
Figure 111: The collected APT mass spectrum from poly(3-alkylthiophene) thin film deposited by electrospray ionization on Al pre-sharpened APT specimen. The labeled peaks on the spectrum ( $15 < m/z < 190 \text{ Da}$ ) were identified as single charged alkane fragments: $C_nH_{\sim 2n}^+$ , with $n = 1, 2, \dots, 12$ . The peak at $190 \text{ Da}$ and its successive peaks at the interval of $12 \text{ Da}$ were identified as di-thiophene molecules having different amounts of attached alkane according to the mass/charge ratio. The numbered peaks (0 to 48) after $320 \text{ Da}$ are identified as quadra-thiophene molecules with different amounts of alkane attached. Reproduced from [142]. ....	191
Figure 112: APT specimens prepared from $\sim 1 \mu\text{m}$ thick film of porous silicon filled by polyaniline. The specimen preparation was carried out according to the standard FIB technique in (a) top configuration (b) cross-section configuration. ....	192
Figure 113: The 3D reconstruction of APT measurement on a specimen prepared from PSi filled with Pani. (a) The 3D reconstructed volume of the specimen according to the monoatomic ions of C (represented by red dots) and Si (represented by green dots). (b) The distribution of C within the pores are shown in a zoomed view (side and cross-section) of a slice of the reconstructed volume having a height from $150$ to $210 \text{ nm}$ , where the same color code was used to represent the C and Si ions. (c) The 2D concentration maps of C ( $C^+$ , $C^{++}$ ), Si ( $Si^+$ , $Si^{++}$ ) and silicon oxide ( $SiO^+$ , $SiO_2^+$ ) for the same slice of the specimen shown in (b). The color bars show the ionic concentration according to the all ranged peaks on the spectrum. ....	195
Figure 114: Comparison among the collected mass spectra at different laser powers. Each spectrum corresponds to $300,000$ collected events, where the major peaks are also identified on the figure. Please note that the y axis has an arbitrary unit and the figure only compares the position of the peaks (mass-to-charge ration) rather than the counts. ....	196
Figure 115: Correlation histogram obtained from the double-hits ion pairs detected in the APT analysis of PSi filled by Pani. The two dissociation tracks in the figure are: 1: $SiO_2 + dissSi + +O^+$ . and 2: $Si_2O_2 + dissSiO_2 + +O$ . The color bar shows the relative counts. ....	198

Figure 116: APT mass sepctrum for C60-doped P3HT polymer, obtained from an APT tip prepared by dip coating (a) and FIB lift-out technique (b). The molecular peaks for the polymer were absent in case of FIB lift-out sample prep. The spectra are reported from reference [136]. .....199

Figure 117: Issued certificate from the length department of INRIM (NMI of Italy) for the dimensional characterization of the prepared microstructured Si templates as the potential reference material of 3D ToFSIMS.....210

Figure 118: schematic representation of the process flow for the preparation of a potential reference specimen for APT. ....211

# Chapter 1

## Introduction

The aim of this doctoral project is to develop and fabricate different 3D heterogeneous micro and nano structures as the potential reference materials for different 3D compositional/chemical analysis techniques: time-of-flight secondary ion mass spectrometry (ToFSIMS), Grazing incidence X-ray fluorescence (GIXRF) and atom probe tomography (APT). The development of the reference materials and calibration standards is an essential step in metrology for an accurate and traceable quantification and the 3D reconstruction of the measured volume.

Industry is increasingly expanding the library of materials and moving towards advanced heteronomous systems with 3D architectures, which includes both inorganic materials (e.g. devices and nanolayered systems) and organic materials (e.g. advanced coatings and smart optical films). This is the case for a wide range of industries including semiconductor, steel, automotive, 3D printing and medical industries (e.g. pharmaceuticals and implants). For instance, the 3D device architecture such as SiGe based FinFETs is currently entered in the production at the 22 nm nodes. The next generation of devices is typically envisioned to include more complex 3D architectures (e.g. gate all around horizontal-nanowire FET) as well as the materials engineering [1]. Obviously, the performance of such complex 3D heterogeneous systems is also determined by the 3D distribution of the chemical and/or the elemental composition, e.g. dopant profile, at nanometric scale. The realization of such complex 3D systems/devices makes the 3D-metrology a crucial step in the development of the advanced materials and the new 3D architectures as well as for the quality control in the manufacturing of the final devices/products. To address this fast-growing need in industry, metrology should provide accurate elemental and chemical 3D measurements with a spatial resolution (both the lateral and the depth) down to the nanometric scale in accordance with the needs of the industry (e.g. down to sub nanometer scale for semiconductor industry).

Regarding the 3D chemical mapping, time-of-flight secondary ion mass spectrometry (ToFSIMS) is a potential enabler for characterization of the 3D organic or organic-inorganic systems with a depth resolution better than 1 nm and a lateral resolution down to 100 nm [2], where the other chemical mapping techniques e.g. X-ray photoelectron spectroscopy (XPS), typically cannot provide the required lateral resolution. The extension of the ToFSIMS analysis for characterization of 3D micro and nanostructured systems exhibits several technical and metrological challenges [3]. In particular several technical improvements have been suggested and implemented, including the development of a hybrid ToFSIMS and scanning probe microscope (SPM) tool [4]. However, the reliability of such an analysis has not been yet metrologically evaluated mainly due to the absence of any 3D reference material and calibration standard for this technique. In Chapter 2, I will address this issue in more detail and in particular the preparation of the potential 3D organic-inorganic reference microstructures for this technique will be discussed.

Regarding the 3D metrological in semiconductor industry, the ion based elemental mapping techniques such as Rutherford backscattering spectrometry (RBS) and secondary ion mass spectrometry (SIMS) typically do not offer the required spatial resolution. There are technical limitations in SIMS to further confine, i.e. focus/reduce, the ion beam into a smaller area and improve the lateral resolution [5]. Alternative, concepts such as self-focusing SIMS and 1.5D SIMS were introduced which enable the extraction of the composition and doping profile for 3D nanostructures even with the characteristic dimensions below 100 nm [6], [7]. Although such promising techniques are shown to be capable of providing rich statistics on a large scale, their metrological assessments (i.e. accuracy) are still lacking due to the absence of a 3D reference material.

The scanning probe microscopy (SPM)-based techniques, e.g. scanning spreading resistance microscopy (SSRM), are usually two-dimensional and they can only provide limited elemental information, e.g. carrier profiling. Although the extent of the SSRM analysis for the characterization of the 3D devices was shown to be successful [8],[5], such an analysis is still mainly limited to the carrier profiling. The X-ray based techniques such as X-ray photoelectron spectroscopy (XPS) and X-Ray diffraction (XRD) do not provide sufficient lateral resolution. The XPS is a surface sensitive technique which provides elemental composition and chemical information on the specimen surface. The XRD is typically used for the characterizing of the crystalline structure of the material.

Grazing incidence X-ray fluorescence (GIXRF) is another analytical technique which is well-established for the depth profiling (1D analysis) of nanolayered systems. The reference-free GIXRF is currently employed for the traceable quantification of thin films and multi-layer systems [9]. The extension of this technique towards a reliable 3D characterization of irregular heterogeneous systems and 3D nanostructures is still under development. Obviously, such an improvement also requires well-characterized 3D structures. In Chapter 2, we will discuss the current limitations of this technique and the preparation of the

potential reference structures (as a test vehicle) with the characteristic dimensions below 20 nm.

Finally, transmission electron microscopy (TEM) and scanning transmission electron microscopy (STEM) are commonly used techniques in semiconductor industry for determining the layer thicknesses and some information on the interdiffusion profiles at the interfaces (e.g. multilayers interfaces) with sub-Å resolution [10]. These techniques are inherently two-dimensional, while in the tomography mode the 3D reconstruction can be obtained based on the several measurements and data fusion. The combination of STEM with energy dispersive X-ray spectroscopy (EDS) allows the 3D elemental mapping (mainly qualitative) at nanometric scale [11]. Nevertheless, the sensitivity of such techniques is typically not sufficient for probing the elemental composition with a concentration below a few percent (i.e. typical of dopants).

In contrary to all aforementioned techniques, atom probe tomography (APT) is an inherent three-dimensional technique, which enables elemental identification and quantification at near-atomic resolution. The basic physical principle of APT is the controlled field evaporation and successive removal of each individual atom from the specimen surface. Field evaporation refers to a physical phenomenon which involves in the ionization, bond-breaking and finally release of the surface atoms from the specimen lattice in the presence of an intense electric field. The fundamentals of APT will be described in detail in Chapter 3.

As the working principle of APT does not rely on the interaction between the electrons (e.g. TEM and EDS) or ion beam (e.g. SIMS and RBS) with the specimen, the sensitivity and the resolution of this technique is free from the fundamental limitations of such interactions. The elemental identification with a sensitivity down to 10 ppm and a near-atomic spatial resolution (down to  $\delta_{\text{lateral}}$ : 2-3 Å,  $\delta_{\text{depth}}$ : 0.5 Å) has been reported for APT analysis. In APT, each evaporated ion from the specimen surface is immediately accelerated towards the position sensitive detector. The impact position of each ion on the detector can be traced back to its original position on the specimen apex thus enabling to reconstruct its original spatial location. The elemental identification is based on time-of-flight mass spectrometry (ToF), using the trigger of the laser (or voltage) pulse and the arrival time on the detector for the calculation of time-of-flight.

Although, the APT analysis of 3D devices such as the 3D dopant profile in a metal-oxide-semiconductor field effect transistor (MOSFET) [12] and the composition of a single SiGe Fin structure [13] were reported with the nanometric resolution, there are still several metrological challenges remaining for a reliable APT analysis in both bulk and the 3D nanostructured materials. A list of some major metrological challenges which currently hamper the reliability of APT analysis are reported as follows:

- Lack of reference material: currently there is no available reference material or a calibration standard for APT analysis. This hampers the metrological assessments in view of the accuracy and the repeatability for this technique. In addition, the absence of the reference material limits

the understanding of the physical mechanism underlining inaccurate quantifications for some compounds, e.g. quantification depending on the electric field, as the reference value is not well identified. Thus, such studies typically rely on other complementary techniques, e.g. SIMS and RBS, which might not be necessary a traceable measurement and makes such an analysis even more challenging.

- Limited field-of-view (FOV) and its determination: in every APT measurement only a limited region of specimen volume can be probed and the rest of the specimen volume simply remains undetected. The probed region is typically referred as the FOV. Since, the FOV is an unknown parameter during the APT measurement, it acts as an additional unknown parameter during the reconstruction making the data reconstruction more complex. In addition, the FOV for non-hemispherical tip shapes, e.g. UV laser induced asymmetric tip shape, is not yet well understood as the reconstruction protocols are only designed for ideal hemispherical tip shapes and they are unable to accurately determine the FOV for non-hemispherical tip shapes.
- Calibration of the reconstruction parameters: the reconstruction of the original positions of the atoms in the specimen volume based on the detected events during the APT measurement, is referred to as the data reconstruction, which is typically performed according to standard reconstruction protocols, e.g. Bas protocol [14]. As the result, the reliability of the reconstructed volume (even for an ideal hemispheric tip shape) relies on the degree of knowledge on the reconstruction parameters, e.g. detection efficiency and image compression factor, these parameters have to be identified prior or during the data reconstruction. However, currently there is no traceable method to calibrate the reconstruction parameters, thus even for an ideal hemispherical tip shape the reconstruction does not have any metrological traceability and apparently no uncertainty can be associated to such a reconstructed volume.
- APT analysis of organic and organic-inorganic systems: by the invention of the laser-assisted APT, analysis of non-metallic specimens became possible in APT. However, the extent of such an analysis on polymers and organic molecules is not yet well studied. In particular, even the technical challenges for such an analysis were not yet well addressed.

In this thesis, we will try to address and potentially resolve some of the aforementioned limitations in the APT analysis with the focus on the development of a potential reference material for APT which has a maximum FOV (full tip imaging). The motivation for this attempt is that the full tip imaging feature (FOV equal to the tip size) allows a potential route for an accurate self-calibration of all the reconstruction parameters with the quantifiable uncertainties. Thus, such a

methodology can pave the way towards an accurate compositional analysis as well as a more reliable 3D data reconstruction in APT with the quantifiable uncertainties.

In Chapter 2, I will describe the preparation of the potential reference organic-inorganic microstructures for 3D ToFSIMS as well as the inorganic 3D nanostructures for GIXRF. In Chapter 3, the fundamentals of APT analysis, field evaporation process and the laser-tip interaction will be described in detail. In Chapter 4, I will first discuss the electric field distribution around the APT specimen (both in the near and the far field), ion trajectories and the corresponding FOV for a hemispherical tip shape. Then the FOV for the UV-induced asymmetric tip shape will be experimentally evaluated. A new APT specimen design which can maximize the FOV (full tip imaging) in APT analysis will be suggested and its performance and the optimum dimensional parameters will be evaluated according to the finite element analysis of the electric field lines and the ion trajectories. Finally, the feasibility of full-tip-imaging in APT, following our proposed specimen design, will be experimentally demonstrated. To do so, we will discuss a new specimen preparation process, based on standard lithography and etching technique, which allows to prepare multiple APT specimens in a reproducible fashion and with a minimized tip to tip variations in view of the tip radius and the shank angle. In Chapter 5, we will experimentally evaluate the laser tip interaction in APT analysis with UV and green laser light. In particular, the local distribution of the electric field across the specimen diameter and its variation along the analysis depth for different experimental conditions will be discussed. Relying on a well-characterized B doped SiGe reference system, the accuracy of the APT analysis with UV and green laser light will be evaluated for different experimental conditions (electric field) and the optimum condition will be identified. Finally, the repeatability of APT analysis in view of the Ge and B quantification will be assessed. In Chapter 6, the state-of-the-art APT analysis of organics material will be described in detail. We will discuss the feasibility of APT analysis of an organic-inorganic system (polyaniline-porous silicon nanocomposite). The possible fragmentation and dissociation of the molecular structure in our APT measurement will be discussed and the remained challenges for such an analysis will be addressed.

## Chapter 2

# Preparation of 3D organic/inorganic micro and nano structures for 3D ToFSIMS and GIXRF

Industry is progressively moving towards complex 3D architectures composed of advanced materials and heterogeneous systems, which include both organic materials (e.g. advanced coatings) and inorganic materials (e.g. devices and nanolayered systems). Such 3D architectures are currently utilized in several industries such as semiconductor, 3D printing and medical industries (e.g. pharmaceutical industry). Obviously, the performance of such complex 3D systems is also determined by the 3D elemental distributions, e.g. dopant distributions, or chemical compositions at the nanometric scale. Thus, 3D metrology should address the need of the industry for an accurate measurement of the 3D elemental distributions or chemical compositions with a 3D spatial resolution (both lateral and depth) down to the nanometric scale.

The development of different 3D chemical/ compositional analysis techniques at such a high spatial resolution has been the topic of several studies [5], [15]. In this content, time-of-flight secondary ion mass spectrometry (ToFSIMS), grazing incidence X-ray fluorescence (GIXRF) and atom probe tomography (APT) are among the potential enablers to resolve the 3D spatial resolution at the nanometric scale. The metrological evaluation of the APT analysis in view of accuracy and the repeatability of the compositional analysis and the reconstructed volume will be discussed in detail in the next chapters.

ToFSIMS is a well-established technique for chemical/elemental mapping (two-dimensional analysis) as well as depth profiling (one-dimensional) of different organic and inorganic materials and nanolayered systems, whereby it is widely employed in both industrial and research laboratories for such a purpose.

However, the extension of such an analysis to 3D micro and nanostructured systems exhibits several technical and metrological challenges [3]. Several technical improvements have been suggested and implemented to push ToFSIMS as a reliable 3D analysis technique for the industrial applications, including the development of a hybrid ToFSIMS and scanning probe microscope (SPM) tool [4]. Despite the remarkable improvements in this area, the reliability of such an analysis has not been yet metrologically evaluated in view of accuracy and repeatability of the 3D reconstructed volume. This is mainly due to the absence of the 3D reference structures and calibration standards for this technique.

Similarly, reference-free GIXRF is also a well-established technique for the traceable quantification and depth profiling of thin films and multi-layer systems [9]. The extension of this technique to 3D analysis of irregular heterogeneous systems and nanostructures is still under development. Obviously, such an improvement also requires the well-characterized 3D nanostructures as a reference sample to evaluate different aspects of such a complex analysis. Therefore, the absence of the 3D reference materials and the calibration standards is currently limiting the integration/development of the available 3D compositional/chemical analysis techniques as the reliable and traceable metrological tools. In addition, it hampers further improvements in different aspects of such an analysis, including the development of the reliable protocols and the practice guides.

In order to address this need, in this project we have developed a range of well-characterized potential 3D reference structures with the ordering and the characteristic dimensions resembling those exploited in the industrial applications. In particular, these 3D reference structures consist of different constituents having well-defined compositions and well-defined morphologies with different characteristic dimensions ranging from 50  $\mu\text{m}$  down to sub 20 nm.

The preparation and the traceable characterization of organic-inorganic 3D reference structures for 3D ToFSIMS will be discussed in Section 2.1. In addition, the preliminary ToFSIMS analysis on these developed reference structures will be briefly reported in Section 2.1.4. In Section 2.2, the preparation and the characterization of different 3D heterogeneous nanostructures with characteristic dimensions ranging from some hundreds of nanometers down to sub 20 nm will be discussed in detail. The application of such 3D nanostructures as the test vehicle for 3D compositional analysis in GIXRF will be also reported in Section 2.2.4. Please note that a part of the work described in this chapter has been previously published [16] and [17].

## **2.1 Preparation of reference 3D microstructures for 3D ToFSIMS**

Before the detailed discussion on the preparation of different 3D reference structures for 3D ToFSIMS, the fundamentals of this technique will be first

briefly described in this section. In particular, we will briefly describe the state-of-the-art 3D analysis in ToFSIMS and metrological issues remaining for such an analysis. Then the design, preparation and the traceable characterization of the developed 3D reference structures will be discussed in the next sections.

### 2.1.1 Fundamentals of 3D ToFSIMS

Time-of-Flight secondary ion mass spectrometry (ToFSIMS) is a highly surface-sensitive analytical technique, which can provide surface spectroscopy (i.e. composition and molecular information from the surface), surface imaging and chemical mapping, depth profiling (e.g. thin layers and interfaces) and possibly 3D analysis of a region of the specimen volume. The schematic representation of the different operation modes is shown in Figure 1.

In this technique, the solid surface is bombarded by a pulsed primary ion beam (e.g. Cs, Ar, and  $\text{Bi}_n$ , where  $n=1\dots7$ ) having an energy typically in a range between 1 to 30 keV. The particle energy is then transferred to the atoms of the solid by the so-called "billiard-ball-type" collisions. As a result, a cascade of colliding atoms is created within the solid in the vicinity of the initial impact. Some of these propagating collisions return to the surface and result in the emission of particles which can be atoms or atomic clusters [18]. The atoms or clusters which become ionized during the course of their escape from the solid surface, are called secondary ions. These ionized particles are accelerated towards the flight tube and their mass-to-charge-ratios are determined by the time-of-flight mass spectrometry.

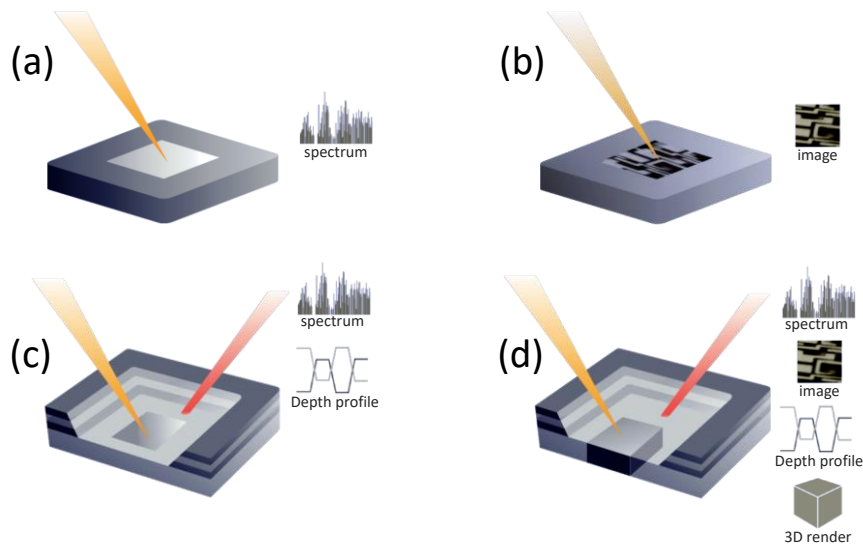


Figure 1: Schematic representation of four operational modes in ToFSIMS: (a) Surface spectroscopy (b) Surface imaging (c) depth profiling (d) 3D analysis. Reproduced from [4].

To do surface analysis, typically a low energy primary beam is employed such that secondary particles are only created from the topmost (or two) atomic layers. Such a soft interaction allows large and non-volatile molecules to escape from the surface with a minimum degree of fragmentation. In particular, the use of heavy ion species such as Bi, Au or their clusters  $\text{Au}_n$ ,  $\text{Bi}_n$  ( $n=1\dots7$ ) can result

in a significant improvement in the sensitivity for molecular ions and a drastic reduction in the fragmentation of the polymer structures [18]. The time-of-flight mass spectrometry of the secondary ions identifies the detailed molecular fragments and the elemental composition of the specimen surface with a mass resolution up to 12,000 [4].

Surface imaging is possible by focusing the pulsed ion beam into a small spot and rastering it over the specimen surface. Such an analysis mode can determine the lateral distribution of different molecules/elements on the specimen surface. A lateral resolution down to the sub-100 nm [2] and 60 nm [4] was achieved by ToFSIMS, which is mainly determined by the primary pulsed beam and its focus condition.

For depth profiling, modern instruments use a combination of two separate ion beams whereby one ion beam sputters the crater and the other pulsed beam progressively analyzes the bottom of the crater in an automated switching mode between the erosion and the analyzing, referred to as "dual beam depth profiling". This allows an accurate depth profiling of inorganic and organic films, and nanolayers. Under optimized operational conditions, the sputter beam erodes the surface at high current and low energy, whereby the process does not alter (or as little as possible) the surface under analysis. This is a crucial criterion for organic materials, which tend to decompose easily during the sputtering process which results in the loss of some detailed information regarding the chemical structure of the surface molecules. ToFSIMS is currently a well-established technique for depth profiling of both organic and inorganic materials and nanolayered systems, whereby different metrological aspects (e.g. accuracy and repeatability) of such an analysis has been evaluated [19]. This is supported by a range of available reference materials and the calibration standards for both organic and inorganic films and multi-layer systems by NPL [20],[21] and NIST [22].

Finally, the qualitative 3D visualization of the specimen structure and its chemical distribution can be obtained by combining the spectral and depth information, whereby the 3D image is retrieved by stacking the 2D images obtained during the subsequent sputtering steps [15]. The qualitative 3D imaging for planar structures (e.g. multilayer systems) is a well-established technique. However, the 3D imaging of 3D structures exhibiting strong topography and/or considerable differences in the sputter yields over the specimen volume (e.g. mixed organic-inorganic systems) is typically challenging and different corrections are required [23],[24].

In order to overcome the aforementioned limitations, a hybrid ToFSIMS and scanning probe microscopy (SPM) was developed by IONTOF (TOFSIMS V). Such a hybrid measurement setup allows in-situ SPM measurement and ToFSIMS analysis by transferring the sample stage back and forth. The measured surface topography (by SPM) at different analysis depths can be combined with the ToFSIMS depth profile (iteratively) to compensate for the topography modulations developed due to the differences in sputter yields of different constituents [23]. Hence, this hybrid instrument allows corrections for the reconstruction artefacts created due to all topography modulations, as caused by

the differences in the sputter yields, and/or by the original 3D topography of the structured specimens. As a result, the 3D reconstruction of complex 3D structured specimens composed of a mixture of organic and organic-inorganic constituents can be also realized in this configuration [25].

However, as a recently developed methodology, different metrological aspects of such a complex data fusion, chemical data (by ToFSIMS) and topography (by SPM), have not been yet well explored. In particular, several challenges still remain to metrologically assess the performance of such a complex analysis, in view of the accuracy and repeatability of the reconstructed volume. The absence of a 3D reference material is among the main limitations preventing such a metrological evaluation. This also hampers further improvements in the data fusion step and finally the development of the reliable reconstruction protocols for an accurate and traceable 3D imaging in ToFSIMS.

To address this need, in this project we have developed several well-characterized 3D organic-inorganic microstructures which can potentially be used as a reference material for 3D imaging in ToFSIMS. These 3D reference structures consist of constituents with well-defined compositions/chemistries (irganox, polystyrene and silicon) in well-defined 3D morphology such as a cubic shape repeated over a large area. The design, preparation and the characterization of such 3D structures are described in the following sections.

### **2.1.2 Design and fabrication**

The design for the 3D reference structures in our study was in line with the application, metrological needs and the current limitations of 3D ToFSIMS. As discussed in the previous section, the hybrid ToFSIMS-SPM instrument was developed to overcome the challenges in the 3D analysis of irregular systems and 3D structures exhibiting strong topography and/or strong differences in the sputter yields of different constituents. However, the metrological aspects of such an analysis still needs to be developed.

To support this methodology, the design of the reference structures in our study was in the form of 3D microstructures (strong topography) composed of organic-inorganic constituents (strong differences in the sputter yields).

A double layered organic system (irganox and polystyrene) confined in a cubic shaped structure within the inorganic 3D microstructures (Si template) was selected as design shape in this project. In particular, the 3D Si template was designed in three model-systems consisting of square cross-section holes having different in-plane dimensions ( $50\times 50$ ,  $30\times 30$  and  $5\times 5\ \mu\text{m}^2$ ) and a fixed depth increment of  $2.3\ \mu\text{m}$ , repeated over an area about  $0.6\times 1\ \text{mm}^2$ . The design of these three model-systems is shown in Figure 2 and Table 1. The realization of the 3D organic-inorganic heterogeneous microstructures was achieved by the deposition of the organic layers. Such a configuration allows the use of the planar organic layers, far from the microstructures area, as a reference for the calibration of the sputter yields and the chemical information. Thus, the well-defined chemistry/composition criterion for the preparation of the 3D reference structure

can be assessed by a ToFSIMS measurement on the planar organic layers on the same sample.

Table 1: Design for the inorganic template (Si microstructure) in three model-systems.

Model	#1	#2	#3
Template material	Si	Si	Si
Sample Dimension [cm <sup>2</sup> ]	1.5 × 1.5	1.5 × 1.5	1.5 × 1.5
Structured area [mm <sup>2</sup> ]	~ 0.6 × 1	~ 0.6 × 1	~ 0.6 × 1
Square dimension [μm <sup>2</sup> ]	50 × 50	30 × 30	5 × 5
Pitch [μm]	50	30	5
Depth [μm]	2.3	2.3	2.3

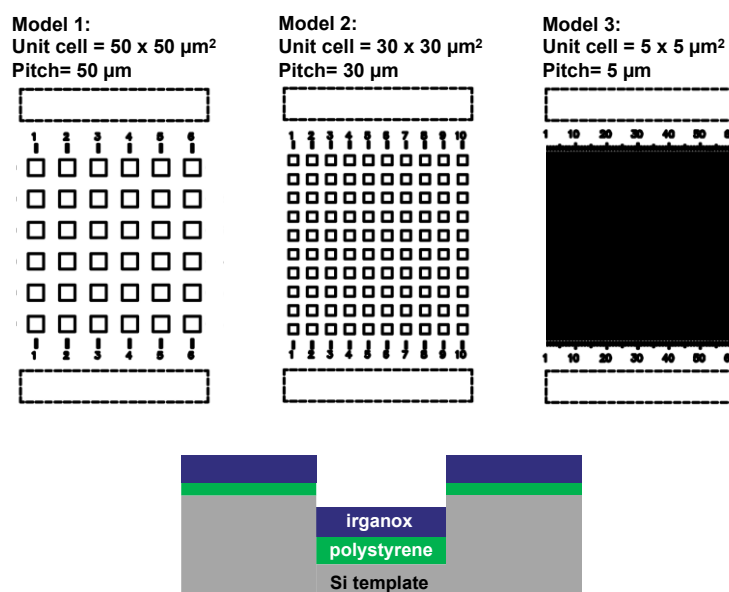


Figure 2: Template design for the reference structures in three model-systems. The image at the bottom schematically represents the cross-section for one of the above square shape unit cells after the depositing of the organic layers

The inorganic templates were prepared in the Si substrate according to the standard lithography and etch process. In particular optical lithography was used to pattern a Si (100) substrate and the successive pattern transfer was carried out by deep reactive-ion etching (DRIE). The recipe for the etch process is reported in Appendix A.

The microstructured Si templates were then filled with polystyrene (10300 g/mol) by spin coating (30s at 2000 rpm) of the toluene solution at the concentration of 150.0 mg/ml. The successive irganox1010 layer was deposited by the evaporation at NPL. The latter was the planar reference material for ToFSIMS developed by NPL [21]. The SEM images of the bare templates and the filled 3D structure is shown in Figure 3. As previously discussed, the preparation of both planar and 3D structured organic-inorganic systems on the same specimen allows the use of the planar structure as the reference for the calibration of sputter yields and the chemical information. In addition, irganox1010 (NPL planar reference for ToFSIMS [21]) was used to fill the 3D microstructures in our study,

which allows to assess the well-defined chemistry criterion for the preparation of the potential reference structure for 3D ToFSIMS.

In the next section the traceable dimensional characterization of the inorganic templates together with the morphological characterization of the organic layers will be discussed in detail.

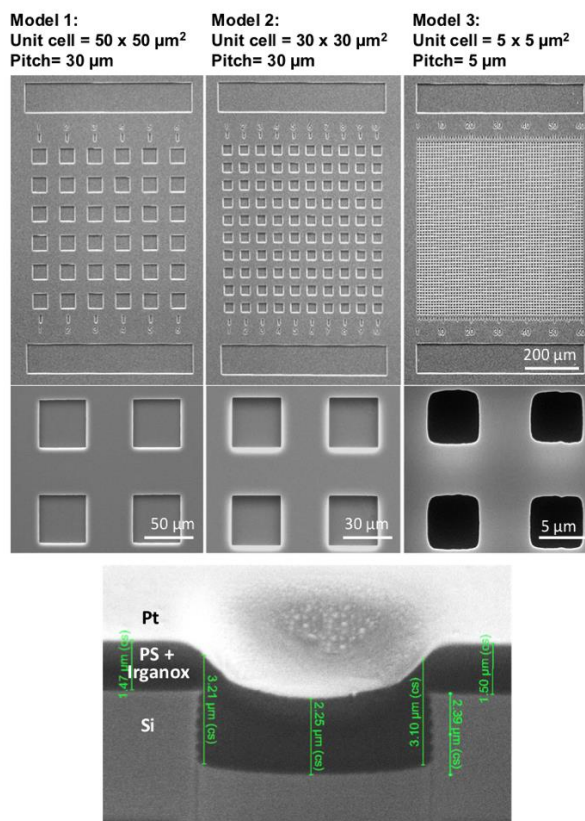


Figure 3: SEM micrographs of the microstructured Si templates prepared according to the designed model-systems (on top). The SEM cross-section image for one of the 3D microstructures (model 3), filled with polystyrene and irganox.

### 2.1.3 Traceable dimensional characterization

As discussed in the previous section, a potential calibration sample for 3D ToFSIMS, has to be well characterized in terms of its chemistry/composition as well as in terms of its morphology and dimensions. The well-defined chemistry criterion for the preparation of the potential calibration sample for 3D ToFSIMS, has been discussed in the previous section. In this section, we will discuss the morphological characterization of both inorganic and organic 3D structures.

The traceable dimensional characterization of the Si templates has been carried out with a calibrated optical profilometer at the department of INRIM (NMI of Italy). In particular, we have measured the average area and depth for the square shaped holes and their associated uncertainties. The traceable results of these measurements for all three developed model systems are shown in Table 2 and the issued certificate is reported in Appendix A.

Table 2: Traceable dimensional characterization of structured Si templates using a calibrated optical profilometer.

Parameter	Model 1		Model 2		Model 3	
	mean	uncertainty U	mean	U	mean	U
Average unit cell area [ $\mu\text{m}^2$ ]	2636	53	972	29	32,1	2,5
Average depth [ $\mu\text{m}$ ]	2,371	0,042	2,353	0,033	-	-
Depth of the top trench [ $\mu\text{m}$ ]	-	-	-	-	2,338	0,011
Depth of the bottom trench [ $\mu\text{m}$ ]	-	-	-	-	2,331	0,011

We did a similar morphological analysis after the deposition of each organic layer (polystyrene and irganox). In particular, the relative depth of the 3D microstructures formed after the deposition of each layer was measured with the optical profilometer (see Figure 4) and the average value is reported in Table 3. Please note that the uncertainty assessment for depth measurement of the structured polystyrene and irganox layers is not available at the moment due to the lack of the proper length standard and the established protocols.

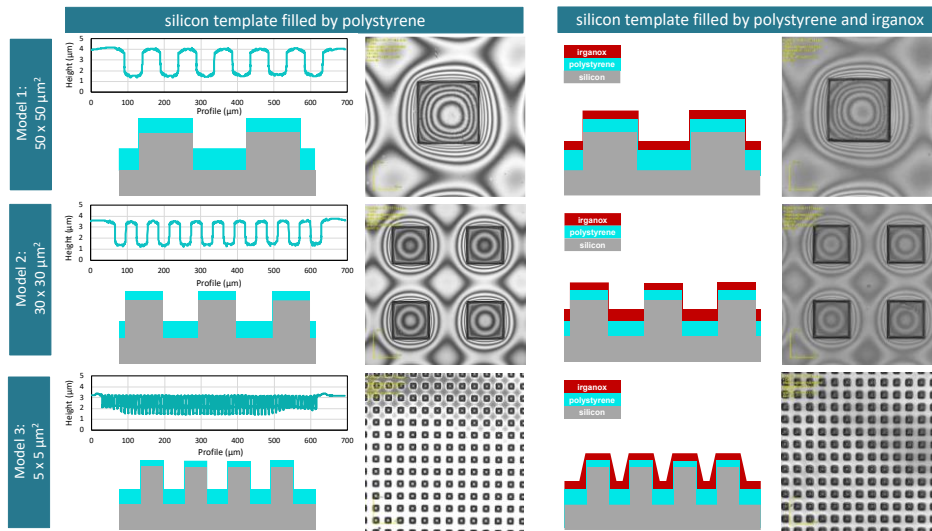


Figure 4: Morphological characterization of the 3D microstructures after the deposition of each organic layer (polystyrene and irganox). The measurements were carried out by the optical profilometer.

Table 3: Average relative depth, measured after the deposition of each organic layer (polystyrene and irganox). The measurements were carried out by the optical profilometer.

	Model 1 50 × 50 μm	Model 2 30 × 30 μm	Model 3 5 × 5 μm	Schematic representation
Average depth for 3D microstructured Si [μm]	2.371	2.353	2.335	
Average relative depth of 3D microstructures after the deposition of polystyrene [μm]	1.5	2.5	2.5	
Average relative depth of 3D microstructures after the deposition of polystyrene + irganox [μm]	1.5	2.5	2.5	

### 2.1.4 Preliminary 3D ToF-SIMS analysis

The preliminary ToFSIMS analyses were carried out at IMEC using ToFSIMS V equipped with the in-situ SPM. In this document, the preliminary results reported by the ToFSIMS group of IMEC will be briefly described. Please note that the reported results in this section were not part of this PhD work.

As discussed in Section 2.1.2, the reference structures in this project were designed to have both planar organic layers and the 3D structured organic-inorganic systems on the same specimen. This allows the use of the planar structure as the reference for the calibration of sputter yields and the chemical information. To determine the sputter yields of the different organic layers (polystyrene and irganox), a depth profile was acquired on the reference planar layer surrounding the 3D microstructures. The measurement conditions and the obtained profile are shown in Figure 5. In order to calculate the sputter yields, the crater depth was measured (by in-situ SPM) in each organic layer along the analysis depth at the positions indicated by the arrows in Figure 5. The calculated sputter yields based on the measured crater depths, for irganox and polystyrene are reported in Table 4. The obtained values showed a good agreement with the reported sputter yields for the same polymers in the literature (references in Table 4).

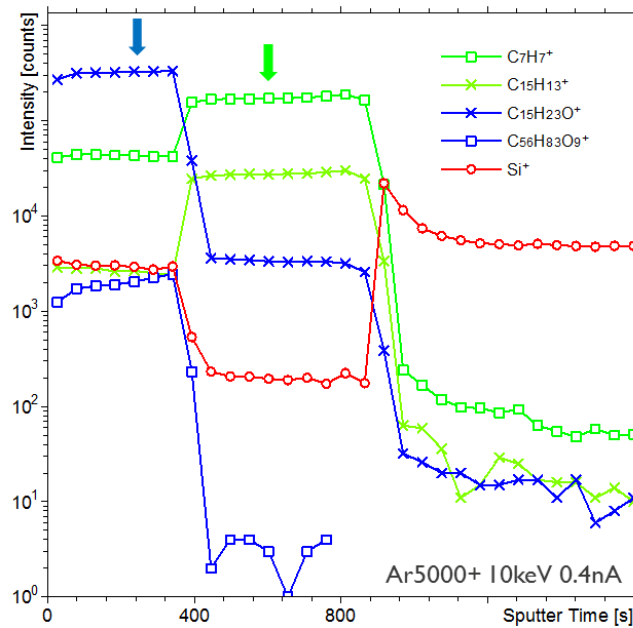


Figure 5: Depth profile for the reference planar organic layers. The molecular fragments of the irganox1010 ( $C_{15}H_{23}O^+$ ,  $C_{56}H_{83}O_9^+$ ) and polystyrene ( $C_7H_7^+$ ,  $C_{15}H_{13}^+$ ) are labeled in blue and green color respectively. The Si signal is shown in red color. Reported by the ToFSIMS group of IMEC.

Table 4: Extraction of sputter yields from the planar reference organic layers. The measured crater depths were used to estimate the sputter yields with the reported standard deviations (S). The obtained results are in good agreement with the reported values in literature (see the last column). Measurement conditions were: 10keV  $Ar^{+5000}$  sputter beam (0.4 nA). Reported by the ToFSIMS group of IMEC.

Layer	Thickness [nm]	S [nm]	Sputter yield [ $nm^3/PI$ ]	S [ $nm^3/PI$ ]	Sputter yield in literature [ $nm^3/PI$ ]
Irganox1010	712.77	2.18	73.2	0.02	71.5 <sup>(1)</sup>
Polystyrene (17kDa)	170.22	5	34.5	0.1	34.6 <sup>(2)</sup>
Si	<1nm	-	<0.003	-	-

(1) Niehuis et al., Surf. Interface Anal. 2013, 45, 158–162.

(2) Cristaudo et al., Surf. Interface Anal. 2014, 46, 79–82.

The ToFSIMS measurement on the 3D structured systems was carried out with the same measurement conditions as the reference planar layers. The obtained depth profile for the model 3 ( $5 \times 5 \mu m^2$ ) is shown in Figure 6. Due to the differences in the thickness of the organic layers at the bottom and top of the Si structures, the obtained depth profile from the 3D microstructures are complex and the slopes of the rising and leading edges at the interfaces are large.

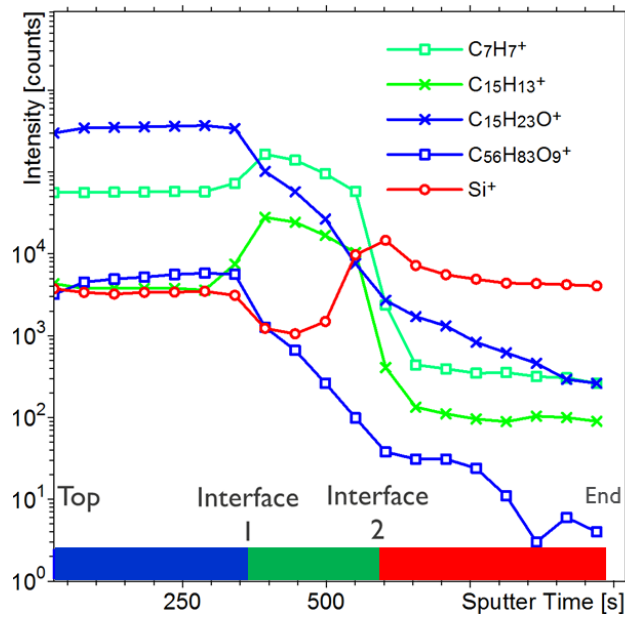


Figure 6: Depth profile obtained from 3D microstructured organic-inorganics systems from model 3 ( $5 \times 5 \mu\text{m}^2$ ). The molecular fragments of the irganox1010 ( $\text{C}_{15}\text{H}_{23}\text{O}^+$ ,  $\text{C}_{56}\text{H}_{83}\text{O}_9^+$ ) and polystyrene ( $\text{C}_7\text{H}_7^+$ ,  $\text{C}_{15}\text{H}_{13}^+$ ) are labeled in blue and green color respectively. The Si signal is shown in red color. Reported by the ToFSIMS group of IMEC.

The chemical maps and corresponding SPM images (both topography and phase) were taken at four different analysis depths: in irganox, interface between irganox/polystyrene, interface between polystyrene/Si and at the end of the analysis. The comparison among the different maps is shown in **Error! Reference source not found.** As can be seen in Figure 7, the sequences of the chemical maps and the SPM images can partially reassemble the actual 3D structure of the 3D organic-inorganic system for the model 3 ( $5 \times 5 \mu\text{m}^2$ ). In particular, the calculated sputter yields and the SPM measurements were used as a model to manually estimate the thickness of each layer (irganox and polystyrene) at the top and bottom of the Si structures. The extracted layer thicknesses for this model is shown in Figure 8, which was found to be in good agreement with the organic layer thickness measured by SEM from the FIB cross-section (see Figure 8).

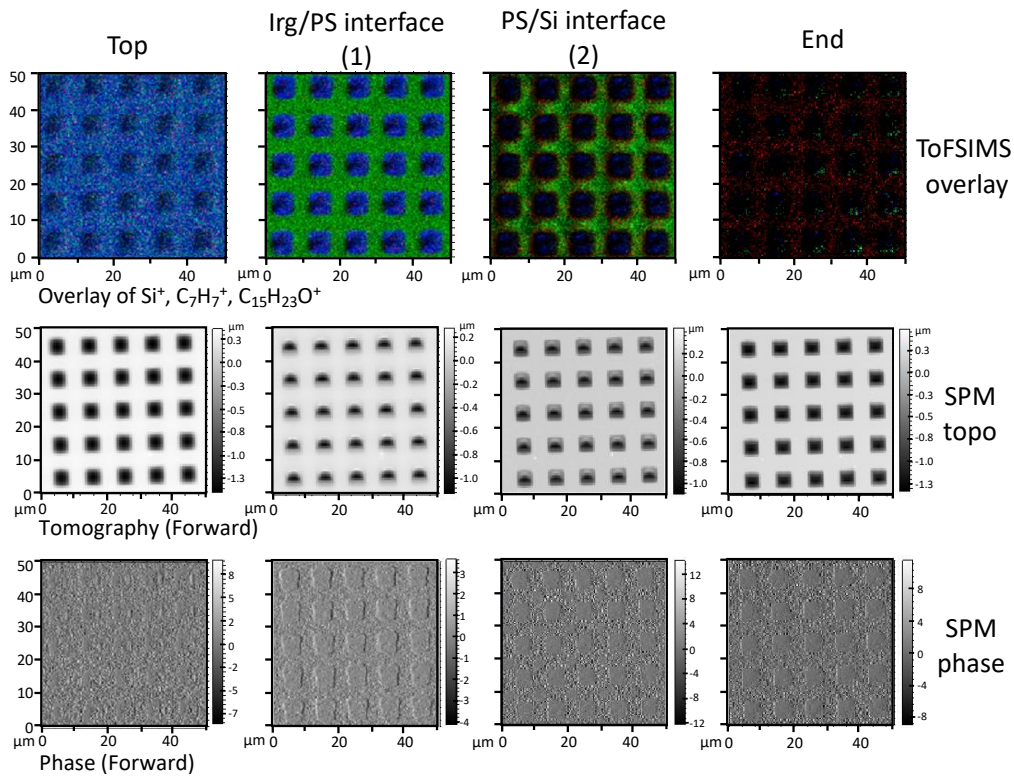


Figure 7: Chemical maps obtain from ToFSIMS (first row) at different analysis depth (see the main text). The molecular fragments of the irganox and polystyrene are indicated in blue and green color respectively, while the Si signal is shown in red color. The corresponding SPM images, topography (second row) and phase (third row) are also shown below the chemical images. Reported by the ToFSIMS group of IMEC.

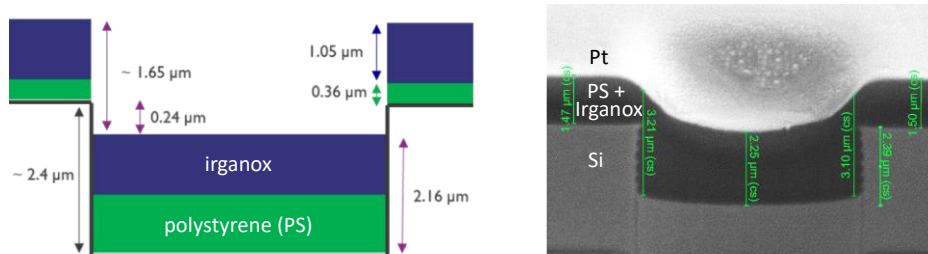


Figure 8: The comparison between the estimated layer thickness obtained from ToFSIMS measurement according to the sputter yields (irganox and polystyrene) and the SEM cross-section image of the same specimen model 3 ( $5 \times 5 \mu\text{m}^2$  structures). Reported by the ToFSIMS group of IMEC

Finally, the preliminary 3D reconstructed volume obtained from the combination of chemical maps and the topography information (from SPM), is shown in Figure 9. The 3D reconstructed volume for the top organic layers (region between the holes) shows a good agreement with the original structure of the sample, while the 3D reconstructed volume for the irganox at the bottom of holes drifts gradually towards a conical shape. Further analysis of other model systems is required to understand better and evaluate the data reconstruction.

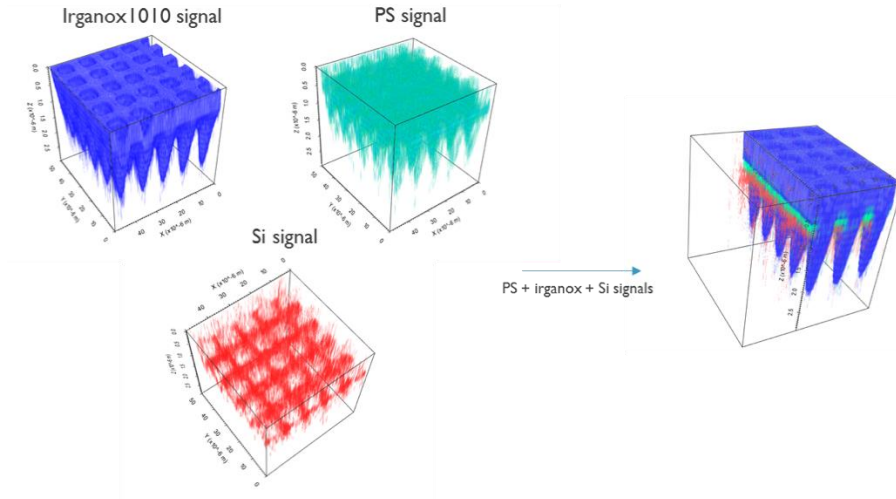


Figure 9: 3D reconstructed volume for the developed 3D structure in model 3 ( $5 \times 5 \mu\text{m}^2$ ), according to the combination of the chemical maps (from ToFSIMS) and the topography (from SPM). Reported by the ToFSIMS group of IMEC.

## 2.2 Preparation of 3D nanostructures for GIXRF

In this section, we will briefly describe the fundamentals of GIXRF and the current state-of-the-art analysis of 3D structures in this technique. In particular, we will discuss the current limitations and the metrological challenges remaining for the analysis of 3D structures with GIXRF. Then, the preparation of the 3D nanostructures with feature sizes ranging from some hundreds of nanometers down to sub 20 nm will be discussed in detail.

### 2.2.1 Fundamentals of GIXRF

Grazing incidence X-ray fluorescence (GIXRF) is a non-destructive analytical technique, which is currently well-established for the quantification of mass depositions, elemental depth profiling of nanolayered materials and the analysis of the interfaces. We will first briefly describe the fundamentals of X-ray fluorescence (XRF) and then the quantification and depth profiling in GIXRF.

X-ray fluorescence (XRF) analysis is based on the analysis of the emitted X-rays fluorescence resulting from an ionized atom as the result of the interaction of a highly energetic electromagnetic radiation with the specimen surface. These emitted X-rays have specific characteristic (fluorescence) energies corresponding to the ionized elements, while their intensity is proportional to the strength of the ionizing source as well as the elemental concentration [26]. These element-specific X-rays are emitted as the result of the electron transition events. The physical process underlying the emitted X-rays fluorescence is discussed as follows.

For a stable atom, the electrons occupy discrete energy levels (K, L<sub>1</sub>, L<sub>2</sub>, L<sub>3</sub>, M<sub>1</sub>, ...), which are ordered according to their decrease in the binding energy. The binding energy is defined as the energy required to remove an electron from a given orbit. By the interaction of electromagnetic radiation with the atoms, the

ionization can occur depending on the energy of the incident radiation. In particular, to eject an electron from the  $i^{\text{th}}$  shell of a specific atom, the photon energy must be greater than (or equal) the electron binding energy of the corresponding shell, which is tabulated for different elements in the textbooks [26]. The ionization is referred to as a process whereby an electron is ejected from the inner orbital of an atom leaving a vacancy behind. This vacancy is then filled by an electron from the outer orbitals (relaxation). Such a transition corresponds to an energy loss equal to the differences between the binding energies of the two states, which may appear as an X-ray emission (will be discussed in the next paragraph). Each X-ray transition has a certain probability, while the K-to-L<sub>3</sub> transition ( $k_{\alpha 1}$ ) is known to be the most probable transition [26].

The X-ray emission is not the only electron relaxation mechanism and the Auger effect is the other competing relaxation mechanism for an ionized atom. The fluorescence yield  $\omega_i$  is then defined as the ratio of the number of emitted X-rays to the total number of ionizations events, which can be approximated as [27]:

$$\omega_i = Z^4 / (A_i + Z^4) \quad 2.1$$

where  $Z$  is the atomic number and  $A_i$  is a constant approximately equal to  $10^6$  and  $10^8$  for K and L shell respectively. Thus, the fluorescence yield increases (for a given  $i$ ) with the atomic number and it becomes greater than 95% for the K shell X-rays of atomic number  $> 78$ .

On the other hand, the fraction of the incident photons  $F_p$  (from the radiation source) which can interact with the electrons of a specific element is given by [26]:

$$F_p = 1 - \exp(-\mu\rho x) \quad 2.2$$

where  $\mu$  is the mass attenuation coefficient,  $\rho$  and  $x$  are density and the thickness of the sample respectively. The mass attenuation coefficient varies as a function of incident photon energy, whereby it drops significantly for the incident photon energies below the binding energy of the specific electron states (referred to as the absorption edge). Finally, for a surface illuminated by an X-ray beam, the incident beam interferes with the reflected beam, leading to the formation of the X-ray standing wave (XSW) field above the specimen surface. This XSW field can strongly modify the excitation intensity in the vicinity of the specimen surface. The characteristics of the XSW field, e.g. intensity distribution and wavelength, strongly depend on the incident photon energy and the incident angle [28]. In particular, the intensity distribution of XSW can strongly enhance the emitted fluorescence intensity for those atoms inside the XSW and reduce the contribution of others. In the conventional XRF measurement, the X-ray beam has typically an incident angle of  $45^\circ$  which results in the emitted fluorescence X-ray from the specimen depth (up to a few micrometer) [26]. Thus, one can identify the elemental compositions in this region of the specimen. This non-destructive analytical technique can be used for both qualitative and quantitative analysis of the material composition.

In contrast to the conventional XRF, the total-reflection XRF (TXRF) is a surface elemental analysis technique, which typically is used to measure the contaminations and impurities on the specimen surface. In TXRF the incident angle between the X-ray beam and the specimen surface is below the critical angle  $\theta_{crit}$  (will be defined later) for the total external reflection (typically at 70% of  $\theta_{crit}$ ). This results in a small penetration depth (a few nanometers) and the reflection of the majority of exciting photons at the surface. In particular, since the refractive indexes of all materials in the X-ray wavelength range are smaller than one, the incident beam is totally reflected for the incident angles smaller than a critical angle  $\theta_{crit}$  [29]. This critical angle depends on both material parameters (e.g. atomic number and the atomic density) and the photon energy [30].

In the grazing incidence XRF (GIXRF), the incident angle between the X-ray beam and the specimen surface is varied around the critical angle  $\theta_{crit}$  (typically from 0° to 35°). This angular scan enables depth profiling of the mass deposition along the specimen depth [31]. For instance, the fluorescence signals of the nanolayers show different angular dependencies, which allow their accurate elemental depth profiling by GIXRF [31]. In addition, GIXRF gains from the enhancement of the emitted fluorescence intensity caused by the XSWs in view of signal level. The quantification and depth profiling in GIXRF are described as follows.

### **Quantification in GIXRF**

The quantification in the standard XRF relies on an appropriate reference material (i.e. calibration standard) that has an elemental matrix as similar as possible to that of the specimen, to compensate for the unknown instrumental parameters as well as the atomic fundamental parameters [32]. Besides the limited availability of reference materials as compared to the rapidly growing material libraries, the potential differences in the spatial elemental matrix may cause the inaccuracy in such an analysis.

Vice versa, the reference-free XRF spectrometry relies on radiometrically calibrated instrumentation and the knowledge of the atomic fundamental parameters [32], whereby the uncertainty (both type A and B) of the quantification can be calculated according to the available analytical expressions and the known uncertainties. The quantification in reference-free GIXRF is performed according to the Sherman equation [33], which correlates the mass deposition per unit area of an element  $i$  to the measured fluorescence intensities for that element. The detailed description of such an analysis can be found in reference [34].

The high sensitivity of GIXRF for the determination of mass deposition and elemental composition even at very low content, combined with its traceable quantification in reference-free methodology, makes the reference-free GIXRF a promising technique for the calibration and assessment of the reference materials for other analytical techniques.

## **Depth profiling in GIXRF for planar structures**

The angular scan of the incident beam with respect to the specimen surface allows the depth profiling of the elemental composition by GIXRF, whereby the analysis depth can vary from a few nanometers down to hundreds of nanometers [32]. Since the intensity of the fluorescence emission, at a given incident angle, is determined by the XSW field, the in-depth variation of the XSW field intensity is used as a sensor to probe the elemental depth profiling. The XSW field intensity (for a given incident angle and beam energy) depends on the material structure and the optical constants of the material [28]. Therefore, to improve the reliability of GIXRF analysis, the X-ray reflectometry (XRR) measurement is typically carried out simultaneously with the GIXRF measurement to provide additional information about the optical constant, layers thicknesses and the density variations along the specimen depth [35]. Finally, the elemental depth profiling in GIXRF is based on the forward calculation of the XSW field intensity and the angular dependent fluorescence emission at a given depth profile and compare the simulated data with that of the experiment. Further details of such an analysis can be found in reference [34].

## **GIXRF analysis of 3D structures**

As previously discussed, the accurate knowledge of the distribution of the XSW field and the effective excitation intensity allows the traceable depth profiling of the deposited mass and the elemental composition by the reference-free GIXRF analysis. For homogeneous planar systems, the XSW field can be calculated by the available software packages, such as IMD [36]. Such a 1D calculation of XSW has been reported to yield a reliable calculation of XSW intensity distributions even for isolated nanoparticles deposited on the flat surface [37]. However, for a high deposition density, the interaction among the nanoparticles starts to influence the calculated XSW. Despite the use of factors suggested to also take into account the surface condition (e.g. defining a roughness), the calculated 1D intensity distributions typically have large errors for such non-planar systems [38], [39].

To overcome this limitation of 1D XSW calculations for nanoparticles, a complementary Geometrical Optics (GO) technique was developed [40]. This approach is based on the calculation of each X-ray path within the specimen volume, taking into account the refraction, reflection and transmission at the different interfaces (both vertical and horizontal). In the GO approach, the geometrical boundary conditions and different periodicities can be taken into account [41] and the feasibility of such an analysis by GIXRF has been demonstrated for several 3D structures [39], [40]. One of the main limitations of the GO approach is that this technique requires accurate knowledge of the morphology of the 3D structures as an input parameter. Thus, other complementary analyses are required (e.g. GISAXS) to morphologically characterize the 3D structured specimen under the investigation.

To date, GIXRF is not yet well-established for the compositional analysis of 3D nanostructures and irregular heterogeneous layers, mainly due to the complexity in the calculation of XSW field intensities. To further develop and assess the reliability of the XSW field intensity calculations for 3D nanostructures, 3D reference materials are needed as a test vehicle.

In this project, we have developed different 3D nanostructures with a high degree of uniformity with respect to their composition and dimension (e.g. shape and size) and different characteristic dimensions ranging from some hundreds of nanometers down to sub 20 nanometer. We have well characterized the prepared 3D nanostructures in terms of the structural dimensions and their uniformity over a large area. These well-characterized 3D nanostructures can potentially also be utilized as a test vehicle for other 3D analytical techniques such as 3D ToFSIMS and APT. The preparation and characterization of the 3D nanostructures will be discussed in detail in the following sections.

### **2.2.2 3D structures with sub micrometer scale**

In order to investigate the sensitivity of GIXRF analysis of the lateral ordering of 3D nanostructures, we have prepared several Cr and Al based nanostructures with different lateral ordering and dimensions in collaboration with the Physikalisch-Technische Bundesanstalt (PTB). In particular two groups of Cr nanostructures were prepared with an identical structural shape and dimension, while their lateral ordering were completely different: one in the form of an ordered array and the other one randomly distributed (see Figure 10). Both Cr nanostructures had an identical square shaped unit cell, with the dimension of  $300 \times 300 \times 20 \text{ nm}^3$  (length  $\times$  width  $\times$  height), repeated over an area about  $1 \times 15 \text{ mm}^2$  and an identical lateral density (number of repeated structures per unit area). In addition, an array-like ordered Al nanostructures was also prepared with a smaller lateral dimension of  $200 \times 200 \times 20 \text{ nm}^3$  (length  $\times$  width  $\times$  height).

The Al nanostructures were prepared on a Si (100) substrate. Electron beam lithography (EBL) was used to pattern the deposited resist (130 nm thick PMMA) on the cleaned substrate. Then a 20 nm thick film of Al (by sputtering) was deposited uniformly over the samples. Finally, the realization of 3D nanostructures was obtained by the lift-off process. The preparation of the Cr nanostructures was carried out with a similar procedure on a silicon (100) substrate with a 300 nm thick thermally grown  $\text{SiO}_2$  at Physikalisch-Technische Bundesanstalt (PTB).

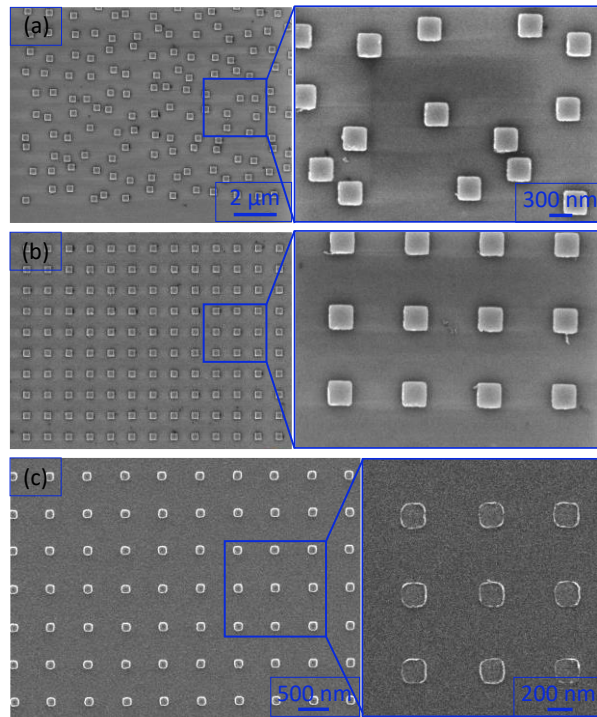


Figure 10: SEM image of the 3D Cr and Al nanostructures: (a) Cr randomly distributed, (b) Cr array-like ordered, (c) Al array-like ordered.

### 2.2.3 3D nanostructures at sub 20 nm scale

We have developed different 3D nanostructures with structural ordering and dimensions comparable to industrial applications (e.g. technology node), with feature sizes from 19 nm down to 13 nm.

The ISO 35:2017 guide defines reference material (RM) as "material, sufficiently homogeneous and stable with respect to one or more specified properties, which has been established to be fit for its intended use in a measurement process". This requires the 3D reference nanostructures to have a high degree of uniformity, in view of structural ordering and dimensions, over a large area (i.e. entire patterned sample). To overcome the current limitations of the conventional lithography techniques in patterning sub 20 nm features and to be aligned with the aforementioned requirements for the preparation of reference material, the 3D nanostructures in this study were prepared by exploiting the self-assembly of di-block copolymers (DBC) as a lithography mask as discussed in detail in the next section. We have also studied the pattern transfer of sub 20 nm feature sizes into the different substrates (Si, SiO<sub>2</sub> and Ge). In particular, we studied in detail the influence of DBC feature size (from 19 nm down to 13 nm) on the pattern transfer into Si.

#### Self-assembly of DBC

The di-block copolymers (DBC) are a special class of macromolecules composed of two incompatible and chemically distinct polymeric blocks. By a proper thermal process, at a temperature above their glass transition temperature,

these blocks can phase-separate and self-assemble into a highly ordered pattern over a large area (e.g. entire sample area).

The phase-separation of the polymeric blocks can be realized in different morphologies (cylinders, spheres, lamella and gyroid) mainly depending on the relative fraction of the two polymeric blocks [42], while for a given morphology, the short-range characteristic dimensions (e.g. periodicity) are determined by the molar mass of the block copolymer (BCP) [43].

Among the different morphologies, the perpendicularly oriented cylinders have a particular structural ordering in a hexagonally packed order, which is also suitable for the lithography applications. In that case by selectively removing one of the constituent blocks, well-ordered pillars or holes structures can be obtained [43]. The short-range characteristic dimensions, diameter ( $d$ ) and center-to-center distance ( $L_0$ ), of such a morphology, can be finely tuned by the molar mass of the BCP as shown in Figure 11.

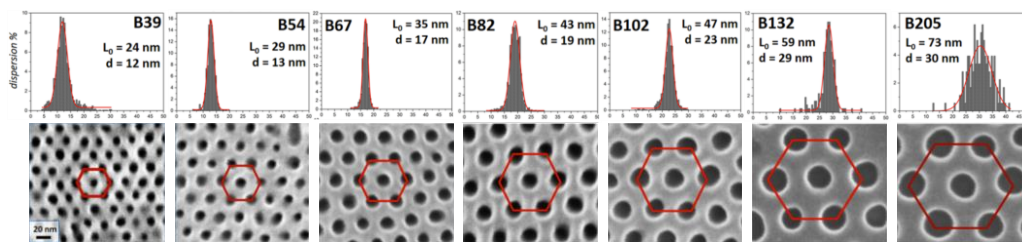


Figure 11: SEM images of the perpendicularly oriented cylinders (at bottom) and the distribution of pore diameter (on top) calculated for different PS-b-PMMA BCP on a large area. The BCPs have molar masses ranging from 39 to 205 kg/mol. The reported values for pore diameter ( $d$ ) and center-to-center distance ( $L_0$ ) were rounded to the nearest integer. Reproduced from [43].

The capabilities of DBCs in perpendicularly oriented cylindrical morphology, make DBCs strongly appealing for the preparation of reference structures in our study. In particular, the compatibility of self-assembly of DBCs with pattern transfer application allowed us to overcome the limitation of other conventional lithography techniques (e.g. EBL) in patterning the dense structures at sub-20 feature sizes over a large area.

For a properly neutralized substrate, the pore diameter ( $d$ ) and center-to-center distance ( $L_0$ ) have a small dispersity (see Figure 11) over a large patterned area, especially for BCPs having molecular weights of 54, 67 and 82 kg/mol [43]. This is compatible with the degree of the uniformity required for the preparation of the reference structures in our study, where the average parameters (e.g. pore diameter and center-to-center distance) and their distributions (i.e. standard deviation) must be known.

Different aspects of DBCs for achieving well-ordered perpendicularly oriented cylinders were widely studied in the literature for the polystyrene-block-poly (methyl methacrylate) (PS-b-PMMA) BCP, including the surface neutralization [44], the influence of the film thickness [45] and the thermal processing [46], [47]. However, the pattern-transfer of DBC structures into the underneath substrate (e.g. Si and SiO<sub>2</sub>) was not well-explored yet. To prepare different 3D reference structures in this project, the pattern-transfer of the DBC mask (e.g. into Si and SiO<sub>2</sub>) was an essential step to realize the 3D nanostructures.

In this project, to study the pattern-transfer of the DBC masks into Si substrate, we have prepared several PS-*b*-PMMA DBC masks in the perpendicularly oriented cylinders with different characteristic dimensions (i.e. diameter of cylinders). A brief description of the procedures used for the self-assembly of DBCs, will be described as follows. In this project, the self-assembly of PS-*b*-PMMA DBCs in perpendicularly oriented cylinders were carried out according to the procedure developed by Ferrarese L.F., et al [43]. This procedure is schematically depicted in Figure 12.

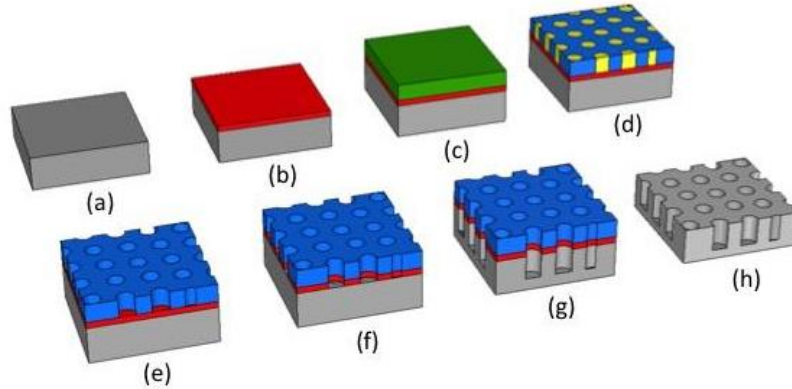


Figure 12: Schematic representation of the experimental procedures used for the self-assembly of PS-*b*-PMMA DBCs in perpendicularly oriented cylinders on the Si substrate and its successive pattern transfer. (a) Substrate cleaning and functionalization. (b) Deposition and grafting of random copolymer (RCP). (c) Deposition of block copolymer (BCP). (d) Phase-separation and self-assembly of PMMA (in yellow color) in perpendicularly oriented cylinders. (e) Selective removal of the PMMA cylinders. (f) Removal of RCP from the bottom of the cylinders. (g) Pattern transfer into the Si substrate. (h) Removal of the residuals of PS mask.

A (100) Si substrate with a dimension of  $1 \times 1 \text{ cm}^2$  was selected for the preparation of all the specimens in this study. In order to clean the substrates and promote the concentration of hydroxyl groups on the surface, a bath in Piranha solution  $\text{H}_2\text{SO}_4/\text{H}_2\text{O}_2$  (3:1) at  $80 \text{ }^\circ\text{C}$  for 40 min) was carried out. Then, the samples were rinsed in  $\text{H}_2\text{O}$ , cleaned in an ultrasonic bath of isopropanol and finally dried by  $\text{N}_2$  flow. To achieve well-ordered perpendicularly oriented cylinders, surface neutralization by a brush layer of P(S-*r*-MMA) random copolymer (RCP) was reported to be an effective method by many authors [47] as such a brush layer can balance the surface interaction and interfacial energy [48]. In this study, a RCP solution (9 mg in 1 ml Toluene) was deposited on the cleaned surface by spin coating (30 s at 3000 rpm). Then, the grafting of the RCP chains was obtained by annealing the specimens using the rapid thermal processing (RTP) at  $250 \text{ }^\circ\text{C}$  for 300 s according to the procedure described in [43]. Finally, the excess non-grafted chains were removed (ultrasonic bath of Toluene) and about 3.3 nm thick grafted RCP layer (measured by ellipsometry) was obtained on top of the Si substrate.

To prepare different DBC masks having each a different pore diameter (i.e. cylinder diameters), we have selected three asymmetric PS-*b*-PMMA DBCs (i.e. three different molar masses), which according to reference [43] allow a better uniformity in view of the characteristic dimensions (pore diameter and center-to-center distance) with respect to other molar masses. These three asymmetric PS-*b*-

PMMA DBCs had the molar masses of  $M_n = 54, 67, 82$  kg/mol and their characteristics are reported in Table 5. For the sake of simplicity, each DBC was labeled according to its molar mass as B54, B67 and B82.

The deposition of DBCs on the grafted RCP, was carried out by spin coating (30 s at 3000 rpm) of each DBC solution (9 mg in 1 ml Toluene). As the result, we obtained about 30 nm thick layer of DBC on top of the grafted RCP for all the DBC groups. To achieve the self-assembly of DBCs in the perpendicularly oriented cylinders (Figure 12d), all the specimens were annealed in RTP tool, according to the conditions suggested in reference [43].

Table 5: Characteristic of DBC masks: DBC molar mass ( $M_n$ ), polystyrene block molar mass ( $M_n$  styrene), polystyrene volume fraction ( $f$ ), polydispersity Index (PDI), average cylinder diameter ( $d$ ), average center-to-center distance ( $L_0$ ), DBC film thickness ( $h$ ). The aspect ratio was calculated as  $h/d$ .

Sample	$M_n$ [kg/mol]	$M_n$ Styrene [kg/mol]	$f$	PDI	$d$ [nm]	$L_0$ [nm]	H [nm]	Aspect ratio [-]	Porosity [%]
B54	53.8	37.0	0.71419	1.07	$13.0 \pm 1.0$	$28.8 \pm 0.5$	30	2.3	18.5
B67	67.1	46.1	0.71353	1.09	$17.1 \pm 1.0$	$35.0 \pm 1.0$	30	1.8	21.4
B82	82.0	57.0	0.72121	1.07	$19.0 \pm 1.0$	$42.9 \pm 0.7$	30	1.6	17.7

The removal of the PMMA cylinders was carried out by the UV exposure and immersion of the specimens in the acetic acid bath according to the procedure described in [43]. Finally, to obtain the DBC masks, an isotropic oxygen plasma treatment was carried out to remove the thin RCP layer from the bottom of the pores and cross-link the PS chains in the structured PS masks (see Figure 12d). Please note that, a long oxygen plasma treatment can result in a pore enlargement, as discussed in reference [49]. Thus, to minimize the pore enlarging, a thin RCP layer ( $\sim 3$  nm) has been utilized in this study, whereby we expect the pore enlarging to remain much less than 1 nm according to the erosion rate suggested in [49].

In Figure 13, the SEM image of one of the self-assembled DBCs (molar mass: 82 kg/mol) is shown which confirms the formation of the perpendicularly oriented cylinders in a hexagonally packed in-plane ordering. The in-plane morphology of the same specimen after the removal of the PMMA cylinders and the RCP thin film was investigated by the atomic force microscope (AFM). As the AFM tip (tip diameter  $\sim 10$  nm) cannot deeply penetrate in such narrow pores (diameter  $\sim 19$  nm), the reported depths of the pores by the AFM measurements are not accurate. Indeed, we investigated the in-plane morphology of the PS mask in the area between the pores (see Figure 13b) by this technique. We observed an arithmetic average surface roughness ( $R_a$ ) of  $\sim 2$  nm over the analyzed area ( $250 \times 250$  nm<sup>2</sup>).

In the next section, the pattern transfer of the prepared DBC masks into the Si substrate will be discussed in detail.

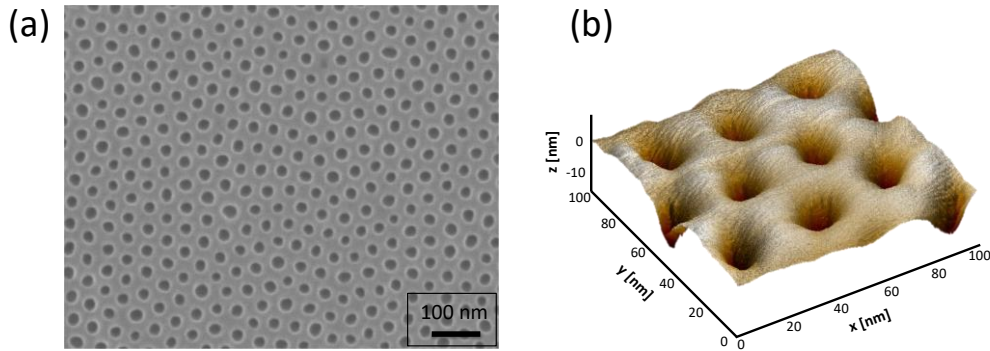


Figure 13: (a) SEM image of the self-assembled DBC (B82) before the selective removal of the PMMA cylinders. (b) AFM height map of the same sample after the removal of the PMMA cylinders and the RCP thin film.

### Pattern transfer at sub 20 nm scale

In this section, we will briefly describe the current state-of-the-art pattern transfer into the Si substrate for feature sizes at sub 20 nm. Then we will discuss in detail our study on the influence of DBCs pore diameter (from 19 to 13 nm) on the pattern transfer into the Si substrate.

The successful transfer of sub 20 nm patterns into the Si substrate, was reported by several authors, where typically a sacrificial hard mask was used to improve the etch selectivity during this process [50], [51], [52]. The hard mask can be either realized by an intermediate pattern transfer step, e.g. metal or an oxide (typically  $\text{Al}_2\text{O}_3$ ,  $\text{SiO}_2$  and Cr) [53], or alternatively by a sequential infiltration synthesis (SIS) technique [54], [55], [56]. For low aspect ratio etch applications, this methodology (i.e. hard mask) is redundant and can potentially become detrimental for the overall process through introducing additive materials and increasing the process complexity. Alternatively, the use of a soft mask (e.g. DBC mask) combined with a highly selective etch process (e.g. reactive-ion etching) is a viable strategy for the low aspect structures.

The reactive ion-etching (RIE) of Si for micrometric and nanometric patterns (typically features  $> 50$  nm) has been extensively studied in the literature for both shallow and deep etch applications. The latter is typically referred to as deep reactive-ion etching (DRIE), which requires also a special RIE tool. Several aspects of this process for different plasma chemistries and different aspect ratios were well investigated including: aspect ratio dependence etch (ARDE) [57],[58], influence of feature size on the apparent etch depth (commonly referred to as RIE-lag) [59] and influence of pattern density (MICRO-loading) [60],[61]. These "RIE effects" will be discussed later in this section.

The extension of the RIE process for pattern transfer applications at sub 20 nm features is still largely unknown and all the aforementioned effects are still not well evaluated in this scale. In addition, improvement in the sidewall characteristics for etch applications at sub 20 nm scale, e.g. FinFet fabrication, are still required [62].

In this project, we have studied several RIE etch processes and chemistries which can potentially be utilized for Si etch applications at sub 20 nm scale. In

particular three main chemistries are currently used in the DRIE and RIE of Si, including F, Cl and Br-based plasmas. The Cl and Br-based etch chemistries were demonstrated to etch high-aspect ratio Si structures even for features sizes below 15 nm [63]. Alternatively, F-based etch chemistries (e.g. SF<sub>6</sub> and CHF<sub>3</sub>) are commonly used in most laboratories and industry owing to the higher safety level as compared to the other chemistries. The Bosch process, fluorocarbon mixing mode (also referred as to Pseudo Bosch [64]) and the Cryogenic process are among the widely used F-based etch processes for the DRIE application. We will briefly discuss these processes and their potential capabilities to etch sub 20 nm patterns.

The Bosch process (also referred to as gas-chopping process) is a well-developed process for the high aspect ratio Si etch applications and it is used widely in micro electro-mechanical systems (MEMS). This process was first introduced by Lärmer [65] and has been developed further during the last two decades. The Bosch process is an alternating etch process based on the switching of the plasma between the etch step (e.g. SF<sub>6</sub> gas) and passivation step (e.g. C<sub>4</sub>F<sub>8</sub> gas). The main limitation of this process to etch the nanostructures is the scalloping shape of the sidewalls, i.e. saw-teeth shape, which is created due to the alternating nature of this process. Although, this process was demonstrated to be capable of etching high aspect ratio nanopillars (diameter ~ 50) [66], the extension of this technique to etch sub 20 nm features is still challenging.

The mixing mode process (also referred to as Pseudo Bosch [64]), is another fluorocarbon based etch chemistry (typically SF<sub>6</sub> and C<sub>4</sub>F<sub>8</sub> gases), whereby both etching and passivation are done simultaneously in single plasma chemistry. This process is capable of etching high aspect ratio Si structures with smooth vertical sidewalls. Therefore, this process is a viable candidate for Si etch through the nanometric patterns [67]. The drawback of this process is its relatively high degree of physical etching required to eliminate the passivation formed at the bottom of etch (e.g. bottom of trenches). As a result, the selectivity of this etch process (between Si and polymeric mask) is typically poor, thus this process is mostly suitable for etch applications using a hard mask (e.g. Al<sub>2</sub>O<sub>3</sub>).

In the Cryogenic etch process, both etching and passivation are done simultaneously using SF<sub>6</sub>-O<sub>2</sub> chemistry [68]. By cooling the wafer to a temperature between -100° and -140° C, the reactivity of Si and O to form a thin film of SiO<sub>x</sub>F<sub>y</sub> (as the passivator) increases and very smooth vertical sidewalls can be obtained at this temperature range [69]. In contrast to fluorocarbon based chemistries, in the Cryogenic etch process the reactive neutrals (F and SF<sub>x</sub>, x=1 to 5) are the etchant species instead of F-based ions [69]. As a result, this process is predominantly a chemical etch, whereby only a low degree of physical milling is required to remove the inhibitor layer and the etch products from the horizontal surfaces (i.e. bottom of etch) [59]. This makes the Cryogenic process a highly selective Si etch for pattern transfer applications using a soft mask, whereby a selectivity up to 100:1 (Si - optical photoresist) was reported for this process [70]. The capabilities of the Cryogenic process to etch Si with high selectivity, smooth

sidewalls and very thin inhibitor layer makes this process extremely suitable for etch applications at sub 20 nm pattern size [71].

In this project, we have investigated the application of the Cryogenic etch of Si for pattern transfer of a 30 nm thick nanopatterned PS masks, obtained by self-assembly of DBC, with the pore diameters below 20 nm. We will discuss that the narrow pores of DBC masks reduce significantly the Si etch rate at the bottom of the pores and hamper the selectivity of the etch process (Si to PS) even for the very low aspect ratio structures.

The patten transfer in this project was carried out by Plasmalab 100 RIE tool and the recipe is reported in Appendix A. In order to compare the Si etch rate through the nanopatterned PS mask, i.e. B82 DBC mask having the largest pore diameter, and a bare Si substrate, we processed the B82 DBC sample with a bare half masked Si substrate (by an optical resist) together in the RIE tool. We have repeated the RIE process for different etch durations ( $t_{\text{RIE}}$ ) ranging from 20 to 240 s. After the etch process, the residuals of polymeric masks were stripped by oxygen plasma. The etch depth for the nanopatterned Si structures were measured by ellipsometry (M-200U spectroscopic ellipsometer) using the one-layer model (Si-void), according to the procedure described in [49]. The etch depth for half masked bare Si samples was measured by a stylus profilometer (Tencor P10).

In Figure 14 the evolution of the measured etch depth as a function of etch duration is reported for both the nanostructured and the bare Si substrates. For the bare substrates, we observed a linear increase of the etch depth as a function of the etch time ( $t_{\text{RIE}}$ ) with the slope corresponding to an etch rate about 60.2 nm/min. Vice versa, for the nanostructured Si, using the B82 DBC mask, we observed two distinct trends in the etch depth (see Figure 14 b), whereby for the etch durations  $20 < t_{\text{RIE}} < 120$  s, etch depth increased up to 27 nm (at 120 s), corresponding to an etch rate about 14.9 nm/min. For  $t_{\text{RIE}} > 120$  s, we observed a quasi-linear decrease in the etch depth with a slope slightly lower than that of the ascending region.

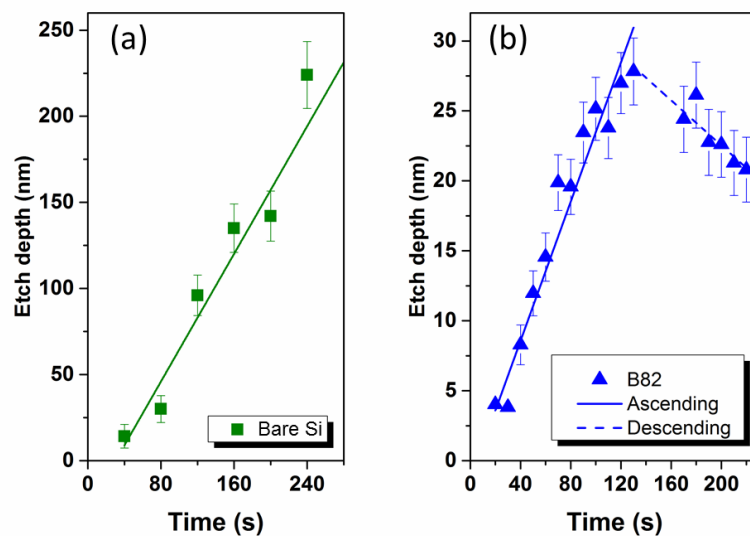


Figure 14: The measured etch depth as a function of RIE etch time ( $t_{\text{RIE}}$ ) for the bare Si substrates (a) and the nanostructured Si by the B82 DBC pattern (b).

This implies that for  $20 < t_{\text{RIE}} < 120$  s, the etch rate through the nanopores of the B82 DBC mask was about 25 % slower than that of bare Si.

To better understand these two distinct etch trends for the B82 DBC mask, we investigated the surface morphology of the nanostructured Si by AFM. As shown in Figure 15, our analysis indicated that for  $20 < t_{\text{RIE}} < 120$  s, the region of substrate between the adjacent pores had a smooth surface with a roughness comparable to that of unprocessed Si wafer ( $R_a \sim 0.2$  nm), while we observed an increase in the surface roughness ( $R_a \sim 0.6$  nm) for the specimen etched at  $t_{\text{RIE}} = 170$  s. Please note that the region between the adjacent pores were initially masked by the PS (DBC mask), whereby we expect to have a surface roughness comparable to that of unprocessed Si wafer in this region of the specimen, similar to what observed for those specimens processed at  $20 < t_{\text{RIE}} < 120$  s.

For the specimen etched at  $t_{\text{RIE}} = 200$  s, a certain degree of waviness ( $R_a > 3$  nm) was developed on the specimen surface (the area between the adjacent pores) during the etch process, which suggests that the DBC mask was completely degraded and the substrate was etched without any mask. As the AFM tip cannot deeply penetrate in the narrow pores of the Si nanostructures, the reported depth values in Figure 15 cannot be used to extract the etch depth.

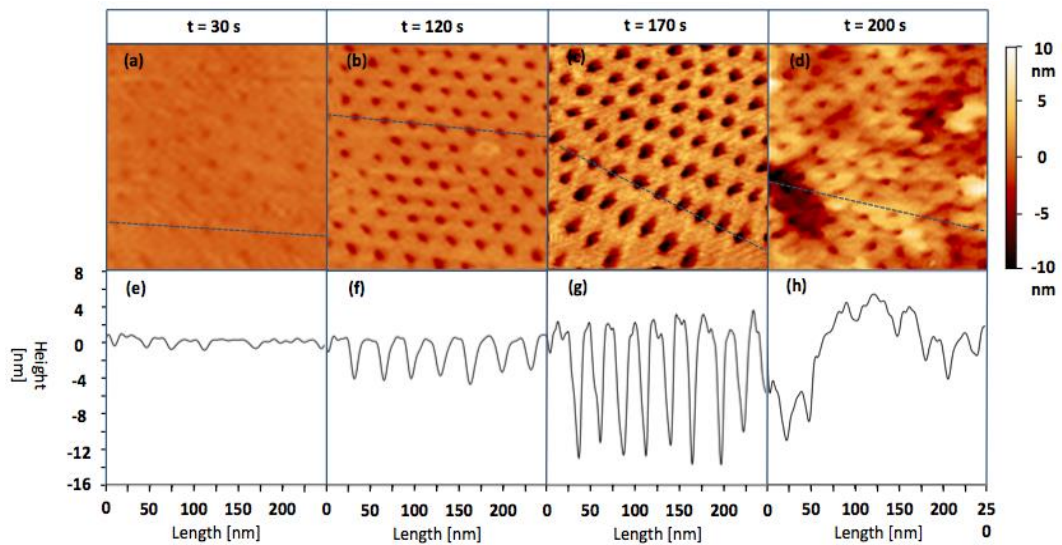


Figure 15: Surface morphology of nanostructured Si after the pattern transfer from B82 DBC mask: (a–d) AFM micrographs, (e–h) transversal AFM depth profiles. The measured area was  $250 \times 250$  [nm]<sup>2</sup> for all the samples. Note that the measured depth of pores by AFM cannot be used to extract the depth of etch, due to the limitation of the AFM tip to deeply penetrate inside the narrow pores.

To investigate the influence of DBC pore diameter on the pattern transfer into Si, we have processed also the B67 and B54 DBC masks, having pore diameters of 17 and 13 nm respectively, according to the process window obtained from B82 mask ( $20 < t_{\text{RIE}} < 120$  s). In Figure 16a, the obtained etch depths as a function of etch time are reported for different DBC masks. Our analysis clearly indicated that at each  $t_{\text{RIE}}$ , the depth of etch in nanostructured Si was higher for the larger pore diameter. Please note that, for the short etch durations ( $t_{\text{RIE}} \leq 30$  s), the pattern transfer into Si was not yet realized. Thus, the measured etch depths by

ellipsometry (using one-layer model) were not reliable for this range of  $t_{\text{RIE}}$ , which is also highlighted in grey colour in Figure 16a. This will be discussed later by SEM images in Figure 18.

Based on the obtained linear relation between the etch depth and etch time for  $20 < t_{\text{RIE}} < 120$  s (see Figure 16a), we have calculated the etch rate for each DBC mask and the results are compared in Figure 16b. As can be seen, the etch rate was slightly higher for the DBC masks with the larger pore diameter, whereby the etch rate for the B82 mask was higher than the B67 (by about 6 %) and the B54 (by about 16 %). Vice versa, the etch rates through all the DBC masks were significantly lower than that of the bare Si (see Figure 16a), whereby the etch rate obtained from the bare Si was about 4 times higher than the one obtained from the B82 DBC mask which has the largest pore diameter.

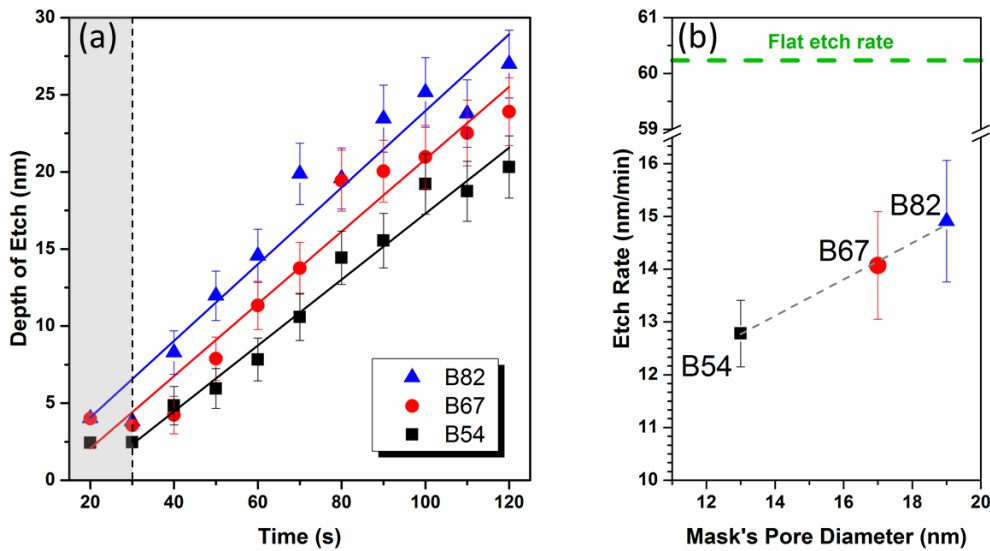


Figure 16: (a) Etch depth in Si as a function of RIE etch time ( $t_{\text{RIE}}$ ) for the DBC masks having different pore diameters. (b) The calculated etch rates for the different DBC masks as a function of their pore diameters. The etch rate for the bare Si is also indicated by a green dashed line.

In order to explore different aspects of the pattern transfer of DBC masks, we have compared the in-plane morphology of the nanostructured Si with the original pattern of the DBC masks by calculating the pore diameter for all the Si nanostructures, processed at  $t_{\text{RIE}} < 120$  s. The calculation of the pore diameters was carried out by analyzing the SEM images taken on a large area, using ImageJ software. As shown in Figure 17, the pore diameter in all the three groups of nanostructured Si was enlarged as the etch duration was increased. We observed that the pore diameters of the nanostructured Si were smaller than that of DBC mask for B82 and B67 groups by operating at a  $t_{\text{RIE}}$  range shorter than 55 and 70 s respectively. This can potentially be assigned to an incomplete pattern transfer, while for B54, the pore diameter of the nanopatterned Si was reached to that of DBC mask only for  $t_{\text{RIE}} > 110$  s.

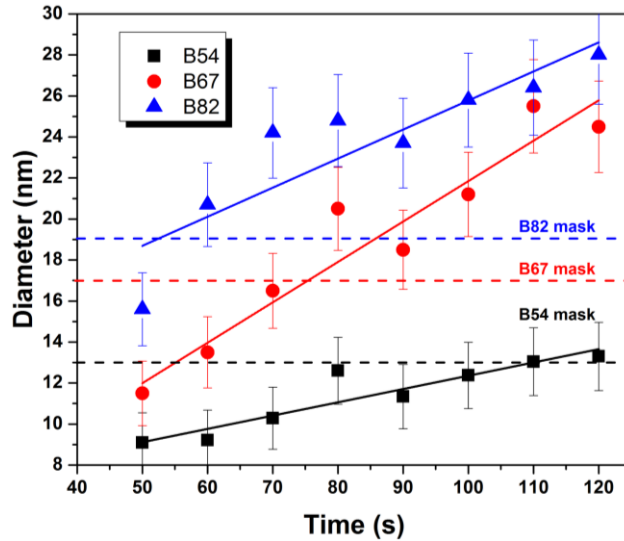


Figure 17: Evolution of the pore diameter in Si as a function of etch time for the three groups of DBC masks. The mask diameter for each DBC group is also indicated by a dashed line in the figure. The reported pore diameters were calculated from the SEM images. For  $t_{RIE} < 50$  s, due to the insufficient contrast in the SEM images, the pore diameters were not reported.

Finally, by combining the in-plane morphological analyses performed by the SEM and the AFM on the Si nanostructures, we classified four operational windows as a function of  $t_{RIE}$ , as shown in Figure 18. These operation windows are: (A) Incomplete pattern transfer, (B1) Good pattern transfer, (B2) Appearance of roughness surface and (C) Distorted zone.

For  $t_{RIE} \leq 30$  s (operation window A in Figure 18), the SEM images clearly indicate that the hexagonally packed pattern of the DBC masks is partially absent by the missing pores, thus the pattern transfer was incomplete. This also explains the unreliable ellipsometry measurement (poor  $R^2$  fit) observed in Figure 16 for  $t_{RIE} \leq 30$  s. The operation window classified as B1 was determined according to two criteria: the complete realization of the original hexagonally packed pattern of the DBC masks (from SEM images) and a negligible change in the surface roughness of the Si substrate in between adjacent pores (from AFM). For  $t_{RIE} > 120$  s, the surface roughness of the Si substrate in between adjacent pores, was increased gradually (according to AFM analysis), which implies that the mask degradation was started at this stage of the etch process. In addition, we observed also a slight decrease in the etch depth (see Figure 14) for  $t_{RIE} > 120$  s. Please note that for both B1 and B2 operational windows, the DBC pattern was completely transferred into the Si substrate, while in B2 the Si substrate in between adjacent pores was partially etched. Finally, for a longer etch duration,  $t_{RIE} > 200$  s for B82,  $t_{RIE} > 170$  s for B67 and  $t_{RIE} > 150$  s for B54, we observed distortion in the surface morphology in both SEM images and the AFM maps, thus this region of the process was classified as the distorted zone C.

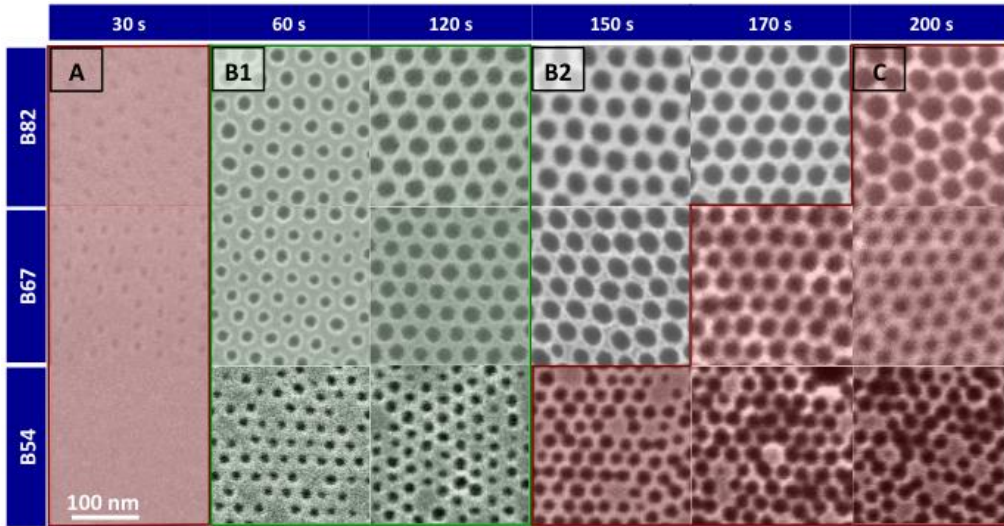


Figure 18: SEM image of the nanopatterned Si structures after the pattern transfer of the DBC masks using different etch durations. Four operation windows were identified (see the main text for the criteria) as: (A) Incomplete pattern transfer. (B1) Good pattern transfer. (B2) Appearance of roughness surface. (C) Distorted zone.

Our analysis suggests that the main limitation to achieve a higher etch depth is the apparent selectivity between the Si and the PS mask (i.e. DBC mask), which is also influenced by the pore diameter of the DBC masks. To evaluate whether a thicker mask can allow a higher maximum achievable etch depth, we prepared a series of 40 nm thick DBC masks from the B54 family, which corresponds to about 33 % increase in the mask thickness. It is worth noting that the characteristic dimensions of the 40 nm thick masks, pore diameter ( $d$ ) and the lattice spacing ( $L_0$ ), were identical to that of 30 nm thick DBC masks. Finally, we repeated the same RIE etch process on the thicker masks and the results for both mask thicknesses are compared together in Figure 19.

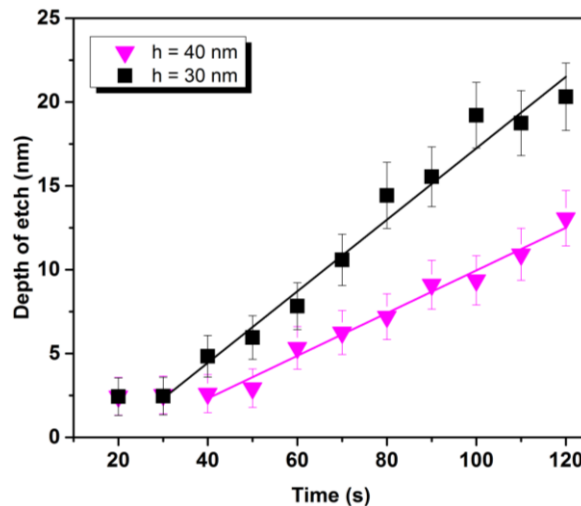


Figure 19: Comparison between etch behavior of B54 DBC masks having different thicknesses: 30 nm and 40 nm. The horizontal axis shows the etch duration.

Our analysis clearly indicates that for the thicker DBC mask (40 nm thick), the pattern transfer was started with a short delay ( $\sim 50$  s) and the observed etch rate was about 40% slower than that of 30 nm thick mask (7.6 versus 12.8

nm/min). Therefore, the increase in the mask thickness resulted in a drop in the etch rate and negatively impacted the maximum achievable etch depth.

To physically understand and explain the observed feature-dependent etch behavior through the narrow pores of DBC masks, several aspects of the RIE etch process must be taken into account. The RIE etch performance for pattern features down to 50 nm, has been studied in the literature [59], [72], [73], while the influence of smaller features (e.g. at sub 20 nm) is still not well explored. Typically at that scale (features > 50 nm), the influence of the mask feature size on the etch rate is referred to RIE-lag [74]. Beside the minimum mask feature size, another main difference between the presented DBC pattern and the aforementioned studies is the pattern density, whereby our DBC pattern is densely distributed over a large area of the sample, while the reported nanometric patterns in the literature, typically obtained by EBL, were distributed over a smaller area with much lower pattern density. These differences in the patterns (coverage area and the density) can result in a sensible variation of etch rate, which is known as MACRO-loading and MICRO-loading effects. This will be discussed in detail for our DBC masks in the next paragraphs.

The MACRO-loading in RIE process describes the commonly observed drop in the etch rate as the overall amount of exposed Si (unmasked area) increases. This is due to the higher consumption of fluorine-based reactive species (radicals for Cryogenic process) for higher Si loads [69]. To avoid the influence of MACRO-loading in our experiments, all the specimens were prepared in the same dimension ( $1 \times 1 \text{ cm}^2$ ) and for each etch process, the samples from the different DBC groups (B54, B67 and B82) were loaded together on a 6-inch Si carrier wafer.

The MICRO-loading is another RIE effect which can influence the etch rate and limit the final achievable etch depth. This effect accounts for the local Si load (unmasked areas) according to the mask pattern, thus the MICRO-loading strictly depends on the pattern density and can cause the local depletion of reactive species [58]. This can result in the appearance of the different etch depths across the area of a processed wafer according to the local densities of the pattern [61],[75]. We have investigated the potential influence of MICRO-loading caused by the differences in the porosities of the different DBC masks (see Table 5).

As can be seen from Table 5, the B67 DBC mask had the highest porosity (~21.4%) as compared with the other DBCs, where the B54 and the B82 have a porosity about 18.5% and 17.7% respectively. The achieved etch rate and the maximum etch depth for the B67 were in between the other two masks (see Figure 16). Our analysis clearly indicates that there is no distinct relation between the obtained etch rates and the porosities of the DBC masks (i.e. pattern density), thus the observed systematic variation of etch rates for the different DBC masks cannot originate from the MICRO-loading.

We have investigated other known RIE effects which can potentially influence the etch rate and the maximum achievable etch depth. For the high aspect ratio Si structures, a gradual decrease in the etch rate is typically observed as the etch depth increases (for a given feature size). This effect is commonly

referred to as "aspect ratio dependent etch (ARDE)"[66]. Thus, the ARDE can be characterized by plotting the etch rate as a function of the aspect ratio of the structure (or etch depth) for a given pattern size.

However, in our experiments, the measured etch rates for all the DBC masks were constant along the different process (in different etch depths). Indeed, our low aspect ratio Si nanostructures can be classified in the very first region of ARDE Plot (etch rate versus aspect ratio), where the variation of the etch rate, for each individual pattern size, is not yet noticeable. Thus, also ARDE could not have any influence on the observed etch behavior in our study.

Finally, by excluding the contribution of the aforementioned RIE effects, we attributed the observed trend of the etch rate for the different DBC masks to a purely feature size-dependent etch process. As discussed previously, the feature size-dependent etch, also referred as RIE-lag, is not yet well evaluated for sub 50 nm feature sizes, while, for larger features, this effect was reported to be caused by the similar physical sources as ARDE [69]. The latter has been widely studied in the literature, due to its vital impact on the fabrication of the high aspect ratio structures for MEMS. The four main physical sources for these RIE effects are typically reported as: Knudsen transport of neutrals/ions, neutral/ions shadowing (also referred as ion angular distribution (IAD)) and image force (IF). [74], [76],[77]. Nevertheless, the type of etch process (mixing mode or alternating), etch recipe (type of gases, temperature, pressure, etc) and the feature size (e.g. pore diameter) can greatly impact the role of the aforementioned phenomena, thus there are many controversies about the main source of the ARDE and feature size-dependent etch process.

In this study, we used the Cryogenic etch process (using SF<sub>6</sub> and O<sub>2</sub>) to etch all the specimen. This process is known to be predominantly based on a chemical etch rather than on ion milling. Opposite to the Bosch process, in the Cryogenic etch process neutrals are the reactive species instead of reactive ions [69]. For high aspect ratio structures, the depletion of fluorine-based reactive neutrals at the bottom of etch (e.g. bottom of Si pores) was reported to be the main source of ARDE effect in the Cryogenic [78]. Since the mean free path of neutrals in a plasma (typically in mm range) are much larger than the DBC pores, the transport of the fluorine-based neutrals and the etch products through the narrow channels of DBC masks/nanostructures are described by Knudsen transport [58]. This transport model, described the probability of fluorine-based neutrals to reach the bottom of the etch (e.g. bottom DBC pores), which depends on several parameters of both plasma (e.g. pressure and temperature) and the characteristic of the channel (e.g. DBC pore diameter), which is typically expressed as the aspect ratio of the channel [78].

Finally, according to the described studies from literature, we attribute the observed feature size-dependent etch from the different DBC masks to the Knudsen transport of the fluorine-based neutrals through the narrow channels of the DBC mask/Si nanostructures. Similar to what suggested by Blauw, M. A., et al [78], the simulation of the neutral transport through the narrow channels of

DBC can help a better understanding of this process and potentially overcome the observed limitations by improving the plasma parameters accordingly.

### Realization of 3D heterogeneous nanostructures

In the previous section, the pattern transfer of DBC masks into the Si substrate has been discussed in detail. By combining the capabilities of the self-assembly of DBCs and a precise pattern transfer by RIE, we were able to prepare different 3D Si nanostructures in the form of a holey Si with high control over the pore diameter, periodicity and the structure depth. We have extended our pattern transfer process also to SiO<sub>2</sub>, Ge and SiGe substrates, whereby the DBC patterns can be also realized in form of 3D nanostructured SiO<sub>2</sub>, Ge and SiGe with feature sizes down to 13 nm.

These well-developed etch processes can be applied to transfer the DBCs patterns also to multi-layer systems (e.g. SiGe/Si), thus 3D heterogeneous nanostructures can be also realized with the high control over the dimensional parameters. As the test samples, we have prepared several 3D heterogeneous nanostructures by the deposition of Al (~ 10 nm, by evaporation) over the nanostructured Si, SiO<sub>2</sub> and DBC mask (B67). The schematic representation of the prepared specimens together with the SEM images of a B67 DBC mask before and after the Al deposition are shown in Figure 20.

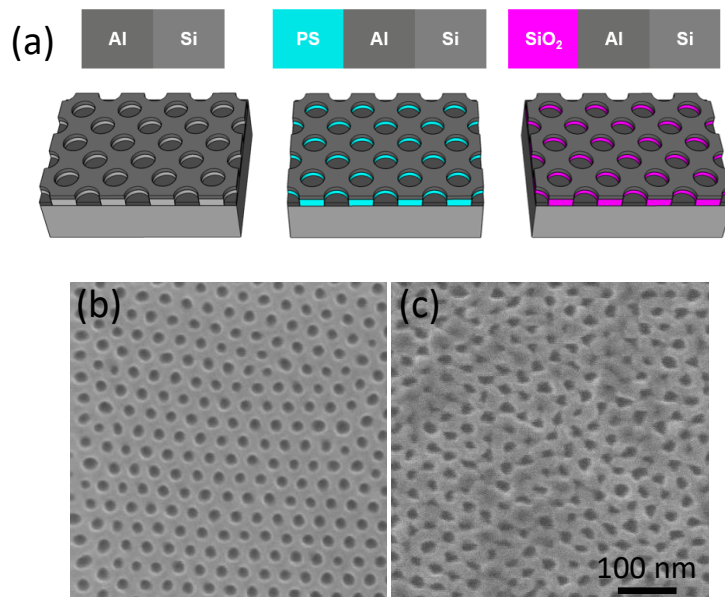


Figure 20: (a) Schematic representation of the prepared 3D heterogeneous nanostructures by the deposition of Al over the nanostructured Si, SiO<sub>2</sub> and the B67 DBC mask. (b) The SEM image of a self-assembled DBC mask (B67) before the deposition of Al. (c) The SEM image of the same mask after the deposition of Al.

### 2.2.4 Preliminary GIXRF analysis

In this section, we will briefly report the preliminary reference-free GIXRF analysis of the prepared 3D nanostructures. The reference-free GIXRF analysis was carried out at Physikalisch-Technische Bundesanstalt (PTB) using the

synchrotron facility of BESSY II. Please note that the reported results in this section were not part of this PhD work.

The reference-free GIXRF measurements for both array-like ordered and randomly distributed Cr reference nanostructures, were carried out at a photon energy of 7 keV. The obtained angular fluorescence profiles from the Cr-K signal are reported in Figure 21. The X-ray standing wave (XSW) field and its angular dependency was calculated for both Cr nanostructures according to the procedure described in [31], whereby each Cr block was assumed to have a perfect cubic shape with a nominal dimension of  $300 \times 300 \times 20 \text{ nm}^3$ . The modeled fluorescence angular profile and the experimental profile (GIXRF measurement) are compared together in Figure 21b, for the randomly distributed Cr nanostructures.

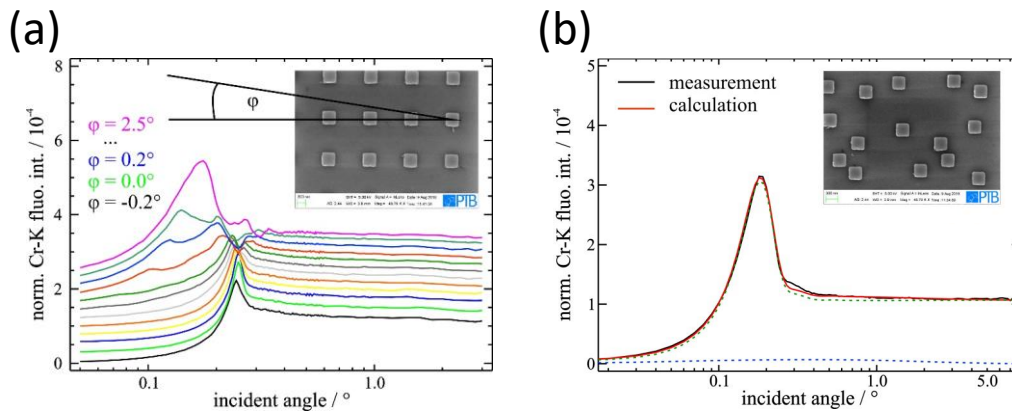


Figure 21: (a) Experimental GIXRF curve for array-like ordered Cr nanostructures as a function of the incident angle for the different in-plane orientations indicated by  $\phi$  angle (see the inset). (b) The comparison between the experimental fluorescence signal with GIXRF (black) and calculated model (red). The green-dotted curve indicates the fraction of GIXRF signal by the XSW excitation. The blue-dotted curve describes the direct excitation at the sides of the structures.

In addition, the GIXRF angular fluorescence profiles for the different in-plane incident angle  $\phi$  were measured by rotating (in-plane) the specimen with respect to the incident beam (see Figure 21a). For the array-like ordered structures, a strong dependency of the angular fluorescence profiles as a function of the in-plane incident angle  $\phi$ , has been observed (see Figure 21a), while for the randomly distributed structures, the angular fluorescence profiles at the different in-plane incident angles  $\phi$  were identical. The successful modeling of XSW combined with reference-free quantification is expected to reveal more characteristic dimensions for the Cr nanostructures.

For each reference Cr nanostructure, the nominal Cr mass deposition was estimated according to the Cr density and the morphology of nanostructures (cubic shape with the dimension of  $300 \times 300 \times 20 \text{ nm}^3$ ). In Table 6, the quantified Cr mass deposition by GIXRF for both reference nanostructures are compared to the nominal values.

Table 6: Comparison between the nominal Cr mass deposition, calculated according to the Cr density and the structural morphology, and the quantified value obtained from the reference-free GIXRF analysis.

Sample	Nominal Cr mass deposition [nm/mm <sup>2</sup> ]	Quantified Cr mass deposition [nm/mm <sup>2</sup> ]
Cr nanostructure array-like ordered	12.9	12.7 ± 1.3
Cr nanostructure Randomly distributed	12.9	12.0 ± 1.2

For the 3D nanostructures with characteristic dimensions below 20 nm, the calculation of XSW fields were not available as the moment and GIXRF analysis of those specimens can only provide the deposited mass of Al. The experimental GIXRF angular fluorescence profiles for the 3D heterogeneous structures shown in Figure 20 (nanostructures Al on top of the nanostructured SiO<sub>2</sub> or the DBC mask), are reported in Figure 22. The labeled numbers on the figure (#1 and #2) correspond to the GIXRF measurements carried out on two different specimens prepared according to the same procedure.

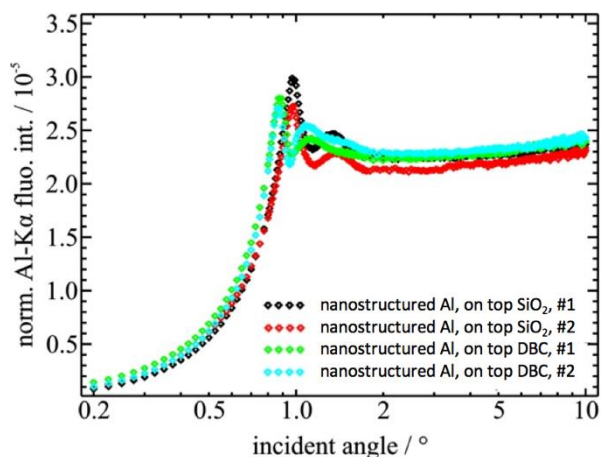


Figure 22: Comparison among GIXRF angular fluorescence profiles (Al-K signal) for different nanostructures obtained from DBC masks (see the inset).

The calculation of XSW fields for the 3D nanostructures are still ongoing research activity in PTB, whereby the successfully calculated angular fluorescence profiles can be compared to that of GIXRF measurements to determine all the morphological characteristics of the measured specimens.

## 2.3 Conclusion

In this chapter, we have briefly described the current state-of-the-art ToFSIMS and GIXRF analysis of 3D micro and nanostructures, in view of their reliability and traceability. Regarding 3D ToFSIMS analysis, we discussed that the recently developed hybrid ToFSIMS-SPM instrument allows corrections for the reconstruction artefacts created due to both topography modulations, caused by the differences in the sputter yields, and the original 3D topography of the structured specimens and its evaluation along the analysis depth. However, huge challenges still remain to metrologically assess the performance of such a

complex analysis, in view of the accuracy and repeatability of the 3D reconstructed volume. In particular, the absence of any 3D reference material and the calibration standard is among the main limitations, which prevents such a metrological evaluation and hamper the further improvements in the data fusion and development of more reliable reconstruction protocols.

We discussed that GIXRF is not yet a well-established technique for the compositional analysis of 3D nanostructures and irregular heterogeneous layers, mainly due to the complexity in the calculation of X-ray standing wave (XSW) field. To further develop the calculation of XSW field for 3D structures and experimentally assess its reliability, the 3D reference materials are needed as a test vehicle.

In this project, we have developed several well-characterized potential organic-inorganic 3D reference microstructures for 3D ToFSIMS. These 3D microstructures composed of a double-layered organic system (irganox and polystyrene) confined within the microstructured Si template in three different model-systems. The traceable dimensional characterization of the Si templates was carried out by a calibrated optical profilometry and the results were reported by the associated uncertainties and the issued certification from the Length Department of INRIM (NMI of Italy). Similarly, the morphology of each organic layer was measured by the optical profilometer. The design of the reference material in this project allows the use of the planar organic layers, far from the 3D microstructured region, as a reference for calibration of the sputter yields and the chemical information.

To prepare 3D nanostructures for GIXRF (as test vehicle) with structural ordering and dimensions comparable to those industrial applications (e.g. technology node), we exploited the self-assembly of di-block copolymers (DBC) as a lithography mask. The DBCs in the perpendicularly oriented cylindrical morphology allow the preparation of a well-ordered lithography mask on a large area (e.g. entire sample area) with the tunable characteristic dimensions at sub 20 nm scale.

We have studied in detail the pattern transfer of DBC masks into the Si substrate by reactive-ion etching (RIE) using the Cryogenic process. In particular the feature size-dependent etch of Si at sub 20 nm scale has been investigated in detail using PS-b-PMMA DBC masks with different pore diameters, ranging from 19 to 13 nm. Our results clearly indicate that the etch rate on the bare Si substrate (unmasked substrate) was about 450% higher than that obtained through the narrow pores of all the DBC masks. This corresponds to a remarkable decrease in the etch selectivity (Si to PS) from 15:1 to less than 1:1. In addition, the Si etch rate through the pores of DBC masks dropped about 14% as the pore diameter reduced from 19 to 13 nm. Furthermore, our analysis revealed that by increasing the thickness of DBC masks by 33%, the etch rate dropped about 40%, which implies that a thicker DBC mask cannot improve the maximum achievable etch depth, vice versa it has a negative impact on etch rate and the maximum achievable etch depth. We attributed the observed etch behavior to the Knudsen

transport of fluorine-based neutrals through the narrow channels of DBC masks/Si nanostructures.

By combining the capabilities of self-assembly of DBCs and the precise pattern transfer by RIE, we were able to prepare different 3D nanostructures in form of holey Si, SiO<sub>2</sub>, Ge and SiGe with characteristic dimensions below 20 nm and high control over the pore diameter, periodicity and the depth of the structures. The developed 3D nanostructures are suitable as the test sample for GIXRF analysis, where the characteristic dimensions and their distributions over a large area are known.

## Chapter 3

# Fundamentals of atom probe tomography

This chapter aims to introduce atom probe tomography (APT) and to discuss the basic physical principals of this technique. Atom probe tomography is an inherently three-dimensional microscopy technique, which enables elemental identification and quantification with a sensitivity down to 10 ppm, as well as to determine the atomic distribution of different elements in the material at near-atomic spatial resolution (down to  $\delta_{\text{lateral}}$ : 2-3 Å,  $\delta_{\text{depth}}$ : 0.5 Å). The basic physical principal of APT is the controlled field evaporation and successive removal of each individual atom from the specimen surface. Field evaporation refers to the physical phenomenon of the release of surface atoms from the lattice in the presence of an intense electric field. This process involves ionization, bond-breaking and finally release of the surface atoms. Typically, the electric field required to field evaporate an atom from the surface is on the order of a few volts/nm.

To induce such an intense electric field, the APT specimen needs to be prepared as a sharp needle with a tip radius typically below 100 nm. Due to the small tip radius, any applied electric potential (typically 1-10 kV) leads to a strong field enhancement at the tip apex such that the required electric field can be generated. The schematic of the APT measurement chamber is depicted in Figure 23.

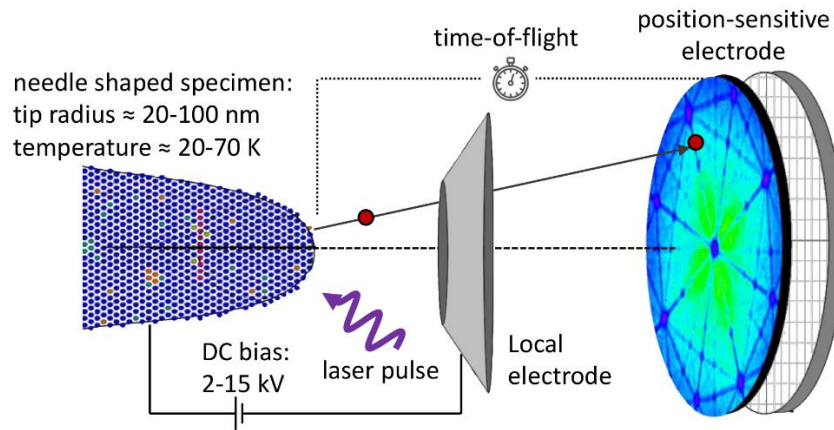


Figure 23: Schematic representation of APT measurement setup in laser mode using local electrode.

Since field evaporation is a probabilistic phenomenon and to avoid multiple ion generation at the same time, the removal rate of surface atoms is finely controlled using an additional voltage pulse or laser pulse, such that only a few atoms are evaporated every hundred pulses. Upon evaporation, each evaporated ion is immediately accelerated towards the positive sensitive detector, following trajectories determined by the electric field lines. The impact position of each ion on the position sensitive detector can be traced back to its original position on the specimen apex thus enabling to reconstruct its original spatial location. Obviously, the calculated position only reflects the original atom location provided that no migration of surface atoms occurs prior or during the field evaporation. Hence, the specimen is cooled down to a temperature typically below 70 K to minimize the surface migration and thus improve the lateral resolution of an APT measurement. Given the small radius of the APT tip ( $< 100$  nm) relative to the detector ( $\sim 10$  cm in diameter), a magnification in the order of  $\sim 10^6$  is usually observed in APT. Furthermore, element identification is based on time-of-flight mass spectroscopy (ToF), using the trigger of the laser (or voltage) pulse and the arrival time on the detector for the calculation of time-of-flight. With present instrumentation, a mass resolving power up to 1200 can be achieved in APT.

Finally, after the evaporation of all atoms of the specimen (more specifically limited to the depth of interest), the original three-dimensional distribution of all the atoms is calculated following a reconstruction protocol whereby the impact position of all the ions on the detector is translated into the original atomic positions on the specimen (laterally) and the evaporation sequence is used to calculate the depth distribution. Hence, APT can enable elemental identification of 3D structures and devices with atomic resolution.

In this chapter, I will explain different models that describe the physics of the field evaporation process in Section 3.1. These models will be compared together and their limitations and capabilities to describe the experimentally observed evaporation behaviour will be discussed in detail. In Section 3.2, the theory of post ionization will be discussed. This theory predicts the successive ionization of evaporated ions at the initial stage of their flight path in the vicinity of tip apex, in the presence of an intense electric field. Then in Section 3.3, the evaporation probability and evaporation rate will be discussed based on the introduced field

evaporation models and post ionization theory. I will continue by describing the laser tip interaction and explaining the physical phenomenon behind laser assisted APT in Section 3.4. Finally, the requirements for the APT specimen and the current available specimen preparation techniques for semiconductor and organic materials will be discussed in Section 3.6.

### 3.1 Theory of field evaporation

Field evaporation is the physical phenomenon by which a surface atom is ionized and subsequently removed from its own lattice under the application of an intense electric field. Once a DC bias is applied to a needle-shaped specimen, the induced electric field causes the polarization of the surface atoms. If this electric field is sufficiently intense, then field evaporation can happen.

There are two main theories for field evaporation which will be discussed in this session. The first theory is the image hump model by Müller [79]. This theory suggests that the atom is fully ionized before it is removed from the surface. While in the theory of the charge-exchange model, proposed by Gomer [80], the atom is gradually ionized while it is escaping from the surface. Despite the differences between these two models, both are based on thermodynamic considerations and suggest that field evaporation happens when the thermal agitation energy overcomes an energy barrier. This energy barrier is the energy which bonds an atom to the surface and is reduced by the application of an electric field.

The physical mechanism underlying the field evaporation can be visualized using one-dimensional potential energy diagrams as shown in Figure 24. In the neutral state, the potential energy of the surface atoms can be approximately described by Lennard-Jones potential model [81]. Depending on the distance between the atom and the surface, the interaction force (and the corresponding potential energy) varies from a repulsive or attractive force which can be explained by Pauli repulsion and Van der Waals force. At a certain distance (equilibrium bond length) the repulsive and attractive forces are balanced and the potential energy is minimum (potential well) [81]. In the absence of an electric field the surface atoms, in the neutral state, are located within the potential well and the energy to remove an atom from the surface is the supplementary ( $\Lambda$ ).

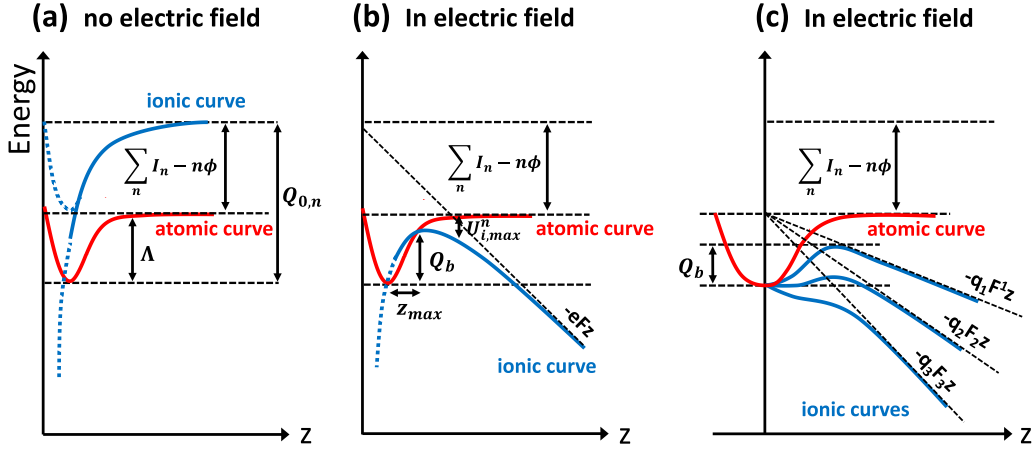


Figure 24: 1D potential energy diagram versus distance from the surface. (a) In the absence of electric field, atoms are bonded to the surface with cohesive energy  $\Lambda$ , while ions are attracted to the surface by image force. The required energy to  $n$ -times ionize and remove an atom from the surface is  $Q_{0,n}$ . (b) In the presence of electric field and by considering only the electrostatic repulsive force  $eF$  (neglecting other intrinsic repulsive forces), an energy barrier  $Q_b$  must be to overcome to  $n$ -times ionize and remove an atom from the surface. This diagram shows the classical description of barrier height in the original Müller model. (c) The quantum description of barrier height  $Q_b$  which is known as charge-exchange model. In this model, the electrostatic Maxwell stress is also taken into account which can pull out the atom from the surface. The corresponding energy barrier  $Q_b$  in this model is lower than the approximated value by Müller model (b). Reproduced from the reference [82].

While, for an atom in the ionic state, the potential curve is shifted upward by the ionization energy required to transfer an atom from the neutral state to  $n$ -fold charge ( $\sum_1^n I_i$ ), minus the energy gained by the surface (material) due to the release of  $n$  electrons ( $n\phi_e$ ), where  $\phi_e$  is the work function of the surface (see Figure 24a) [82]. Hence, the required energy ( $Q_{0,n}$ ) to both  $n$ -times ionize and remove an atom from the surface can be estimated by Born–Haber cycle as [82]:

$$Q_{0,n} = \Lambda + \sum_1^n I_i - n\phi_e \quad 3.1$$

Where  $\Lambda$  is the sublimation energy,  $I_i$  is the  $i^{\text{th}}$  ionization energy and  $\phi_e$  is the work function of the surface. The values of these energies are tabulated for most elements and can be found in the textbooks [83]. Having a higher potential energy for the ionic state relative to the atomic state, implies that ionic state (in the absence of an electric field) is metastable. In the presence of an electric field, the ionic potential curve and the corresponding energy to ionize and remove the atom are influenced by the repulsive force between the ion and the surface [82]. In the following sections the two theories for field evaporation under the application of electric field are discussed in detail.

### 3.1.1 Image hump model (Müller model)

The image hump model was proposed by Müller et al. [79]. In this model, the field evaporation is described as a thermally activated process over an energy barrier which is reduced by the application of an electric field. At low temperature (zero Kelvin), the energy barrier  $Q_b$  is defined as the difference between the

binding energy and the maximum of the ionic potential energy  $U_i(z)$  as shown in the Figure 24b. Hence, atoms are assumed to be fully ionized before the evaporation and their removal from the surface. By assuming the electrostatic image force as the attractive force, corresponding to  $-\frac{n^2 e^2}{16\pi \epsilon_0 z}$ , and the electrostatic coulomb force as the repulsive force, corresponding to  $-neFz$  (where  $n$  is the ionization state,  $e$  is the electron charge,  $\epsilon_0$  is the dielectric permittivity of the vacuum and  $F$  is the electric field strength), the potential energy of  $n$ -fold ionized atom in the presence of the electric field can be approximately written as:

$$U_i^n(z) \approx \left( \sum_1^n I_i - n\phi_e \right) - \frac{n^2 e^2}{16\pi \epsilon_0 z} - neFz \quad 3.2$$

where  $I_i$  is  $i^{\text{th}}$  ionization energy,  $\phi_e$  is the work function of the surface. The distance where  $U_i^n(z)$  is maximum ( $z_{\text{max}}$ ) can be calculated from:

$$\frac{d(U_i^n(z))}{dz} = 0 \quad \xrightarrow{\text{Maximum}} \quad z_{\text{max}} = \sqrt{\frac{ne}{16\pi \epsilon_0 F}} \quad 3.3$$

Then the maximum of this potential energy is given by:

$$U_{i,\text{max}}^n = -\sqrt{\frac{n^3 e^3 F}{4\pi \epsilon_0}} \quad 4.4$$

Then the barrier height  $Q_b$  for field evaporation is given by:

$$Q_b(F) = Q_0 - U_{i,\text{max}}^n$$

$$Q_b(F) = \Lambda + \sum_1^n I_i - n\phi_e - \sqrt{\frac{n^3 e^3 F}{4\pi \epsilon_0}} \quad 3.5$$

The value of the electric field strength which reduces the barrier energy  $Q_b$  to zero is called evaporation field,  $F_{\text{evap}}$  which can be written as:

$$F_{\text{evap}} = \frac{4\pi \epsilon_0}{n^3 e^3} \left( \Lambda + \sum_1^n I_i - n\phi_e \right) \quad 3.6$$

Although for a given material, depending on the ionization-state  $n$ , different values of fields can be extracted from Equation 3.6, the lowest value of the obtained field is defined as the evaporation field. This classical approach to

predict the low-temperature evaporation field ( $F_{\text{evap}}$ ) does not match the experimental values for most materials. This discrepancy is addressed later in this section. The experimentally observed  $F_{\text{evap}}$  for most materials are tabulated in the textbooks [83]. For most metals,  $F_{\text{evap}}$  varies in the range of 10 to 60 V nm<sup>-1</sup>. Finally, the barrier height  $Q_b(F)$  for the electric fields close to the  $F_{\text{evap}}$  can be approximated by a linear relation:

$$Q_b(F) \approx \frac{1}{2} Q_0 \left( 1 - \frac{F}{F_{\text{evap}}} \right) \quad 3.7$$

This linear relation has been experimentally validated only for the electric field between  $0.8F_{\text{evap}}$  to  $0.95F_{\text{evap}}$  and deviations out of this range were reported [84]. In general, the agreement between the original Image hump model (Equation 3.7) and the experimental barrier height  $Q_b$  is poor for most materials. This discrepancy is mainly due to the neglect of many phenomenological parameters in the definition of the ionic potential energy (Equation 3.2). Different authors tried to improve the original Müller model by implementing additional terms to the definition of potential energy. For instance, Tsong [85] proposes an additional energy term  $-\frac{1}{2}\alpha_p F^2$  to the potential energy (Equation 3.2) to consider the polarization effect of surface atoms, whereby  $\alpha_p$  is the surface polarizability of the ions and  $F$  is the strength of the electric field. Also the predicted distance for the Schottky hump ( $Z_{\text{max}}$ ) is too small to ignore the contribution from the ion-core repulsive forces [82]. As this model basically neglects the real potential energy of atoms and ions in the first few nanometers of the surface under the strong electric field (strong cohesive forces), it is not surprising that the Image hump model cannot accurately predict the field evaporation mechanism of all materials.

### 3.1.2 Charge-exchange model (Gomer model)

This model was initially proposed by Gomer et al. [80] to overcome some of the limitations of the image hump model. Unlike the Image hump model, in the charge-exchange model the atoms are gradually ionized, while they are escaping from the surface. Although the original proposed model by Gomer has not been experimentally assessed, it triggered further discussions on the nature of the evaporation process which finally lead to a better understanding of this process [86]. Later, the field evaporation was accepted to be based on charge-drain process [87]. This process describes the gradual drain of the charge from the evaporating atom to the specimen surface, during the field evaporation process.

McMullen [88] proposed a quantum-based approach to describe the charge-drain and field evaporation process. Using one-dimensional density functional theory (1D DFT) for a metallic specimen, McMullen [88] explained that the charge and the field are concentrated on the protruding surface atoms. This implies that under the application of intense electric field, surface atoms are not neutral and they can be considered in a partially ionized state. This partially ionized behaviour of surface atoms has been confirmed by many other authors

[89], [90]. The local concentration of surface charges results in a local enhancement of the electric field according to Gauss's law. This local enhancement of the electric field is discussed in detail in the next chapter.

Furthermore, this concentrated surface charge implies a repulsive force on the corresponding surface atom and cause electrostatic stress, which is known as the local Maxwell stress, on the surface. The intensity of the Maxwell stress can be simply expressed as:

$$T = \frac{1}{2} \epsilon_0 F^2 \quad 3.8$$

where T is the force per unit area of the surface (stress),  $\epsilon_0$  is the dielectric permittivity of the vacuum and F is the magnitude of the electric field. The intensity of the Maxwell stress can easily reach the yield strength of most metals (around 500 MPa) [82]. Hence the charge drain process can be explained as follows. The Maxwell stress is sufficiently intense to pull out the atoms from the surface. This gives rise to the local field enhancement and once the strength of the local electric field becomes sufficiently intense, the complete ionization and successive escape of the atom from the surface (field evaporation) becomes possible (see in Figure 24c).

Kreuzer and Nath [91] analytically estimated the energy barrier using Morse potential. The Morse potential energy of the atoms at the surface,  $U(z)$ , in the absence of the electric field is reported as:

$$U(z) = nD \left( \exp \left[ -2 \left( \frac{z}{l_m} \right) \right] - 2 \exp \left[ - \left( \frac{z}{l_m} \right) \right] \right) \quad 3.9$$

where z is the distance to the atom position, n is number bonds, D is bounding energy of the pair of atoms (similar to sublimation energy  $\Lambda$ ),  $l_m$  is the scaling length (similar to steepness of the potential well in bonding energy curve). Then the maximum adhesion force  $f_m$  which holds the atom to the surface is given by:

$$f_m = \frac{nD}{2l_m} \quad 3.10$$

In the presence of average electric field F on the surface, the potential energy of the surface atoms is modified by the application of Maxwell stress:

$$U_E(z) = U(z) - \frac{1}{2} s \epsilon_0 (\gamma F)^2 z \quad 3.11$$

where s is the surface area,  $\epsilon_0$  is the dielectric permittivity of the vacuum,  $\gamma$  is local field enhancement factor on the protruded atoms which is discussed in Section 4.1.1. Indeed, if the induced Maxwell stress is smaller than maximum adhesion force ( $f_m$ ), a barrier energy  $Q_b$  is predicted for the field evaporation. For a certain applied electric field, the induced stress becomes larger than the  $f_m$  and the barrier energy disappears. The strength of the electric field at low temperature (0 K), which leads to a zero-barrier height for the field evaporation, is given by:

$$F_{evap} = \frac{1}{\gamma} \left( \frac{n}{s} \right)^{1/2} \times \left( \frac{D}{\epsilon_0 l_m} \right)^{1/2} \quad 3.12$$

where  $F_{evap}$  is called evaporation field. For the electric fields lower than evaporation field ( $F < F_{evap}$ ), the energy barrier  $Q_b$  was analytically calculated [84], [91] and the results are reported here:

$$\begin{aligned} \frac{Q_b(F)}{Q_0} = & \sqrt{1 - \left( \frac{F}{F_{evap}} \right)^2} \\ & + \frac{1}{2} \times \left( \frac{F}{F_{evap}} \right)^2 \times \ln \left( \frac{1 - \sqrt{1 - \left( \frac{F}{F_{evap}} \right)^2}}{1 + \sqrt{1 - \left( \frac{F}{F_{evap}} \right)^2}} \right) \end{aligned} \quad 3.13$$

where  $Q_0$  is the barrier height at zero field ( $F=0$ ). This expression has been reported to have a good agreement with experimental observations [92]. For electric field between  $0.8F_{evap}$  to  $0.95F_{evap}$ , this expression can be approximated by the classical linear relation, previously reported in Equation 3.7.

## 3.2 Post-ionization

As described in the previous sections, the theory of field evaporation (image-hump or charge-exchange model) predicts the required electric field to evaporate an atom depending on the degree of ionization. However, the experimentally observed degree of ionization, the so-called charge state ratio (CSR), is usually higher than the predicted value. The charge state ration (CSR) of the element  $x$  is defined as  $x^{i+} / \sum_1^n x^{i+}$ , where  $x^{i+}$  is the frequency of the  $i^{\text{th}}$  ionization ( $i=1, 2, \dots$ ). This discrepancy is explained by the theory of post-ionization.

The proposed model by Haydock and Kingham [93] suggests that ions leave the surface mainly in the single charged state and while they are passing through the intense electric field, they may re-ionize again in the vicinity of the apex by tunneling of an electron back to the specimen surface. The probability of electron tunneling (so post-ionization) can be modeled based on the potential distribution at the given electric field and the distance of the ion from the surface using the Schrödinger Equation [94]. Finally, for most elements, the relative frequency of different charge states at various electric fields were calculated and the results are available in textbooks (so-called Kingham curve) [83]. For instance, the Kingham curve of Silicon is shown in Figure 25.

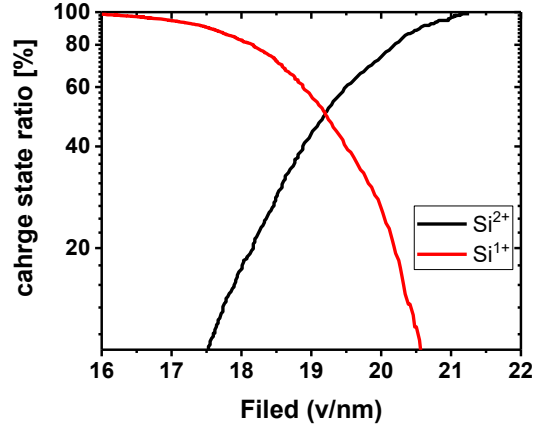


Figure 25: Kingham curve for Si. The vertical axis indicates the CSR of the Si ( $\text{Si}^{2+}/(\text{Si}^{2+} + \text{Si}^{1+}) \times 100$ ) and the horizontal axis shows the intensity of electric field. Reproduced from the reference [94].

Alternatively, a robust procedure was proposed in the reference [95] to experimentally obtain the Kingham curve for a given material (originally for Si). The methodology is based on the Equation 4.5 (which will be discussed in the next chapter), whereby the electric field  $F_i$  at the specimen apex is known to be proportional to the applied voltage  $V_i$ . Thus, a known set of  $F_0$  and  $V_0$  allows the experimental determination of the field  $F_i$  at every given applied voltage  $V_i$  through the ratio  $\frac{V_i}{V_0} = \frac{F_i}{F_0}$ . Whereby  $F_0$  and  $V_0$  are known values referred to as the electric field and the voltage required for the evaporation of a given element (e.g. Si) at 0 K. The value of  $F_0$  can be found in the literature for many elements. To estimate  $V_0$ , the author suggested a set of APT measurements at different laser powers, whereby  $V_0$  can be extrapolated at the zero laser power. This procedure allows the experimental determination of the electric field  $F_i$  and CSRs for a range of applied voltages  $V_i$ , thus the Kingham curve can be plotted accordingly. The experimentally obtained Kingham curve following this methodology showed a very good agreement with the theoretical curve for Si [95].

Furthermore, it has been experimentally shown that CSR and the post-ionization theory are independent from the temperature [95]. This makes post-ionization an extremely powerful tool to determine the local electric field at each instance of the APT measurement. Indeed, the extraction of the local electric field from the applied voltage is not straightforward due to the number of unknown parameters playing a role in the field enhancement mechanism, including: tip geometry, local apex shape and atomic roughness. Hence, through the experimentally extracted CSR and the use of the Kingham curve, one can estimate the local electric field at each instance of the APT measurement.

In this thesis work, the extracted CSR is used to compare the experimental conditions of APT measurements and assess the repeatability of the measurement.

### 3.3 Evaporation rate

For an atom to field evaporate and to successively escape the surface, it must cross the previously described energy barrier  $Q_b$  (Equation 3.5 or 3.15). This can be done either by a thermally activated process (thermal fluctuation) or by

tunneling through the barrier whereby the atom is ionized at the same time. As suggested by Brandon [96], at sufficiently low temperature tunneling through the barrier becomes the more probable evaporation mechanism leading to an almost temperature independent mechanism. Hence, at a given  $Q_b$ , a transient temperature can be defined at which the transition from tunneling to a thermally activated evaporation process occurs [97]. Kingham [98] suggested that this transition temperature is about 40 K for most elements (except very light element), which matches the experimental observations by other authors [99], [100]. The presence of such a temperature transient which differentiates the two mechanisms of evaporation is depicted in Figure 26.

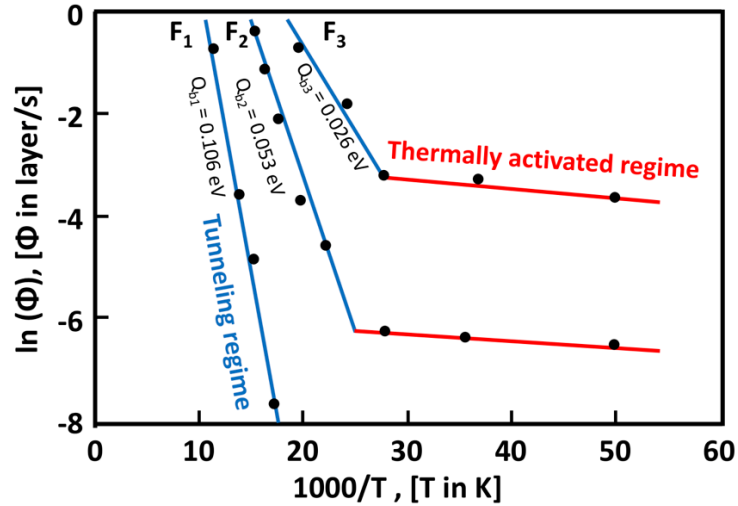


Figure 26: Arrhenius plots for field evaporation of at three different electric fields ( $F_1 > F_2 > F_3$ ). The vertical axis shows the logarithmic scale of the evaporation rate in layer per second. The experimental data points are indicated by black dots on the figure. At each electric field, the data points were interpolated by two linear functions: Blue (tunneling regime) and red (Thermally activated regime). The corresponding barrier height  $Q_b$  at each electric field ( $F_1$ ,  $F_2$  and  $F_3$ ) is also reported in the figure. The transient between thermally activated regime and tunneling regime can be seen at low temperature ( $T < 40$  K) for  $F_1$  and  $F_2$  plots. Reproduced from the reference [100].

Although the base temperature is typically around 40-50K, the temporarily (picosecond) temperature increase as induced by the laser pulse [101] implies that the field evaporation in laser-assisted APT is usually based on the thermally activated process. The thermal agitation vibrates the atoms on the surface, where the component of this oscillation normal to the surface pushes the atoms towards the outside with a frequency  $\nu_0$ . The probability for an atom during such an oscillation to overcome the barrier  $Q_b$ , which holds the atom on the surface, and successively leave i.e. the evaporation event, is called the probability of field evaporation,  $P_{\text{evap}}$ . This probability can be modelled by the Maxwell-Boltzmann equation:

$$P_{\text{evap}} \propto \exp\left(-\frac{Q_b(F)}{k_B T}\right) \quad 3.14$$

where  $k_B$  is the Boltzmann constant and  $T$  is the absolute temperature of the surface. To simplify,  $Q_b(F)$  can be assumed as the classical term in Equation 3.7:

$Q_b(F) = \frac{1}{2}Q_0 \left(1 - F/F_{evap}\right)$ . Once the vibration frequency  $\nu_0$  and the probability of field evaporation  $P_{evap}$  are described, the evaporation rate  $\Phi_{evap}$ , defined as the number of atoms evaporated per second, can be described by the Arrhénius law:

$$\Phi_{evap} = \nu_0 \exp\left(-\frac{Q_b(F)}{k_B T}\right) \quad 3.15$$

where  $\nu_0$  is the frequency of the normal component of ion vibration in its bonding well. Note that in reality, the evaporation rate needs to be calculated taking into account the laser pulse length, temporary temperature evolution and laser frequency. The Equation 3.15 has been experimentally evaluated by several authors and the deviation is reported only at low temperature, corresponding to tunneling regime [102],[100]. As expected, the vibration frequency  $\nu_0$  depends on the temperature, while it has been also reported that  $\nu_0$  decreases as the strength of the electric field increases. For instant by 10 % increase in the field,  $\nu_0$  is reported to drop from  $10^{13}$  Hz to about  $10^{11}$  Hz [92]. Hence, the evaporation rate in Equation 3.15 strongly depends on both electric field (through  $\nu_0$  and  $Q_b$ ) and temperature (through  $\nu_0$  and  $T$ ). Hence, various combination of electric field (barrier height) and temperature can lead to a similar evaporation rate for a given element. To derive a relation between the electric field and temperature, the quantum description of barrier height in Equation 3.15 can be approximated by a linear term:

$$Q_b(F) \approx Q_0 \left(1 - \frac{F}{F_{evap}}\right) \quad 3.16$$

Then, by combining the Equations 3.15 and 3.16, at a given evaporation rate  $\Phi_{evap}$ , an approximately linear relation between the field ( $F$ ) and temperature ( $T$ ) can be obtained as:

$$\frac{F}{F_{evap}} \approx 1 + \ln\left(\frac{\Phi_{evap}}{\nu_0}\right) \frac{k_B T}{Q_0} \quad 3.17$$

This linear relation is shown in Figure 27 and it has been experimentally observed for a wide range of materials with a good reproducibility [103], [104]. For a given element, the slope of the field-temperature curve mainly depends on the evaporation rate  $\Phi_{evap}$ . This implies that any further increase/decrease in the electric field or temperature while keeping the other parameter constant, results in an increase/decrease in the evaporation rate  $\Phi_{evap}$  (see Figure 27).

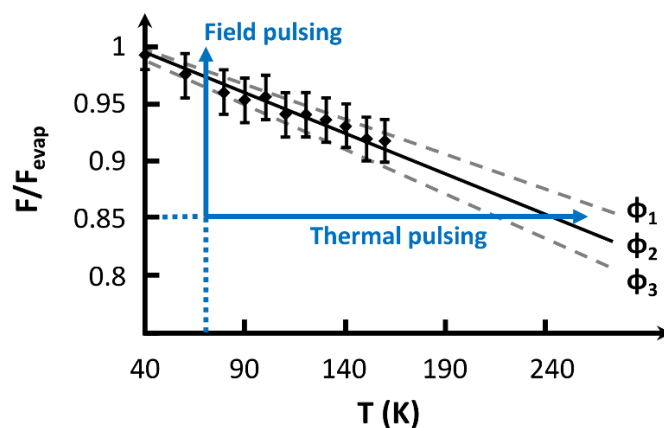


Figure 27: Schematic representation of various combinations of electric field and temperature which can result in field evaporation at three different evaporation rates ( $\Phi_1 > \Phi_2 > \Phi_3$ ). The  $\Phi_2$  curve corresponds to a calibration curve of field and temperature for tungsten tip at fixed detection rate of 0.005 [104]. The schematic view of the pulsing modes at a constant base temperature (Voltage pulsing) or constant DC field (Thermal pulsing) is also depicted in blue.

Hence, the field evaporation can be controlled and triggered either by pulsing the temperature (laser pulse) or the electric field (voltage pulse), while the other parameter is kept constant. Thus, with the right choice of base temperature and pulsing energy, field evaporation is only triggered during the (voltage or laser) pulse and no evaporation is expected in between the pulses. Such a process is required to provide a trigger for the time-of-flight calculation and also to minimize the unwanted DC evaporation as this leads to unidentified species causing a signal background and a loss in sensitivity. Moreover, in multielement samples, DC evaporation of the species with the lower evaporation fields causes a compositional bias.

### 3.4 Laser-tip interaction

In this section, I will briefly introduce the historical background and the improvement in laser-assisted atom probe (LA-AP) technique. Then the state-of-the-art in the physical understanding of the interaction between the pulsed laser light and APT tip will be discussed in more detail.

The idea of using laser pulses to evaporate a field emitter was already introduced by the group of E. W. Muller in the 60'ties. However, due to the instability of the lasers at that time, the first laser-assisted atom probe analysis was only reported about a decade later (end of 1970s) by Block and Tsong [105]. The analysis at that time suffered from poor mass resolution (due to the long laser pulse) and reproducibility (need to focalize the laser in view of the low energy per pulse). At the end of 1980s, Tsong successfully demonstrated the use of ultrashort laser pulses (psec to nsec) for the analysis of metallic and nonconductive specimens (i.e. silicon, Silica, III-V semiconductors) [106]. Finally, at the beginning of 2000, ultrafast lasers (femtosecond) combined with high energy (amplified laser system) became available, which eliminated the need for strongly focalized laser. As a result, the analysis of metallic and semiconducting specimens with better mass resolution was reported [107].

As mentioned earlier a laser-assisted atom probe enables the analysis of nonconductive and semiconductor materials which are usually not feasible using the voltage pulses. Indeed, the high electrical resistivity of nonconductive materials broadens the voltage pulse such that the amplitude of the electric field at the apex is reduced and its time dependence enlarged. This then leads to a poor mass resolution in the ToF spectrometry. Furthermore, it appears that the laser-assisted atom probe also improves the analysis of metallic specimens from many aspects. For instance, by using the laser pulsed APT, the induced mechanical stress on the tip is less as compared to the case of voltage pulsing since a smaller electric field is required whereby also the induced stress is no longer cyclic causing mechanical fatigue. This reduces the risk for rupture of brittle or fragile specimens such as multilayers [108]. Beside broadening the field of application to nonconductive and semiconductor materials, laser pulsing generally improves the performance of APT analysis in terms of mass resolution, signal to noise ratio through decreasing the evaporation time and the energy spread during the pulses [109]. Some of these aspects are discussed in more detail in this section.

Although, the interaction of light with matter is well studied and explained for materials with known optical properties (known refractive index), the physical interaction between the laser pulse and the APT tip is not yet fully understood at this moment. This is mainly due to the nanometric dimension of the specimen which necessitates to consider effects as field enhancement, diffraction and plasmonic excitation as well during the laser-tip interaction. In general, the framework for describing the contribution of laser pulse in the evaporation process is based on Maxwell-Boltzmann equation for evaporation probability  $P_{\text{evap}}$ , introduced in Section 3.3:

$$P_{\text{evap}} \sim \exp\left(-\frac{Q_b}{k_B T}\right) \quad 3.18$$

where  $Q_b$  is the height of the energy barrier,  $k_B$  is the Boltzmann constant and  $T$  is the apex temperature at the instant of the evaporation process. Hence, the effect of the laser pulse on the evaporation process must be through a temperature rise ( $T$ ) or via reduction of the barrier height  $Q_b$ , through further enhancement of the electric field. Although it is widely accepted that a temperature rise (thermal pulse) is the main mechanism of field evaporation, the possible reduction in the barrier height is also discussed in this thesis.

Three potential mechanisms of laser-assisted field evaporation process are: Thermal pulsing, photo ionization and optical pulsing. These possible field evaporation mechanisms are discussed in detail in the following sections.

### 3.4.1 Thermal pulsing

In laser-assisted APT, thermal pulsing is currently accepted to be the main mechanism for field evaporation of both metallic and nonconductive materials. In principle, the obvious result of the laser-tip interaction is the absorption of a part

of the laser energy by the specimen and its transformation into thermal energy. This laser-induced heating combined with the constant cooling of the tip (cf. the heat sink at the tip bottom) leads to an increase and successive decrease of the apex temperature. The resulting temperature evolution at the tip apex, commonly referred to as “thermal pulsing”, triggers the field evaporation process.

In this section, the physical phenomena besides the laser absorption are first discussed for both metallic and semiconductor materials. Then the formation of the temperature pulse and the cooling mechanisms will be briefly explained.

**Laser absorption in metals:** when a laser interacts with a metallic substrate (bulk material), the photons from the laser interact with the electrons in the conduction band and excite them to higher energy levels. Then, these hot electrons relax their energy through electron-electron scattering (femtosecond time scale) and electron-phonon scattering (picosecond time scale) which leads to a temperature rise in the metal lattice [82]. The real laser-tip interaction for a nanometric tip is more complex and other effects need to be taken into consideration, including the laser polarization, the diffraction of the incoming light, the collective excitation of surface electrons. For instance, the apex of a tip (as a discontinuity between the metal and the vacuum) diffracts the incoming light in all directions. Then this diffracted beam interacts with the incident and reflected beams and enhances the oscillating surface current on the laser side of the tip surface [82]. The hemispheric apex of the tip can give rise to the absorption of the incident beam at the apex by collective excitation of surface electrons (surface plasmonic) for certain excitation wavelengths [110].

The 3D map of the absorption efficiency for an Al tip at two different laser wavelengths was simulated by numerically solving Maxwell’s equations for the 3D tip shape using the finite difference method in the time domain [82] and the results are reported in Figure 28. The figure indicates the presence of some local maxima of absorption on the laser side of the tip by a distance equal to the laser wavelength  $\lambda$ . For a larger wavelength, the first local maximum is located at the distance equal to  $\lambda/4$  from the apex as shown in Figure 28c. While, for shorter wavelengths ( $\lambda=515$  nm and 360 nm), the first absorption maximum is located very close to the apex ( $Z=20$  nm) which corresponds to excitation of surface plasmon resonance (Figure 28c inset). This absorption map indicates that the incident beam is either strongly absorbed (at the local maxima) or completely transmitted (for other positions) depending on the tip radius. The presence of the maxima is interpreted as the interference between the diffracted beam from the apex with the incident and reflected beam enhancing the oscillating surface current at the shank surface. In addition, the absorption density decays rapidly along the depth ( $\sim \frac{1}{\sqrt{Z}}$ ) as shown in Figure 28c.

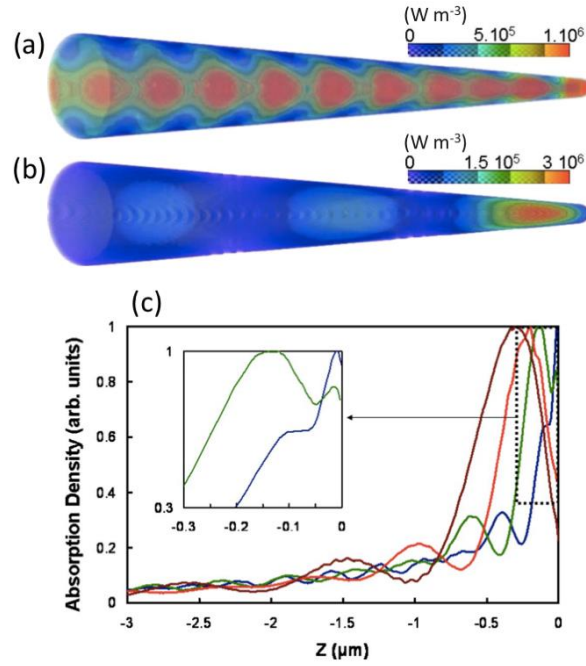


Figure 28: The absorption map of Al tip in the incident laser with axial polarization obtained by finite difference simulation in time domain. (a) laser wavelength equal to 355 nm (b) laser wavelength equal to 1200 nm. (c) Normalized absorption density profile along the tip axis for  $\lambda=360$  nm (blue),  $\lambda=515$  nm (green),  $\lambda=800$  nm (red), and  $\lambda=1200$  nm (brown). In the inset, the zoom of absorption profiles at the apex for  $\lambda=360$  nm (blue) and 515 nm (green) is shown. Reproduced from the reference [111].

**Laser absorption in semiconductors:** the optical properties (refractive index) of semiconductor materials depends on the band structure which varies according to the doping level and defects. At cryogenic temperature (below 40 K) the conduction band is empty and the laser photons can only interact with the electrons in the valence band. Hence, depending on the photon energy, this interaction can either lead to an absorption event, which promotes an electron to the conduction band and creates an electron-hole pair, or the material is transparent to this laser light. In case of a bulk direct band-gap semiconductor, if the photon energy ( $E_{\text{photon}}$ ) is larger than the direct band-gap ( $E_{\text{photon}} > E_{\text{gap}}^{\text{direct}}$ ), the laser light is strongly absorbed at the surface (penetration depth of a few nanometers) and all the photon energy is transferred into carrier energy, while for ( $E_{\text{photon}} < E_{\text{gap}}^{\text{direct}}$ ), the absorption probability of photons becomes negligible and the material becomes transparent to the laser energy [112]. The indirect band-gap semiconductors show a similar behaviour whereby for a photon energy well above the indirect band-gap ( $E_{\text{photon}} \gg E_{\text{gap}}^{\text{indirect}}$ ) the photon absorption is assisted by the phonons (to conserve the momentum). Vice versa for a photon energy below or close to the indirect band-gap ( $E_{\text{photon}} < E_{\text{gap}}^{\text{indirect}}$ ), the absorption probability reduces to a much lower value and the laser can penetrate deeply inside the bulk material (up to 1 mm) [112].

This behaviour is schematically depicted for silicon illuminated with three different photon energies in Figure 29. The photon energy for IR laser (1.2 eV) is just above the indirect band-gap of silicon (1.15 eV) which enables a small transition window for phonon interaction in the momentum space, hence the absorption is weak. For the green laser, the photon energy is higher which also

corresponds to a wider window for phonon interaction giving rise to the photon absorption. For the UV laser, the photon energy (3.6 eV) is just above the direct band-gap of silicon (3.4 eV) which leads to a strong absorption at the surface with small penetration depth.

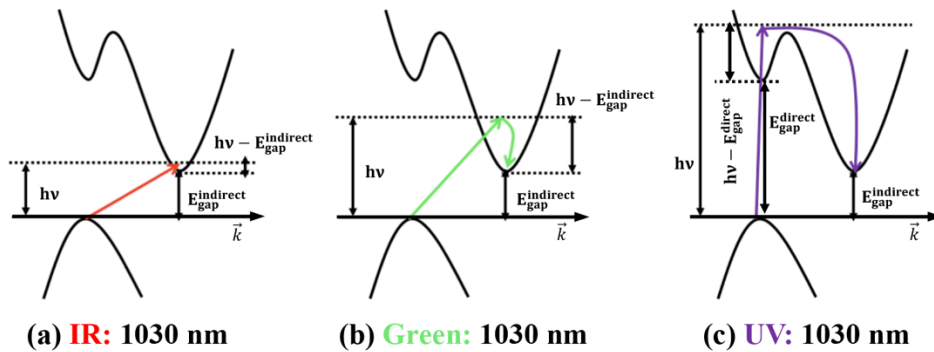


Figure 29: Schematic representation of photon absorption in the silicon for three different wavelengths. Reproduced from [113].

After the absorption of the photon energy, a semiconductor experiences several excitation and relaxation mechanisms before reaching the equilibrium state. As mentioned earlier, the photon energy is first transferred to the valence electrons and then to the semiconductor lattice through the relaxation mechanisms. As suggested in reference [114], the electron and lattice processes involved in the laser excitation, can be classified in four main regimes: carrier excitation, thermalization, carrier removal and thermal and structural effects. The list of possible processes and their corresponding timescales are reported in Figure 30. For direct band-gap semiconductors, the carrier excitation is mainly the result of a single or multiphoton photon absorption (Figure 30a), which take place in a few femtoseconds timescale. For indirect band-gap semiconductors, a phonon-assisted absorption mechanism is required. After the excitation, the carriers are redistributed by carrier-carrier and carrier-phonon scattering in both the valence and conduction bands (Figure 30d to f). By considering the small carrier energy of the emitted photons, many scattering events take place before reaching the thermal equilibrium. This leads to a thermalization within a few picoseconds. At this point, both carriers and lattice are at the same temperature and the material is considered to have a well-defined temperature.

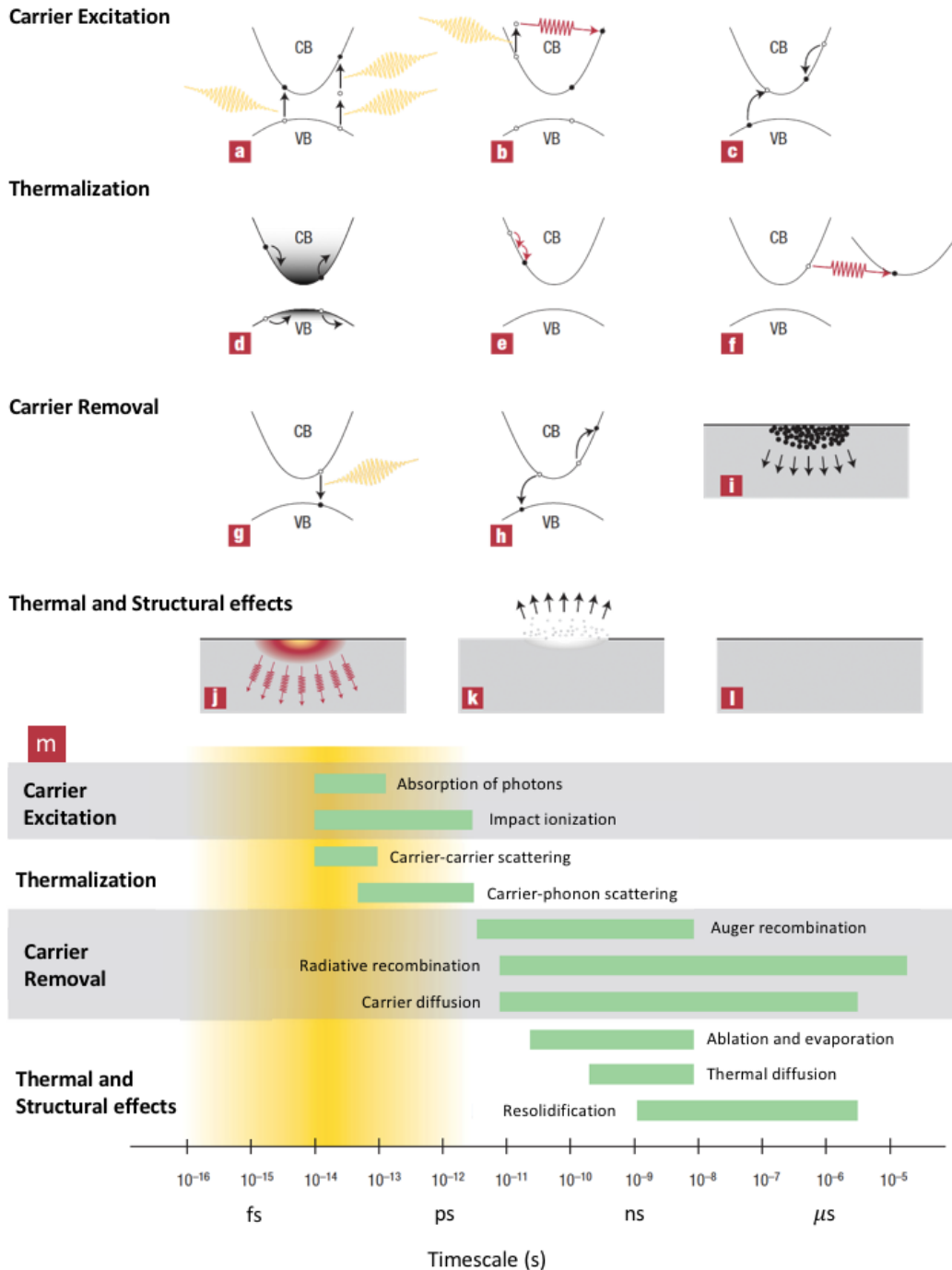


Figure 30: Electron and lattice excitation and relaxation mechanism for a direct band-gap material, excited by the laser photons. (a) multiphoton absorption, (b) free-carrier absorption, (c) impact ionization, (d) carrier distribution, (e) carrier-carrier scattering, (f) carrier-phonon scattering, (g) radiative recombination, (h) Auger recombination, (i) diffusion of excited carriers, (j) thermal diffusion, (k) ablation and (l) resolidification or condensation. (m) The timescales for all the aforementioned processes involved. Reproduced from [114].

By considering the timescale for field evaporation mechanism, which is in the order of few picoseconds [92], one can expect the complete thermalization of carriers-phonon before the field evaporation process.

Once the thermalization is completed, there is an excess of free carriers compared to that of thermal equilibrium. These additional carriers are removed by either diffusion or recombination process, including radiative recombination or Auger, surface and defect recombination (Figure 30g to i) in a timescale longer

than the field evaporation process (hundreds of nanoseconds to microseconds). Finally, after the removal of the excess carriers, the material is at the same condition as when heated by conventional means and it can experience various thermal and structural effects, as reported in Figure 30j to l. It is worth mentioning that the various processes involved in the electrons and phonon excitation took place simultaneously and they overlap in time spanning over femtoseconds up to microseconds.

Similar to metallic specimen, the absorption map for semiconductors with a real three-dimensional tip shape can be computed by solving Maxwell's equations using finite-difference time domain. The absorption maps for a silicon tip with an initial radius of 35 nm and a shank angle of  $4^\circ$  using three different laser wavelengths is reported in Figure 31, from the reference [113]. The laser light propagates along the x direction from the top (k vector) with a linear polarization parallel to the tip axis (vector  $F_{opt}$ ). As mentioned earlier in the case of IR laser,  $E_{photon} < E_{gap}^{indirect}$  and the penetration depth of the laser can be much deeper than the thickness of the APT tip. Hence, the laser light experiences a series of reflection and diffraction events inside the 3D volume of the tip, which can obviously interfere. As a result, absorption maxima appear within the tip volume. Moreover, the absorption maxima are far from the tip apex (Figure 31a inset), which corresponds to an absorption of the energy in the depth (in z direction) of the tip. For the Green laser (Figure 31b), a similar absorption pattern can be seen, where the photon energy is mainly absorbed in the 3D volume of the tip. However, using the green laser the absorption maxima are much closer to the apex of tip (Figure 31b inset). This is favorable in APT, since the ideal scenario is just to heat the apex of the tip and leave the 3D volume remain cold even during the laser pulse. This will be discussed in more detail later in this section.

Finally, for a UV laser, the photon energy is larger than the direct band-gap of the silicon ( $E_{photon} > E_{gap}^{direct}$ ). This leads to a strong absorption of the photon energy at the tip surface in the direction of laser incident light (Figure 31c). This absorption map is very similar to the one reported for metals (Figure 28). The presence of local absorption maxima on the silicon tip surface using UV laser is clearly reported in reference [82], similar to the one of reported for metallic specimen. The main important difference between the absorption map obtained from the UV laser compare to the Green or IR is that the photon absorption is very strong on the tip apex (mainly the laser side) which gives to stronger rise of the local apex temperature even for the similar amount of absorbed energy. The practical impact of this effect will be discussed in more detail later in this section.

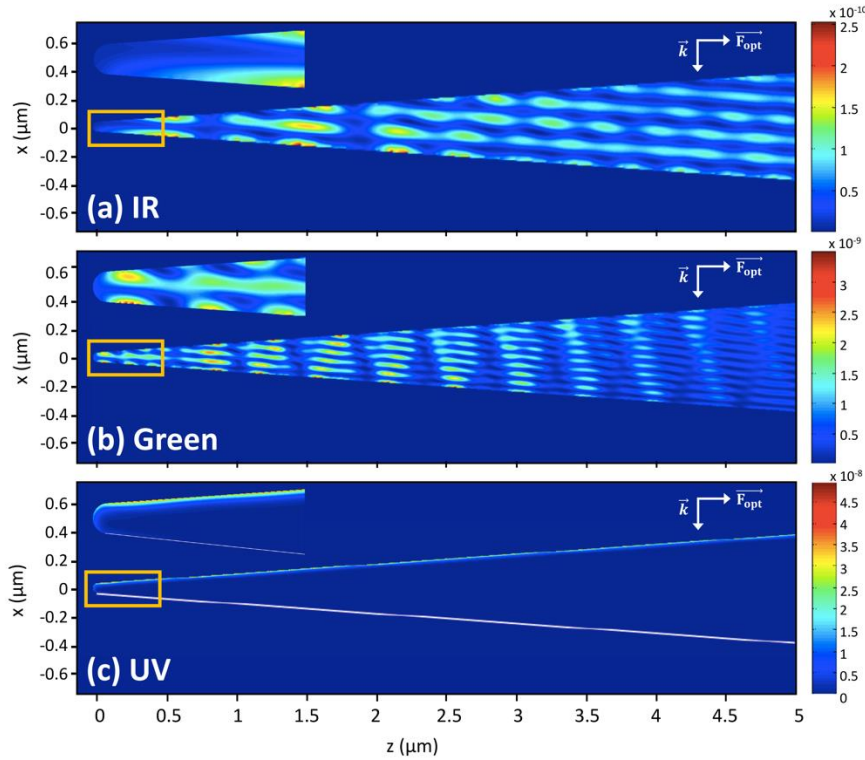


Figure 31: The absorption map computed by finite-difference time domain simulation for a silicon tip with apex radius of 35 nm and a shank angle of  $4^\circ$ , using three difference wavelengths (a) IR at the wavelength of 1030 nm, (b) Green at the wavelength of 515 nm, (c) UV at the wavelength of 345 nm. The laser comes from top (vector  $\vec{k}$ ) and it is polarized parallel to the tip axis (vector  $\vec{F}_{opt}$ ). The unit for the colorbar is  $J/m^3$ . The insets show the zoom view of the first 450 nm (in Z direction) of the absorption maps. Reproduced from [113].

In addition, it has been reported that the optical properties of semiconductors can be affected by the presence of an intense electric field [115]. For instance, once a strong DC electric potential is applied to an insulator (semiconductors at cryogenic temperature typically acts as an insulator), an intense electric field is generated inside the specimen [116]. This results in the formation of free carriers (by field-assisted ionization process [116]), which are then moved toward the specimen surface in the direction of the applied electric field (screening process). Hence, the generated electric field, inside the specimen, only appears in a narrow skin from the specimen surface [82]. This generated electric field modifies the band structure [115] and causes band-bending [117], which enables subband-gap photon absorption ( $E_{photon} < E_{gap}$ ), as it reduces the band-gap to lower value ( $E'_{gap}$ ), as schematically represented in Figure 32. This subband-gap photon absorption can improve the absorption probability versus photon energy.

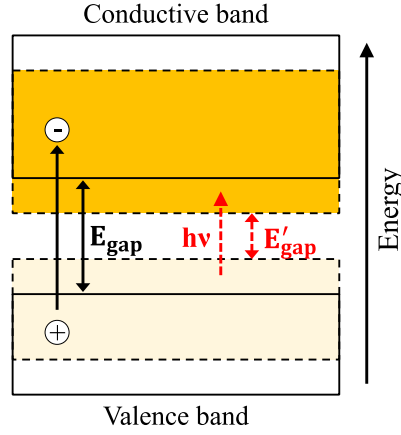


Figure 32: Schematic representation of the reduction in the band-gap under the presence of an intense electric field within the semiconductor bulk material. The dotted rectangles are the schematic of the new band structure, where the new band-gap ( $E'_{gap}$ ) is shown by a dotted red arrow. The required photon energy to be absorbed by the material in the presence and absence of the electric field is indicated by black and dotted red arrow. Reproduced from [82].

**Temperature pulse and cooling process:** as discussed previously, by the interaction of a femtosecond laser pulse with a nanometric AP tip, part of the laser energy is absorbed and transformed into the thermal energy (thermalization) on a few picoseconds timescale. The maximum temperature that can be reached at the specimen surface depends on various parameters linked to the specimen (tip geometry and material) and the laser pulse (i.e. laser wavelength, spot condition and its focus). Kellogg [102] experimentally measured the peak temperature of a few hundred Kelvin (60-500 K) through the analysis of the electric field to generate field evaporation at a given evaporation rate. The peak temperature up to 800 K has been also reported for W under 5 ns laser pulse [118].

By assuming that thermal pulsing is the only mechanism for field evaporation, one can assume that barrier height  $Q_b$  remains constant during and after the laser pulse and rewrite the evaporation probability  $P_{evap}(t)$  at the given time  $t$  as a function of apex temperature  $T(t)$ :

$$P_{evap}(t) \sim \exp\left(-\frac{Q_b}{k_B T(t)}\right) \quad 3.19$$

where  $k_B$  is the Boltzmann constant. As described earlier, a few picoseconds after the laser pulse, the complete thermalization of carrier-phonon is expected for semiconductors. Hence, after this timescale, the temperature evolution and the field evaporation only depend on the cooling dynamics, which is similar to the case of a specimen heated by a conventional means. By considering the magnitude of the peak temperature, the cooling process mainly relies on the conductive heat transfer towards the specimen bottom (radiation can be neglected) [104]. According to Fourier's law, the heat flux is proportional to the gradient of temperature. Hence the cooling mechanisms strongly depend on the initial absorbed map of the photon energy, size of the laser spot, thermal properties of the material and the shank angle. If only the tip apex was heated by the laser, the cooling process would have been very quick (picoseconds timescale). While, as it was demonstrated in Figure 31, depending on the laser wavelength and the

absorption properties of the APT tip (material and tip shape), the laser energy can be absorbed deeply in the volume of the APT tip which heats up a large volume of the tip and reduces the local temperature gradient along the tip axis. The variation of temperature can be obtained by solving the thermal diffusion equation in the medium:

$$\frac{\partial T}{\partial t} - \alpha(T) \nabla^2 T = 0 \quad 3.20$$

where  $\alpha$  is the thermal diffusivity at the given temperature  $T$ :  $\alpha = k/\rho C_p$  and  $k$  is thermal conductivity,  $\rho$  is the density and  $C_p$  is the specific heat capacity. For a zero shank angle tip (wire) and assuming one-dimensional problem, Vurpillot et al. [119] reported an analytical solution for the Fourier's law by assuming an initial Gaussian temperature distribution centered on the tip apex. Then by assuming also a constant thermal diffusivity, the apex temperature at the time  $t$ ,  $T_{apex}(t)$ , was reported as:

$$T_{apex}(t) = T_0 + \frac{T_{rise}}{\sqrt{1 + \frac{2t}{\tau_{cooling}}}} \quad 3.21$$

where,  $T_0$  is the base temperature,  $T_{rise}$  is the peak temperature during the temperate rise and  $\tau_{cooling}$  is the cooling time constant given by the size of heated zone  $\sigma$  and thermal diffusivity  $\alpha$ :

$$\tau_{cooling} = \frac{\sigma^2}{\alpha} \quad 3.22$$

The experimental investigation of cooling behavior of W tip using two pump-probe lasers by Vurpillot et al. [120] suggested a very fast temperature decay at the apex surface (less than 1 ns). Further, investigation of the cooling dynamics, by considering the three-dimensional tip shape, is required to better understand the dynamics of this process.

The direct extraction of apex temperature  $T$ , during the course of evaporation, from Equation 3.15,  $\Phi_{evap} = v_0 \exp\left(-\frac{Q_b(F)}{k_B T}\right)$ , is not trivial as the absolute values of the barrier height  $Q_b$  and the evaporation rate  $\Phi_{evap}$  are not directly available. Alternative, in reference [95], a methodology to indirectly estimate the apex temperature from the variation of the evaporation flux  $\Phi_{evap}$  (and the detection flux  $\Phi_{det}$ ) as a function of the applied voltage  $V$ , was suggested. The authors indicated that the voltage ratio  $V_i/V_0$ , where  $V_0$  is the voltage required for evaporation at 0 K, can be experimentally measured and expressed as the ratio of barrier heights  $Q_i/Q_0$ , where  $Q_0$  and is the barrier height at zero field. Then the apex temperature can be calculated based on the slope of the variation of detection flux  $\Phi_{det}$  versus the variation of barrier height as [95]:

$$T = \frac{-1}{k_B \left. \frac{d \ln \Phi_{det}}{dQ} \right|_T} \quad 3.23$$

The above equation was obtained from Equation 3.15, assuming that the variation of  $\Phi_{det}$  is a good representative of the variation of  $\Phi_{evap}$ , for the well-designed experiment (tip shape) [95]. Using that methodology, A.Kumar et al [95] demonstrated that the temperature rise at the tip apex is  $\sim 200\text{-}400$  K depending on the laser power used.

### 3.4.2 Photoionization

Tsong et al. [121] proposed a model to describe the photon-assisted field evaporation (photoionization) through the interaction between the laser photons and the electrons on the specimen surface. Although he experimentally validated his model for Si at a very low laser power [122], there was a controversy about the generalization of this model as the main physical model for the field evaporation [123], [82]. For instance, field evaporation by the photoionization process for metallic specimens has never been observed [106], [83].

Moreover, the contribution of the photoionization process on field evaporation, can only be observed when the thermal pulsing contribution is negligible [82]. This is the case where an extremely low laser power (small laser fluence) is used, which typically results in a lower evaporation rate in comparison to the thermal pulsing process. In another words, typically the field evaporation is dominated by the thermal pulsing mechanism and the photoionization process, if present, only has a very small contribution.

### 3.4.3 Optical pulsing

Laser light as an electromagnetic wave has an inherent electric field, which thanks to APT tip shape, can reach a few volts per nanometer [123]. Hence, it could potentially cause an additional field enhancement at the tip apex and reduce the barrier height required for the field evaporation process [124]. The oscillation frequency for the laser light is on order of  $10^{15}$  Hz ( $\nu = c/\lambda$ ), which corresponds to a time period of about few femtoseconds. While, as mentioned earlier, the typical timescale for field evaporation mechanism, is on order of a few picoseconds [92]. Such a short oscillation period could not reduce the mean value of the barrier height in the time scale required for the field evaporation process [82]. Hence, the effect of optical pulsing on the field evaporation is often excluded.

In case of metallic specimens, the optical rectification effects at the surface of the apex can lead to an ultrafast electric pulse which can potentially contribute to the field evaporation [125]. Optical rectification is a physical phenomenon based on nonlinear second-order processes which can occur by the interaction of laser pulses with non-centrosymmetric materials and the surface of metals, where there

is a discontinuity in the electronic density of the states (nonlinear effect) [82]. This effect generates a second-order polarization in the material which leads to the generation of an electric field (based on electric dipole radiation). In case of a femtosecond laser pulses, the optical rectification can create an electric pulse with a period of a few picoseconds [125] which lies in the same timescale of field evaporation and could potentially play a role in this process by reducing the energy barrier. By recalling Equation 3.5, the reduced barrier height ( $Q_b$ ) by the impact of optical rectification can be approximately written as:

$$Q_b = \Lambda + \sum_1^n I_i - n\phi_e - \gamma(F_{DC} + F_{OR}) \quad 3.24$$

where  $\gamma$  is a material dependent parameter described by [126],  $F_{OR}$  is the generated temporal electric field at the surface of the specimen by optical rectification effect,  $F_{DC}$  is the generated electric field by DC voltage. Although, the role of optical rectification in field evaporation of metals has been experimentally demonstrated [125], further investigation is still required to better understand the contribution of this effect in field evaporation process.

As discussed earlier although thermal pulsing is accepted to be the main mechanism of field evaporation for semiconductors, there are still some experimental observations which cannot be explained by thermal pulsing. For instance, by looking at the mass spectra obtained from semiconductors using LA-APT, two evaporation processes can be identified: a fast evaporation process followed by a delayed evaporation process with a delay time of about a few nanoseconds. The appearance or the relative contribution of these two processes strongly depends on the experimental parameters used during the experiment (i.e. laser parameters and tip shape) [109]. These two evaporation processes (fast and the delayed evaporation) for a  $Si_{28}^{2+}$  are depicted in Figure 33.

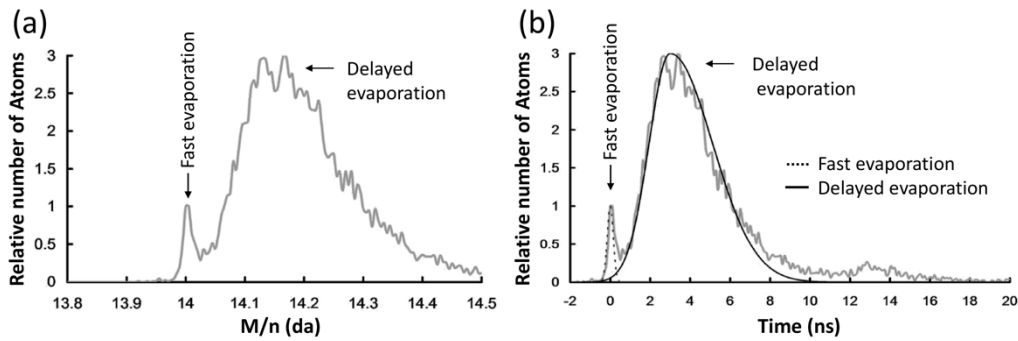


Figure 33: (a) Mass spectrum of  $Si_{28}^{2+}$  peak analyzed by APT at  $\lambda=650$  nm. The fast and delayed evaporation processes are indicated on the spectrum. (b) the conversion of the mass spectrum in time, where  $t=0$  corresponds to the maximum intensity of  $Si_{28}^{2+}$  peak. The fast evaporation mechanism (black dash line) is interpolated by a Gaussian function with a standard deviation of 150 ps. The delayed evaporation (black solid line) starts with a leading edge of about 1.5 ns and ends with a trailing edge which takes about 3 ns. The maximum of the slower process has a delay of about 3 ns respect to the fast evaporation process. Reproduced from [82].

The physical origin of the fast evaporation process is not yet well understood. Although some hypotheses have been suggested, such as thermal ejection for the

confined absorption pattern at the apex, the physical understanding of this fast evaporation is still lacking.

The slow evaporation process originates from the thermal pulsing mechanism. The rising edge of the peaks in a mass spectrum corresponds to the heating process and the time duration it takes for the apex to reach its maximum temperature (1.5 ns in Figure 33b). Typically, the trailing edge of the peaks have a longer decay, which corresponds to the cooling process (3 ns in Figure 33b). Hence, all the aforementioned parameters which have an impact on the cooling dynamics can also strongly influence the peak shapes in the APT mass spectrum. Indeed, in time-of-flight mass spectrometry, time is equivalent to mass and thus a delayed (prolonged) emission will appear as a tail on the mass spectrum. For instance, in case of a Si specimen illuminated with a high laser power in the range of Green or IR wavelength, peaks can decay over several Daltons on the mass spectrum. This corresponds to the absorption of the photon energy in the volume of the Si tip and poor cooling dynamics due to the poor temperature gradient along the tip axis (absorption of the laser in tip volume).

### **3.5 Field emitter apex shape**

As discussed earlier, APT specimens are typically prepared in the form of a sharp needle having a small tip diameter (<100 nm) to generate the intense electric field required to field evaporate the atoms from the specimen surface ( $\sim 10\text{-}60 \text{ V nm}^{-1}$ ). In this section we will briefly discuss the field emitter apex shape after APT analysis for those specimens composed of a single element or diluted systems. The apex shape for heterogeneous or 3D structured specimen will be discussed latter in Section 4.4.3.

Typically, the specimen shape after an APT measurement in voltage mode is considered to be a truncated cone terminated by a hemispheric cap, while the actual apex shape after APT analysis (in voltage mode) is reported to have an ellipsoidal shape with a higher curvature towards the specimen edge [127]. The formation of such an apex shape in voltage mode relies on the quasi uniform probability of evaporation for all the atoms across the specimen surface. In other words, the specimen apex is shaped gradually through the evaporation sequences to create a uniform electric field across the specimen surface. In this project, we used the term “hemispheric apex shape” to describe the emitter apex shape after APT analysis in voltage mode. However, in laser mode, the probability of field evaporation for each individual surface atom is determined by the combination electric field and local temperature during the laser pulse (see Equation 3.19). Hence, the apex shape is also determined by the combination of both the temperature and field distribution across the specimen surface.

As discussed in the previous section, the penetration depth of UV laser light is very shallow (for both metallic and semiconductor materials), and the photon energy is absorbed and transformed to thermal energy at the specimen surface in the direction of laser light incidence (laser side of the tip). As a result, UV laser pulse typically causes preferential evaporation on the illuminated side of the tip

apex and may consequently lead to a significant flattening on this region of the tip. Hence, the specimen apex shape will deviate from the hemispheric shape and become highly asymmetric. In Figure 34 a SEM image of a Si specimen after APT analysis using UV laser together with the numerically predicted absorption map (Figure 34b) are reported from reference [128]. Please note that this deviation from the hemispheric tip shape can be minimized by adopting a lower laser power during APT analysis (i.e. thus having a dominance of the voltage related evaporation process) though the asymmetry in the apex shape (flattening) may not be completely avoided in case of low field materials (e.g. AlGaIn), where measurements are typically performed at an extremely low laser power ( $< 0.1$  pJ) [129].

In contrary, for IR and green laser the penetration depth of the photons is much larger than APT specimen thickness. Hence, after several reflection and diffraction events, the laser energy is absorbed within the specimen volume according to the absorption map determined by the specimen material and geometry. In addition, the local maxima of the absorptions are all predicted to be located within the specimen far from the specimen surface. Hence, the apex temperature typically is predicted to be quasi-uniform [128]. As a result, the probability of the evaporation across the tip is mainly determined by the distribution of electric field and is similar to what is discussed for the voltage mode. Hence, for an APT specimen analyzed under IR or Green laser pulses, regardless of the choice of laser power, a quasi-truncated hemispheric apex shape has been predicted and also experimentally observed [128]. The symmetrical shape is confirmed by the SEM image of a Si specimen after APT analysis using Green laser light in agreement with the predicted absorption map. (Figure 34c and d).

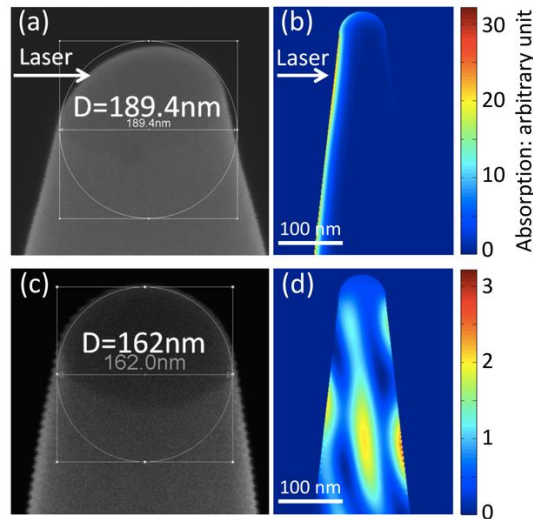


Figure 34: SEM images of specimens after APT analysis using (a) UV laser and (c) Green laser. In (b) and (d) The numerically predicted absorption map for UV and green laser are shown respectively. The laser direction was from left to right for all the figures. Reproduced from reference [128].

## 3.6 Specimen preparation

Specimen preparation is an essential step though challenging as the success of the APT measurement is related to the quality of sample preparation. As discussed earlier, to field evaporate an atom from the specimen, an intense electric field in order of  $10\text{-}60\text{ V nm}^{-1}$ , depending on the field evaporation of the material and the detection rate, is required. To enable the generation of such an intense field and ensure a successful measurement, the APT specimen needs to be prepared in a certain geometry and shape. The main requirements for preparation of APT specimen are listed as follows:

- **Needle-shaped specimen:** The specimen needs to be prepared in the form of a needle shape with a small radius on top (tip radius). Obviously, the feature of interest needs to be located where the needle also needs to be smooth enough such that no additional asperities are present as these could act as a secondary tip.
- **Radius of curvature:** The prepared needle-shaped specimen should have a circular cross-section with a small radius to ensure the field strength required for field evaporation. Any deviation of specimen cross-section from the circular shape will lead to an artefact during data reconstruction as present algorithms are not yet designed to cope with non-hemispherical tip shapes. A typical atom probe tip has an initial radius below 50 nm which during the experiment increases till  $\sim 100\text{-}200\text{ nm}$  (depending on shank angle and depth to be analyzed). Since the standing voltage increases with tip radius, the maximum available supply voltage (usually 15 kV.) sets a limit to the maximum tip radius which can be analyzed. Moreover, the increasing electrostatic force on the tip ultimately leads to the tip rupture. Vice versa, a minimum voltage ( $\sim 2\text{ kV}$ ) is imposed by the fact that otherwise the ion trajectories may be affected by the bias at the entry of microchannel plate. Ideally, the tip should have a cylindrical shape as then the tip radius (and thus magnification) remains constant throughout the analysis. In practice, since most APT tips are fabricated using focused ion beam milling, a certain shank angle is unavoidable. It needs to be minimized ( $< 10\text{ degrees}$ ) as otherwise the radius will increase very rapidly with the depth.
- **Geometry of the needle (micropost):** apart from the apex radius and shank angle, the height of the specimen in respect to the flat substrate (or base holder) has a strong effect on the field enhancement at the apex as well as the trajectories of ions toward the detector. This effect is discussed in detail in Chapter 4.

Conventionally, electrochemical polishing was the most used technique for the preparation of metallic specimens which enables even site-specific sample

preparation (grain boundary) using pulsed electropolishing [83]. This technique is still widely used for metals. Chemical polishing is another technique used in past for the preparation of less conductive specimens. These polishing techniques are not compatible with the semiconductor materials since polishing is performed on the wire-like specimen (not wafers) and the suitable etchants are not yet developed for semiconductors. As such focused ion beam milling has become the dominant approach and will be discussed in more detail in the following section.

### **3.6.1 Focused Ion-Beam milling (FIB)**

This technique is the most widespread sample preparation method as it allows specimen preparation from a wide range of material including metals, semiconductors, nonconductive materials (i.e. oxides) and even some organic materials. Moreover, the combination of fine focused ion beam and SEM imaging allows for site-specific specimen preparation (i.e. fin, single device, nanowire, grain boundary, etc) in various configurations (cross-section, backside, different angles). Up to now many FIB based specimen preparation protocols have been suggested to improve the measurement success or even to enable the preparation of different site-specific specimens [130],[131]. In particular, lift-out methods using dual beam FIB and building on the experience developed for transmission electron microscopy (TEM) techniques are adopted for APT specimen preparation [132].

The procedure involves several steps, starting from the deposition of a capping layer *ex-situ* (i.e. Ni, Cr thin film) or *in-situ* (usually Pt) using the gas injector in the dual beam tool (Figure 35a). In the next step, a part of the substrate, containing the region of interest (lamella) is extracted and is transferred to the pre-fabricated carrier post (Figure 35b to d). Then a portion of the lamella is welded to the carrier post and the rest of the lamella is detached while it is still attached to the micromanipulator (Figure 35e to f). In the next step, annular milling is used to shape/sharpen the chunk of the specimen into a sharp needle with a small apex radius around 100 nm (Figure 35g to i). Finally, a low energy Ga beam (5 or 2keV) is used to remove the Ga damaged shell around the tip or even the remainder of the cap layer (Figure 35k to n). In this thesis work the protocol described in the reference [133] was adopted for the preparation of all the samples. The SEM images of two commercially available types of pre-fabricated carrier posts are indicated in Figure 36.

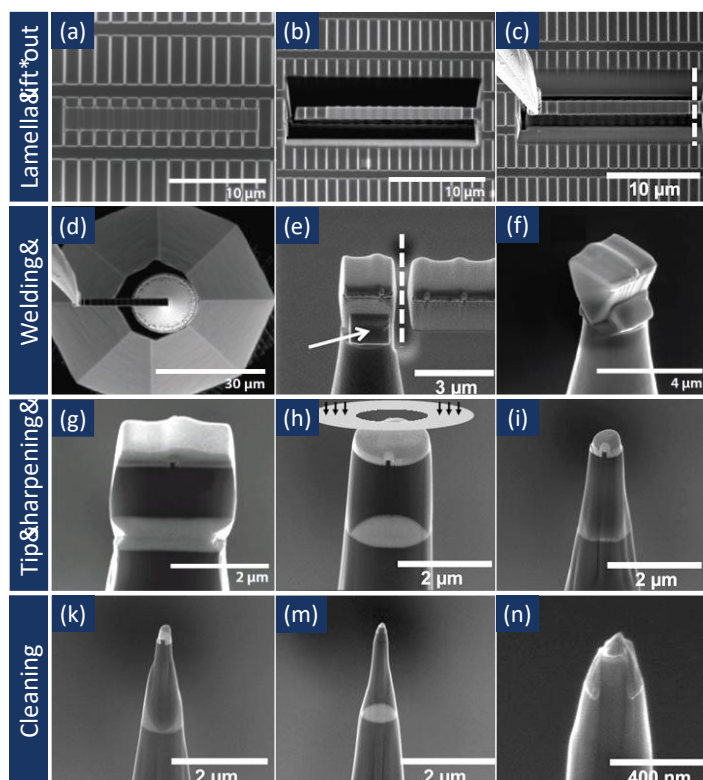


Figure 35: The standard specimen preparation using FIB based technique. (a) deposition of a Pt capping layer over the region of interest. (b) Ion milling around the side of the region of interest, which is covered by Pt cap, and the successive V shape milling and preparation of cantilever wedge (lamella). (c) Removal of the lamella by in-situ micromanipulator. (d) Fine positioning of the lift-out lamella on top of the career micropost. (e) Welding the one side of the lamella to the career post using Pt deposition and cut the rest of the lamella. (f) Welding the other side of V-shaped wedge. (g) Realigning the region of interested to start the tip sharpening step. (h) Annular milling the chunk of material into the cylindrical shape. (i) Further milling with the annular pattern while the diameter of the pattern is progressively reduced. (k) Final cleaning step with low energy beam (2 or 5 keV) without any pattern to reduce the tip diameter and remove the FIB induced damages. (m) low and (n) high magnification image of the final specimen for APT analysis. Reproduced from the reference [133].

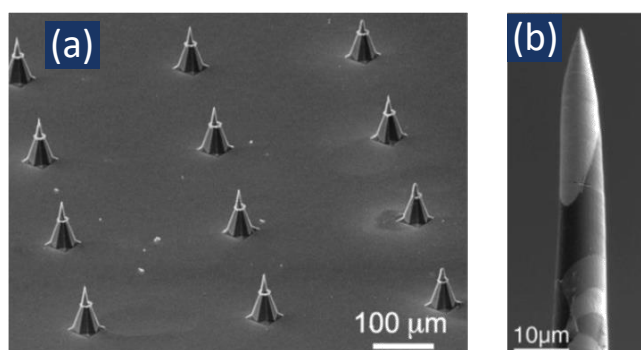


Figure 36: SEM images of a commercially available array of career microposts from Cameca (a) and single tungsten wire (b).

The design of the pre-fabricated carrier post (height and evolution of the diameter across height) may have a significant effect on the electric field and the trajectories of ions as will be discussed in detail in the next chapter. Indeed, in case of tall microposts ( $>100 \mu\text{m}$  height), the electric field on the apex is no longer affected when the actual specimen is reduced in height during the evaporation process as the total height (micropost height + lamella thickness) is completely dominated by the micropost height. This is favorable to maintain

maximum field enhancement independent from the thickness of the lamella and provides a better repeatability in field distribution around the tip.

Since all the energy of the Ga-beam is deposited in the specimen, damage accumulation becomes inevitable together with the incorporation of the Ga-atoms. The effect of this ion beam interaction is manifold: amorphization, Ga implantation, intermixing of phases and regions with different compositions and generation of defects [83]. The Ga implantation and related amorphization was already studied for the case of TEM lamella formation. Depending on the Ga-energy the thickness of the induced amorphized shell was reported to be ~ 20-30 nm [134].

With respect to the FIB damage for an APT specimen, an extensive damage in the topmost area of the tip must also be considered. The use of a capping layer to protect the ROI close to the specimen surface from this interaction is a standard procedure. Moreover, since the extent of the damage layer on the shank scales with the Ga<sup>+</sup> energy, a final low Ga energy clean (5 or 2 -1 keV) is suggested. Note that the dose used in that “cleaning” step needs to be sufficiently high to remove the thick amorphous layer produced by the higher energy beam.

An estimate of the thickness of the damaged layer can easily be obtained by calculating the stopping range of the Ga<sup>+</sup> ions using Monte Carlo simulations. For instance, in Figure 37 the range of Ga implantation in steel is shown for two different energies. In comparison to APT measurements of the Ga profile [130],[83]. The experimentally observed Ga implantation depth was 3x deeper than the predicted range by the simulation as the simulations do not consider the accumulation with high dose nor any diffusion. Moreover, the simulations assume an amorphous material whereas the sample itself was crystalline. Hence, some channeling may have increased the penetration depth as well [53].

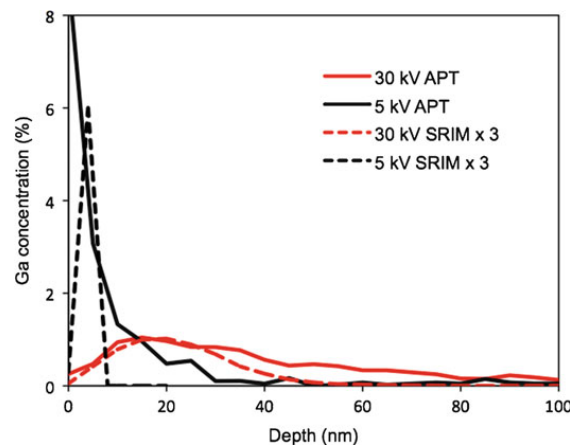


Figure 37: The comparison among the extent of Ga implantation in steel predicted by Monte Carlo simulation (dash lines) and measured by APT (solid lines) for two different milling conditions (30 kV in red and 5kV in black). Reported from reference [83].

A special case is represented by the preparation of samples containing organic materials. At present, very little data are available regarding the possible FIB-induced damage and its extent on polymers and organic materials. Moreover, in such a case also chemical modifications (bond breaking) need to be considered which can be much more sensitive than modifications in inorganic solids. For

instance a study on a 100 nm ultramicrotome section (no FIB involved) of polyacrylamide polymer using X-ray absorption near-edge structure (XANES) showed that even electron imaging (at 5 kV) induces considerable chemical damage to the polymer [135]. Vice versa, only a minor damage has been reported for various FIB conditions. Nevertheless, based on the spectral degradation in ToFSIMS when analysing organic materials (characteristic for fragmentation and damage accumulation), one should expect fragmentation to occur in relation to FIB sample preparation. It is however not straightforward to diagnose as the field evaporation process itself also may lead to a break-up of molecules. However, the APT mass spectra of a C<sub>60</sub>-doped P3HT polymer, sandwiched between an Al contact and a Si substrate, and prepared by FIB lift-out technique, showed only mono atomic ions of carbon (C<sup>+</sup>, C<sup>2+</sup>), without any molecular peaks of the polymer (Figure 38b) [136]. Using another sample preparation method (dip coating) the APT spectra of the same polymer clearly indicated the molecular peaks for the polymer (Figure 38b). A similar observation was also reported for resin where the monoatomic ions of carbon (C<sup>+</sup>, C<sup>2+</sup>) were reported to be the most dominant peaks [137].

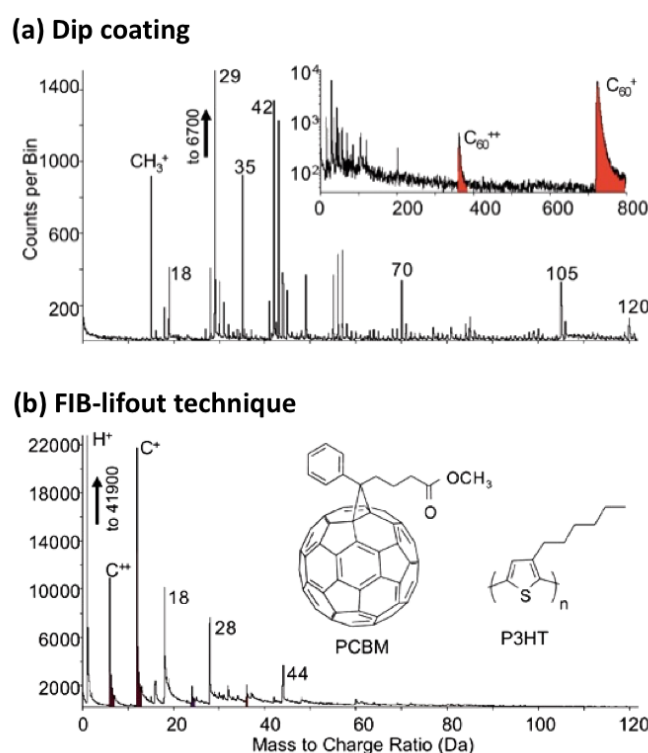


Figure 38: An example of APT mass sepctar for C<sub>60</sub>-doped P3HT polymer, obtained from an APT tip prepared by dip coating (a) and FIB lift-out technique (b). The molecular peaks for the polymers are absent in case of FIB lift-out sample prep. The spectra are reported from reference [136].

A more sophisticated study on the possible impact of the electron imaging and the Ga<sup>+</sup> ions on the fragmentation and damage to the molecular structure during FIB lift-out sample preparation and the successive sharpening step is clearly required.

### 3.6.2 Preparation of organic materials

Organic materials include a wide range of materials and scientific fields. Some organic materials (including biological materials) are required to be stabilized and protected against deformation, vaporization and degradation during all the steps of the measurement, i.e. sample preparation, handling and analysis in APT chamber. For instance, chemical stabilization using cross-linking agents and cooling the specimen are among the stabilization techniques which can potentially minimize the alternation of the molecular structure of some organics [138]. Regarding the bio-minerals and geological materials, sample preparation is not much of the challenge and FIB based sample preparation has been shown to be an effective technique [139]. In case of fully organic materials, including polymers and biological materials, sample preparation is a challenging step, due to their low mechanical rigidity and sensitivity to chemical-induced damage, i.e. cross linking. Indeed, among the limited studies on analysis of fully organics materials in APT, many studies were focused mainly on the sample preparation [137], where in some cases, no successful APT measurement has been reported using the developed sample preparation technique [140],[141]. In the following sections, the current state of the art sample preparation techniques for fully organic materials are briefly discussed.

**Dip coating:** so far, dip coating is the most successful sample preparation technique for APT analysis of polymeric thin films. In this technique, a sharp APT tip (i.e. prepared by electropolishing) is dipped into a solution containing the organic material under the investigation. In some cases, the sharp tip is reshaped in APT chamber, prior to the dipping, to remove the possible contamination and reshape the apex. This technique is reported to be successful for APT specimen preparation from polymer films [142] self-assembled monolayers [143], [144] and proteins [145].

**Conductive template:** the idea behind this specimen preparation method is to embed the nonconductive organic material in an electrically conductive matrix (i.e. conductive polymers or carbon nanotube). Then the prepared APT specimen of such a system (i.e. using FIB or dip coating) should have a better electrical conductivity, which enables the electric field at the tip apex and the measurement yield. The conductive polymers have been proposed as a potential matrix for the analysis of organics, owing to their relatively high electrical and thermal conductivities combined with their good solubility in various solvents [141]. Although, in the same study, sample preparation was reported to be successful using mold-replication technique, the application of such a method is not yet exploited for APT analysis of organics. The potential use of carbon nanotube as a conductive template for analysis of biomolecules (e.g. glycine) was also introduced in literature [138], whereby the author reported the problem of the mass overlap between the carbon nanotube and glycine.

**Cryo-preparations:** this APT specimen preparation technique was first developed for the analysis of liquid–solid interfaces in APT [146]. The potential application of such a sample preparation for some organic materials is still under investigation. As discussed earlier in this section, some organic materials (including biological materials) are required to be stabilized and protected against deformation, vaporization and degradation during the sample preparation step. Cooling the specimen down to cryo temperature, during the sample preparation, is a viable approach to minimize the extent of the mentioned damages to biological materials [147]. Due to the enormous potential of a such sample preparation in biology, a complete cryo sample preparation setup for APT, including cryostage for FIB and direct cryo transfer unit to the LEAP chamber, has been already developed for a LEAP system (i.e. in Eidgenössische Technische Hochschule Zürich and University of Michigan). Despite this progress in the hardware development, very few papers have been published on the analysis of biological materials in APT using cryo preparation. An improvement in the application of APT analysis in biology has been predicted by using cryo-preparation by several textbooks [148] ,[83].

### 3.7 Conclusion

In this chapter, I discussed the currently available theoretical models describing the field evaporation process and the successive post ionization of the evaporated ions in the vicinity of specimen apex. The described theoretical models were also compared in terms of their validity and limitations to match the experimentally observed evaporation behavior. Finally, the quantum description of the charge exchange model (charge drain) was referred to as the most accurate theoretical model to predict the physical phenomenon of field evaporation and the corresponding barrier energy. In this model, ionization and escape of the ions from the surface occur simultaneously, in which the charge concentration maximizes on the most protruding atom on the surface and the Maxwell repulsive stress causes an additional contribution on the charge concentration. In the presence of a strong enough electric potential, this stress causes the complete ionization and escape of the most protruding atoms. Then the barrier height for the field evaporation was derived based on the potential energy of the surface atoms

The post ionization theory is also discussed in detail. The successive post ionization of evaporated ions in the vicinity of tip apex was discussed, whereby the probability of this post ionization process strongly depends on the intensity of the electric field in the vicinity of the tip. Hence, the charge state ratio (CSR) has been introduced as a strong means to estimate the intensity of electric field and to compare the experimental conditions. Then, the probability of evaporation and the evaporation rate were explained based on the introduced theoretical models and the dependency of the evaporation rate on the electric field and temperature has been discussed in detail.

Furthermore, the laser tip interaction has been also discussed for both metallic and semiconductor materials. Different possible mechanisms of field evaporation

by laser pulsing have been explained and the thermal pulsing was identified as the main mechanism of field evaporation in laser La-APT. Indeed, as the laser energy is absorbed and transferred in thermal energy by APT tip, the induced thermal agitation of the surface atoms activates the field evaporation mechanism. Depending on the laser wavelength and the tip material and shape, the photon energy was shown to be absorbed in the specimen surface (for UV laser) or in the volume of the specimen (for IR laser for Si tip). The absorption pattern of photon energy was discussed to have a strong impact on the cooling dynamics and mass resolution of APT analysis.

Finally, the sample requirements for APT specimen have been discussed in detail. The currently available specimen preparation techniques for semiconductor and organic specimens have been introduced and the possible drawback and the limitation of each technique was also explained in detail.

# Chapter 4

## Field-of-view in atom probe tomography

In this chapter, we will present the current understanding of field-of-view (FOV) in APT for different tip shapes, together with our contribution to this understanding. In addition, a novel specimen design and preparation technique will be proposed, which maximizes the FOV in APT and enables full tip imaging. This proposed process allows the fabrication of multiple APT specimens in a reproducible fashion and with a minimized tip to tip variations in view of tip radius and shank angle.

To achieve this, we will first discuss the distribution of the electric field at the specimen surface, in the close vicinity of the apex as well as in between the specimen and detector in Section 4.1. The current understanding of the electric field on both the mesoscopic and microscopic scale will be discussed and the validity of our developed finite element simulation to predict the electric field on the mesoscopic scale will be assessed. In Section 4.2 the ion trajectories and their dependency on the electric field distribution will be discussed in detail. As described in Chapter 3, the ions emitted from the specimen surface are immediately accelerated towards the detector by the strong electric field in between the specimen and the detector (or local electrode). The flight path of the ions (so-called ion trajectory) is mainly determined by the electric field distribution created in between the specimen and detector. These ion trajectories are not straight lines and are typically bent towards the detector center by the intense electric field in the vicinity of specimen apex.

In Sections 4.3 to 4.4, image magnification and 3D data reconstruction in APT will be briefly introduced. In particular, the currently available reconstruction protocols and their limitations to reconstruct the actual 3D specimen volume will be discussed. The understanding of the 3D data reconstruction is an essential step towards our detailed discussion in FOV, which is explained in Section 4.5. In this section, the current understanding of the FOV

for symmetric tip shape and asymmetric tip shape (UV light induced) will be described in detail whereby some new aspects of the APT measurement are explored.

Finally, in Section 4.6 the feasibility of full-tip-imaging in APT following our proposed specimen design will be demonstrated. We will also discuss the sample design and its optimization based on finite element analysis. In addition, the specimen preparation process together with the results of the related APT experiment will be described in detail.

## 4.1 Electric field

As explained earlier in Section 3.6, to generate the intense electric field required for field evaporation (in the order of  $10^{10}$  V/m), the APT specimen needs to be prepared in the form of a sharp needle with an apex radius typically below 100 nm. The intensity of this generated electric field at the specimen surface as well as the field distribution above the surface can be estimated by electrostatic considerations. In this context, the generation of the electric field for a simple metallic sphere will be first discussed. For conductive materials, solving Maxwell's equation assumes the surface charge to be a thin uniform film across the surface boundaries. Starting from this consideration, for a single metallic sphere with a radius of  $R$  which is biased to a DC voltage  $V$ , the induced surface charge  $Q$  has a uniform density  $\sigma$  over the sphere surface. Then Gauss's law describes the generated electric field vector to be perpendicular to the sphere surface with a uniform magnitude all over the surface. The magnitude of the electric field  $F$  can be written as:

$$F = \frac{\sigma}{\epsilon_0} \quad 4.1$$

Where  $\epsilon_0$  is the dielectric permittivity of the vacuum. Then, using Coulomb's law, the magnitude of the electric field  $F$  and the electric potential  $V$  at the sphere surface can be derived as the follows:

$$F = \frac{1}{4\pi\epsilon_0} \frac{Q}{R^2} \quad , \quad V = \frac{1}{4\pi\epsilon_0} \frac{Q}{R} \quad 4.2$$

This equation indicates the equipotential property of a metallic surface, which originates from the uniform density of electric charges across the surface of a given conductive sphere. Similarly, the electric field  $F$  has also the same magnitude all over the sphere surface (Equation 4.2) and its direction is perpendicular (outward) at each point on the surface. The schematic representation of the electric field direction and the uniform charge density at the surface for a metallic sphere is depicted in Figure 39.

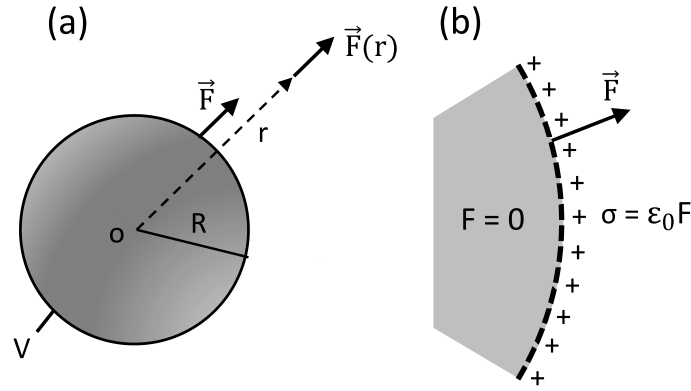


Figure 39: Schematic representation of electric field direction (a) and the uniform charge density (b) at the surface of metallic sphere having a radius of  $R$ . Reproduced from reference [82].

Finally, by combining the descriptions of electric field and potential in the Equation 4.2, a linear relation between the magnitude of electric field  $F$  and applied electric potential  $V$  at the surface can be obtained for a metallic sphere:

$$F = \frac{V}{R} \quad 4.3$$

In addition, the electric field outside the metallic sphere, at a distance  $r$  from the center ( $r > R$ ) can be written as:

$$\vec{F}(\vec{r}) = \frac{V}{R} \left( \frac{R^2 \vec{r}}{\|\vec{r}\|^3} \right) \quad 4.4$$

Hence, the magnitude of the electric field strongly drops as the distance from the sphere surface increases ( $F \sim 1/r^2$ ).

In order to accurately describe the electric field at the APT specimen surface as well as at a certain distance from the specimen apex (in vacuum), further electrostatic aspects need to be taken into consideration. For instance, the real APT specimen is not exactly an isolated sphere and as such an assumption of uniform charge density is not valid anymore. In addition, neglecting the atomic roughness at the specimen surface can cause a significant error in the estimation of the actual electric field in the vicinity of tip apex. The distribution of the electric field at the specimen apex and also around the tip are discussed in detail in the following sections.

#### 4.1.1 Electric field at the specimen surface

In this section, an analytical expression for the magnitude of the electric field at the surface of an isolated sphere has been derived. The real APT specimen is not exactly an isolated sphere and instead, it has a needle shape specimen with a certain shank angle and apex shape. To account for the actual APT specimen shape and estimate the magnitude of electric field at the apex of the specimen, Gomer [149] proposed to use an additional correction factor to the analytical expression of the electric field at the surface of an isolated sphere. He assumed the

APT specimen as a truncated cone with quasi-hemispheric apex and he suggested to add an additional dimensionless factor  $k_f$  to Equation 4.3 in order to account for the difference in geometry of the APT tip and the isolated sphere:

$$F = \frac{V}{k_f R} \quad 4.5$$

where  $V$  is the applied electric potential,  $R$  is the radius of hemispheric apex and  $k_f$  is called field factor.  $k_f$  can be experimentally calculated in field ion microscopy (FIM) by knowing the tip radius and measuring the required voltage to reach the theoretical field evaporation for the specimen material ( $F_{\text{evap}}$ ). Indeed, the field factor  $k_f$  characterizes the electrostatic environment around the tip apex. Numerical simulations reveal that the field factor depends on many parameters including: shank angle, specimen to detector (or local electrode) distance, shape of the specimen, position of the specimen holder in respect to the tip apex and finally the entire electrostatic environment of the chamber (including detector or local electrode shape) [150], [151]. This will be discussed in more detail in Section 4.1.2

Nevertheless, the estimated electric field at the specimen surface using Equation 4.5 relies on many assumptions which are far from resembling the physical properties of the apex surface. For instance, the specimen apex was assumed to have a hemispherical shape with an atomically smooth surface. Hence, the charge density is also assumed to be constant across the apex surface. Although the actual mesoscopic shape of the tip apex can be included by numerical calculation of electric field, the assumption of the emitter surface being as a continuous and smooth medium with a uniform charge density is incorrect. In reality (microscopic scale) the surface is composed of atoms which impact on the actual electric field distribution at the specimen surface. A more realistic description implies a variation in the local curvature at atomic scale and even a field penetration inside the material. To accurately estimate the local field distribution at the specimen surface, quantum calculations are required such as the calculations of the charge distribution above the Au (110) surface using density functional theory (DFT) [152] ( Figure 40).

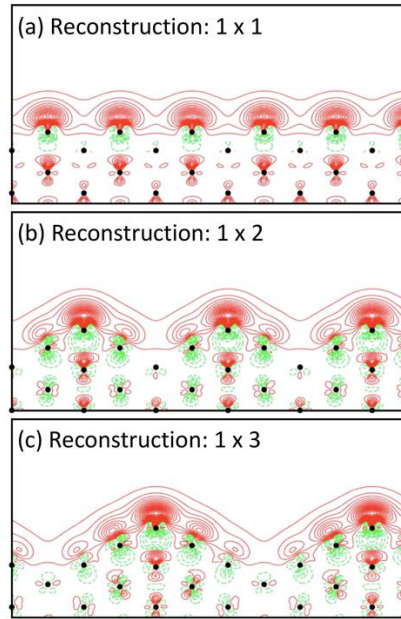


Figure 40: Local field enhancement and charge distribution for different Au (110) surfaces obtained from quantum calculations: (a) 1x1, (b) 1x2, and (c) 1x3 missing-row surface reconstruction. The positions of the ions are indicated by black dots and the positive and negative contours for charges are plotted in red and green respectively. Reproduced from reference [152].

The accumulation of excess charge density on top of the surface is evidenced for all the three surface reconstructions in Figure 40 and increases for higher degree of missing rows in the surface reconstruction (from a to c in Figure 40). Indeed, through the surface reconstruction, the surface becomes atomically more rough with taller protrusions. To minimize the surface energy on these protrusions the electric charges redistribute themselves to an excess charge concentration along the surface normal [152]. This results in a local field enhancement on top of the protrusions (atomic roughness). Similar results have been reported on other surfaces by various authors [153], [154]. This concentration of surface charges results in more intense repulsive Maxwell stress on the protrusions and reduces the barrier energy for field evaporation further, as described earlier in Section 3.1.2.

An interesting conclusion which can be drawn from the quantum calculations, is that the pattern of the charge concentration at the surface (on the most protruding regions) as predicted by quantum calculations is very similar to the classical approach, where the charged surface is treated as the geometrical object and the field enhancement is calculated following Gauss's law. This suggests that by considering the geometry of the surface as an atomic representation, one can estimate the local electric field at each point on the surface (i.e. using finite element simulation) by considering the local curvature at the atomic scale. Each atomic protrusion (i.e. kink site and terraces) can give rise to the local electric field.

The microscopic variation of the electric field at the surface implies that the actual field at each position on the tip surface is much different from the average field  $F$  (Equation 4.5). For instance, in Figure 41a the local electric field distribution on top of most atomic terraces of the cubic lattice structure is reported

[89], where the electric field distribution was computed based on the distribution of surface charges using the classical electrostatic Robin's equation. As can be seen, there is a strong variation of the electric field as a function of the distance from the terrace center, whereby the maximum electric field appears on the edge position of the top most atomic terrace. This study suggests that an additional local field enhancement factor  $\gamma$  on the edge positions of the crystalline terraces would lead to a better estimate of the strength of the electric field. By defining:

$$\gamma = \frac{F_{local}}{F_{average}} \quad 4.6$$

where  $F_{local}$  is the local electric field at each position on the surface and  $F_{average}$  is the average electric field estimated using the tip radius and  $k_f$  factor (Equation 4.5). The distribution of  $\gamma$  over the apex surface for a metallic specimen having a FCC lattice structure is reported on Figure 41b. The value of  $\gamma$  is reported to vary in a range between 1 to 1.8.

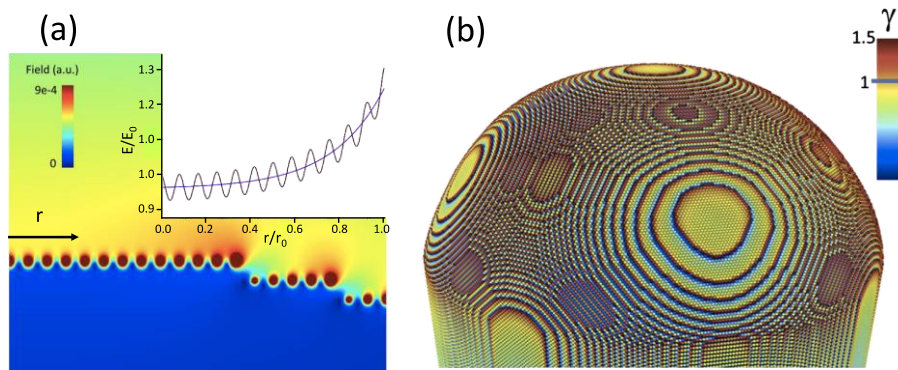


Figure 41: (a) Distribution of electric field in the vicinity of  $\langle 001 \rangle$  terrace for a specimen having a simple cubic lattice structure. The inset shows the relative intensity of electric field above the first terrace as a function of the distance from the terrace center (indicated by  $r$ ). The intensity of the electric field progressively increases toward the terrace edge. (b) The local field enhancement factor  $\gamma$ , computed on the 3D apex surface of hemispheric metallic tip with FCC structure. The  $\gamma$  maximizes at the edge positions of crystalline terraces. Reproduced from reference [89].

This local variation of the electric field (i.e. charge concentration) imposes a strong electrostatic Maxwell stress on the surface atoms, which may cause surface rearrangement, migration and eventually can adjust the distribution of the electric field [90]. The impact of Maxwell stress on the field evaporation process has been discussed in earlier in Section 3.1.2.

Up to know the distribution of the electric field at the apex of a metallic tip has been discussed, which typically has a field penetration depth of less than one atomic layer [154]. In the case of non-metallic materials (semiconductors or insulators), a penetration of the electric field over a few atomic layers inside the material is predicted [154]. In order to understand this field penetration in non-metallic materials, the physical properties of such material are needed to be considered. At cryogenic temperature (below 40 K) and in the absence of laser illumination, semiconductors act as an insulator material, whereby the conduction band is empty and the valence band is occupied with all the electrons (zero free carrier density). Hence the resistivity of such a material is very high. By considering then the small cross-section area of an APT specimen, a strong

resistance  $R_{tip}$  ( $10^{16}$ - $10^{18}$  ohm) can be estimated for a tip. The typical electron current  $I_{evap}$  generated by the ion emission is on the order of a few fA. Simply using Ohms' law, one can estimate the voltage drop ( $\Delta V_{ohm} = R_{tip} \times I_{evap}$ ) over the tip to be on the order of several hundred volts. In addition, at high electric field, deformation of the band diagram close to the apex surface (band bending) can impose an additional voltage drop  $\Delta V_{bb}$  up to a few volts at the vicinity of the tip surface [117]. Under the laser illumination the density of charge carriers can increase significantly (photo absorption process) which leads to a reduced or even eliminated voltage drop ( $\Delta V_{ohm} = \Delta V_{ohm} + \Delta V_{bb}$ ) (see Figure 42). The laser tip interaction for band-gap materials was discussed in detail in Section 3.4.

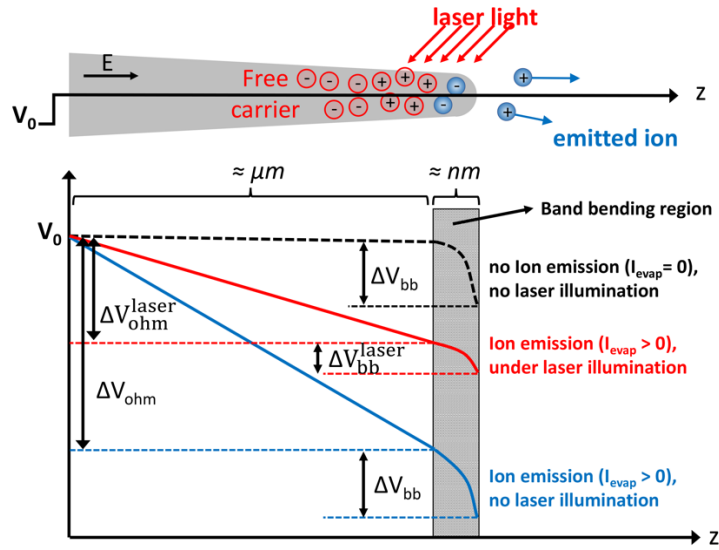


Figure 42: Schematic representation of voltage drop along the APT specimen height for insulating material. At the presence of strong electric field, the band bending causes voltage drop in the vicinity of the apex. The ion emission (evaporation event) can cause carrier generation and the corresponding electric current  $I_{evap}$ . Under the laser illumination the charge density increases significantly which improve the conductivity in the specimen depth. The voltage drop along the specimen depth is shown: in the absence of ion emission and no laser illumination (dashed black line), in the presence of ion emission and no laser illumination (solid blue line), in the presence of ion emission and laser illumination (solid red line). Reproduced from reference [82].

#### 4.1.2 Electric field around the specimen

As discussed in Section 4.1.1, an APT specimen is not an isolated object in the space and to accurately calculate the distribution of electric field around the tip, the entire electrostatic environment around the specimen (including local electrode, detector and chamber walls) needs to be taken into consideration. In addition, to accurately estimate the distribution of the electric field in the vicinity of the tip apex, and the apex surface, the impact of other microscopic features on the tip surface, such as crystallographic structure and atomic roughness, also needs to be taken into account. In this context, the electric field around the specimen is commonly categorized in two regions: near-field and far-field region. The distribution of electric field in the vicinity of tip apex (sub-micrometer scale) is typically referred to as near-field, while the distribution of electric field far from the apex (up to the meter scale) is referred to far-field.

In this PhD work the motivation to study the electric field distribution around the specimen is to mainly estimate the ion trajectories and to assess the FOV as a function of tip geometry. Thus, the accurate calculation of the electric field at the apex surface is not much of the interest. On the other hand, considering the currently available computational power, such a 3D numerical calculation is also computationally demanding and can be done only for certain applications. Hence, in our study, the apex surface is considered as an atomically smooth surface and microscopic scale considerations (i.e. crystallographic orientation) were excluded from our analysis. For a finite system in three-dimensional space, which ends by a closed surface  $S$ , the Gauss's law can be written as:

$$\Phi_E = \frac{Q}{\epsilon} \quad 4.7$$

where  $\Phi_E$  is the sum of the electric flux entering into this system,  $Q$  is the total charge of the system and  $\epsilon$  is the permittivity of the medium. The sum of electric flux  $\Phi_E$  entering through the surface boundary of the system can be obtained by:

$$\Phi_E = \oiint_S F \cdot ds \quad 4.8$$

where  $F$  is the electric field vector at each point on the surface boundary. The total charge  $Q$  of the system can be also written as a function of charge density  $\rho$  over the volume:

$$Q = \iiint_V \rho \, dv \quad 4.9$$

Finally, by combining the Equations 4.7 to 4.9, the integral form of Gauss's law for a closed system can be written as:

$$\oiint_S F \cdot ds = \iiint_V \frac{\rho}{\epsilon} \, dv \quad 4.10$$

The integral form of Gauss's law shows that the accumulated electric charge in the volume of the system can be evaluated by mapping the electric field on the boundary of the system. The Gauss's law can be also be written in differential form:

$$\nabla \cdot F(r) = \frac{\rho(r)}{\epsilon_r} \quad 4.11$$

where,  $r = x\hat{i} + y\hat{j} + z\hat{k}$  is the position vector in the space. The differential form of Gauss's law describes that the distribution of electric field  $F(r)$  as function of charge density  $\rho(r)$  over the entire volume of the system. However, in practice the Equation 4.11 cannot be solved directly, since the electric field is usually unknown on the boundaries of the system. Hence, to solve the above equation, the

Gauss's law is written first as function of the electric potential, where, the distribution of electric field  $F(r)$  as a function of electric potential  $V(r)$  is:

$$F(r) = \nabla \cdot V(r) \quad 4.12$$

Finally, by substitution the Equation 4.12 into 4.11, the differential form of Gauss's law can be written as a function of the electric potential  $V(r)$ :

$$\nabla^2 \cdot V(r) = \frac{\rho(r)}{\epsilon(r)} \quad 4.13$$

In mathematics, such a partial differential equation is known as the Poisson equation. Although the Poisson equation can be solved analytically for simple geometries (i.e. isolated sphere), typically this equation needs to be solved numerically over the system volume. In this project, to estimate the distribution of electric field around the specimen, finite element method (FEM) has been used to solve the Poisson equation starting from the known boundary conditions. The choice of FEM over finite volume methods was based on its flexibility in terms of solving complex multi-scale triangular meshes.

In this project to estimate the electric field around the APT specimen, we used COMSOL Multi Physics software package which allows triangular mesh generation and solves the above described Poisson equation using FEM over the control volume. We assumed the specimen to be at equipotential, i.e. neglect any field penetration inside the material, and to have atomically smooth surfaces. In addition, the specimen and the local electrode were assumed to be perfectly symmetric with respect to the tip axis. This assumption simplifies the actual three-dimensional problem into an axisymmetric problem, which is basically a type of two-dimensional problem and reduces significantly the computational power. The schematic representation of the boundary problem used in our FEM is shown in Figure 43.

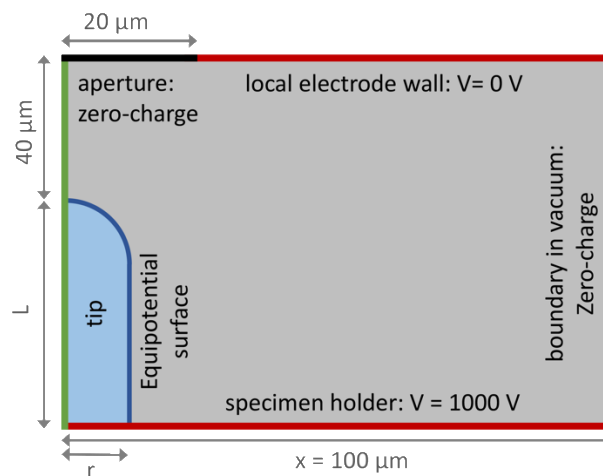


Figure 43: Schematic representation of boundary condition problem and the system design for finite element analysis using COMSOL multi physics software package. To reduce the computational power, only a part of chamber volume ( $x = 100 \mu\text{m}$ ) is considered in our analysis, where the distribution of the electric field is unaffected from the choice of  $x$ . The defined boundary conditions are as the follows: zero-charge (in black), fixed applied potential (in red), equipotential (in blue) and internal axisymmetric boundary (in green).

The specimen is assumed to be a tall cylinder having a small radius  $r$  and height of  $L$ . The actual dimension for the local electrode aperture and the specimen to detector distance in LEAP 5000 APT instrument has been considered in our study. Please note that the figure is not in scale.

The entire volume (see Figure 43) was meshed using a triangular mesh generator of COMSOL software package. In particular, a very fine mesh was created in the vicinity of tip apex and the mesh grid was adjusted to have a gradually coarser mesh size far from the tip apex. Finally, the mesh size was reduced gradually to reach a fine enough size, in which the distribution of electric field becomes approximately unaffected from the choice of the mesh size. The generated mesh around a specimen having a diameter of 60 nm and a height of 50  $\mu\text{m}$  is shown in Figure 44.

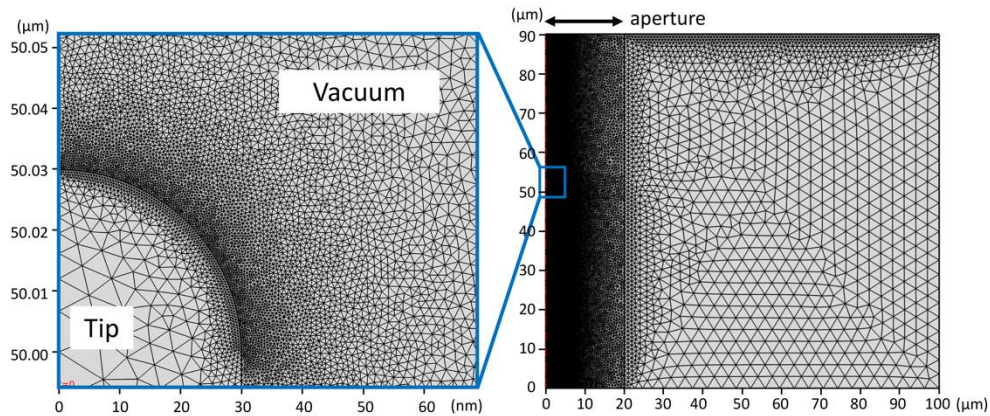


Figure 44: Generated triangular mesh for the two-dimensional control volume described in Figure 43. A fine mesh size was employed in the vicinity of tip apex to capture the variation of the electric field close to the apex (inset). The tip diameter and height were fixed to 60 nm and 50  $\mu\text{m}$  respectively.

Finally, the Poisson equation 4.13 was solved for an applied electric potential of 1 kV and the results are reported in Figure 45. As can be seen the magnitude of the electric field drops significantly as the distance from the tip apex increases, e.g. roughly by a factor 10 – 100 as the distance from the specimen apex varies from 80 to 600 nm respectively. The calculations emphasize the importance of the electric field distribution in the vicinity of specimen apex on the ion trajectories in their very early stage of their flight. The impact of field distribution on the ion trajectories will be discussed in the next section.

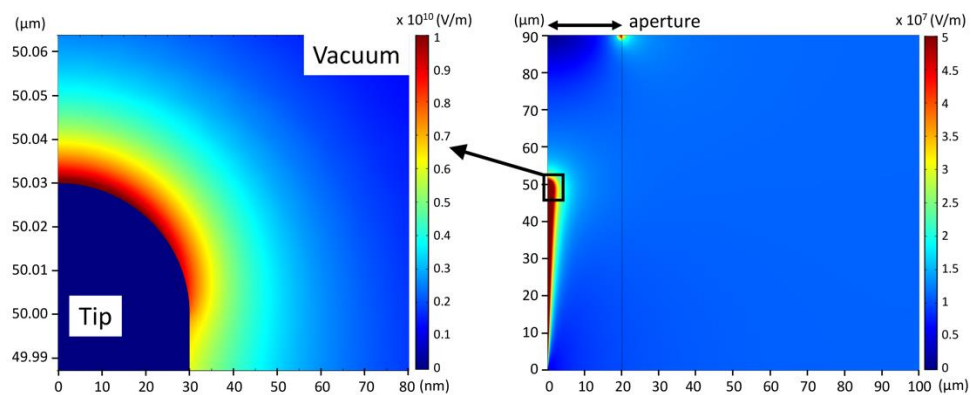


Figure 45: Finite element simulation of electric field around the APT specimen (diameter: 60 nm, height: 50  $\mu\text{m}$ ) at 1 kV applied potential. The color bar indicates the magnitude of the electric field in V/m. The magnitude of electric field drops significantly as the distance from tip apex increases e.g. it drops about an order of magnitude at 80 nm away from the tip apex.

To verify the validity of our FEM, the magnitude of the electric field at the tip apex was compared to the simulated data in the literature. In the first step, the validity of the simulation was evaluated against the linear relation between the applied electric potential and the magnitude of the electric field ( $F = V/k_f R$ ). To do so, the magnitude of electric field at the tip apex was investigated as a function of applied voltage (from 1kV to 10 kV) for different specimens, having a fixed diameter of 60 nm and heights in a range between 5 to 120  $\mu\text{m}$  (corresponding to different field factors  $k_f$ ) and the results are reported in Figure 46a. As expected, the magnitude of electric field and applied voltage have a linear relation with a slope described by  $1/k_f R$ . Hence, for each specimen dimension,  $k_f$  can be also calculated from the simulated data.

Finally, the validity of FEM was compared and assessed using a numerical study in literature. In this context, the specimen dimension (diameter and height) was varied in a range described in reference [151] and the field enhancement factor  $k_f$  was calculated for each specimen dimension and the obtained results were compared with the values reported by reference [151] in Figure 46b. As can be seen, the simulated field factors  $k_f$  match well with the reported values in literature with an average deviation below 1%. Please note that the reported  $k_f$  is the average value over the apex surface up to the launch angle equal to  $30^\circ$  (according to what is reported in [151]), whereas the field enhancement varies across the apex surface for hemispherical apex shape (see Figure 45). The variation of  $k_f$  across the specimen diameter will be further discussed in the section.

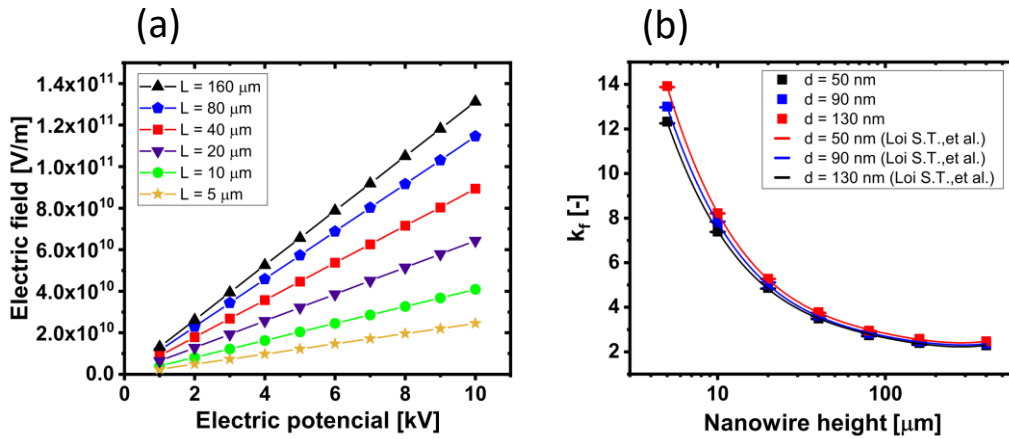


Figure 46: Validity assessment of finite element analysis (FEA) of the electric field at the specimen apex. (a) the expected linear trend between the magnitude of electric field and applied potential ( $F = V/k_f R$ ) was investigated for six different tip heights having the same tip diameter of 60 nm. The slope of each line is determined by the  $1/k_f R$ . (b) The validity of our FEA has been compared and assessed by a numerical study by Loi S. T., et al. [151]. In particular field factor  $k_f$  has been calculated for different tip dimensions (different diameters and heights) as described in this reference. A good agreement between the simulated data and values of  $k_f$  reported in this reference has been obtained with average deviation below 1%.

In addition, Figure 46b shows the impact of tip height and diameter on the field enhancement at the tip apex, as indicated by field factor  $k_f$ . As can be seen, as the specimen height was increased from 5  $\mu\text{m}$  to 40  $\mu\text{m}$ ,  $k_f$  dropped

approximately from 13 to 3. For taller tips ( $> 40 \mu\text{m}$ ), the sensitivity of  $k_f$  to the tip height reduces significantly and becomes almost constant for specimens higher than  $120 \mu\text{m}$ . Indeed, this is the reason why the CAMECA standard micro coupons are fabricated in the form of a tall micropost having a height of about  $150 \mu\text{m}$  as this maximizes the field enhancement at the tip apex (low  $k_f$ ) and minimizes the variation of  $k_f$  with respect to the lamella thickness (minimize the tip-to-tip variation of  $k_f$ ). Typically,  $k_f$  for standard APT specimens varies in a range between 3 to 8 depending on the other specimen parameters.

The variation of  $k_f$  with respect to specimen diameter (see Figure 46b) indicates that regardless of the specimen height,  $k_f$  is higher for smaller tip diameters. The dependency of  $k_f$  with respect to the tip diameter is weaker for taller specimens, in which the standard deviation of  $k_f$  (using the three values of tip radius) reduces from about 0.8 to 0.08, as the specimen height was increased from  $5 \mu\text{m}$  to  $200 \mu\text{m}$ .

Nevertheless, the actual APT specimen is not a long cylindrical nanowire and instead it consists of a tip with certain shank angle prepared on top of a micropost, which does not have zero shank angle as well. To account for the actual tip shape, a certain shank angles for both tip and micropost can be defined in the model used in the FEM. The influence of shank angle (both tip and micropost) on  $k_f$  has been also widely studied in the literature [150], [155]. The shank angle is reported to have an opposite impact on the field enhancement at tip apex, in which a higher shank angles results in a higher  $k_f$  [151], [156]. In this project, the motivation for the study of the electric field is to improve the FOV using a new specimen design consisting of a nanowire tip on top of a zero shank angle cylindrical micropost. We will discuss that as the field lines originating from the flat area on top of the micropost compress further the ion trajectories, this configuration can improve the FOV in the APT analysis. Hence, the impact of shank angle on  $k_f$  was not investigated any further in our analysis. The related simulations will be used later in Section 4.6.1.

Apart from the specimen parameters, also the instrumental parameters can have a remarkable impact on the electrostatic environment around the tip. This has been also widely studied in the literature [150], [151] and the specimen to local electrode distance and aperture diameter of the local electrode are reported as the two most critical parameters. For the LEAP 5000 both aforementioned parameters are equal to  $40 \mu\text{m}$  as shown in Figure 43.

## 4.2 Ion trajectories

As discussed in the previous chapter, the ions evaporated from the specimen surface are immediately accelerated towards the detector (or local electrode) due to the intense electric field in the vicinity of specimen apex. Hence the ion trajectories are mainly determined by the electric field lines in between the tip and the detector as well as by the initial position of the emitted ions on the apex surface [157]. Hence, an estimation of the electric field distribution in between the

tip and the detector was an essential step towards the calculation of ion trajectories.

In this project, to estimate the ion trajectories we used the particle tracing package of the COMSOL multi physics software. A fixed number of charged particles (20 particles) uniformly distributed on the tip apex, were released in the previously calculated electric field distribution in between the apex and local electrode. A unit charge was assigned to each particle and the particle-particle interaction force was neglected in our model. By knowing that the particle mass directly influences the particle velocity but has a negligible impact on the ion trajectory, a fixed mass equal to the average mass of Si atom was assigned to all the particles ( $4.66 \times 10^{-24}$  g). This particular choice for particle mass was made to have also an estimation of the ion velocity during their flight path. After the release of the particles from the apex surface, they immediately accelerate in the electric field (as the force field), in which the particle velocity  $\vec{v}$  can be written as:

$$\frac{d}{dt}(m\vec{v}) = q(\vec{F}) \quad 4.14$$

where,  $m$  is particle mass,  $q$  is particle charge and  $\vec{F}$  is the electric field vector calculated for every point in the control volume. Since the magnitude of particle velocity in our study is much smaller than the speed of light ( $v \ll c$ ), the Lorentz factor  $\left(1 - v^2/c^2\right)^{-1/2}$  is small enough to neglect the relativistic corrections. By solving the above equation, the particle velocity distribution and the corresponding ion trajectory can be determined for every particle released from the specimen apex.

Since the solution is time dependent, the time duration window of the solver was used long enough to capture the entire trajectories up to the aperture position of the local electrode. While the time increment ( $dt$ ) was reduced gradually to obtain a final solution (velocity distribution and trajectory) approximately independent from the choice of the time increment. The calculated ion trajectories for a  $50 \mu\text{m}$  long nanowire having a diameter of  $60 \text{ nm}$  are reported in Figure 47, whereby the adopted time increment and analysis duration were adjusted to  $2 \times 10^{-12}$  and  $4 \times 10^{-8}$  s respectively.

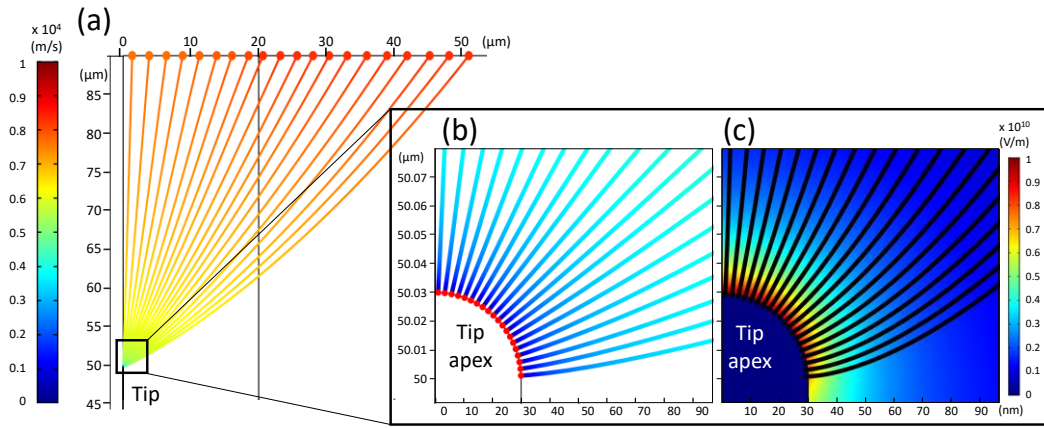


Figure 47: Finite element analysis of ion trajectories and electric field lines for a 50  $\mu\text{m}$  long nanowire with a diameter of 60 nm. The apex was uniformly covered by 20 particles having the unit charge and mass of  $4.66 \times 10^{-24}$  g. After the release of particles in the presence of the calculated electric field, their trajectories towards local electrode were tracked and reported in (a). The color bar indicates the magnitude of the ion velocity at each stage of the flight. The inset (b) shows the enlarged view of the particle trajectories in the vicinity of the tip apex with the same color code as the main plot (a). The electric field lines, generated from the tip apex are also reported in (c), where the color map shows the magnitude of the electric field at the applied potential of 1000 V.

Our FEA shows that ion trajectories are compressed towards the aperture window, meaning that the trajectories are bent instead of having straight paths. The compression of the trajectories was induced by the electric field force during their flight (equation 4.14). The enlarged view of the particle trajectories and the electric field lines are shown in Figure 47b and c. The electric field lines determine the acceleration pattern for the traveling ions (equation 4.14), which directly impacts the ion velocity as well as the ion trajectories. Our analysis clearly illustrates that the ion trajectories and field lines have a slightly different pattern (see Figure 47b and c). Indeed the velocity  $\vec{v}$  and displacement  $S$  of the particle can be written as  $\frac{d\vec{v}}{dt} = \frac{q(\vec{F})}{m}$  and  $S = \int v dt$ , linking the field lines to the second derivative of trajectories (or equivalently displacement  $s$ ). The obtained velocity distribution in the vicinity of the tip apex (see Figure 47b), shows that the particles reach a velocity of about 4000 m/s at the first 50 nm of their flight, while the estimated maximum velocity is about 8340 m/s at the local electrode position (40  $\mu\text{m}$  above the tip). This underlines the important role of electric field distribution in the vicinity of specimen apex, where the electric field intensity is maximum. The important role of electric field lines, in the vicinity of apex, on the ion trajectories is also discussed in literature [151], [157].

Nevertheless, the ion trajectories and ion velocities are also impacted by the electric field even at larger distances from the apex resulting in the curved shape of the trajectory through the entire flight path. This implies that by controlling the electrostatic environment around the tip, one can modify the electric field lines around the specimen and finally modify the ion trajectories, while the electric field distribution (field lines) in the very vicinity of the apex is mainly determined by the apex shape. This will be discussed further in detail in Section 4.6.1.

In order to estimate the actual ion trajectories and implement it for 3D data reconstruction, one needs to accurately consider also the initial position (at microscale) of evaporated ions from the specimen surface. This requires accurate

knowledge of the surface geometry and the distribution of the atoms on the surface. Hence, the accurate 3D electric field distribution in near-field (nanometer scale in the vicinity of specimen apex) also needs to be calculated. Such a complex multi-scale analysis has been reported by finite element/finite difference method and ion trajectories were calculated for the different crystallographic orientations of surface atoms [158], [159].

However, even such an analysis is not sufficient to predict the actual ion trajectories during the APT analysis. Indeed, there are a number of phenomenological effects involved at the microscale during the field evaporation process that can impact the initial trajectories of ions. For instance, the topology of surface atoms does not remain constant during the evaporation sequences (even after removal of one complete layer). This alters the initial position of atoms as well as the local electric field distribution which is known to affect the initial trajectory of ion and is referred as trajectory aberration [160]. The influence of such a trajectory aberration on the 3D spatial resolution of APT analysis has been studied for pure materials [158] as well as precipitates in the main matrix [161] and different models have been suggested to implement the effect of the microscale atomic distribution on 3D reconstruction and finally improve the 3D resolution of APT data reconstruction. The implementation of such analysis in APT data reconstruction is a challenging task, mainly due to the lack of knowledge on the local tip shape and limitations in the computational power. Some preliminary studies using a combined TEM-APT analysis has been reported in the literature [162]

Alternatively, currently, there are simple projection models available which approximately relate the projected ion position on the detector to its original position on the specimen surface, without calculating the field lines and ion trajectories. The two main available models are “Point-Projection” and “Radial Projection with Angular Compression”. Although the common data reconstruction methods available in the commercial APT software packages are based on the point-projection model, both models will be briefly discussed in the following sections.

### **4.2.1 Point-Projection model**

The point-projection model is commonly used by most commercial APT software packages to 3D reconstruct APT data. In this model, the trajectories of the ions are assumed to be a straight line, instead of the actual bent curve, which passes through the original position of the ion at the specimen surface and the hit position on the detector [83]. Then, the intersection of this straight line with the tip axis (point P, in Figure 48 is called the projection point. This point is behind the center of the spherical cap (point O, in Figure 48 with a distance equal to  $\xi(R-1)$ ), where the factor  $\xi$  is called image compression factor and it reflects the degree of compression in the ion trajectories (bending) toward the detector [83].

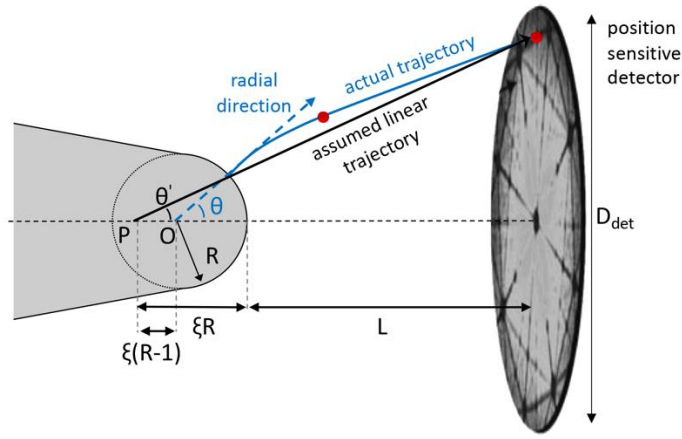


Figure 48: Schematic representation of point-projection model and the definition of image compression factor  $\xi$ . Reproduced from [83].

The observed impact angle of ion trajectories ( $\theta'$ ) can be simply derived from the original launch angle of the ion ( $\theta$ ) and image compression factor ( $\xi$ ) [83]:

$$\theta = \theta' + \arcsin((\xi - 1) \sin \theta') \quad 4.15$$

Assuming the radius of the hemispheric cap ( $\sim 100$  nm) to be negligible with respect to the specimen to detector distance ( $L \sim 10$  cm), the observed impact angle can also be written as [83]:

$$\theta' \approx \arctan\left(\frac{D}{L}\right) \quad 4.16$$

Please note that the presence/absence of local electrode does not have any impact on the above derived equations. Finally, for a given launch angle, image compression factor  $\xi$  can be derived from Equations 4.15 and 4.16. Hence, to experimentally compute  $\xi$ , one needs to have accurate knowledge on the launch angle ( $\theta$ ), the corresponding hit position on the detector ( $D$ ) and the specimen-to-detector distance ( $L$ ). The experimental calculation of  $\theta$  is not straightforward and requires accurate knowledge on the local tip shape at the given sequence of evaporation. In addition, to experimentally assign a hit position on the detector ( $D$ ) to a given atom position on the specimen surface, a sort of marker (e.g. an interface or elemental contrast) is required.

Alternatively, for crystalline specimens, by indexing the pole structures on the detector hit map, or so-called desorption image, and assigning the pole patterns to the major crystallographic planes at the surface of the specimen (similar to Figure 49a),  $\xi$  can be experimentally calculated [163]. The schematic representation of  $\xi$  for given pole positions and crystallographic planes is depicted in Figure 49b.

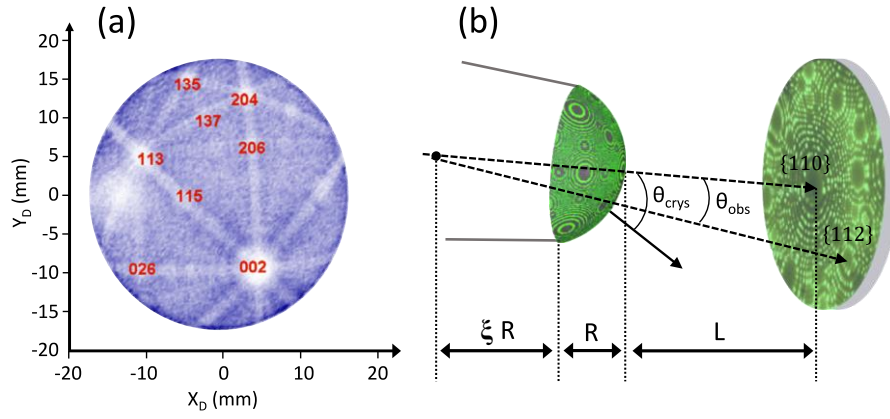


Figure 49: (a) Detector hit map (desorption image) for pure Al after collection of 300,000 events. The main poles are indexed by red color on the hit map. The schematic representation of the image compression factor ( $\xi$ ) as a function of the angle between the major crystallographic planes ( $\theta_{crys}$ ) and the corresponding angle between the indexed poles on the desorption image. The figure is reproduced from the references [83] and [163].

Following this protocol, for small angles, the image compression factor can be written as the ratio of the angle between the major crystallographic planes  $\theta_{crys}$  and the angle between the observed poles  $\theta_{obs}$ , calculated using the equation 4.16.

$$\xi \approx \frac{\theta}{\theta'} \approx \frac{\theta_{crys}}{\theta_{obs}} \quad 4.17$$

For instance,  $\xi=1$  corresponds to the zero compression or radial projection and  $\xi = 2$  corresponds to stereographic projection. The exact value of image compression factor varies for each APT measurement in a range typically between 1.3 to 2. The image compression factor mainly depends on the distribution of electric field lines between the specimen and detector (or local electrode). Hence, any parameter which influences the electrostatic environment around the tip, can potentially impact the compression of ion trajectories. Similar to the field factor  $k_f$ , parameters like shank angle, shape of the specimen and the entire electrostatic environment of the tool chamber are reported to have a direct impact on  $\xi$  [83]. This makes image compression factor ( $\xi$ ) and field factor ( $k_f$ ) two inherently correlated parameters. An empirical dependency of these two parameters have been numerically predicted in literature [164], [151] and a power law relation has been suggested as the following:

$$k_f = C\xi^3 \quad 4.18$$

where  $C$  is a coefficient of the fit which is reported to be equal 1 in [164] or a function of applied voltage [151]. It is worth mentioning that there is no physical explanation for such a power law dependence, which mainly arises from the lack of any analytical expression for  $\xi$  as a function tip geometry. The validity of such a dependency, Equation 4.18, has been assessed both experimentally and numerically for various tip shapes by several authors. For instance, finite element simulation of a metallic specimen with truncated hemispheric tip shape indicated a strong dependency of both  $k_f$  and  $\xi$  on the variation of shank angle and

specimen-to-detector distance [164], in which the power law relation between  $k_f$  and  $\xi$  (Equation 4.18) has been reported to remain valid for various combination of shank angles and specimen-to-detector distances (Figure 50a). The variation of both  $k_f$  and  $\xi$  as a function of radius of curvature has been also experimentally investigated for Al alloys [165] and the experimentally observed dependency between  $k_f$  and  $\xi$  was compared with the previously predicted power law (Equation 4.18) and the results are reported in Figure 50b [85].

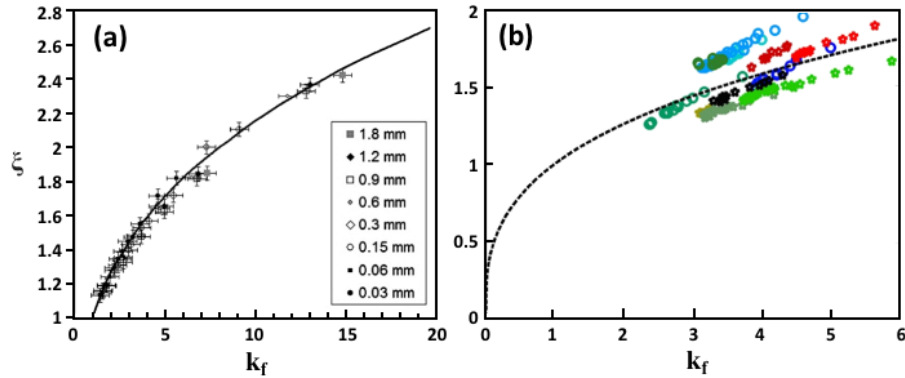


Figure 50: Relation between image compression factor ( $\xi$ ) and field factor ( $k_f$ ). (a) numerically obtained trend by finite element analysis of a hemispheric tip shape with different shank angles (1 to 30 degrees) and specimen-to-detector distances (0.03 to 1.8 m) [164]. (b) Experimental observation of the relation between  $\xi$  and  $k_f$ , extracted from different measurements on Al alloys (different colors codes) for a range of radius of curvatures. The expected power law is also indicated with a dashed line. Reproduced from reference [165].

Although the experimentally observed dependency in reference [165] roughly follows the numerically predicted trend, the power law cannot accurately describe the experimental data. The author [165] attributed this discrepancy to the assumptions made during the FEA, including the absence of the bias at the entrance of the detector (no purely free-flight after the local electrode). A similar explanation is also made in reference [164], stating that LEAP chamber (after the local electrode) is not a zero-field region and  $\xi$  varies according to the specimen-detector bias voltages.

Another complication of the image compression factor is its small variation across the specimen surface. Although such a variation is known, traditionally in most simulations only the average  $\xi$  over a small angular distance from the tip axis was reported which leads to the misleading suggestion of a constant  $\xi$  over the tip surface. However, a finite element simulation of the electric field and image compression factor across the tip surface of a truncated hemispheric cap (with 60 nm tip radius and 10 degrees shank angle) clearly indicates the slight variation (3%) of  $\xi$  and  $k_f$  depending on angular distance from the specimen axis (launch angle  $\theta$ ) [151]. Furthermore, the predicted slope for the variation of  $\xi$  as a function of  $\theta$  is steeper for larger angles, which indicates a larger deviation of  $\xi$  for larger angles which were not reported in that study. The variation of  $\xi$  across the specimen surface (different launch angles) will be discussed further using our developed FEA in Section 4.6.1.

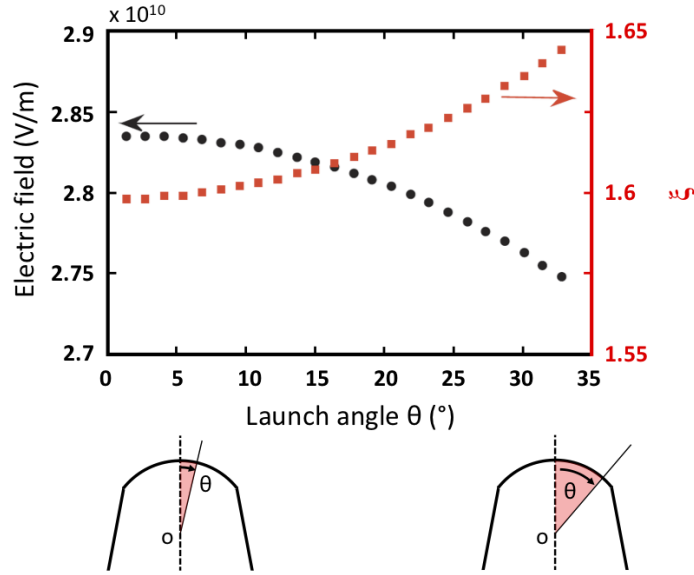


Figure 51: Variation of the magnitude of electric field and image compression factor ( $\xi$ ) as a function of launch angle  $\theta$  (angular distance from the specimen axis). The analysis was obtained by finite element simulation of a truncated hemispheric cap with 60 nm tip radius and 10° shank angle. Reproduced from reference [151].

Finally, considering the assumptions in the point-projection model the validity of the model is limited small angles with respect to the tip axis [166]. The validity range of point-projection model is discussed in more detail in the following section.

#### 4.2.2 Radial projection with angular compression

Similar to the point-projection model, radial projection with angular compression is another model to describe the trajectories of ions in APT. In this model, the distance between the crystallographic poles on the field desorption image (in meter) is directly related to the crystallographic plane directions on the specimen (in angle) as the follows [83]:

$$D = k_{\theta} \theta_{crys} \quad 4.19$$

where  $D$  is the distance between crystallographic poles on the field desorption image,  $\theta_{crys}$  is the angle between the major crystallographic planes (see Figure 49b) and  $k_{\theta}$  is a factor describing the compression of the ion trajectories. Similar to  $\xi$ , in the point-projection model,  $k_{\theta}$  depends on the electrostatic environment around the specimen.

For small angles ( $\theta_{crys}$ ) the two projection models yield a quite similar results, while for larger angles the radial projection with angular compression is known to more accurately describe the desorption image in field-ion microscopy [167], [168]. The validity of the two projection models to describe the desorption image of pure Al has been compared in reference [4] for a wide range of angles and the results are reported in Figure 52. As can be seen, the radial projection with angular compression model more accurately fitted the experimental data points for

the entire range of launch angles with a linear function expressed by  $k_\theta$  (see Equation 4.19). Vice versa the point-projection model was unable to describe this linear trend and has a relatively high error for wider angles ( $\theta > 30^\circ$ ). This is compatible with the previously described variation of  $\xi$  over different launch angles  $\theta$  (Figure 51), which states that the point-projection with a constant  $\xi$  is unable to accurately describe the projection of ions for a wide range of launch angles (non-linear behavior).

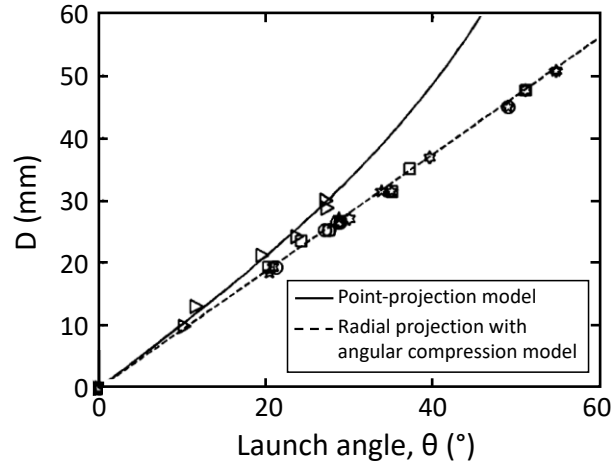


Figure 52: The accuracy of radial projection with angular compression model versus point-projection model to describe the projection of ions and formation of desorption map for pure Al. The distance between the poles on the desorption map ( $D$ ) is plotted against the crystallographic angles on the specimen (planes direction) in degrees. The markers are the angular distances of the poles from the origin of the projection, while the radial projection with angular compression model is plotted in dash line and point-projection in solid line. Reproduced from reference [83].

Although the radial projection with angular compression model more accurately describes the desorption image, it is not currently used in most the state-of-the-art APT data reconstruction protocols. Indeed, most reconstruction protocols are based on the point-projection model which was originally developed for small-angle-FOV APT. The need to reconsider the existing projection model for wide FOV atom probes is highlighted in the literature [83]. This issue could be even more pronounced in the case of future instruments with wider or even full FOV. This will be discussed further in Section 4.6.3.

### 4.3 Image magnification

Image magnification  $M$  in APT is defined as the ratio between the distance of two arbitrary features on the specimen surface ( $d$ ) and the projected distance of the corresponding image on the detector ( $D$ ). By considering the dimension of the specimen (diameter  $\sim 100$  nm) and the detector diameter ( $\sim 80$  mm), a magnification in order of  $10^6$  is typically expected in atom probe microscopy. In the point-projection model, by assuming that the radius of the hemispheric cap is negligible with respect to the specimen-to-detector distance ( $L$ ), the image magnification can be written as a function of  $\xi$ :

$$M = \frac{D}{d} \approx \frac{L}{\xi R} \quad 4.20$$

For radial projection with angular compression model, the magnification can be calculated as a function of  $k_\theta$ :

$$M = \frac{D}{d} = \frac{D}{R\theta} = \frac{k_\theta}{R} \quad 4.21$$

Regardless of the choice of the projection model, the magnification in APT has an inverse relation with respect to the tip radius  $R$ . This implies that usually the magnification decreases as a function of depth in view of the shank angle which causes a variation of  $R$  as a function of depth.

## 4.4 3D data reconstruction

Generally, data analysis in APT includes several steps, including correction of the time of flight (ToF), the extraction and calibration of the mass spectrum and finally the 3D reconstruction of the data. The output of the APT measurement is usually a data set containing the raw data and some experimental conditions used during the measurement. This raw data is generally an array containing many rows, being sequences of the detected events, and some columns mainly including the X and Y position of the ion impact on the detector, the mass to charge ratio (Da), the time of flight and the voltage (V).

The 3D reconstruction is the reverse projection of the 2D detected events to a 3D volume corresponding to the original volume of the specimen (within the FOV), by extracting the third dimension (depth position) from the sequences of the detected ions and other parameters. In this context, data reconstruction has two main steps, which starts from the reverse projection of the lateral position of ions on the specimen surface and the calculation of the depth coordinate. To do so there are several reconstruction protocols, e.g. the Bas et al protocol [14], which typically share some common main assumptions and hypotheses. For instance, they mainly rely on the ordered sequence of evaporation meaning that ions are assumed to be evaporated layer-by-layer from outer shell toward the center (negligible field penetration depth). Some other assumptions include [83]: a point-projection with constant image compression factor for all the ions, the specimen is cylindrically symmetric with a hemispheric cap, a similar evaporation field exists for all the ions and a similar atomic volume for the entire specimen (not suitable for some irregular heterogeneous systems). In this thesis, the Bas reconstruction protocol [14] is briefly described.

### 4.4.1 Bas reconstruction protocol

The Bas et. al. reconstruction protocol [14] is based on the point-projection model, following the aforementioned assumptions. i.e. ordered sequence of evaporation and the reverse projection of lateral position of ions on the specimen surface can be derived using the magnification and the impact position on the detector. The image magnification in Equation 4.20 can be simplified as [83]:

$$M_i = \frac{D_i}{d_i} \approx \frac{L}{\xi R_i} \quad 4.22$$

where,  $M_i$  is the local magnification,  $D_i$  is the impact position on the detector and  $d_i$  is the ion distance on the specimen for the  $i^{\text{th}}$  detected event. Similarly, the in-plane component of the ion position ( $x_i$  and  $y_i$ ) for the  $i^{\text{th}}$  evaporated ion on the specimen surface can be written using the  $X_{Di}$  and  $Y_{Di}$  impact position on the detector and the local magnification ( $M_i$ ):

$$x_i = \frac{X_{Di}}{M_i} \quad \text{and} \quad y_i = \frac{Y_{Di}}{M_i} \quad 4.23$$

The depth extraction ( $dz$ ) is based on the evaporated volume within the FOV ( $V_{\text{evap}}$ ) which is expressed as:

$$V_{\text{evap}} = \int_0^{z_{\text{max}}} S_a(z) dz \quad 4.24$$

where,  $S_a$  is the analyzed area of the specimen surface lying within the FOV. This parameter can be also expressed using the average atomic volume  $\Omega$  as follows:

$$S_a = \frac{n_{\text{evap}}}{\eta} \Omega \quad 4.25$$

where  $n_{\text{evap}}$  is the number evaporated atoms lying in the FOV,  $\eta$  is the detection efficiency and  $\Omega$  is the average atomic volume.  $S_a$  can also be written as a function of specimen radius. Since the tip radius increases with the specimen depth ( $z$ ), according to the specimen shank angle, the variation of the tip radius needs to be determined. In the original Bas protocol, the local tip radius is determined using the instant specimen voltage at the detected event, while the tip radius can be generally determined by assuming a fix shank angle  $\beta$  or even using the tip image from electron microscopy (SEM/TEM). These three techniques for the determination of tip radius evolution along the specimen depth are briefly summarized in Table 7.

Table 7: Comparison between different currently available techniques for the determination of specimen radius along the specimen depth. Please note that for all the three techniques the specimen shape is assumed to remain a truncated cone terminated by a hemispherical cap throughout the analysis.

	Voltage curve	Shank angle	Tip image
<b>Required inputs</b>	- Voltage evolution (V) - Field evaporation ( $F_{evap}$ ) - Field factor ( $k_f$ )	- Initial tip radius ( $R_0$ ) - Shank angle ( $\beta$ )	- SEM/TEM image of the specimen
<b>Function</b>	$R = \frac{V}{k_f F_{evap}}$	$R = R_0 + \frac{\sin(\beta)}{1 - \sin(\beta)} z$	- R(z) is extracted based on the tip image using the pixel size
<b>Pros</b>	- Possibility to define variable shank angles - Easy (no need to tip imaging)	- Can be extracted from FIM (no need to tip imaging)	- Possibility to define variable shank angles - based on the tip image
<b>Cons</b>	- Relies on the knowledge of $k_f$ and $F_{evap}$ - Same $F_{evap}$ for the entire specimen: not suitable for multilayers and 3D heterogeneous structures	- $R_0$ is needed - A fix shank angle is assumed at different depths	- Tip imaging is needed - limited resolution of the image

In the Bas protocol, by assuming the launch angle to be small, the analysis area  $S_a$  is first considered to be a plane tangent to the specimen, instead of real tip curvature (see Figure 53). To account for the hemispherical tip curvature, instead of the assumed tangent plane, a correction term will be introduced later.

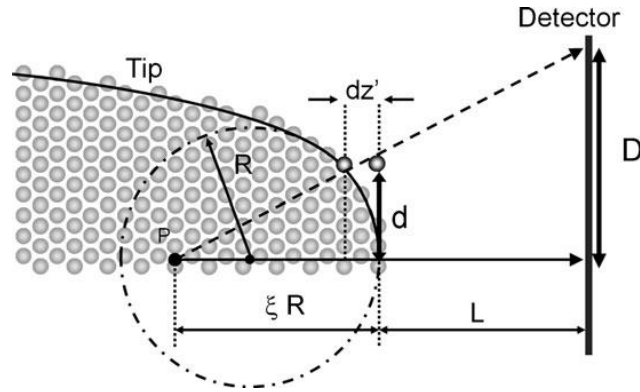


Figure 53: Schematic representation of the correction factor to account for tip curvature instead of the tangent plane. Reported from reference [83].

Then  $S_a$  is expressed as a function of local magnification  $M_i$  and the detector area  $S_D$ :

$$S_a = \frac{S_D}{M_i^2} \quad 4.26$$

Finally, by combining the Equations 4.25 and 4.26 one can derive the depth increment as the function of applied voltage:

$$dz = \frac{\Omega L^2 k_f^2 F_{evap}^2}{\eta S_D \xi^2 V^2} \quad 4.27$$

where,  $\Omega$  is the average atomic volume,  $L$  is the specimen-to-detector distance,  $k_f$  is field factor,  $F_{\text{evap}}$  is the field evaporation of the specimen main element,  $\eta$  is the detection efficiency,  $S_D$  is detector area,  $\xi$  is image compression factor and  $V$  is the applied voltage. To account for the hemispherical tip curvature, instead of the assumed tangent plane, a correction factor  $dz'$  to be added into the depth increment can be calculated based on simple triangle similarity rules (Figure 53):

$$dz' = R_i \left( 1 - \sqrt{1 - \frac{x_i^2 + y_i^2}{R_i^2}} \right) \quad 4.28$$

Finally, the reconstructed  $z$  position for  $i^{\text{th}}$  ion is calculated by accumulating  $dz$  as the follows:

$$z_i = \left( \sum_1^i dz \right) + dz'_i \quad 4.29$$

More precise data reconstruction protocols have been proposed by Geiser [169] and Gault [157]. The main difference between the reconstruction protocols is the derivation of the depth increment ( $dz$ ). For instance, the protocol proposed by Gault [157] is not based on the assumption of small launch angle and instead the Equation 4.13 is directly employed for the calculation of launch angle and used for the data reconstruction. Currently, there are many commercially available software packages (i.e. IVAS, TAP3D) for 3D data reconstruction and analysis which work based on the available protocols.

There are several reconstruction parameters (i.e. detection efficiency) which are commonly used by all the reconstruction protocols, in which the accuracy of the final 3D reconstructed data is essentially determined by the degree of knowledge and its accuracy in defining such parameters. In the next section, the reconstruction parameters together with the currently available techniques to derive and calibrate them will be discussed.

#### 4.4.2 Calibration of reconstruction parameters

In general, to 3D reconstruct the APT data a set of main reconstruction parameters are required whereby some are the user defined parameters and some are instrumental parameters and have a fixed value:

- Image compression factor ( $\xi$ )
- Detection efficiency ( $\eta$ )
- Specimen radius along the depth ( $R$ )
- Atomic volume of the specimen (material property)
- Depending on the reconstruction/calibration protocol other parameters may also be needed, such as: applied voltage, field factor  $k_f$ , evaporation field of the material  $F_{\text{evap}}$  (for voltage-based reconstruction), SEM/TEM

image of the specimen (for specimen shape reconstruction) and shank angle.

Obviously, the accuracy of the reconstructed data is determined by the degree of knowledge and accuracy in defining the aforementioned reconstruction parameters, as well as by the validity of the hypotheses and assumptions made in the reconstruction protocol. Even small variations in some of the reconstruction parameters (i.e.  $\xi$  and  $k_f$ ) may result in a significant drift in the 3D reconstructed shape (radius and height). In this section, several techniques to derive and calibrate the reconstruction parameters are discussed:

**Image compression factor ( $\xi$ ):** Currently there are several available techniques to calibrate  $\xi$  using crystallographic direction or nanostructural features within the reconstructed volume (i.e. known layer thicknesses, position/size of certain features, flatness of the interface, etc). The calibration of  $\xi$  using crystallographic direction can be done either by Field Ion Microscopy (FIM) prior to the APT measurement or directly from the desorption image. Then the distance  $D$  between the poles can be used for the calculation of the observed angle  $\theta_{obs}$  on the desorption map using Equation 4.16. Finally, by knowing the theoretical angle  $\theta_{crys}$ ,  $\xi$  can be calculated from the Equation 4.17 ( $\xi \approx \frac{\theta_{crys}}{\theta_{obs}}$ ). Obviously, this approach is only applicable to crystalline materials with a certain crystalline direction, such that more than one pole structure is within the FOV (i.e. Aluminum 111). As mentioned earlier,  $\xi$  can be calibrated also by using a nanostructural feature within the analysis volume. However, the use of nanostructural features may require additional information (i.e. layer thickness) from a complementary technique such as TEM or SIMS. In this approach, the user fine tune the value of  $\xi$  to reach the known dimension and/or shape of the feature in the reconstructed tomogram (i.e. layer thickness, flatness of the interface). Hence, the calibrated value of  $\xi$  relies on the degree of knowledge on the feature dimension and/or shape and it is less accurate with respect to the previous technique.

**Detection efficiency ( $\eta$ ):** this parameter is mainly a characteristic of an instrument and stands for the capability of the detection system to detect all the ions within the FOV and ranges from  $\sim 30$  to  $80\%$ . This parameter is mainly determined by ion incident angle and the open-pore area of the micro channel plate (MCP) [148]. In practice, the detection efficiency is calibrated once during the maintenance/calibration of the instrument and the obtained value is used for the data reconstruction of other measurements. Any deviation of this parameter from the actual value leads to an underestimation or overestimation of the reconstruction volume (Equation 4.27). Different techniques have been suggested to derive or estimate the detection efficiency. For instance B. Gault proposed a method to extract the detection efficiency based on the crystallographic directions [163]. In this method, the interplanar spacing ( $dz$ ) is first obtained by tuning other

reconstruction parameters ( $\xi$  and  $k_f$ ). Then the value of  $\eta$  can be fine-tuned, while  $dz$  is kept constant by adjusting  $k_f$  simultaneously,  $dz \sim F_e^2 k_f^2 / \eta \xi^2$ , (see Equation 4.27) to match the reconstructed angle between crystallographic directions to the theoretical value. The estimation of detection efficiency using the current available techniques, relies on the knowledge of at least another reconstruction parameter (i.e.  $\xi$ ). This may lead to the propagation of additional errors in the estimated value of the detection efficiency. Furthermore, using the current available methods, calculation of the associated uncertainty for the detection efficiency is not available.

**Specimen radius at different depths (R):** as previously described in Table 7, there are three main methods to determine the specimen radius  $R$  along the specimen depths (voltage curve, shank angle and tip image). The pros and cons of each method have been also summarized in the same table. For the shank angle method, the user should define a fixed shank angle for the entire depth of the specimen. The shank angle can be calculated using the FIM images at two different depths of the specimen as the following. The specimen radius  $R$  can be calculated from the ring pattern formed in the FIM image and by knowing the distance between the atomic planes for the indexed crystallographic direction [170]. Then, by calculating  $R$  at two different depths, one can calculate the shank angle and assume it to be constant for the entire specimen depth. The shank angle can be similarly calculated using the desorption map and the ring patterns around the main pole:

$$R = \frac{nd}{(1 - \cos(\theta))} \quad 4.30$$

where,  $\theta$  is the angular distance between two poles,  $n$  is the number of rings between the poles and  $d$  is the interplanar spacing. Then, by calculating  $R$  at two different depths, one can calculate the shank angle and assume it to be constant along the entire specimen depth. In case of the tip imaging method, the uncertainty of the radius extracted is mainly defined by the pixel size and the resolution of the image. Finally, the evaluation of tip radius from the voltage curve is usually done from the Equation 4.5, where the accurate knowledge about both electric field  $F$  and the field factor  $k_f$  is required. The electric field can be estimated from the Kingham curve and the procedure to calibrate  $k_f$  is described in the next paragraph.

**Field factor ( $k_f$ ):** this parameter is not among the main reconstruction parameters and it is only needed when the voltage curve method is used for extracting radius evolution along the tip depth.  $k_f$  can be determined based on the FIM image and using Equation 4.5 ( $F = \frac{V}{k_f R}$ ). Hence, to calibrate  $k_f$  using this equation the radius  $R$  and the electric field  $F$  are needed to be calibrated first following one the aforementioned techniques.

To conclude, by using the combination of aforementioned calibration techniques, it is possible to calibrate all the required reconstruction parameters and proceed with the 3D data reconstruction. The accurate calibration of all the reconstruction parameters may become challenging in some analyses. By my knowledge there is no metrological approach available at the moment to calibrate all the reconstruction parameters accurately without relying on certain assumptions. Obviously, none of the available techniques can provide the uncertainty or even its estimation for all main reconstruction parameters.

In the next section the deviation of 3D reconstructed data from the original structure of the specimen will be discussed and different sources for this possible mismatch will be introduced.

### 4.4.3 Common artefacts and lateral resolution

Any discrepancy between the reconstructed data and the original structure of the specimen is considered as a measurement artefact. The artefacts can be divided into two main categories: imperfection of reconstruction protocols, deviation of ion trajectories from the theoretical one and modification of the atom arrangement within the sample prior to the evaporation. The current state of reconstruction protocol and their assumptions have been discussed in the previous section and we will mainly discuss the other types of artefacts. The errors in the APT analysis can be induced by many physical mechanisms, including surface diffusion, thermal velocity, rolling-up effect and trajectory aberration (see Figure 54). These mechanisms are schematically shown in Figure 54 and they are briefly described [82]:

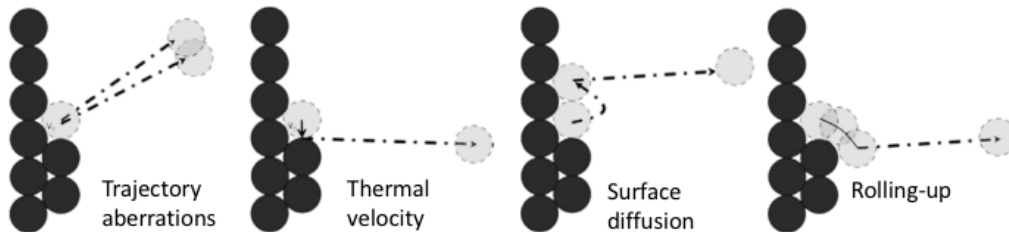


Figure 54: Schematic representation of some common artefacts which degrade the lateral resolution of APT analysis. Reproduced from reference [82].

**Trajectory aberration:** the local distribution of electric field lines in the vicinity of the specimen surface defines the ion trajectories. When the actual distribution of the field deviates from the one assumed in the reconstruction protocol (e.g. the field distribution for a perfectly smooth hemispherical apex shape), the actual ion trajectory will deviate from the expected one. Hence the procedure applied during the reconstruction will reposition the atom incorrectly as this deviation from the ideal field distribution is not taken into account. We use the term trajectory aberration to indicate this discrepancy which will result in a loss of lateral resolution. The trajectory aberration usually appears in the form of high and low density zones on the detector hit map, which finally transforms into high and low atomic density zones in the reconstructed volume respectively.

In case of a pure crystalline specimen (single evaporation field), by operating at low temperature the sequences of evaporation are mainly determined by the arrangement of atoms on the apex surface according to the crystallographic structure (ordered evaporation). While when operating at high temperature, the order of evaporation may be perturbed and atoms can evaporate from two successive layers at the same time (on the same lateral site). Such a mechanism causes a local variation in the electrostatic environment (in sub-nanometer scale) and results in trajectory aberration and a slight reduction in both lateral and depth resolution [171].

A similar scenario exists for specimens composed of more than one species (diluted system), where the sequences of evaporation are governed by both field evaporation and atomic roughness. In this case, the preferential evaporation or retention of the solute (or dopant) with respect to the main matrix can modify the local curvature and the corresponding field distribution which finally leads to trajectory aberration [161].

For heterogeneous systems, where the regions are composed of species with different evaporation fields (i.e. multilayers, Fin embedded in an oxide, etc), the tip shape will be strongly affected by the preferential evaporation of the zones consisting of low field species. As an example, for thin multi-layer systems or at the interface between thick layers, the apex surface typically consists of atoms belonging to more than one layer. By considering the differences in the evaporation fields and the related evaporation probabilities, the tip shape deviates from its initial shape and a sort of topography may develop at the apex surface. For instance, the evaluation of tip shape through the analysis of metallic multi-layer system has been studied in the literature [172] and the simulated results together with TEM image after APT measurement are reported in Figure 55. As can be seen, a strong variation of tip shape along the analysis depth was predicted (from Figure 55b to Figure 55i). In addition, there is a significant variation of local curvature across the apex surface at each sequence of evaporation (Figure 55c to i).

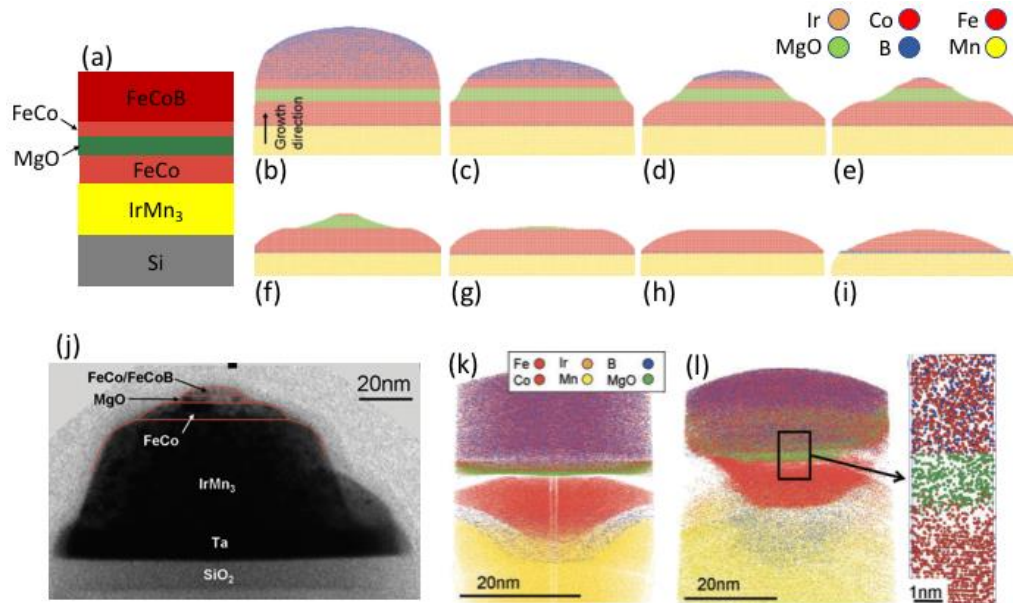


Figure 55: Evolution of tip shape for a metallic multi-layer system consisting of species with different evaporation field. (a) Schematic representation of the layers. (b) to (i) evolution of tip shape for different sequences of evaporation obtained by finite element simulation. (j) TEM image of the specimen apex shape after several sequences of evaporation. Different radii of curvature have been induced due to the differences in the field evaporation of the layers. (k) 3D reconstructed volume from the simulated data, whereby a considerable distortion is predicted due to the induced artefacts by trajectory aberration. (l) 3D reconstructed volume obtained from the APT measurement, whereby similar to the predicted shape the trajectory aberration caused an artefact in the reconstructed volume. The inset shows atomic plains in the FeCo layer. Reproduced from reference [172].

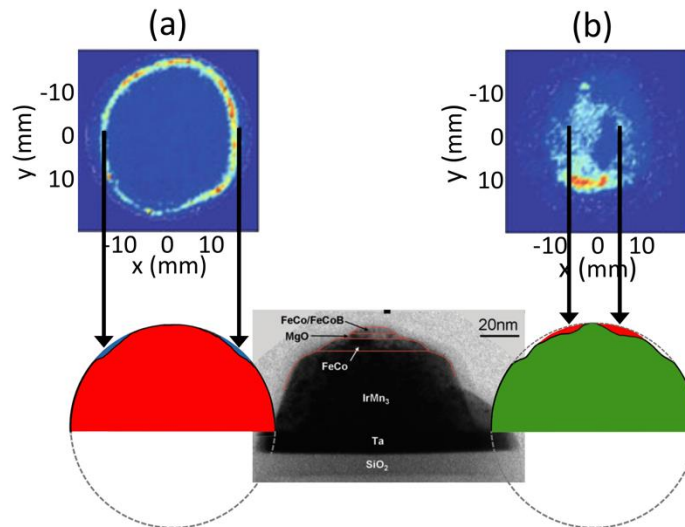


Figure 56: (a), (b) Trajectory aberration and formation of zones with high and low density on the desorption map for the same multilayer system reported in the Figure 55. (a) The position of the dense ring on the desorption map, is assigned to the local dips on the tip shape. The TEM image of the tip shape is also reported. Each desorption map contains 10,000 events. Reproduced from reference [83].

This variation of local curvature (originated from different evaporation field species) causes a trajectory aberration which appears as a strong artefact on the 3D reconstructed data (see Figure 55k and l), such the reconstructed volume can deviate substantially from the original shape of the specimen. In addition, as it was mentioned earlier, this local variation in the radius of curvature can induce zones with high and low densities on the desorption map as a result of trajectory aberration. This effect is shown for the previously discussed multilayers system

(Figure 55) in Figure 56. The local distortions in the apex shape (corresponding to the interfaces between two layers) appear as a dense ring on the hit map. We observed a similar pattern (dense ring) on the desorption map, corresponding to the interface between crystalline and amorphous SiGe, which will be discussed in Section 4.5.2.

**Thermal velocity:** Atoms at the apex surface vibrate with a velocity which depends on the thermal agitation energy. By considering the Maxwell distribution of velocity, the average kinetic energy for an atom at temperature  $T$  is equal to  $3k_B T/2$  and the average transverse velocity ( $V_t$ ) is  $\sqrt{\frac{k_B T}{m}}$ , where  $m$  is the atomic mass and  $k_B$  is the Boltzmann constant. This velocity is the initial velocity of the atom before field evaporation from the specimen apex. For most materials at cryogenic temperature ( $20 < T < 70$  K),  $V_t$  is in a range of 40 to 200 m/s [82], which is not considered within the current reconstruction protocols. The lateral displacement ( $\Delta L$ ), on the detector induced by the thermal velocity  $V_t$  can be estimated as  $\Delta L \approx V_t t_{\text{flight}}$ , where  $t_{\text{flight}}$  is the time of flight. This displacement can potentially degrade the lateral resolution of the reconstructed volume and blurs the FIM image [173]. By considering the image magnification, a lateral displacement corresponding to  $1 \text{ \AA}$  on the apex has been reported for Aluminum.

**Surface diffusion:** in the absence of an electric field, adatoms on the specimen surface can migrate from one atomic position to another neighbor position by a thermally activated process called random walk [174]. The surface atoms can also undergo surface migration at sufficient thermal energy. In the presence of a large applied potential, surface atoms become polarized under the strong electric field gradients at the specimen surface, which can be described by a local enhancement factor  $\gamma$  (see Section 4.1.1). This is similar to the quantum description of the charge concentration at the protruding atoms, which induces a strong Maxwell stress on the surface atoms and finally facilitates the diffusion process. In this context, in the presence of electric field, surface migration is not a random walk process (only thermally driven) but instead atoms preferentially migrate towards the region with higher concentrated charges (high electric field). This process is known as directional walk (both thermally and field driven) [175]. Since field evaporation and surface diffusion are both a thermally activated process, there is a sort of competition between these two processes to occur on the surface atoms before their evaporation [90]. The probability that surface atoms experience a diffusion process before their removal depends on the surface diffusion barrier ( $Q_{\text{jump}}$ ), the evaporation energy barrier ( $Q_b$ ) and the residence time of atoms on the surface. The latter mainly depends on the evaporation rate and the surface area of the specimen apex. By considering the Arrhenius law, the residence time for diffusion ( $t_{\text{dif}}$ ) can be written as  $t_{\text{dif}} \sim \frac{1}{\nu_0} \exp\left(\frac{Q_{\text{jump}}}{k_B T}\right)$ , where  $\nu_0$  is the vibration frequency of atoms and  $k_B$  is the Boltzmann constant. A similar expression can be written for the evaporation residence time ( $t_{\text{evap}}$ ) as

$t_{\text{evap}} \sim \frac{1}{\nu_0} \exp\left(\frac{Q_b}{k_B T}\right)$ . Finally, the ratio between the residence times can be written as  $\frac{t_{\text{evap}}}{t_{\text{dif}}} \approx \exp\left(\frac{Q_b - Q_{\text{jump}}}{k_B T}\right)$ . In voltage mode, typically the evaporation barrier height is small for normal evaporation rates ( $Q_b < 0.1$  eV), while the barrier height for surface diffusion is reported to be much higher for most materials ( $0.15 < Q_{\text{jump}} < 1.1$  eV) [176]. Hence, the ration of  $t_{\text{evap}}/t_{\text{dif}}$  in voltage mode at cryogenic temperature is very small ( $< 0.001$ ), which implies that evaporation process occurs much quicker than surface diffusion. Hence in voltage mode, the influence of surface diffusion is negligible, unless the analysis temperature becomes high (i.e.  $T > 200$  K) or the diffusion barrier  $Q_{\text{jump}}$  is very small [82]. In laser mode, the apex temperature during the evaporation is considerably higher, while the duration of this high temperature region is very short following the short laser pulse duration. Hence, only high laser energy results in significant surface diffusion [82]. In diluted alloys, some solutes (i.e. N, P and C) were observed to be more prone to surface migration toward the defined crystallographic direction, while the diffusion of the main matrix was reported to be negligible [177], [178]. The actual behavior of such a directional diffusion is not well understood at the moment.

**Rolling-up:** This type of artefact is observed mainly near the edges of atomic terraces. Rolling-up describes a mechanism for evaporation of surface atoms in which a surface atom instead of evaporating from its original position, first experiences a short-range migration by rolling around one of the neighbor atoms by means of diffusion (i.e. from the kink site to the top of step edge). Then, the atom escapes from the new position, where the field is sufficiently high to field evaporate the migrated atom [179] (see Figure 54). This effect can cause small distortions in the desorption map and reduces the lateral resolution of the analysis.

All these mechanisms can potentially cause measurement artefacts, some of which can be minimized or even eliminated by adopting the proper experimental conditions during the APT measurement (i.e. base temperature, laser power and detection rate). However, measurement artefacts cannot be avoided in case of specimens, consisting of regions with different evaporation fields. Indeed, due to the preferential evaporation of the zones consisting of low field species, the tip shape deviates (even locally) from the initial hemispheric shape which affects the lateral resolution and the 3D reconstruction volume due to the trajectory aberrations and the lack of the reconstruction protocol to deal with a non-hemispherical tip shape. Some of the induced measurement artefacts can be improved later by post processing, (i.e. by artificially changing the reconstructed volume), which requires an accurate knowledge on the 3D distribution of these regions in the specimen volume using other complementary techniques (i.e. TEM imaging) in addition to the development of proper protocol to modify the reconstructed volume [13].

## 4.5 Field-of-view (FOV)

In atom probe microscopy, or traditional ion microscopy, only a part of the specimen volume (typically core central region) can be analyzed. Typically, only the ions evaporated from the core central volume of the specimen can reach the detector, while the trajectory of ions evaporated from outer shell of the specimen (including side wall) are laterally extended as such that they cannot hit the limited size of the detector. Then field-of-view (FOV) is commonly defined as an area of the apex surface from which the evaporated ions can reach the detector. F. Vurpillot defined the FOV as “the maximum size of an object than can be observed in AP.” [82]. The representation of FOV in field ion microscopy is depicted in Figure 57, where only the central area of the apex surface marked by an orange dashed line (Figure 57a) , was projected on the detector (Figure 57b).

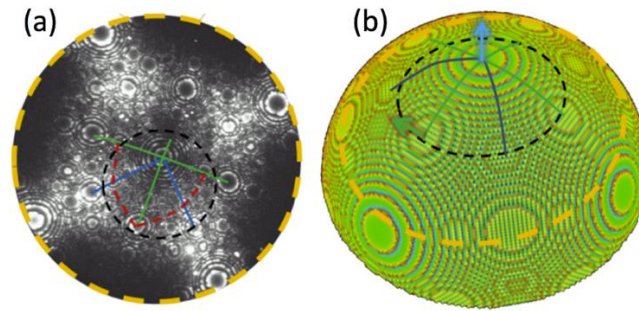


Figure 57: Representation of field-of-view (FOV) in atom probe microscopy for Al (face centered cubic lattice). (a) Desorption image of the surface atoms measured in field ion microscopy. (b) 3D representation of surface atoms for FCC lattice of Al. FOV is depicted with orange dash line, crystallographic directions are indicated by green  $\langle 011 \rangle$  and blue  $\langle 002 \rangle$  arrays and finally zones axis are indicated by solid lines, following the color code of crystallographic directions. Reproduced from reference [82].

FOV plays an important role in many aspects of APT analysis. For instance, it has a major role in 3D data reconstruction, in which without the accurate knowledge on FOV, or equivalently the dimension of the probed volume, a severe compression/extension may appear on the 3D reconstructed volume. In addition, the identification of FOV is crucial for APT analysis of 3D devices where the localized variation of composition is intended to be probed across the specimen apex. Moreover, an accurate knowledge of FOV is essential for many fundamental studies, including laser tip interaction.

FOV is mainly determined by the solid-angle-of-detector together with the ion trajectories. Hence, this parameter depends on both specimen and tool parameters. The schematic representation of FOV versus solid-angle-of-detector is shown in Figure 58. The solid-angle-of-detector ( $\alpha$ ) is defined based on the detector diameter ( $D_{det}$ ) and the distance between the specimen to the detector ( $L$ ):

$$\tan(\alpha) = \frac{D_{det}}{2(L + \xi R)} \approx \frac{D_{det}}{2L} \quad 4.31$$

According to the definition of the solid-angle-of-detector, this parameter only depends on the tool parameters (design of the APT instrument or specimen alignment). Please note that the presence of the local electrode only impacts the

ion trajectories (and thus the FOV) and it has nothing to do with the solid-angle-of-detector.

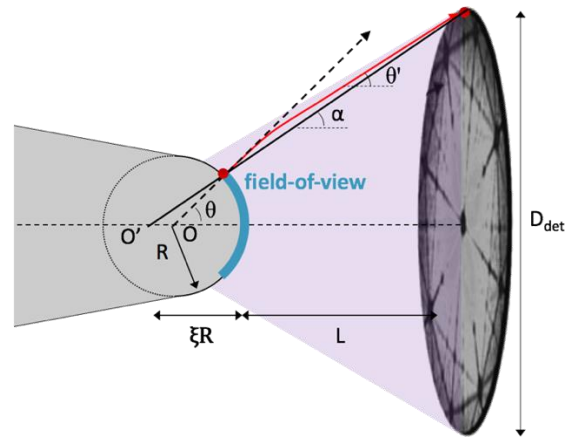


Figure 58: Schematic comparison between field-of-view (FOV) and solid-angle-of-detector for a hemispheric apex shape. The trajectory of the last ion within the FOV is schematically represented in red. The corresponding image compression factor ( $\xi$ ) is also depicted.

For a given APT tool, the FOV varies from specimen to specimen according to the distribution of the ion trajectories. For instance, if the ion trajectories are further compressed toward the specimen axis, a larger area of the apex surface would be detected leading to a larger FOV. Hence, the accurate knowledge on the distribution of ion trajectories is an essential step towards the prediction of FOV. As discussed in Section 4.2, the ion trajectories can be either estimated by numerical simulation (i.e. finite element analysis) or described by a compression factor (i.e.  $\xi$  in point projection model) based on an existing projection model, whereby the value of the compression factor needs to be experimentally determined during the APT analysis.

As discussed earlier in Section 4.4.3, any deviation of the apex shape from an atomically smooth hemispherical shape results in trajectory aberrations and deviation of the ion trajectories from what is described by the reconstruction protocols. Thin multi-layer systems have been introduced as an example in which the apex shape typically deviates from the hemispherical shape through the APT analysis. The observed reconstruction artefacts, due to the trajectory aberration were also discussed for such a heterogeneous system.

A modification of ion trajectories as a result of a strong variation in the apex shape (or local curvature), may potentially affect FOV by projecting a part of trajectories, which are expected to be in FOV, out of the detector window or vice versa. Such potential variation in the FOV, due to the deviation of apex shape from smooth hemispheric shape, has not yet been well studied in the literature.

The experimental investigation of the FOV for non-hemispherical tip shapes is typically challenging as the reconstruction protocols fail to accurately determine the actual probed region of specimen volume. On the other hand, to numerically investigate the FOV in APT, one has to simulate the electric field distribution in the entire APT chamber (actual dimensions) and compute the trajectory of each individual atom accordingly and finally reconstruct back the data using one of the available reconstruction protocols. Obviously, such an analysis requires a

massive computational power. Traditionally to reduce such demanding computations, in most numerical studies of the data reconstruction the detector was assumed to have a hemispherical shape (around the tip) and the specimen-to-detector distance was assumed much smaller than the actual distance [84], [180]. Such a configuration does not allow accurate study of the FOV and the numerical analysis must be performed on the real dimensions.

In this project we have experimentally investigated the FOV for one specific example of a non-hemispheric tip shape whereby the asymmetric tip shape is induced by high power UV laser. In the next sections, the state-of-the-art understanding of FOV together with my contribution to this understanding will be discussed for hemispherical tip shapes and the asymmetric tip shapes induced by UV laser.

#### 4.5.1 Field-of-view for hemispherical tip shape

As discussed in Section 3.5, the apex of a tip for metallic or semiconductor materials made of a pure element (or diluted systems) typically has a hemispherical shape after APT analysis in voltage mode or laser mode using IR and Green wavelength. While for the UV laser, a degree of asymmetry, depending on the choice of laser power, is commonly observed where the illuminated side of the specimen is typically more flattened versus the shadow side. In this section the FOV for hemispherical tip shape is described in detail.

For a hemispherical tip shape, the field enhancement at the tip apex was shown to be uniform across the apex (in mesoscale) and can be estimated using the field factor  $k_f$ . The ion trajectories can be also approximated by the point-projection model i.e. the ion trajectories are assumed to be straight lines instead of actual curved paths to their projection point is not located at the center of the hemisphere. The latter is described by the image compression factor ( $\xi$ ). As discussed in Section 4.2.1, this model has been experimentally assessed by many authors. The exact value of  $\xi$  does vary with specimen shape and needs to be experimentally determined for each analysis. The  $\xi$  can be calibrated using several techniques as discussed in Section 4.4.2.

Finally, by considering the limited detector area (or equivalently solid-angle-of-detector) and the values of  $\xi$  (typically from 1.3 to 2), only ions emitted from the core central region of the apex can reach the detector and the ions evaporated from the outer shell will hit the local electrode or the chamber walls. To calculate the FOV and determine the area of the specimen apex from which the evaporated ions can reach to the detector, the 3D reconstruction of APT data is required. Indeed, the 3D reconstructed volume includes  $\xi$ , the efficiency, the atomic density and the variation of the tip radius along the depth. This 3D-volume has the same shank angle as the original tip but its radius is smaller than that of the original specimen, corresponding to the FOV. Please note that the exact shank angle (not necessary constant along the specimen depth) can be only reconstructed if a high-resolution tip image was used for the calibration of the radius during the 3D data reconstruction, while other radius calibration techniques (voltage profile and

shank angle) are typically less accurate in reconstructing the exact tip shape. The detailed comparison between different calibration techniques has been discussed in Section 4.4.2. Hence, following an accurate reconstructed 3D volume, the FOV at each position in the specimen depth (z direction) can be determined by the diameter of the reconstructed data.

To conclude, the FOV for hemispherical tip shapes can be identified and calculated from the reconstructed 3D data, provided that the data reconstruction was carried out based on the calibrated reconstruction parameters. If the apex shape deviates from the hemispherical shape, the current reconstruction protocols are unable to accurately reconstruct and determine the exact FOV. In the next section, the FOV for the asymmetric tip shape induced by UV laser will be discussed in detail and we will see how the FOV can be shifted toward one side of the apex for such an asymmetric tip shape.

#### **4.5.2 Field-of-view for UV-induced asymmetric tip shape**

Currently, laser-assisted APT using UV wavelength is widely employed for the analysis of metallic and non-metallic specimens. Also the APT instrument used in this project, CAMECA LEAP 5000 XR, is based on a fixed laser source at UV wavelength. As discussed earlier, the UV laser pulse typically causes preferential evaporation on the laser illuminated side of the specimen apex and may consequently lead to a significant flattening of this region of the tip. Although this deviation from the hemispherical tip shape can be much reduced by adopting a low laser power during the APT analysis, the asymmetry in the apex shape (flattening) cannot be completely avoided mostly in case of some low field material (i.e. Ga and In).

The FOV for a such asymmetric tip shape is not well understood at the moment. For instance, Koelling S., et al. [128] experimentally observed a shift in the FOV toward the shadow side of the tip when switching the laser wavelength from green to UV laser. This was interpreted as a reshaping of the apex shape from a symmetric towards an asymmetrical one respectively. The author reported that the observed shift was reversible by switching back the laser from UV to green wavelength. However, they could not physically explain such an observed shift in the FOV and their predicted trend did not match their experimental data.

In this project, to understand the FOV in UV-assisted APT, we carried out a combined APT-TEM study on a bulk specimen prepared following a dedicated specimen preparation protocol. In particular, to accurately track the FOV in APT, a sort of marker in the specimen volume (i.e. local elemental contrast) is required. On the other hand, the presence of local elemental contrast in the specimen volume is known to impact the tip shape and cause trajectory aberration, due to the differences in the field evaporation of different elements. Hence, to track the FOV with a minimized difference in the local evaporation fields, we developed a new FIB based specimen sharpening protocol to induce a thick amorphized shell around the crystalline core of the prepared specimen for crystalline Si and SiGe wafers. The interface between the crystalline/amorphized core of the specimen

can then act as a marker to track the FOV in APT analysis. In this configuration both amorphized and crystalline phases consist of a similar element and a minor local variation in the apex shape was observed at the interface between different phases (small trajectory aberration), which will be discussed in more detail.

To induce a thick amorphized shell around the specimen volume, we have slightly modified the standard specimen sharpening protocol. In the developed protocol, the annular milling was stopped once tip diameter reached around 100 nm. Then instead of low Ga energy clean (5 or 2 keV), the specimen was bombarded with 30 keV Ga ion energy (without any pattern), until the tip reached a diameter of  $\sim 60$  nm. This procedure leads to the amorphization of approximately 30 nm thick layer of crystalline Si (and SiGe) all over the specimen diameter. A Si/SiGe crystalline (100) multi-layers system (see Figure 59a) was selected for the preparation of APT specimen in this study. This specific choice of multi layers system was made to use also the interfaces between the layers as an additional marker to track the FOV at the corresponding sequence of evaporation, which will be discussed further in this section.

The TEM image of one the specimens prepared with this protocol is reported in Figure 59b. As can be seen, the thickness of an amorphized shell remains approximately constant ( $\sim 30$  nm) along the specimen depth. We have also evaluated the degree of repeatability for our developed specimen preparation protocol by TEM imaging of three different specimens prepared according to this protocol. Our analysis indicated a quasi-repeatable specimen shape in terms of amorphized layer thickness along the specimen height (variation  $< 10\%$ ).

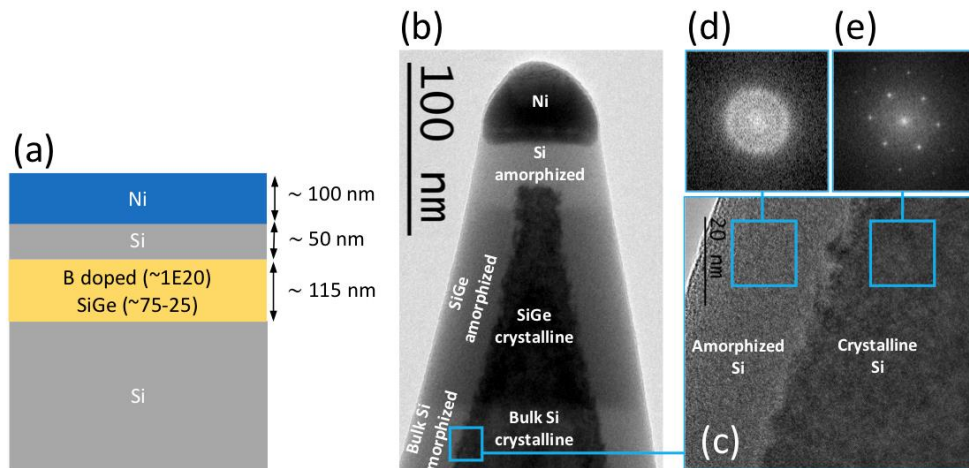


Figure 59: TEM images of a prepared APT specimen according to the developed FIB based sharpening protocol, where as a thick amorphized shell was induced by the FIB damage (Ga ions) around the crystalline core of the specimen. (a) schematic representation of the wafer used for the preparation of the APT specimen. (b) TEM image of the prepared specimen using the developed protocol. Each material on the image is labeled based on the image contrast. (c) zoom view of the interface between amorphized and crystalline interface in bulk Si. (d) and (e) the fast Fourier transform of a part of the TEM image shown in (c), corresponding to the amorphized and crystalline phase respectively. The periodic pattern in (e) clearly indicates the presence of ordered crystalline structure in the dark core region of the specimen image.

Since the interfaces between crystalline/amorphized SiGe (and Si) are among the markers used in our study to track the FOV, an in-depth understanding of the behavior of such an interface in APT is an essential step prior to the main study. Our analysis suggests that the interface between the crystalline/amorphized Si and

SiGe appears as a dense ring on the detector hit map. We have experimentally investigated such a projection using a combined APT-TEM study, which is discussed in detail below. In Figure 60, the 3D APT data reconstruction of one of the specimens prepared according to the described protocol is shown. The APT measurements were carried out in the Laser Assisted Wide Angle Tomographic Atom Probe (LAWATAP) tool using a relatively high UV laser power, corresponding to a Si CSR of about 20%.

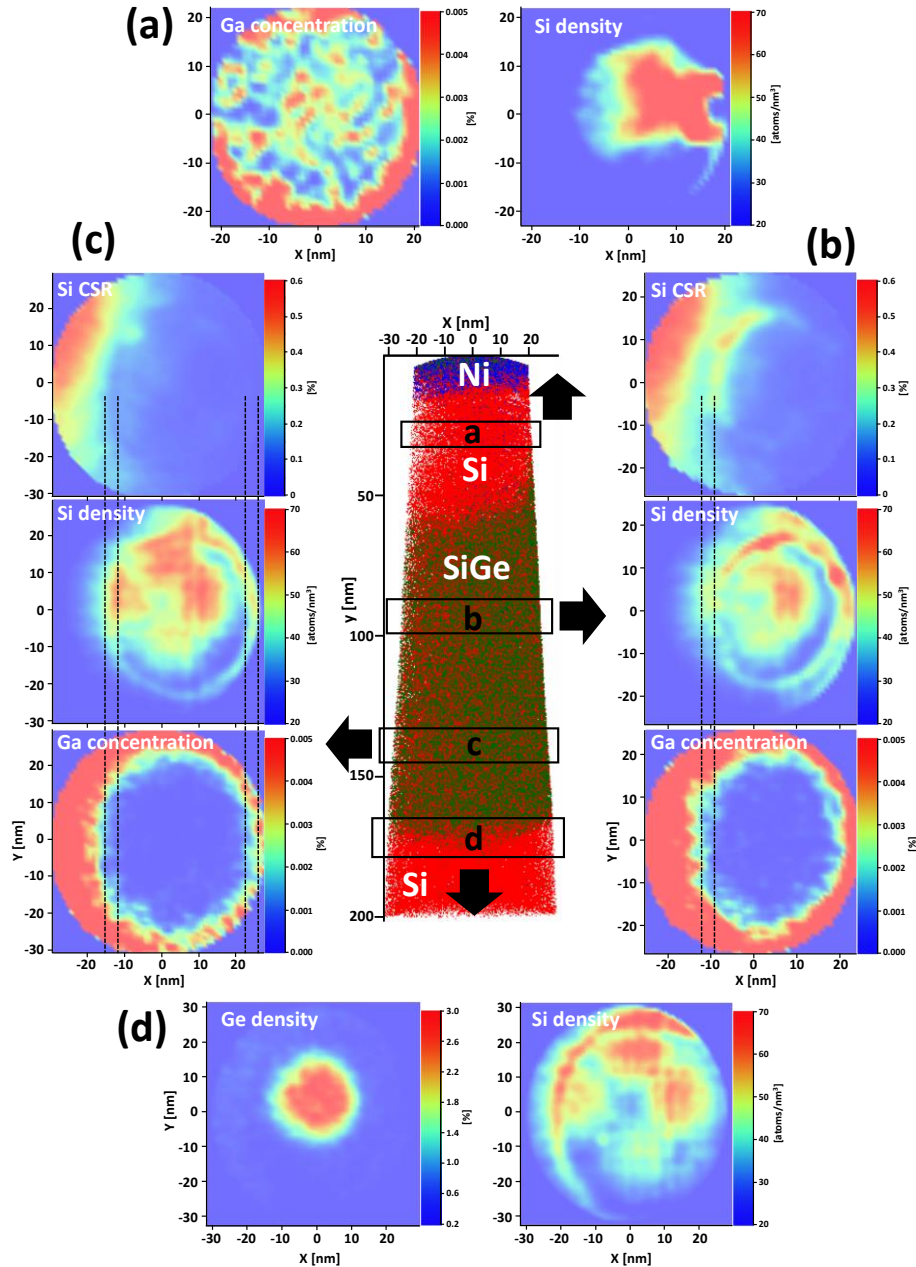


Figure 60: 3D reconstruction of APT measurement on a specimen prepared according to the developed specimen preparation protocol. (a) The 2D Ga atomic concentration and Si density maps for a slice of the specimen from height of 20 to 30 nm. The 2D Si CSR, Si density and Ga atomic concentration maps are plotted for the slice of specimen from a height of 80 to 96 nm (b) and 130 to 146 nm. (d) The 2D Ge atomic concentration and Si density maps are plotted at the interface between SiGe and bulk Si, corresponding to a slice of specimen with a height from 170 to 186 nm. The lateral position (in x direction) of the observed ring and its diameter are compared for different 2D maps by drawn dash line in (b) and (c). The APT measurement was carried out in LAWATAP tool using UV laser wavelength at a laser power corresponding to Si CSR of about 20 %.

The reconstructed 3D data shown in Figure 60 matches quite well the TEM image of the specimen reported in Figure 59, in view of the layer structure (Ni, Si, SiGe and Si) and the corresponding layer thicknesses. Please note that thickness of the Ni cap in this specimen was thinner than the one shown in Figure 59, where the majority of this layer (Ni is the first layer) was milled away during the FIB specimen preparation.

To investigate the projection of crystalline/amorphized interface in our reconstructed 3D data, the 2D Si density and Ga concentration maps were plotted at four different positions along the specimen depth (Figure 60 a to d). In Figure 60a the 2D Ga concentration and 2D Si density map of a slice reconstructed data between the height of 20 to 30 nm are shown. According to the TEM image of a similar specimen (see Figure 59), this top region of the specimen is supposed to be fully amorphized by the induced Ga damage of the FIB. The 2D Ga concentration map confirms the extent of the Ga penetration all over the specimen volume, which can potentially prove that this region was fully amorphized. By considering the employed laser power and the short distance from the Ni interface, the apex shape at this very beginning stage of the APT measurement was not yet shaped completely. The 2D Si density map also indicates that a higher density at the laser illuminated side (or bright side) of the tip. Hence, the information regarding the possible crystallographic patterns cannot be extracted from this density map.

According to the TEM image in Figure 59, the core central region of the specimen remained crystalline in the SiGe layer, while the outer shell (thickness ~ 30 nm) was amorphized. In addition, the TEM image suggests that the diameter of the crystalline region of the specimen increased as a function of specimen depth, while the thickness of amorphized shell remains approximately constant. The corresponding APT analysis of this region of the tip (SiGe layer), shows a dense ring on the 2D density map, in which the crystalline pattern (pole and zone lines) are visible only inside the dense ring area (Figure 60b to d) and there is no crystalline pattern outside the ring. Please note that, in the top part of the SiGe layer, the diameter of the dense ring is small and crystalline patterns are barely visible inside the ring pattern (Figure 60b). While, as the diameter of the ring pattern increases along the analysis depth, the clear pattern of pole and zone line pattern becomes visible inside the dense ring on the 2D Si density map (Figure 60 c and d). This suggests that ions evaporated from the core crystalline region of the specimen might be projected within the dense ring pattern and the ions emitted from the amorphized shell region might be projected outside the ring pattern. By assuming this projection pattern, one can deduce that the observed dense ring corresponds to the crystalline/amorphized interface.

To further investigate this observed projection pattern, we have tracked the extent of the Ga penetration depth across the specimen diameter by plotting the 2D Ga concentration maps at several positions along the specimen depth (within the SiGe layer). We observe that the Ga concentration was negligible inside the ring pattern and it sharply increases across the ring border to a concentration of about 0.5 % and finally remains approximately constant outside the ring pattern

(Figure 60b and c). Our analysis of the extent of the Ga penetration depth clearly shows that Ga ions (from FIB) were laterally penetrated inside the SiGe region of the specimen only up to the ring pattern and the concentration of Ga inside the ring was negligible. This confirms our previously observed projection pattern by the density map, in which the region inside the ring pattern can be assigned as the reconstruction of the crystalline core region of the specimen and the region outside the ring as the amorphized shell region of the specimen.

Finally, a comparison between the reconstruction APT data in Figure 60 and the TEM image of a similar specimen in Figure 59, also confirms that the diameter of the ring pattern in the reconstructed data matches approximately the diameter of crystalline core region of the specimen at different depths. The observed ellipticity shape in the ring pattern will be discussed later in more detail. Hence, according to the described three experimental proofs (Si density, Ga concentration and ring dimension), we assigned the observed ring pattern on the APT density map to the crystalline/amorphized interface, in which the reconstructed region inside the ring pattern was assigned to the crystalline core of the specimen and the reconstructed region outside the ring pattern was considered as the projection of amorphized outer shell of the specimen.

In order to understand how the crystalline/amorphized interface was projected as the dense ring on the detector hip map, we have studied first the behavior of similar systems reported in literature. The observed dense ring in our study has a quite similar shape to the reported ring by Marquis E. A., et al. [172] at the interface of a multi-layer structure system (see Figure 56). However, the density of the ring pattern in our study was much lighter than what was reported in the literature, in which the entire border of the ring pattern was barely visible on the density map. According to specimen apex shape (i.e. hemispherical shape) at the interface between the layers in the multi-layer structure, the underneath layer acts as an outer shell for the remaining atoms from the above layer. The author attributed the formation of the dense ring to the trajectory aberration due to the strong variation in the tip curvature [172]. The formation of such a reconstruction artefact due to the local variation in the tip curvature has been reported by several authors [181], [13].

To further investigate the observed ring in this study and evaluate whether it was created from a trajectory aberration due to the local variation in tip curvature, we performed a combined TEM-APT analysis. We carried out a series of APT measurements on the specimens prepared according to the previously described protocols, whereby the APT measurements were stopped in the bulk Si region or at the interface between bulk Si and SiGe layer. Then, specimens were removed from APT chamber and imaged immediately by TEM. In order to analyze the TEM /STEM images, each image was rotated carefully to align the specimen axis perfectly on the vertical direction. To do so, the image was finely rotated to have approximately the center of every horizontal segment of the specimen image aligned on a unique vertical line, which corresponds to the tip axis.

Before the detailed discussion on the image processing and the calculation of the local curvature across the specimen diameter, the definition of curvature is

first explained in this paragraph. In mathematics, curvature is defined as the deviation of a surface (3D object) or a curve (2D object) from being a flat plane or line respectively [182]. For any point P on a given curve, a unique circle or line exists which closely approximates this curve near the point P. This circle is usually called osculating circle. Then the curvature at the point P can be defined as the reciprocal of the radius of the osculating circle at this point:

$$k_P = \frac{1}{R_P} \quad 4.32$$

where,  $k_P$  is the curvature at the point P and  $R_P$  is the radius of the osculating circle at the same point of the curve. Alternatively, the curvature at point P is defined as the magnitude of rate of change in the unit tangent vector at the same point:

$$k_P = \left\| \frac{dT_P}{ds} \right\| \quad 4.33$$

Equation 4.33 allows a better physical understanding of the definition of local curvature. By assuming a particle moving along a curve with a velocity magnitude equal to 1 m/s. The ratio of the velocity components can be interpreted as the tangent vector (T) of the particle trajectory (ratio of derivatives of the displacements). Similarly, the magnitude of the particle acceleration can be interpreted as the curvature (see Equation 4.33).

In our study the tangent vector at each position on the specimen apex was calculated from the TEM image using a developed MATLAB code. To do so, the gray scale TEM image was first converted to a binary image, based on a user defined contrast threshold. Then the boundary pixels on the specimen apex were identified from the binary image. Although the tangent vector at every point of apex boundary can be calculated from the 2D data set by either numerical derivation or by fitting a single line at each pixel of the curve, special care needs to be taken to minimize the calculation errors. Since, in our study the magnification of TEM images were adopted to capture the entire tip apex in one image, the obtained images have a limited resolution. By considering the limited resolution of TEM images and inherent 2D projection of TEM technique, the extracted apex boundary had a limited resolution (see Figure 61c).

We observed that the direct numerical derivation of the apex shape, using x and y coordinates of boundary pixels, on such discrete space results in a wrong horizontal tangent vector for the majority of pixels on the specimen apex. To reduce the calculation errors in the numerical derivation of apex shape, the tangent vector (first derivative) at each pixel P of the apex boundary was calculated by fitting a line to a range of pixels centered at the pixel P (see Figure 61c). The choice of the number of pixels used in this calculation has an important effect. When the number of pixels (i.e. five pixels) for the line fitting is too small, a wrong horizontal tangent line for majority of points on the apex is found. Hence, to more accurately calculate the tangent vector, the line fitting was done on a

larger number of pixels centered at the pixel P. In Figure 61a the calculated tangent vectors from the TEM image in Figure 61b is reported, where 81 pixels were used to fit tangent line at each position on the apex. Please note that line fitting over too many pixels also results in a smoothing effect on the variation of the tangent lines (and curvature) and hides the actual local variation of tip shape. Nevertheless, in this study, we are more interested in the qualitative variation in the gradient of tangent vector (curvature) rather than calculating the exact values. Hence, our study is not too sensitive to the choice of number of pixels used for fitting the tangent lines as long as the desired information could be extracted.

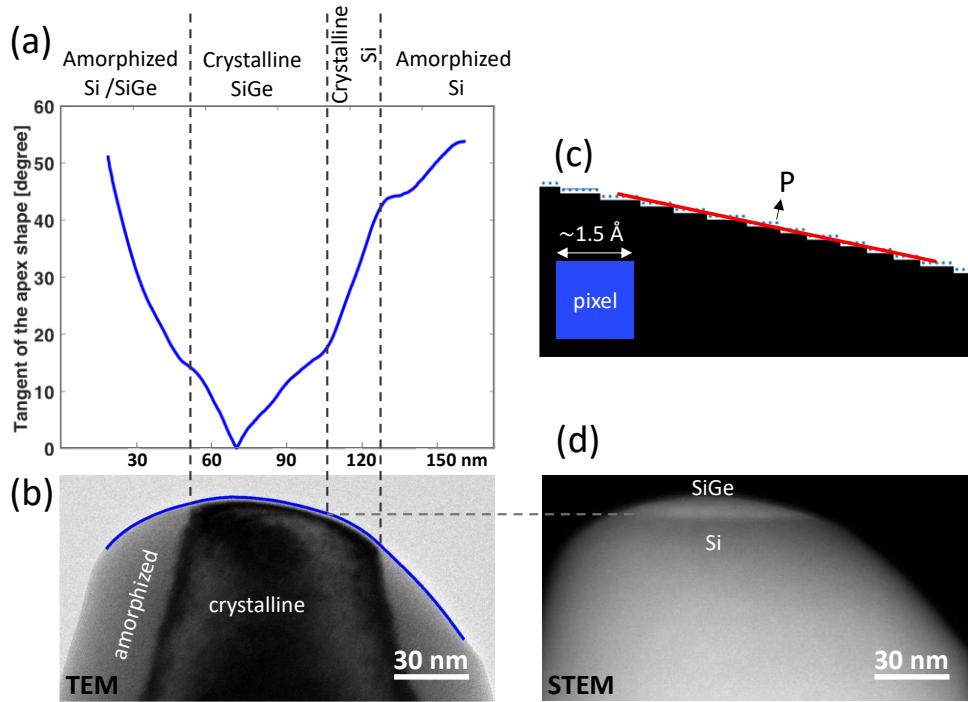


Figure 61: Estimation of local apex curvature from the TEM image of the APT specimen, which its APT measurement was stopped at SiGe/Si interface. (a) Calculated tangent vector at each pixel P of the apex boundary by fitting a line to 81 pixels centered at the pixel P. (b) Identification of apex boundary on the TEM image of the specimen apex. (c) A zoom view of the apex border defined on the binary TEM image. A fitted line centered at the pixel P over 50 pixels is also shown in red. (d) High-angle annular dark-field scanning TEM (HAADF) image of the specimen shown in (b), where the remained SiGe at the interface is visible on the top most region of the specimen.

As can be seen from Figure 61a, the gradient of the tangent vectors clearly varies at interfaces between amorphized and crystalline phases as well at the interface between SiGe and Si. According to Equation 4.33, these variations in the gradients of tangent vector correspond to a local variation in the tip curvature. We also tried to extract the local curvature by calculating the gradient of tangent vectors on the tip apex. However, due to the limited resolution of TEM image and also the numerical technique used in this study, the calculation of the second derivative of the tip shape (curvature) had a relatively high error (noise) and we decided not report the calculated results.

Finally, similar to the what discussed by Marquis E. A., et al. [172], we attributed the formation of the dense ring on the APT hit map to the trajectory aberration created due to the variation in tip local curvature. Please note that, the variation in the local curvature in our study at the position of

amorphized/crystalline interfaces is much smaller in compared to the results reported by Marquis E A, et al. [172], where the strong differences in the field evaporation of different elements of the multilayer structure led to large curvature variations at the interfaces of layer structures (see Figure 56). Similarly, the variation of density over the ring pattern in our study was much smaller than what was reported in [172], which made the complete visualization of the ring more challenging in our data analysis.

To better understand whether the predicted variation in the local curvature was due to a small dip or a protrusion on the specimen surface at the interface between crystalline/amorphized phases, we have plotted the 2D Si CSR maps at two different specimen heights in Figure 60. As can be seen, the ring pattern corresponds to a region with slightly lower CSR value primarily visible on the shadow side of the tip. Hence, we assign the ring pattern to a low field region corresponding to a tiny dip in the apex shape. The formation of local dips as a low CSR region is well known in the literature [13].

As discussed previously, the main target of our study was to investigate the FOV for an asymmetric tip shape induced by UV laser, which is currently not yet well understood in the literature. Koelling S., et al. [128] have experimentally observed a shift in the FOV toward the shadow side of the tip, by reshaping the apex shape from a symmetric to an asymmetric by switching the laser wavelength from green to UV. However, the exact explanation of their observations remained limited. In this project we focused on the physical understanding of the FOV whereby we used the ring pattern as a marker to track the FOV since it is a direct projection of the crystalline/amorphized interface.

The TEM image of a prepared specimen before APT (see Figure 59b) shows that the core crystalline region of the specimen was aligned quasi-symmetrically with the specimen axis whereby the thickness of the amorphized shell on both sides of the specimen remained constant ( $\sim 30$  nm) along the specimen depth. Hence the interface between the crystalline/amorphized region has also a quasi-circular shape centered at the specimen axis. Please note that according to the TEM images of three specimens at several rotation angles, there exists a small degree of ellipticity in the specimen shape, while the thickness of amorphized shell remained quite similar for all the images.

Despite this quasi-symmetry in position of the core crystalline region with respect to the tip axis, the 3D reconstruction of the APT data shown in Figure 60 indicates that the dense ring pattern, corresponding to the crystalline/amorphized interface, is off-center with respect to the reconstructed tip axis (or similarly detector center). More specifically it is shifted in the x-direction towards the laser illumination side. This implies that the FOV was shifted towards the shadow side of the specimen, similarly to what reported by Koelling S., et al. [128]. As expected from the TEM image, the diameter of the dense ring in the 3D reconstructed APT data increases progressively along the analysis depth in the SiGe layer, while it remained off-center corresponding to the same shift in the FOV. Please note that, the poles/zone lines patterns and ring position are also slightly off-center in the y direction, which is due to the slight miss alignment

between the detector and the fixed specimen position in our APT tool (LAWATAP). Indeed, we always observe a fixed shift of crystalline patterns in y direction for all the measurements carried out on this tool.

On the other hand, we observe that at the interface between the SiGe layer and the bulk Si, the detected Ge ions form a gradually shrinking circular disc centered at the detector hit map until they finally disappear. In particular at the interface, the 2D concentration map of Ge (Figure 60b) is reduced to a very small region nevertheless still centered at the detector. This implies a dual behavior in the FOV during this sequence of evaporation: on the one hand we observed a strong shift in the FOV towards the shadow side of the tip (according to the position of the ring), while on the other hand the remaining SiGe ions remain centered at the detector. We have repeated this APT measurement with different UV laser powers leading to different degrees of asymmetry in the tip shape. Our analysis indicates that regardless of the specimen apex shape (as induced by different choices of laser power), the Ge ions at the interface between SiGe and bulk Si, always shrunk in a circular disc centered at the detector hit map.

To better understand this dual behavior in the FOV at the interface between SiGe and bulk Si layers and to further investigate the origin of the observed shift in the FOV, we carried out a combined APT-TEM study. We repeated the APT measurement with the same condition of what was used for the specimen in Figure 60 (Si CSR  $\sim$  20 %), while the measurement was stopped at the interface between SiGe and bulk Si, when the pattern of the Ge ions shrunk to a small disc (diameter of about 1/2 of the detector) centered at the detector hit map. Then, the specimen has been taken from the APT chamber and immediately loaded in the TEM chamber. Since, the motivation of this TEM imaging was to image the flattened side of the specimen and to correlate the image to the corresponding side of the APT detector, the radial orientation of the specimen (respect to tip axis) must be identified during the TEM imaging. To do so, the specimen has been tilted and imaged several times in the TEM chamber until the maximum asymmetry of the apex shape was observed. To assign this side of the specimen as the illuminated side by laser, the specimen was tilted back inside the TEM chamber to ideally reach 90° radial rotation and to see the expected symmetric apex shape, corresponding to the perpendicular side to the laser illumination direction. Due to the limitation in realigning the image in TEM view window (specimen axis was not perfectly aligned to the axis of the holder), the maximum possible rotation was about 70° (instead of 90°). We obtained a quasi-symmetric apex shape even at 70 ° tilt angle which is shown in Figure 62.

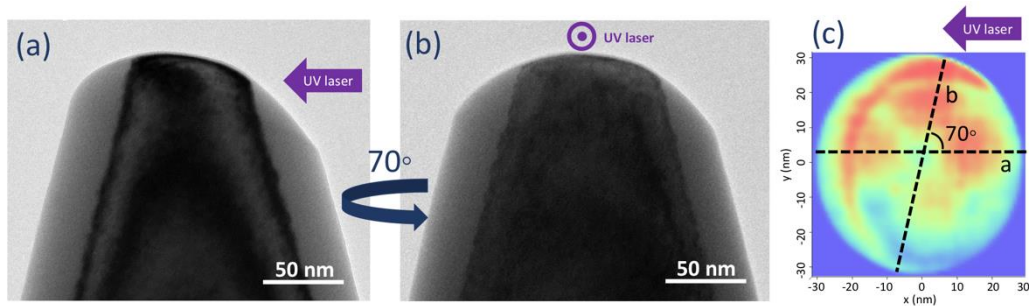


Figure 62: TEM images of the APT specimen at different radial orientations respect to specimen axis: (a) The laser illuminated side (b) The shadow side. The direction of laser illumination has been approximately shown on the figures. (c) The orientation of the captured TEM images are indicated by the dash lines on the APT 2D density map obtained from the last 3 M detected events. The APT measurement was carried out in UV laser mode (Si CSR  $\sim$  20 %) and the measurement was stopped at the SiGe/bulk Si interface.

Then the TEM/STEM image of the specimen at the laser illumination side was correlated to the APT hit map obtained from the last 300,000 events, corresponding the SiGe/Si interface. To do so, a part of the detector hit map corresponding to the direction of the TEM image (similar to the horizontal line shown in Figure 62c) was considered for this analysis, which is shown in Figure 63a. To visualize all the interfaces on the detector hit map, the same hit map was plotted twice, whereby Figure 63a represents only the Si ions, while both Si and Ge ions were plotted in Figure 63b. The interfaces between amorphized/crystalline SiGe (interface I) and amorphized/crystalline Si (interface III) were identified on the hit map according to the position of the observed dense ring in the Si<sup>+</sup> hit map (Figure 63a). While the interface between SiGe and bulk Si was identified based on the position of the outer most Ge<sup>+</sup> ions (in x direction) on the detector hit map shown in Figure 63b. Similarly, the described interfaces were also identified on the TEM image, where the interfaces between amorphized/crystalline SiGe and Si were identified according to the image contrast in the bright-field scanning TEM image. Due to the lack of contrast in the bright-field image, the interface between SiGe and Si was identified from the high-angle annular dark-field STEM (HAADF) image. In order to identify also the tip axis on the TEM image, we calculated the center of several horizontal segments of the specimen (similar to the lines shown in Figure 63c) and the tip axis was plotted as a vertical line which approximately passed through all the centers.

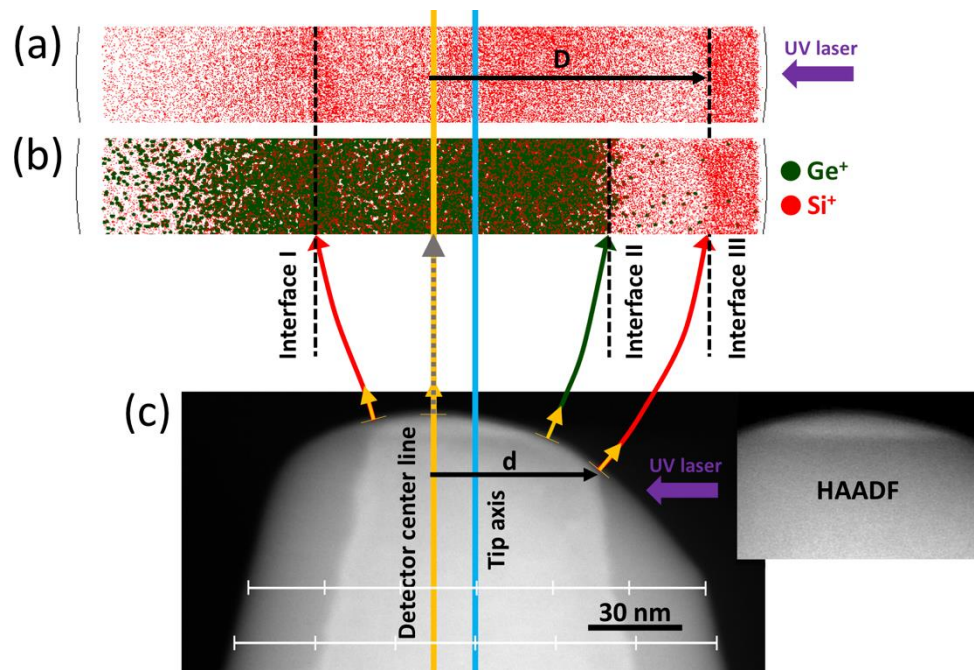


Figure 63: Correlation of the TEM image of the specimen after the APT measurement to the APT hit map in the corresponding direction, where the APT measurement was stopped at the interface between SiGe and bulk Si. (a) A central slice of APT hit map for the last 300,000 detected events, where the  $\text{Si}^+$  ions are represented by red dots. (b) The same APT hit map shown in (a), while the  $\text{Ge}^+$  ions are also shown in green dots. (c) Bright-field scanning TEM image of the specimen after APT measurement together with high-angle annular dark-field scanning TEM (HAADF) image in the inset. The identification of the tip axis, detector center line and the interfaces are discussed in the text. The interfaces are labeled as the following: Interface I: amorphized/crystalline SiGe, Interface II: SiGe and bulk Si and Interface III: amorphized/crystalline Si. The ion trajectories (Si in red and Ge in green) and the normal of the apex (in orange) are schematically represented at the apex for the ions evaporated from the interfaces and the top most part of the tip.

As shown in Figure 63c, only a few nanometers of the SiGe layer remained on the top most region of the specimen, whereas due to the asymmetry of the apex shape, this top region of the tip is not located on the tip axis. Note that, by considering the specimen apex shape, the local maximum of the specimen height is apparently the point where the last atoms from the SiGe layer evaporate from the specimen. Our APT analysis of several specimens suggests that the interface between SiGe and Si always appeared as a quasi-circular disc centered at the detector hit map whereby its diameter gradually decreases as a function of detected events and finally disappears at the center of detector. Hence, our combined APT-TEM analysis reveals that the Ge ions evaporating from the top most part of the tip were projected at the detector center. Therefore, we also identified the corresponding APT detector center position on the TEM image by plotting the detector center line in Figure 63c.

On the other hand, a comparison between the position of the crystalline/amorphized Si interfaces on the TEM image and the corresponding projection positions on the detector hit map, indicates that the FOV was shifted towards the shadow side of the tip. Therefore, only a small region of the amorphized Si on the laser side of the tip was inside the FOV ( $< 7\%$  of detector diameter), while about 30 % of the detector diameter was involved in the projection of the amorphized Si (and SiGe) on the shadow side of the tip.

Finally, the combination of the observed behaviors, i.e. the observed shift in the FOV and the projection of the ions from top most part of the tip at the detector

center, indicates that the center of the FOV (or detector center) dynamically follows the top most region of the specimen and project the ions from this region of the specimen always at the detector center. In case of a symmetric apex shape, the tip axis and the center of the FOV (detector center) are aligned on each other, which corresponds to a null shift in the FOV. While, for an asymmetric apex shape, the distance between the tip axis and the detector center line on the TEM image gives approximately the corresponding shift in the FOV, which is about 13 nm for the reported image in Figure 63c. This calculated shift in the FOV using the TEM image matches approximately the shift seen in the APT 3D data reconstruction (off-center of the ring pattern) shown in Figure 60.

The projection of the ions from the top-most region of the specimen at the detector center can also physically be explained by the ion trajectories and the distribution of the electric field lines in the vicinity of the tip apex. As discussed in Section 4.1, by assuming the APT specimen as an equipotential object, the electric field lines at each position on the specimen apex are perpendicular to the surface. This is valid for any given tip shape including the asymmetric tip shape induced by UV laser. In addition, we also explained that the ion trajectories mainly follow the distribution of the electric field lines though the degree of compression of the trajectories is less than that of field lines in between the specimen and the local electrode. The TEM image in Figure 63c shows that the normal of the local maximum of the apex is almost aligned in the z direction. Hence, the field lines at the top most region of the specimen are perpendicular to the APT detector as well. This has also been verified by finite element analysis of the electric field distribution of a hemispherical apex shape (see Figure 47). Similarly, we expect that ions emitted from this region of the specimen follow a straight flight path and reach the detector center, which is schematically shown in Figure 63c. Our finite element analysis of the ions trajectories for a hemispherical apex shape also confirms that the trajectories of the ions released with a zero-launch angle (local maximum of the apex height) have a straight flight path to the detector center (see Figure 47). That is why we experimentally observed the ions from the remained SiGe interface at the detector center. Please note that the distribution of the electric field lines in the vicinity of tip apex is strongly affected by the crystallographic structure of the specimen (microscale effect), which results in trajectory aberrations and projection of pole and zone lines at the detector center.

We also estimated the local magnification on each side of the tip using the available markers on the specimen (interfaces). In order to calculate the magnification, the horizontal distance  $d$  (in x direction) between each interface and the detector center line was extracted from the TEM image (see Figure 63c). The corresponding projection positions on the detector ( $D$ ) was extracted from the APT hit map. Then the magnification was calculated as  $M = D/d$  and the results are reported in Table 8. Our analysis indicates a strong variation of magnification at different sides of the tip, e.g. the magnification on the shadow side was about 36 % higher than average magnification on the laser side.

Table 8: Estimation of the local magnification in APT analysis for the measurement stopped at the interface between SiGe and bulk Si. The local magnification at each interface position has been calculated and reported together with average magnification on each side of local maximum of the apex height (shadow side and laser side).

Position on the specimen apex	Distance on the detector (D) [mm]	Distance on the specimen (d) [nm]	Magnification [-]
<b>Interface I:</b> Amorphized/crystalline SiGe (shadow side)	14.3	19.9	7.2 E5
<b>Interface II:</b> SiGe/bulk Si (laser side)	21.8	43.3	5.0 E5
<b>Interface II:</b> Amorphized/crystalline Si (laser side)	34.6	62.6	5.5 E5
<b>Average magnification in shadow side</b>	$5.3 \times 10^5$		
<b>Average magnification in laser side</b>	$7.2 \times 10^5$		

The variation of the magnification on the laser side of the specimen can potentially explain why the projection of the ring pattern in Figure 60 (crystalline/amorphized interface) deviated from the circular pattern toward an elliptical shape, whereby the observed ring diameter in the y direction was about 25% higher than that of x direction. The TEM images of the specimen shown in Figure 63, indicate that the maximum variation of the diameter of the core crystalline region in the shank of this specimen was about 10%. Hence, the calculated lower magnification on the laser side of the specimen can be considered as the reason why the quasi-circular interface between crystalline/amorphized phases appeared as an elliptical dense ring pattern on the detector hit map and the corresponding 3D reconstructed data.

To summarize, our study indicates that in UV-assisted APT, the center of the FOV dynamically shifts towards the shadow side of the tip and projects always the ions from the top most region of the specimen at the detector center since they have straight ion trajectories towards the detector. The shift in the FOV depends on the degree of asymmetry induced on the apex shape and can be estimated from the distance between the specimen axis and the detector center line on the TEM image. The detector center line can be identified on the n TEM image of the specimen as the vertical line parallel to the tip axis and passing through the local maximum of the specimen.

## 4.6 Full tip imaging

In the previous sections, the FOV for symmetric and UV-induced asymmetric tip shapes have been discussed in detail. Currently, the FOV for symmetric tip shape is on order of 50-70 % of the specimen apex area (depends on APT tool, i.e. local electrode, detector dimension). This means that a considerable area of the specimen apex is simply remains undetected. In the case of homogeneous bulk specimen or multilayer system, this small analysis volume might not be a severe issue, since the composition is identical across the tip apex and even the core

central volume of the specimen (within the FOV) allows the quantification and compositional analysis with relatively high statistics. In case of a nanostructured specimen or small-scale devices whereby the composition is not uniform across the apex, the currently available FOV imposes a strong limitation on the APT analysis in terms of accuracy (precision) and quality of data reconstruction (accuracy).

Full tip imaging whereby the FOV equals the tip size, allows to maximize the statistics and a self-calibration of some reconstruction parameters such as image compression factor (based on known properties of the specimen) and the detection efficiency. This paves the way for the assessment of the uncertainty for all the reconstruction parameters and potentially enables a more reliable 3D data reconstruction in APT with quantifiable uncertainty.

To improve or possibly maximize the FOV, several solutions have been suggested in the literature, which mainly relies on the improvement/modification of the tool parameters. Some of these solutions follow:

- **Further compression in the ion trajectories:** for a fixed detection system (fixed solid-angle-of-detector), the FOV can be improved by inducing a further compression in the ion trajectories and forcing the trajectories of the ions evaporated from the outer shell to reach the detector. The use of a local electrode is one of the techniques which can compress the ion trajectories further and improve the FOV by some extent. Recent APT instruments are also equipped with electrostatic devices, including electrostatic lenses and post acceleration devices, to compress the ions trajectories and improve the FOV [82].
- **Improving the solid-angle-of-detector by reducing the specimen to detector distance ( $L$ ):** by reducing the specimen-to-detector distance one can increase the solid-angle-of-detector (Equation 4.31) and thus improve the FOV. Such a functionality is available in some APT tools. The main drawback of this technique is the reduction in the flight path of the ions and the corresponding time-of-flight, which finally leads to a reduction in the mass resolution. In other words, there is a compromise between mass resolution and FOV. Recently by the implementation of the large angle-reflectron (electrostatic mirrors) after the local electrode, a strong improvement in both mass resolution and FOV has been achieved in LEAP HR, which may enable the improvement of FOV in future.
- **Improving the solid-angle-of-detector by increasing the detector diameter ( $D_{det}$ ):** this requires a new design of the detection system, including a larger diameter for both the microchannel plate and the position sensitive detector. Such a detection system is not available at the time of this project.

In contrary, we propose a new specimen geometry which maximizes the FOV and could enable to include atoms from the sidewalls of the sample in the APT

analysis. Our concept provides full tip imaging on all existing APT tools without any need to change anything in the hardware. The basic idea starts from a specimen geometry whereby all the ion trajectories are compressed such that they all reach the detector regardless of their point of origin, i.e. the outer shell or sidewalls of the specimen. With the objective to exploit this sample for round robin studies on the uncertainty and detection efficiency, we propose a new process which allows to prepare multiple APT specimens in a reproducible fashion and with minimized tip to tip variations in view of the tip radius and shank angle. The APT tips will be exploited in the preliminary studies preparing for an interlaboratory study focused on the uncertainty budget in APT analysis. This will be discussed further in section 4.6.2.

Such standardized tip shape is also extremely helpful in fundamental studies (e.g. tip-laser interactions) as they allow to eliminate variability contributions in ion-beam damage, retained Ga dose and distribution, tip geometry, heat transfer (shank angle), etc. The detail discussion on the specimen design together with specimen preparation and APT analysis are discussed in the following sections.

#### **4.6.1 Design of specimen shape**

The specimen design to maximize the FOV in APT analysis was inspired from a study in literature [183], where the FOV was observed to be maximized for a 10  $\mu\text{m}$  long GaAS nano wire, grown on a flat substrate. This was achieved by assigning the crystalline pattern observed on the APT hit map to the plane family of nanowire sidewalls. The authors attributed the observed FOV to the compression of ion trajectories toward the detector ( $\xi$  up to 3.8) due to the presence of a flat substrate close to the field emitter.

Based on that observation, we choose a specimen design similar to a short nanowire (i.e. 10  $\mu\text{m}$  long) on top of a flat substrate, similar to what has been shown by [183]. However, such a short distance between tip apex and substrate makes the specimen-to-local electrode alignment extremely challenging and could easily damage the local electrode. In addition, this configuration is far from a standard APT specimen and could result in a discharge between the local electrode and the specimen. Hence, in this study we decided to design a sample consisting of a nanowire on top of a cylindrical micropost. The schematic representation of the proposed geometry for the preparation of APT specimen is shown in Figure 64. Note that this resembles the standard design of the CAMECA micropost, be it with an additional flat substrate on the micropost right below the APT tip.

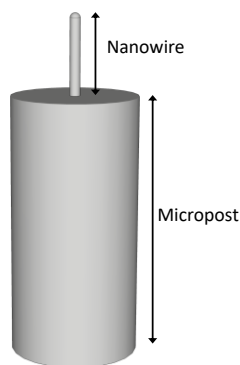


Figure 64: Schematic representation of a new APT specimen design consist of a nanowire prepared on top of a cylindrical micropost. Note that the design is not to scale.

Before investigating the FOV, the feasibility of analyzing such a specimen in APT chamber was first numerically evaluated. As discussed earlier, to trigger the field evaporation from the apex of a field emitter, an intense electric field, in order of  $10^{10}$  V/m, is required. Since the APT tools are commonly designed to work in a range of applied potential between 2 to 15 kV, the specimen design should create enough field enhancement at the specimen apex within this voltage range.

To investigate the field enhancement at the tip apex, we performed finite element simulations of the electric field using the COMSOL software. The detailed description together with its validity assessment are discussed in Section 4.1. In particular, we investigated the magnitude of the electric field at the tip apex for different geometries of the cylindrical micropost (diameter and height) and the nanowire (diameter and height). In a first step, we studied the influence of the micropost dimension (diameter and height) on the electric field enhancement, while the nanowire dimension was kept constant ( $r = 40$  nm and  $l = 800$  nm). The average magnitude of electric field at the apex was estimated at 1 kV applied potential for different microposts having heights in a range between 0.5 to 50  $\mu\text{m}$  and diameters between 1 to 19  $\mu\text{m}$ . The results are reported in Figure 65a. Please note that the range for the micropost dimensions is aligned with practical considerations regarding the feasibility of preparation and the mechanical stability of the micropost. As shown in Figure 65, the field enhancement at the apex is maximized for high aspect ratio microposts (tall and narrow), while it drops by enlarging the post diameter or reducing micropost height (reduction in the aspect ratio). This implies that a high aspect ratio micropost has a better performance in view of field enhancement at the nanowire apex.

To more quantitatively express the influence of the micropost dimension on the field enhancement, the field factor  $k_f$  was also calculated for all the combinations of the micropost dimensions and the results are reported in Figure 65b. Before evaluating the obtained results, the definition of  $k_f$  and the intrinsic difference between the zero degree shank angle NW (this study) and the tapered tip shape (standard APT specimen) are discussed in this paragraph. As discussed in Section 4.1, the field factor is a dimensionless parameter expressing the influence of the geometrical parameters (both specimen and chamber) on the electric field environment around the tip whereby the magnitude of the field

enhancement at the tip apex  $F$  can be written as  $F = V/rk_f$  ( $V$  is the applied potential and  $r$  is the tip radius at the apex).

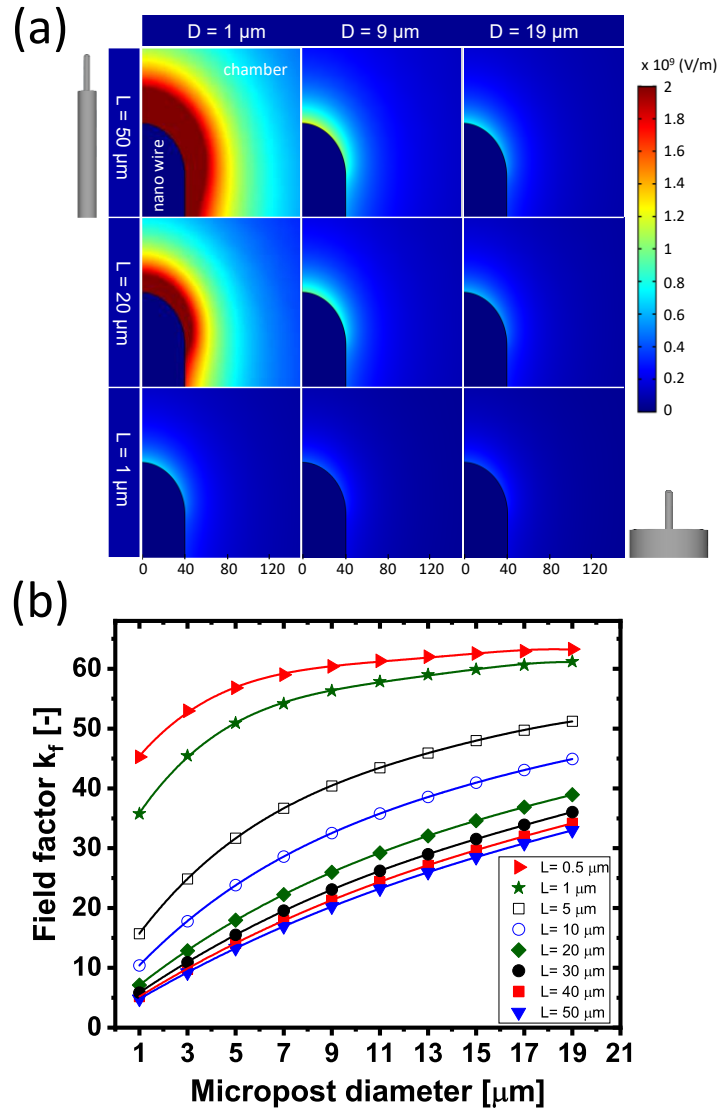


Figure 65: Finite element simulation of the magnitude of the electric field for a nanowire tip shape prepared on top of a cylindrical micropost. (a) Variation of the magnitude of electric field in the vicinity of tip apex depending on the micropost diameter and height. The applied electric potential was 1kV for all the simulations. (b) Field factor  $k_f$  as a function of the micropost diameter and height (legend value). Note that the nanowire dimension was kept constant to a diameter of 80 nm and height of 800 nm for all the simulations.

For a standard APT specimen, the field factor is typically in a range between 3 to 8 [144]. This implies that with this range of  $k_f$  and the practical voltage range (2-15 kV) applied to the tips, with a diameter between 50 to 200 nm, can be analyzed in an APT chamber. Since the magnitude of the electric field is proportional to the inverse of the tip diameter ( $F \sim 1/r$ ) and the radius increases with depth for a tapered tip with a certain shank angle, the potential applied to the tip apex to retain a constant electric field has to be increased along the analysis depth, thereby setting the maximum depth which can be analyzed. However, in case of a nanowire with a constant diameter and thus tip radius, the applied voltage could potentially remain the same along the entire NW height, provided that  $k_f$  remains constant. This implies that for the NWs (diameter < 100 nm) with

a zero-degree shank angle, the maximum allowed field factor  $k_f$  can be higher than the standard APT specimen by a factor of about 3 (for relatively low field elements such as Si and Ge). Hence, according to the finite element analysis, micropost dimensions leading to a field factor up to about 20 (see Figure 65b) can be considered as usable.

Similar to the study on the micropost dimensions, the influence of the nanowire dimension (diameter and height) on  $k_f$  has been studied by finite element analysis. In a first step, the NW height was kept constant to 600 nm and the diameter was varied in a range between 40 to 160 nm. It is worth mentioning that the nanowires having a diameter lower than 40 nm were not considered as they do not have enough mechanical stability in an APT analysis [82]. Ultimately  $k_f$  was calculated for all combinations of NW diameters and micropost dimensions corresponding to a  $k_f$  lower than 25. To better visualize the influence of the NW diameter, the calculated  $k_f$  for this range was normalized to the  $k_f$  obtained for a NW diameter of 200 nm (at each given micropost dimension) and the results are reported in Figure 66a. For the sake of simplicity, only the results corresponding to the micropost height of 20 and 50  $\mu\text{m}$  were reported in this figure, while the other micropost heights had also a similar trend. Our analysis indicates that by the increasing NW diameter from 40 to 160 nm,  $k_f$  decreases by about 30% for most combinations of the micropost dimension. This means that the variation of the NW diameter has a minor influence on  $k_f$  relative to the impact of the micropost dimension. In addition, the variation of  $k_f$  with respect to the NW diameter has a similar trend for all micropost diameters above 3  $\mu\text{m}$ , while for the micropost having the diameter equal to 1  $\mu\text{m}$  the variation of  $k_f$  shows a slightly different behavior. Hence, the influence of NW diameter (in the range of our study) on  $k_f$  can be decoupled from the micropost dimensions when these have a diameter larger than 3  $\mu\text{m}$ .

Similarly, the influence of NW height on the field enhancement factor has been also investigated by FEA. In particular, the NW diameter was kept constant to 80 (and 60 nm) and the NW height was varied in a range between 200 to 1200 nm. The maximum values of the NW height (1200 nm) was chosen according to the feasibility of the realization and the mechanical stability of such a high aspect ratio structure. The calculated variation of  $k_f$  as a function of the NW height for the different combination of micropost dimensions, similar to the previous study, is reported in Figure 66b.

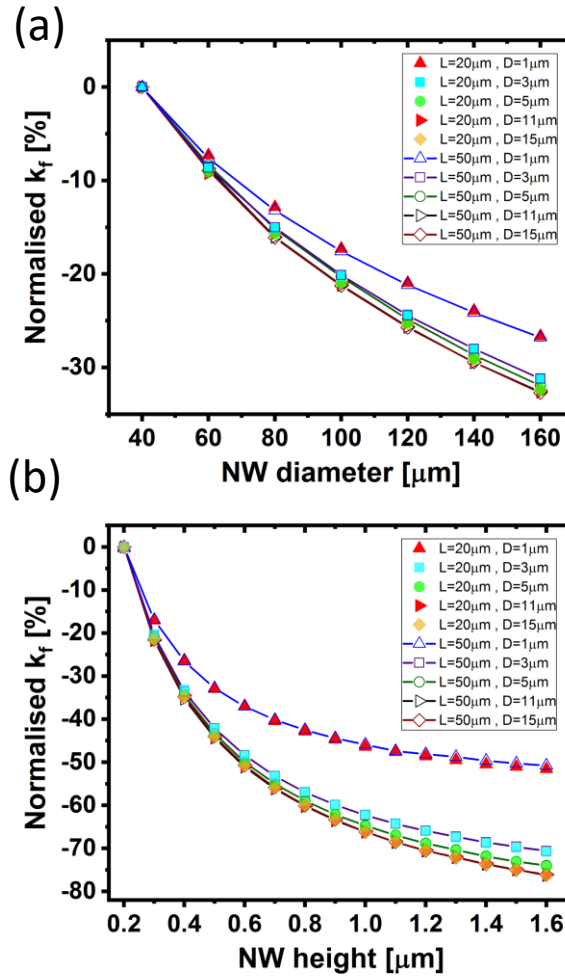


Figure 66: Influence of the nanowire (NW) dimension on the field enhancement at the tip apex as investigated by finite element analysis. (a) Influence of the NW diameter on  $k_f$ , for a range of nanowire diameters from 40 to 160 nm and micropost dimensions (shown in the legend), while the NW height was kept constant to 600 nm. (b) Influence of the NW height on  $k_f$ , for a range of nanowire heights (200 to 1200 nm) and micropost dimensions (shown in the legend), while the NW diameter was kept constant to 80 nm. In both figures, the calculated  $k_f$  for the given range of NW dimension (diameter or height) were normalized to the  $k_f$  obtained from the NW having (a) diameter equal to 80 nm with the same micropost dimension (b) NW having a height equal to 600 nm with the same micropost dimension.

For the sake of simplicity, only the results for the NW diameter equal to 80 nm were reported in this figure, while the data obtained from the other diameters indicate a similar trend. Our numerical analysis suggests that  $k_f$  declines as a function of NW height, for all combination micropost dimension, while its slope progressively decreases toward a null value for very tall NWs.

Similar to the trend obtained from the NW diameter, the variation of  $k_f$  in respect to the NW height has an almost similar trend for all micropost diameters above 3  $\mu\text{m}$ . This implies that the influence of NW dimension (both diameter and height) on  $k_f$  can be approximately decoupled from the influence of the micropost dimension having a diameter larger than 3  $\mu\text{m}$ . It is worth mentioning that the variation of  $k_f$  as a function of NW height could have an important impact on APT data analysis, as it implies that  $k_f$  rises as a function of analysis depth. This behavior is not observed in the standard tip geometry, where the field emitter is far from the flat substrate. This effect will be discussed in more detail in Section 4.6.3. Furthermore, the drop in the slope of Figure 66b suggests that for the tall

NWs field enhancement is less sensitive to the variation of NW height. Hence, taller NWs are more favorable in APT analysis, where the  $k_f$  can be assumed to remain unchanged along the analysis depth.

To better understand the electric field distribution between the APT specimen and the local electrode (both near and far-field) for our specimen design, the electric field lines were also calculated by FEA for different combinations of micropost and NW dimensions. In Figure 67 the distribution of the electric field lines close to the tip apex are compared for the standard APT specimen and the NW tip prepared on the cylindrical micropost with different combinations of micropost dimensions (height and diameter). Note that the NW dimension was kept constant to 80 nm in diameter and 600 nm in height and for the standard APT specimen the same tip diameter was adopted. As can be seen from the figure, the new design of APT specimen creates further compression of electric field lines toward the detector center. In addition, Figure 67a shows that the choice of the micropost diameter has a significant influence on the compression of the electric field lines, e.g. by increasing the post diameter from 1 to 11  $\mu\text{m}$  the extent of the field lines in the radial direction expands more than 50 %, (at  $\sim 600$  nm distance above the apex, see Figure 67a). On the other hand, the variation of the micropost height, even in a wide range, only shows a minor influence on the compression of the electric fields lines (see Figure 67b). We performed similar analyses for other combinations of micropost dimensions (diameter and height) and we obtained the same qualitative trend between the compression of the electric field lines and the micropost height and diameter. This compression increases significantly for the microposts with larger diameters (Figure 67a), while it drops slightly as the post height increases (Figure 67b).

For a fixed micropost height (or diameter), we observed a qualitatively strong correlation between the compression of the electric field lines and the field factor  $k_f$ , i.e. micropost dimensions corresponding to higher  $k_f$  have also more compressed electric field lines towards the detector center. This implies that the field enhancement at the tip apex has an inverse relation to the compression of electric field lines. However, our analysis suggests that  $k_f$  cannot quantitatively be described by the compression of the electric field line. For instance, there are different micropost dimensions (i.e.  $D_1=5 \mu\text{m}$ - $L_1=10 \mu\text{m}$  and  $D_2=10.4 \mu\text{m}$ - $L_2=40 \mu\text{m}$ ), which create the same  $k_f$  value ( $\sim 23.8$ ), but have different compression of the electric field lines.

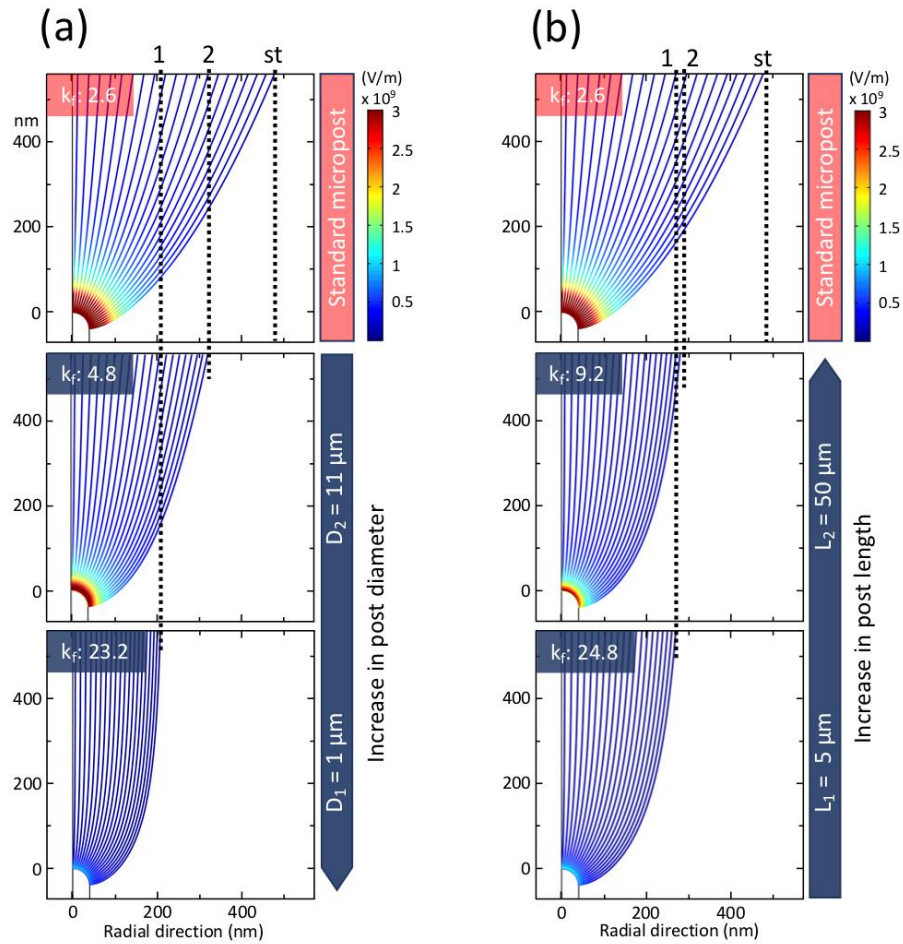


Figure 67: Compression of the electric field lines created at the tip apex for different designs of the APT specimen. (a) The influence of the micropost diameter on the compression of the electric field lines is shown for two different diameters ( $D_1=1$  and  $D_2=11 \mu\text{m}$ ), while the post height was kept constant to  $50 \mu\text{m}$ . (b) The influence of the micropost height on the compression of the electric field lines for two different heights ( $L_1=5$  and  $L_2=50 \mu\text{m}$ ) at a fixed post diameter equal to  $3 \mu\text{m}$ . The nanowire height and diameter were identical for all the figures (diameter:  $80 \text{ nm}$  and height:  $600 \text{ nm}$ ). The field lines were drawn uniformly from the tip apex and the magnitude of electric field is alternatively indicated by the color bar at  $1 \text{ kV}$  applied electric potential.

To explain how the micropost dimension influences the compression of the electric field lines towards the detector center, the direction of the field vector around the tip and the definition of the field lines need to be considered. Indeed, the electric field lines describe the direction of electric field vector in the given medium. In case of our axisymmetric study, the compression of field lines towards the detector center implies that the  $z$  component of the electric field has increased relatively to the radial component ( $r$  direction).

By definition, the direction of electric field (and field lines) at the surface of an equipotential object is along the normal of the surface. Hence, in case of our specimen design, the field lines have to be in the radial direction at the NW and micropost sidewalls, while they are along the vertical direction on the flat areas on the top of the micropost (Figure 68a). As the micropost diameter increases, the weight of the  $z$  component of the electric field above the flat area of the micropost is increased accordingly (see Figure 68b to c). This amplification of the  $z$  component of the electric field extends up to some tents of micrometers above the micropost and modifies the electric field environment around the nanowire and its apex. This increases the slope of the electric field lines originating from the

nanowire sidewalls and the apex, towards a more vertical direction and thus it compresses further the direction of field lines towards the aperture position.

In Figure 68b and c, the electric field lines created around the NW and at the flat area of the micropost are shown for two different micropost diameters, while the micropost height and NW dimension were identical. For the larger micropost diameter (Figure 68a), the presence of the flat area of the micropost has promoted the z component of electric field around the nanowire and caused the field lines to compress further toward the detector center.

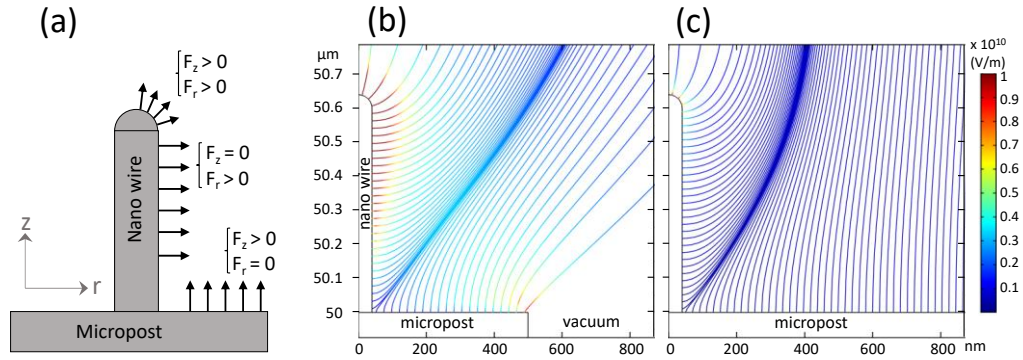


Figure 68: Compression of the electric field lines due to the presence of a flat area on top of the cylindrical micropost. (a) schematic representation of the electric field at the tip apex, nanowire sidewalls and on the flat area of micropost. Distribution of the electric field lines created from the tip apex, nanowire sidewalls and on the flat area of the micropost was plotted for a micropost having a height equal to 50  $\mu\text{m}$  and a diameter equal to 500 nm (a) and 11  $\mu\text{m}$  (b). The nanowire height and diameter were identical for both figures (diameter: 80 nm and height: 600 nm). Note that the electric field lines were drawn uniformly from the specimen surface and the magnitude of electric field is alternatively indicated by the color bar at 1 kV applied electric potential.

This compression of the electric field lines could potentially create also a compression in the ion trajectories and could improve the FOV in APT analysis. As discussed earlier the electric field lines identify the acceleration path for the travelling ions in the APT chamber. To evaluate the performance of our new specimen design in terms of FOV, we studied the ion trajectories in the calculated electric field, using the particle tracing solver in the COMSOL software. Since the electric field in between the specimen apex and the local electrode dominates the particle steering, our finite element analysis was only performed in this region of APT chamber and the trajectories in between local electrode and detector were assumed to be free motion.

To resemble the evaporated ions across the entire specimen apex, a fixed number of particles (i.e. 20 particles) having an arbitrary mass (mass of  $\text{Si}^{28}$  in our study) and a unit positive charge were uniformly distributed across the specimen apex. It is worth mentioning that the choice of particle mass does not have much influence on the ion trajectories and it only influences the time-of-flight. Then the particles were released in the calculated electric field with a small initial velocity (1 m/s normal to the apex) and the trajectory of each particle was calculated using a time dependent solver. The particle-particle interaction was also neglected in this analysis and particles were assumed to have negligible velocity in respect to the speed of light. To minimize the calculation error, the time constant for our analysis was reduced gradually (to  $1 \times 10^{-12}$  s) to reach the trajectory paths which are independent from the choice of the time constant. Such an analysis was carried

out for a wide range of micropost dimensions (diameter and heights) all corresponding to a  $k_f$  lower than 25.

To calculate also the ion trajectories for the standard APT specimen, the standard specimen was modeled as an imaginary long nanowire (120  $\mu\text{m}$ ) with a diameter of 80 nm, similar to the approach reported in the reference [184]. The ion trajectories for this specimen and those the same micropost dimensions of Figure 67 are reported in Figure 69. As can be seen, this new specimen design creates a significant compression of ion trajectories as compared to those for the standard APT specimen, which reaches up to about 70% for micropost having a diameter and height of 11 and 50  $\mu\text{m}$  respectively.

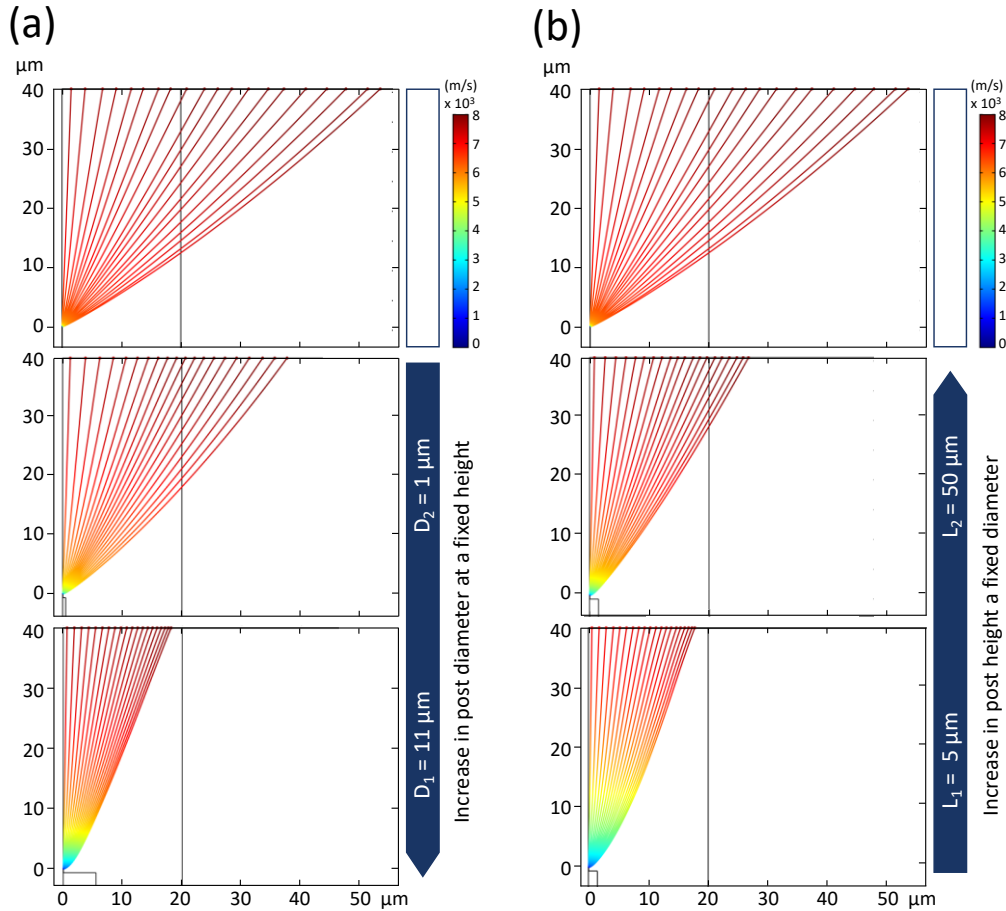


Figure 69: Ion trajectories in between the specimen apex and the local electrode for the standard APT specimen (top) and the proposed specimen design (NW prepared on top of cylindrical micropost). (a) The influence of micropost diameter on the compression of ion trajectories for two different micropost diameters ( $D_1=1$  and  $D_2=11 \mu\text{m}$ ), while the post height was kept constant to 50  $\mu\text{m}$ . (b) The influence of micropost height on the compression of ion trajectories for two different heights ( $L_1=5$  and  $L_2=50\mu\text{m}$ ) at a fixed post diameter equal to 3  $\mu\text{m}$ . Note that the nanowire dimension is identical for all the figures (diameter: 80 nm and height: 600 nm). The color bar shows the magnitude of ion velocity along the traveling path, which was calculated at 1kV applied electric potential.

The compression of ion trajectories increases significantly by enlarging the micropost diameter (Figure 69a) or reducing the height (Figure 69b). A similar analysis of other combinations of the micropost dimensions (diameter and height) shows the same trend between the compression of ion trajectories and micropost dimension.

To investigate how the micropost diameter compresses ion trajectories, the distribution of field lines in the vicinity of the tip apex should be taken into

consideration. As expected, a rough comparison between the trends of the ion trajectories for the different micropost dimensions (see Figure 69) and that of the electric field lines (see Figure 67), indicates that the compression of the ion trajectories roughly follows the trend of electric field lines for different micropost dimensions. Obviously, for a given micropost dimension, the ion trajectories are not identical to the electric field lines, as the latter describes the acceleration of the traveling particles and the ion trajectories are the displacements.

However, a more dedicated comparison between the distribution of the electric field lines (see Figure 67) and the actual ion trajectories (see Figure 69) reveals a number of differences. For instance, the microposts ( $D_1 = 3 \mu\text{m}$ ,  $L_1 = 5 \mu\text{m}$ ) and ( $D_2 = 3 \mu\text{m}$ ,  $L_2 = 50 \mu\text{m}$ ) have almost a similar distribution of field lines (see Figure 67), while the ion trajectories for the first micropost show a higher degree of the compression at the aperture position (see Figure 69). Apparently, the ion trajectories were calculated according to the electric field lines (both magnitude and distribution) and this observed discrepancy clearly indicates the differences between these two parameters (field lines versus ion trajectories). Indeed, the field lines determine the acceleration direction of the traveling ions, which is not necessary the same as their actual displacements (ion trajectories). For instance, the magnitude of the electric field (color map in Figure 67) at each point on the field lines determines the magnitude of the acceleration for the travelling ion. Thus, even if the shape of the field lines (i.e. direction of the electric field) are similar, the differences in the magnitude of the electric field (color map color map in Figure 67) can influence the ion trajectories. As for the above example, although the field lines for the both microposts show a similar distribution, the magnitude of electric fields (color map in Figure 67) was different mostly in the vicinity of the tip apex (field enhancement factors were  $k_{F1}=9.2$  versus  $k_{F2}=24.8$ ).

Therefore, to accurately study the FOV in the APT, the ion trajectories have to be calculated and the qualitative comparisons based on the distribution of electric field lines (e.g. Figure 67) can only give a rough idea of the degree of the compression in the ion trajectories. To quantitatively correlate the compression of ion trajectories to FOV in APT analysis, the image compression factor  $\xi$  was calculated and used as a measure to compare the performance of our new specimen design. As discussed in Section 4.2.1, in the point-projection model the ion trajectories are modeled as a straight line connecting the initial ion position at the apex to the hit point on the detector. The image compression factor  $\xi$  is defined based on the distance between the intersection of this straight line with the tip axis and the center of the spherical apex.

Since in our FEA, the initial particle positions at the apex and trajectories at the aperture position are known, the hit position on the detector can be calculated. This makes the calculation of  $\xi$  rather straightforward, according to Equation 4.20. In particular, the image compression can be written as  $\xi = \frac{Ld_{ion}}{rD_{hit}}$ , where  $L$  is the specimen to detector distance (9 cm for LEAP 5000),  $d_{ion}$  is the initial ion position with respect to the tip axis,  $r$  is the tip radius and  $D_{hit}$  is the distance between the

hit position of the ion on the detector to the detector center. Since, our FEA of ion trajectories only covers a part of the APT chamber (i.e. from the specimen apex to the local electrode), the hit position  $D_{hit}$  on the detector needs to be calculated to estimate  $\xi$ . To do so, the ion trajectories after the aperture position were assumed to be straight lines, as they travel in the field-free region of the chamber. Their slopes can be determined by the ratio of the velocity components ( $\frac{V_z}{V_r}$ ) at the local electrode position, obtained from FEA. In our analysis to calculate  $\xi$ , 10 particles were released from the specimen apex (half circle) in the electric field calculated by FEA at the applied potential of 1kV. Then the corresponding trajectory positions and their slopes, equal to the ratio of velocity components ( $\frac{V_z}{V_r}$ ), were calculated for each particle at the aperture position by FEA. In the next step, the hit position on the detector  $D_{hit}$  was also calculated by knowing the local electrode to detector distance (9 cm on LEAP 5000) and the slope of each ion trajectories. Finally,  $\xi$  was calculated for each particle released from the hemispheric apex. Our analysis suggests that  $\xi$  and  $k_f$  vary across the tip apex as a function of angular distance from the specimen axis (or launch angle). The variation of  $\xi$  and  $k_f$  as a function of launch angle was calculated for a NW having a diameter of 80 nm and a height of 600 nm, mounted on a micropost having a diameter of 5  $\mu\text{m}$  and a height of 20  $\mu\text{m}$  and it is shown in Figure 70.

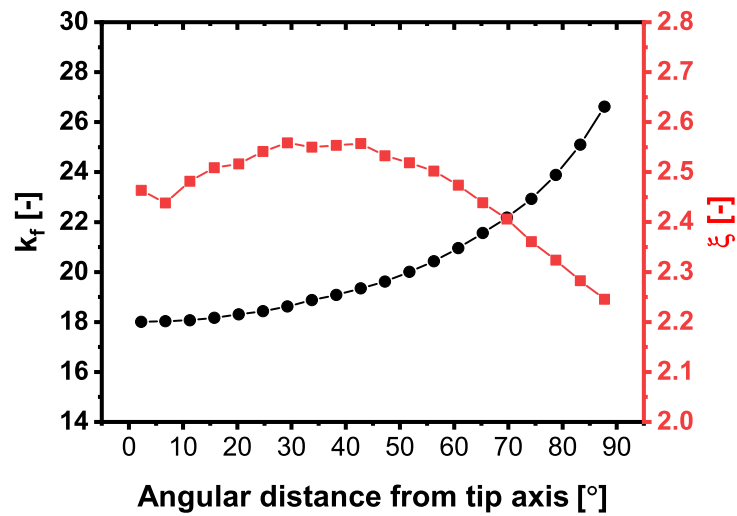


Figure 70: Variation of field factor  $k_f$  (in black) and image compression factor  $\xi$  (in red) as a function of the angular distance from the specimen axis (launch angle). The analysis was carried out by finite element simulation for a nanowire (diameter: 80 nm and height: 600 nm) mounted on top of a cylindrical micropost having a diameter of 5  $\mu\text{m}$  and a height of 20  $\mu\text{m}$ . Note that the calculated  $\xi$  at zero angle had a relatively high error due to the propagation of the error caused in the calculation of the trajectory slope at the aperture position for such a straight flight path.

The observed variation of  $\xi$  and  $k_f$  as a function of angular distance from the specimen, is quite similar to what has been reported for the standard APT specimen [184] (see Figure 51), where only the angular distance up to 35° from the tip axis was reported due to the limited FOV for such a specimen. The variation of  $k_f$  arises from the assumed pure hemispheric apex on top of a shank as compared to a hemispherical shape. But even then the calculations are approximate since in reality the actual apex shape after APT analysis deviates

substantially from hemispherical shape when analyzed using both voltage mode [127] and laser mode [185]. Even an ellipsoidal shape with a higher curvature towards the specimen edge was observed whereby, the tangential continuity between the apex and the sidewalls of the tip is not conserved at the edges of the apex. An apex shape with a uniform field enhancement (same  $k_f$ ) across the tip radius can only be generated after an APT analysis in voltage mode as evidenced by the similar CSR values across the apex. In all other cases, the electric field on the apex shape does not have a uniform magnitude along different radial positions. As a result, the calculated  $\xi$  might be also affected by the variation of  $k_f$  across the tip apex. Our APT experiment confirms that  $\xi$  varies across the tip even in full tip imaging mode as obtained from our new specimen design. This will be discussed later in this document.

To access the validity of our finite element analysis,  $\xi$  was calculated for the standard APT specimen and the result was compared with reported values in literature [184] and [183]. The standard APT specimen was modeled as an imaginary long nanowire with a diameter of 80 nm and height of 100  $\mu\text{m}$ , similar to the approach reported in the reference [184]. To compare the calculated  $\xi$  to the reported values in literature, the average  $\xi$  over the 35° angular distance from the specimen axis was calculated. The obtained average  $\xi$  for standard APT specimen is about  $\xi = 1.41$ , which underestimates the reported values in reference [184] by 10%.

In our study to compare the performance of specimens with different micropost and nanowire dimensions (both diameter and height), the average  $\xi$  across the entire hemispherical apex was used. The calculated average  $\xi$  for a fixed dimension of nanowire (diameter: 80 nm and height: 600 nm) and a wide range of micropost dimensions (diameter and height) corresponding to a  $k_f$  mainly below 25 are reported in Figure 71. Our results predict that the FOV could be improved by increasing the micropost diameter or reducing micropost height. For instance, by enlarging the post diameter from 1 to 11  $\mu\text{m}$ ,  $\xi$  rises about 75% to 85%, depending on the micropost height. Vice versa, the calculated  $\xi$  drops as a function of micropost height. This predicted increase in the image compression factor  $\xi$  could potentially compress all the ion trajectories into the aperture of local electrode and enables full tip imaging during APT analysis as  $\xi$  above 2 is reported to maximize the FOV and result in full tip imaging [183]. Hence, only the micropost dimensions corresponding to  $\xi > 2$ , could theoretically be considered as a design which could enable the full tip imaging feature during APT analysis. To study the optimum dimension for the micropost, also the field enhancement at the tip apex, as represented by  $k_f$ , should be taken into account. For instance, a micropost having  $\xi > 2$ , may not necessarily have a small enough  $k_f$  to create the required electric field at the tip apex. Hence, both factors have to be considered for identifying the optimum dimension for the preparation of cylindrical micropost.

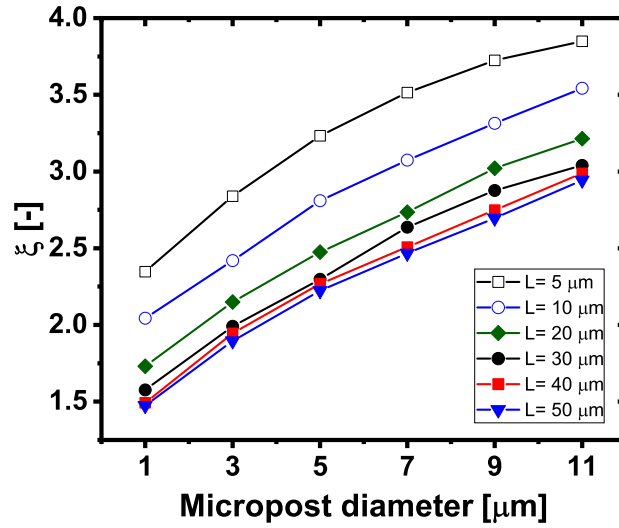


Figure 71: Image compression factor  $\xi$  calculated for different combinations of micropost diameter and height, which are indicated in the horizontal axis and the legend respectively.  $\xi$  was calculated for different micropost dimensions using finite element simulation of ion trajectories at 1 kV applied potential, while the nanowire diameter and height were kept at 80 and 600 nm respectively.

As previously shown in Figure 69, we observed a correlation between the compression of ion trajectories and field enhancement at the apex. To quantitatively assess the predicted relation, the calculated  $\xi$  was plotted versus  $k_f$  in Figure 72, where the data was calculated for a wide range of micropost dimensions (diameter and height), while the nanowire dimension was kept constant a diameter of 80 nm and a height of 600 nm. Our analysis suggests that there is a positive non-linear correlation between  $\xi$  and  $k_f$ , in which  $\xi$  increases as a function of  $k_f$  and even different microposts having a similar  $k_f$  also corresponds to approximately the same value of  $\xi$ .

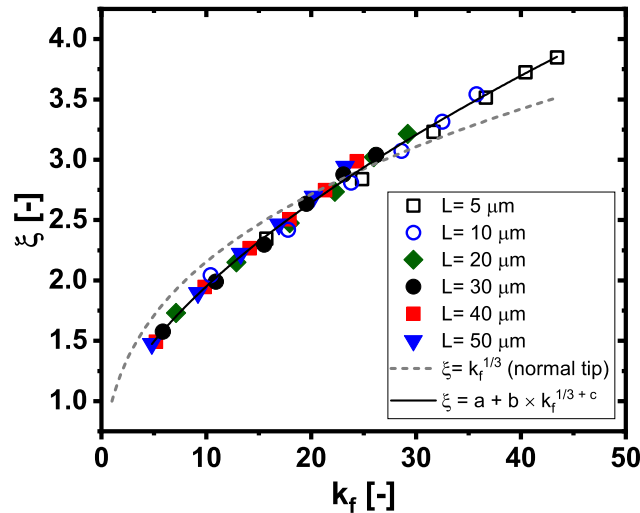


Figure 72: Relation between image compression factor ( $\xi$ ) and field factor ( $k_f$ ) for a nanowire tip shape prepared on cylindrical micropost.  $\xi$  and  $k_f$  were calculated for 36 different specimen dimensions by varying the micropost heights in a range: 5, 10, 20, 30, 40 and 50  $\mu\text{m}$  and micropost diameter in a range: 1, 3, 5, 7, 9 and 11  $\mu\text{m}$ . The nanowire diameter and height were kept constant to 80 and 600 nm respectively. The finite element simulation was carried out at 1 kV applied potential.

For a standard APT specimen, a linear correlation between  $\xi$  and  $k_f^{1/3}$  ( $\xi \approx k_f^{1/3}$ ) has been predicted numerically by several authors [164], [184] and this

trend has been also experimentally validated [165]. This third order relation is unable to describe the obtained behavior for our new specimen design (see Figure 72). Alternatively, we fitted the obtained data set with a slightly different power law function:  $\xi = a + b \times k_f^{\frac{1}{3} + c}$ , where a, b and c were the coefficients of the fit, equal to 0.611, 0.335 and 0.602 respectively (R-square > 0.99).

As a dependency of the relation  $\xi \approx k_f^{1/3}$  on the voltage was observed for a standard APT sample [184], a possible relation between  $\xi$  and V was investigated for our specimen design for a voltage range between 1 to 10 kV. The FEA analysis was performed for different micropost heights (5, 10, 30 and 50  $\mu\text{m}$ ) and diameters (2, 5, and 11  $\mu\text{m}$ ) corresponding to 12 different  $k_f$  values between 5 to 45 and the results show that unlike for the standard specimen design,  $\xi$  and V are uncorrelated (see Figure 73).

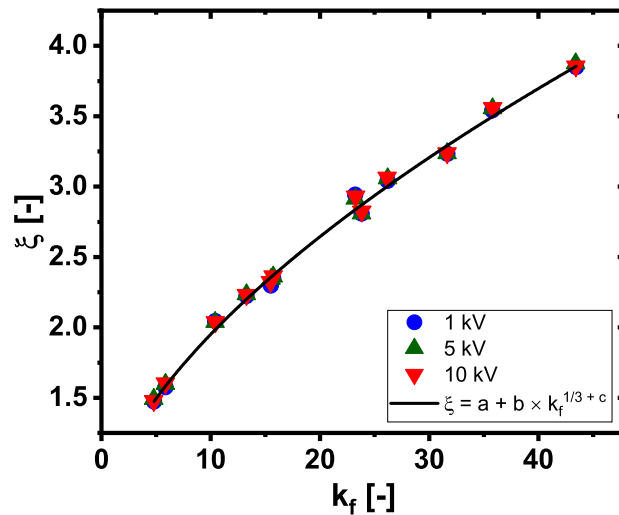


Figure 73: Correlation between image compression factor  $\xi$  and field factor  $k_f$  as a function of the applied potential V for a NW tip shape on top of cylindrical micropost. The applied voltage was varied from 1 to 5 and 10 kV and  $\xi$  was calculated at 12 field factors  $k_f$  corresponding to different micropost heights (5, 10, 30 and 50  $\mu\text{m}$ ) and diameters (2, 5, and 11  $\mu\text{m}$ ), while the nanowire diameter and height were kept constant to 80 and 600 nm respectively.

We also investigated the influence of nanowire dimension (both diameter and height) on  $\xi$ , since the nanowire dimension has a direct influence on the field enhancement at the tip apex (see Figure 66). This modification of the electric field could potentially influence the ion trajectories and the FOV during APT analysis. To investigate such a dependency, the image compression factor  $\xi$  was calculated for different nanowire dimensions.

In the first step, we study the influence of NW diameter on  $\xi$  by varying the NW diameter in a range between 40 to 160 nm, while the NW height was kept constant to 600 nm. We have repeated the same analysis of four different microposts having a height of 50  $\mu\text{m}$  and the diameters of 3, 5, 7 and 11  $\mu\text{m}$  and the results are reported in Figure 74a. Our analysis suggests that the diameter of NW has a positive influence on both  $\xi$  and  $k_f$ . However, the rate of increase in  $\xi$  depends on both  $k_f$  and the NW diameter, in which the variation of  $\xi$  as a function of  $k_f$  changes according to the NW diameter (different lines in Figure 74a). In

other words, the coefficients of the fit (a, b and c) for the previously obtained empirical relation between  $\xi$  and  $k_f$   $\left(\xi = a + b \times k_f^{\frac{1}{3}+c}\right)$  varies according to the NW diameter. The values of the coefficients of the fit used to describe the NW diameter dependence shown in Figure 74a, are reported in Table 9.

The influence of the NW length on  $\xi$  was also investigated using a similar approach. The NW height was varied in a range between 200 to 1600 nm, while the NW diameter was kept constant to 80 nm. The analysis was repeated for four different micropost dimensions and the results corresponding to  $k_f$  values below 35 are shown in Figure 74b. We observed that both  $\xi$  and  $k_f$  rise systematically as a function of NW height. As can be seen from Figure 74b, the NW height has a minor influence on the coefficients of the fit for  $k_f$  values below 20, whereby the  $\xi - k_f$  trend for all NW heights can be fitted with the same coefficients as used for the NW heights equal to 600 nm. However, for  $k_f > 20$  our empirical function is unable to accurately fit the simulated data points. It is worth noting that the reported deviation becomes even larger for higher  $k_f$  values, which are not shown in Figure 74b. Therefore, the coefficients of the fit  $\left(a, b \text{ and } c \text{ in: } \xi = a + b \times k_f^{\frac{1}{3}+c}\right)$  also depend on NW height for higher  $k_f$  values. In this study we did not further investigate any quantitative relation between the coefficients of the fit and dimensional parameters of NW and the dependency of these coefficients to both NW diameter and height have been only discussed qualitatively.

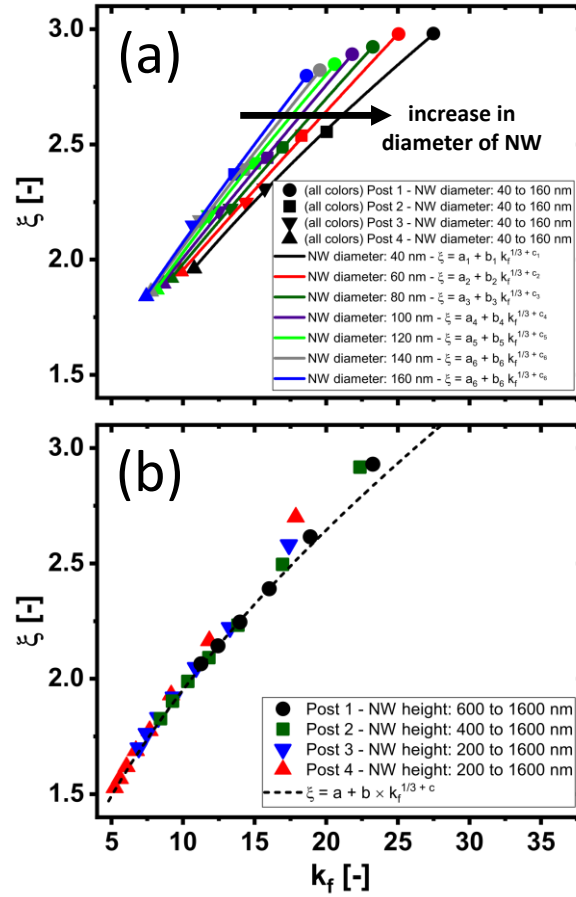


Figure 74: Influence of the nanowire dimensions on the image compression factor  $\xi$  plotted against the field factor  $k_f$ . (a) Influence of NW diameter on  $\xi$ . The NW diameter was varied in a range between 40 to 160 nm, while the NW height was kept constant to 600 nm. The finite element simulation of the ion trajectories and the calculation of  $\xi$  were repeated for four different microposts having a height of 50  $\mu\text{m}$  and diameters of 3, 5, 7 and 11  $\mu\text{m}$ , corresponding to post 1 to 4 in the legend. (b) Influence of the NW height on  $\xi$ . The NW height was varied in range between 200 to 1600 nm, while the NW diameter was kept constant to 80 nm. Note that only the NW height creating a  $k_f$  below 35, were reported in this figure.

Table 9: The coefficients used to fit the empirical correlation between  $\xi$  and  $k_f$  ( $\xi = a + b \times k_f^{\frac{1}{3}+c}$ ) for each data set shown in Figure 74.

Coefficients [-]	Nano wire diameter [nm]						
	40	60	80	100	120	140	160
a	0.751	1.204	1.159	1.161	0.963	1.080	1.043
b	0.258	0.087	0.102	0.102	0.175	0.134	0.145
c	0.317	0.605	0.571	0.584	0.451	0.528	0.518

To conclude, our FEA predicts that nanowire tip prepared on top of a cylindrical micropost can further compress the ion trajectories toward the detector center and can maximize the FOV during APT analysis (full tip imaging). To identify the dimensional window for the preparation of such specimen design whereby full tip imaging becomes possible, the influence of the micropost and the nanowire dimensions (diameter and height) on the image compression factor  $\xi$  and the field factor  $k_f$  have been studied. Our study predicts that the dimensions of both micropost and nanowire can have a significant influence on the field enhancement factor  $k_f$ . However, given the complexity of the NW preparation, its

weak mechanical properties and practical APT considerations, the usable range is confined to 60 - 100 nm for the NW diameter and an aspect ratio of about 10 to 15 (which also defines the length). For this range of NW diameters, only the micropost dimensions corresponding to a  $k_f < 25$  ( see Figure 74) can create the required electric field at the tip apex. It is worth mentioning that the specimens having  $k_f$  lower than 2 are not also suitable for APT analysis, since the bias at the entry of microchannel may influence the ion trajectories.

On the other hand, to compress the ion trajectories and enable full tip imaging, an image compression factor  $\xi > 2$  is required. Our analysis suggests that  $k_f$  and  $\xi$  are dependent parameters, in which  $\xi$  can be calculated by knowing  $k_f$  according to the obtained empirical function  $\xi = a + b \times k_f^{\frac{1}{3}+c}$ . Hence, for a NW having a diameter of about 80 nm and height of about 600 nm, only the micropost dimensions corresponding to  $k_f > 11$  could create  $\xi > 2$  and maximize the FOV.

Finally, we defined the optimum dimensions for the cylindrical micropost as an operation window whereby the selected values for diameter and height lead to an enough field enhancement and maximized FOV (full tip imaging) at the same time. This operation window for a NW with diameter of 80 nm and height of 600 nm is shown in Figure 75.

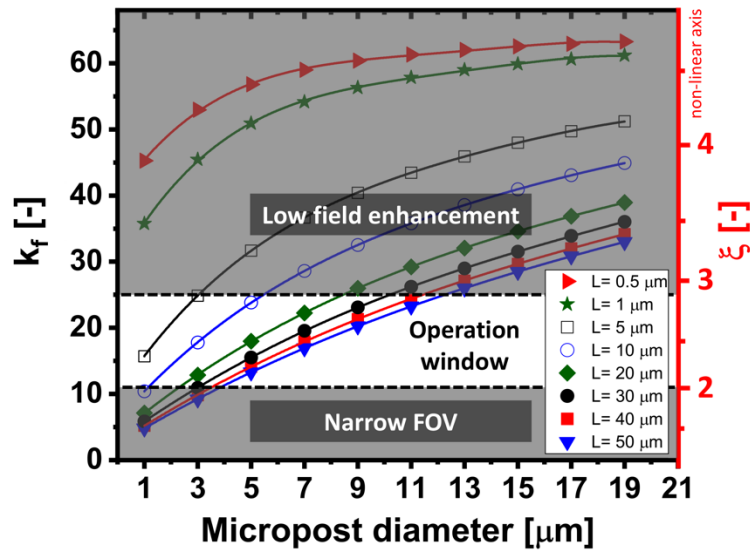


Figure 75: Required dimensions of the cylindrical micropost, which can create enough field enhancement at the NW apex and maximize the field-of-view during APT analysis. This window was calculated for a NW having a diameter of 80 nm and height of 600 nm. The criteria for identifying the operation window were based on:  $2 < \text{field factor } k_f < 25$  and image compression factor  $\xi > 2$ .

## 4.6.2 Specimen preparation

The experimental verification is based on the fabrication of structures with dimensions from the region highlighted in Figure 75. Since the target application for such a NW with the full FOV feature is to be used as a reference structure for APT, the repeatability of the specimen preparation is among the main aspects of our study. The standard FIB based technique does not have enough repeatability to prepare specimens with identical radius or shank angle and typically each specimen has a slightly different shape. Furthermore, preparation of a NW with a

zero degree shank angle is also a challenging task in FIB. Therefore, we propose a new specimen preparation process based on full wafer scale processing, which is based on standard lithography and etching techniques. Our developed process allows high throughput specimen fabrication in a reproducible fashion and with minimized tip-to-tip variations in terms of tip radius and shank angle. In addition, such a process allows high control and flexibility in the preparation of a nanowire with zero degree shank angle with no retained Ga dose. To experimentally evaluate the impact of the different micropost dimensions selected from the operational window reported in Figure 75, a unit cell consisting of 8 chips, each with a different micropost diameter (see Figure 76b) was designed for this purpose. By duplicating the unit cell over the area of a 4-inch wafer, 26 unit cells corresponding to 192 chips and 3072 microposts can be obtained by processing a single wafer. Our chip design was inspired from the standard CAMECA micro coupon, where the chip has a dimension of  $7 \times 3$  mm. We have slightly modified the chip design in the form of two staggered arrays consisting of 8 microposts at each side of the chip (see Figure 76c).

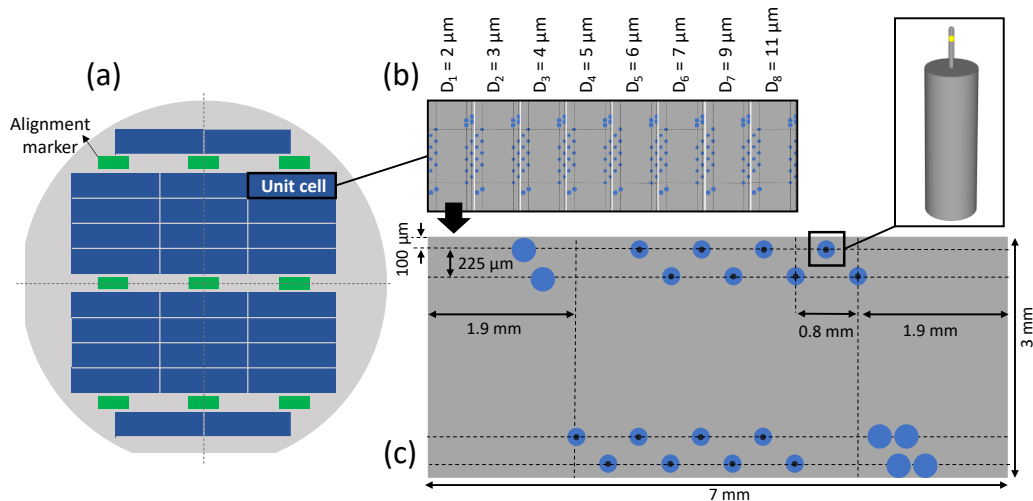


Figure 76: (a) Schematic representation of the 4-inch wafer design consisting of 26 unit cells, shown by blue rectangles. The green rectangles are the alignment markers for the different lithography steps. (b) Schematic representation of a unit cell consisting of 8 different cells each having a fixed micropost diameter from 1 to 11  $\mu\text{m}$ . (c) The chip design consists of 16 micropost in four staggered rows. Each row ends to a single or double circular fiducial to facility the navigation among different microposts using the APT tool.

Our process flow mainly consists of two main steps: the preparation of the nanowire and the micropost. The detailed description of the process flow is reported in Appendix B. We developed our process starting from the preparation of NW with a zero degree sidewall angle on a Si (100) wafer. For this purpose, electron beam lithography (EBL) was used to create a circular pattern (equal to NW diameter) from HSQ resist. Based on a fine EBL dose test, we could derive the optimum electron dose for patterning the HSQ resist in the form of a circular shape with a diameter close to the target value. The SEM image of the EBL pattern after the development is shown in Figure 77a. In the next step, reactive-ion etching (RIE) was used to etch the substrate and transfer the EBL pattern into a NW. To have a better control on the NW height, the recipe was fine tuned to obtain a relatively low etch rate of about 80 nm/min. In addition, the sidewalls

passivation was also optimized, by adjusting the gas flow and the ICP power, to minimize the side wall angles of the NW. With this process close control over the nanowire height and diameter can be obtained. The SEM image of four different NWs with diameters from 40 to 80 nm are reported in Figure 77b. Note that, due to the degradation of HSQ pattern during the etch process, our process is unable to prepare NWs taller than 650 nm. Further process improvement, including an additional hard mask (i.e. alumina) is required to overcome the limitations of the resist degradation and to reach taller NWs.

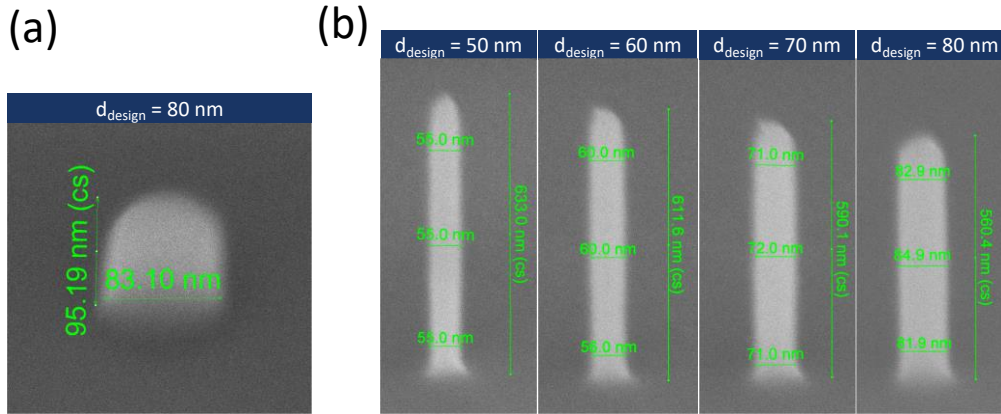


Figure 77: (a) SEM micrograph of a circular pattern of HSQ resist obtained by electron beam lithography (EBL). The target diameter for this pattern was 80 nm. (b) SEM micrograph of four different nanowires after the pattern transfer into the silicon (100) substrate by reactive ion etching technique. The target diameter for each NW is reported on top the of the SEM image. All SEM images were taken at 52° tilt angle using 5 kV in the immersion mode.

The micropost preparation process was developed based on the optical lithography and deep reactive-ion etching (DRIE). A 4-inch lithography mask was designed according to chip design shown in Figure 76. Alignment markers with a dimension ranging from 100  $\mu\text{m}$  down to 1  $\mu\text{m}$  were included in both the optical mask and the EBL design to allow a fine alignment of the optical lithography to the EBL pattern. To obtain a resist thickness of about 4  $\mu\text{m}$ , S1828 optical resist with the proper spinning parameters were selected for our processing. The exposure and development time were finely adjusted to maximize the lithography resolution and improve the lithography pattern towards a cylindrical resist pattern with vertical sidewalls. The SEM images of the patterned resist after the optical lithography process are shown in Figure 78a. We observed that the apparent thickness of patterned resists was thinner than that of the film thickness for cylindrical patterns having a diameter below 3  $\mu\text{m}$ . For instance, the patterned resist with a diameter of 3  $\mu\text{m}$  appeared about 20 % thinner than a pattern having diameter above 4  $\mu\text{m}$  (film thickness). For pattern diameters equal to 2  $\mu\text{m}$ , the apparent resists thickness was significantly thinner (above 50 %) and even the pattern shape strongly deviates from the cylindrical toward an ellipsoidal shape. In addition, we observed that the repeatability of the lithography process, in view of pattern shape and thickness, is poor for the pattern diameter equal to 2  $\mu\text{m}$ . This is mainly due to the resolution of the optical lithography for such a thick resist film where typically a resolution of about 1  $\mu\text{m}$  is reported for this technique using a

thin resist of about 1.5  $\mu\text{m}$ . Therefore, we excluded the preparation of microposts with a diameter of 2  $\mu\text{m}$  from our preparation process,

To etch deep into the substrate, deep reactive-ion etching (DRIE) using the Bosch process was selected as a viable approach since this is typically used in micro-electro-mechanical systems (MEMS) where the feature dimensions are also in order of some tents of micrometers. Further improvement of the standard recipe was required to adopt this process to small feature sizes (down to 3  $\mu\text{m}$ ) in our process as it normally leads to a roughness at the sidewalls which is too large for our purposes. Hence, we have finely reduced the etch step duration to 1.5 s, corresponding to an etch rate of about 80 nm per cycle. This resulted in the relatively smooth sidewalls. The developed recipe for our process is reported in Appendix B. The SEM images of micropost with a diameter of 5 and 3  $\mu\text{m}$  are reported in Figure 78b and c.

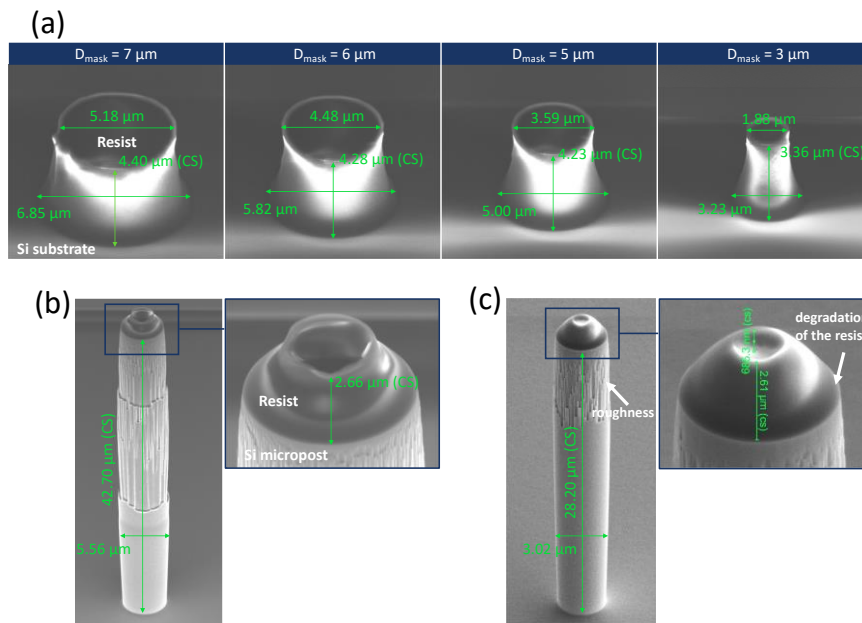


Figure 78: Preparation of a cylindrical micropost using optical lithography and deep reactive-ion etching (DRIE). (a) SEM micrograph of the patterned optical resist obtained from optical lithography process. The target diameter and the actual diameter of each pattern is shown in the figures. An etched micropost with the target diameter of 6  $\mu\text{m}$  (b) and 3  $\mu\text{m}$  (c) are shown. Note that due to the degradation of the resist at the edges of the pattern, a roughness on the micropost sidewalls develops and a slight reduction in the apparent micropost diameter was observed for tall microposts.

We have observed that due to the degradation of the resist thickness at the edges of the cylindrical resist pattern, a surface roughness appeared at the sidewalls of the microposts having a height  $> 20$   $\mu\text{m}$  (see Figure 78b and c). This degradation resulted in a slight deviation of the micropost diameter from the target value for the taller micropost (height  $> 20$ ), similar to what has been shown in Figure 78b. For pattern diameters equal to 3  $\mu\text{m}$ , the resist degradation became a limiting factor to reach micropost heights more than 30  $\mu\text{m}$ . Since the field enhancement at the micropost sidewalls is limited as compared to the nanowire apex, we do not expect that the presence of such a surface roughness on the micropost sidewalls results in any evaporation event. Hence no further optimization of the roughness was pursued.

The SEM images of one of the specimens prepared according to developed process is reported in Figure 79. We prepared several chips each having 16 microposts with a fixed micropost diameter (from 3 to 11  $\mu\text{m}$ ) and height (14 or 36  $\mu\text{m}$ ), while the NW dimension was kept fixed for all the coupons to a diameter of about 80 and a height of 600 nm. It is worth mentioning that the alignment between the EBL pattern (for the nanowire) and lithography mask (for the micropost) was carried out using the mask aligner, where the mask-to-wafer position was adjusted by the mechanical/pneumatical control. As a result, we observed a misalignment of about 200 nm and 700 nm in x,y directions between the NW position and the center of micropost.

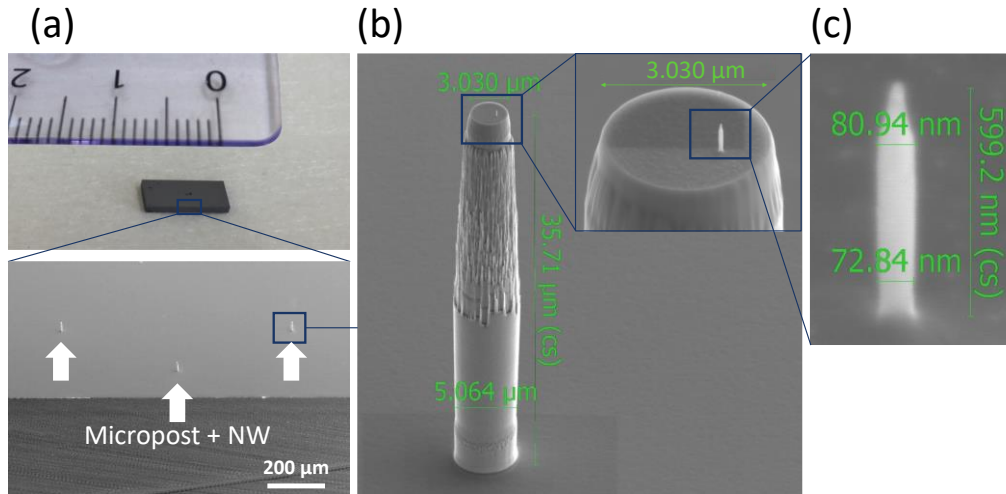


Figure 79: A final APT specimen consisting of a nanowire prepared on top of a cylindrical micropost with the dimensions according to the FEA. (a) Image of the prepared chip in the form of micro coupon consisting of 16 microposts. The inset shows the SEM image from the edge of the prepared chip, where the three microposts can be seen. (b) SEM image of one micropost with the NW prepared on the top. The micropost had a diameter and a height of 5 and 35  $\mu\text{m}$  respectively. Since the edges of the micropost were smoothed by FIB, a reduction in the micropost diameter (to 3  $\mu\text{m}$ ) on the very top part of the post is observed. (c) Enlarged view of the NW prepared on the top of micropost with a design diameter of 80 nm and height of 600 nm. The NW was cleaned by FIB to ensure the complete removal of the oxide resist from the top region of the NW. This caused a tapered shape on the first 80 nm of the NW. All SEM images were taken at 52° tilt angle using 5 kV.

### 4.6.3 Experimental proof of full tip imaging

- To experimentally validate our finite element analysis and prove the feasibility to maximize FOV (full tip imaging) in APT using our specimen geometry, we have performed several APT analyses using our fabricated coupons in a LEAP 5000 XR. Using the available microscope within the system selection of one specific tip and its alignment in front of the local electrode is pretty simple following the standard procedures. The specimen and laser alignment for two coupons having heights of 35 and 14  $\mu\text{m}$  are shown in Figure 80. The specimen alignment for the short micropost (14  $\mu\text{m}$ ) was quite challenging as the flat area of micro coupon became very close the local electrode. Due to the high risk of damaging the local electrode during the specimen alignment or the measurement, we did not proceed with the laser alignment on such a short micropost height.

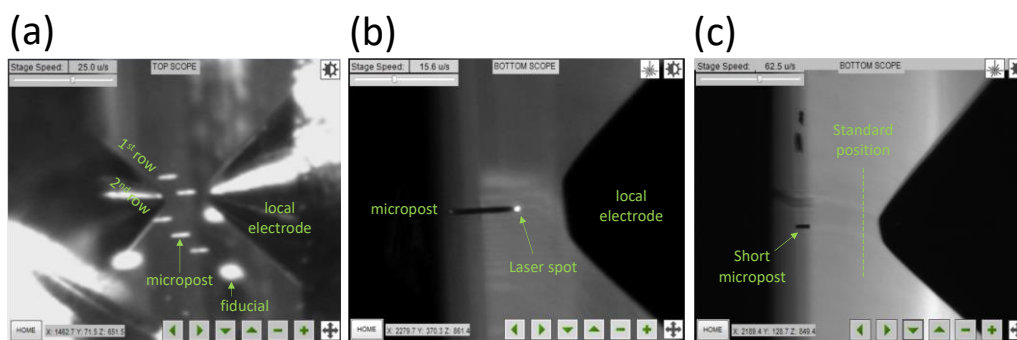


Figure 80: Laser and specimen alignment for the microcoupons with a nanowire tip on top of a cylindrical micropost. (a) Navigation from one micropost to another micropost following the standard procedure suggested by CAMECA for the standard micro coupons. Note that there were two missing microposts in the first row. (b) Alignment of 35  $\mu\text{m}$  long micropost in front of local electrode. The laser alignment was also carried according to the standard procedure. (c) Difficulty in the alignment of a short micropost (14  $\mu\text{m}$  long), where the local electrode became very close to the flat area of the micro coupon.

We proceeded with the APT measurement on five different micropost having a diameter of 11, 9, 7, 5 and 3  $\mu\text{m}$  and height of about 36  $\mu\text{m}$ . For these microposts the NW dimension was fixed to a diameter of 80 nm and height of 600 nm. For the large micropost diameters (11, 9 and 7  $\mu\text{m}$ ), the auto laser scan and fine specimen alignment were not successful. In particular, the ion emission was only detected at a relatively high applied potential (>10 kV) and the detected events extended erratically over a large area on the detector position instead of displaying the common circular shape. Potentially these random emissions originated from the sharp edges of the micropost acting as secondary tips. As such these edges were smoothed by FIB which however did not improve the APT measurement. The SEM inspection after these unsuccessful specimen alignments, showed that the NW was detached from the post in all the cases.

For the smaller micropost (diameter of 5  $\mu\text{m}$ ), the APT measurement was started smoothly at a potential of about 4 kV. The SEM image of this specimen before APT measurement (Figure 80a) shows that the top 145 nm of the NW had a tapered shape with an initial diameter of about 25 nm and the rest of the NW height had a zero degree shank angle with a diameter equal to the design diameter (80 nm). This tapered shape was induced during the FIB clean of the NW to remove remaining oxide resist. The APT measurement was carried out at a pulse frequency of 250 kHz, detection rate of 0.4 % and the base temperature of 50 K. The 40 pJ laser power used in this experiment corresponds to a Si CSR of about 9 % ( $\text{Si}^{++}/(\text{Si}^{2++} + \text{Si}^+)$ ).

The 3D data reconstruction of the data was carried out in IVAS software using the tip profile (SEM image of the NW). The  $\xi$  was finely adjusted to a value of 3.8, in order to match the diameter of the reconstructed data to the NW diameter (80 nm). The 3D reconstructed data together with the SEM image of NW are reported in Figure 81. Since the auto laser scan was accomplished after the detection of about 1.7 M events, the top part of the NW corresponding to about 1.7 M atoms was excluded from the reconstructed data. The height of this region of the NW (region I in Figure 81a) was estimated to be about 75 nm from the SEM image based on the number of detected atoms ( $\sim 1.7$  M) and the detection efficiency (52 % in LEAP 5000XR). As can be seen, the 3D

reconstructed data consists of a tapered region (Region II) and the zero degree-shank angle region (Region III), which have a height of about 70 and 115 nm respectively. These two heights were also highlighted on the SEM image of the NW. The obtained height from the 3D APT data reconstruction matches well the tapered height measured by the SEM image. To visualize the core center of reconstructed data, a section cut of reconstructed volume along the y plane (passing from  $y = 0$ ) is shown in Figure 81c. The section indicates that the reconstructed tip consists of a core central silicon region surrounded by a thick silicon oxide shell. By assigning the oxide shell to the native oxide and the core Si to Si NW, this measurement could potentially suggest that the full tip imaging was achieved. The formation of the thick oxide shell will be discussed later in this section.

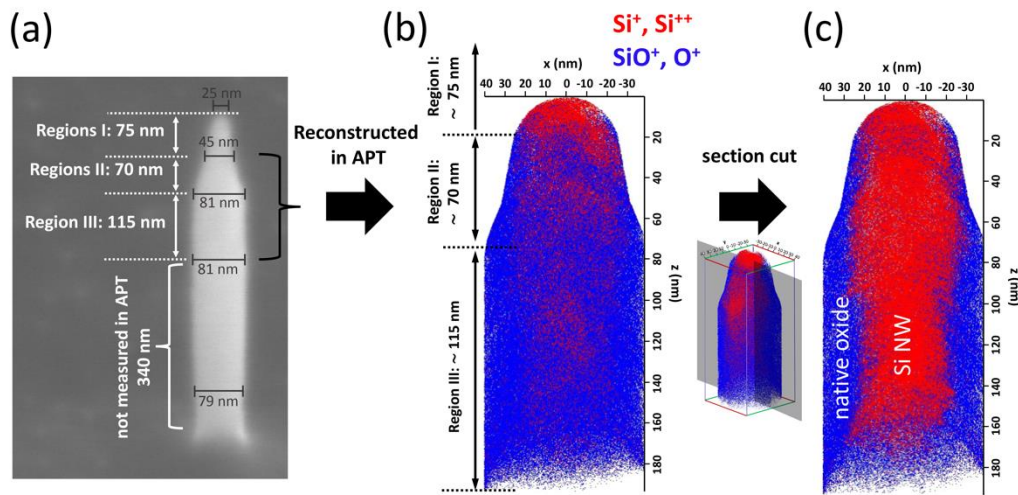


Figure 81: The 3D reconstruction of the APT data obtained from a NW tip prepared on top of cylindrical micropost having a diameter of about  $5 \mu\text{m}$  and height of  $36 \mu\text{m}$ . (a) SEM image of the NW before APT measurement. Three different regions are highlighted on the SEM image: Region I: the unreconstructed top part of NW corresponding to 1.7 M detected events before the auto laser alignment was completely achieved. The height of this region was calculated from the SEM image. Region II and II: tapered and zero degree-shank angle regions of the NW corresponding to 17.3 M detected ions. The height of these two regions were obtained from the APT reconstructed data. (b) 3D reconstruction of APT data, where  $\text{Si}^+$  and  $\text{Si}^{++}$  ions are represented by the blue dots and  $\text{O}^+$  and  $\text{SiO}^+$  ions by the red dots. (c) To visualize the core central region of the reconstructed tip, a section cut along the y plane (with  $y = 0$ ) is plotted.

To confirm the full tip imaging and validate the reconstructed tip shape/volume, the number of detected atoms were compared to the actual number of atoms expected from the corresponding volume of the Si NW. To do so, the number of detected atoms (ranged atoms) from each region of the reconstructed data were extracted from the ion sequence. The results are for the not reconstructed region (region I) 1.7 M ions, for the reconstructed region (region II):  $\sim 3.8$  M atoms and for the shank region (region III):  $\sim 13.5$  M atoms. Then by considering the detection efficiency (about 52 % in LEAP 5000XR) the corresponding number of atoms in the reconstructed volume were calculated and are reported in Table 10. These numbers can be compared to the estimated number of atoms in the NW based on the dimensions in the SEM image of the NW (see Figure 81a).

Table 10: Comparison between the number of atoms detected in APT and the actual number atoms expected from the NW within the reconstructed volume. The expected number of atoms were estimated from the SEM image.

Parameters	Region I: Not reconstructed	Region II and III: Reconstructed data tapered region (II) & shank (III)
Height [nm]	~ 75	~ 185
Detected ions [M ions]	~ 1.7 (ions)	~ 17.4 (decomposed atoms)
Detected ions $\times$ detection efficiency [M ions]	~ 3.3 (ions)	~ 33.4 (decomposed atoms)
Estimated N of atoms from SEM [M atoms]	~ 3.6	~ 36.7
Difference between the number of atoms extracted from SEM and APT	~ 8 %	~ 9 %

Our analysis indicates that the estimated number of atoms from the SEM image is only about 9 % higher than the extracted number of atoms from APT measurement (considering the detection efficiency). This implies that the majority of the ions evaporated from the NW were projected within the detector area suggesting a FOV approaching the full tip imaging. This can be compared to a standard tip analysis in LEAP 5000XR, where the FOV is constrained to  $\sim 50^\circ$  acceptance angle implying that the reconstructed volume contains only about 60 % of the specimen volume. The 9 % mismatch between the extracted number of atoms from APT and SEM can be attributed to the calculation errors originated from the limited resolution of SEM image and some extreme trajectories which do not reach the detector.

To further investigate the distribution of the detected ions and to explore the projection of the observed thick oxide shell in the reconstructed data, the 2D density and concentration maps (atomic concentration) were plotted for a part of the NW from the shank region (height of 100 to 150 nm) in Figure 82.

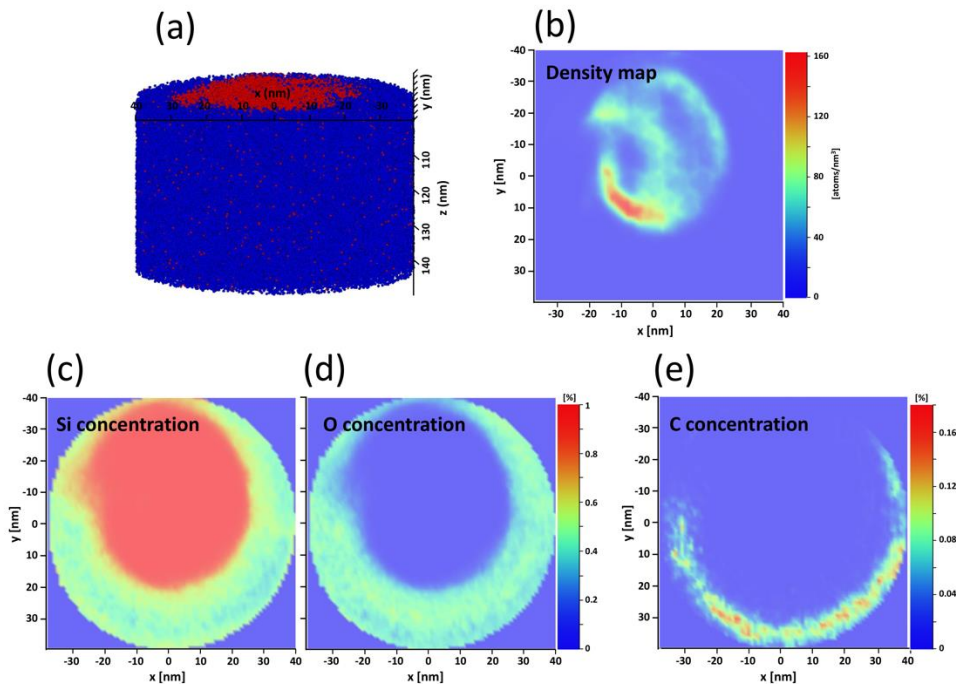


Figure 82: 2D density and concentration maps plotted for a slice of the NW from a height of 100 nm to 150 nm (a). (b) The 2D atomic density map for all decomposed atoms: Si, O and C. The 2D atomic concentration maps were also plotted for Si in (c), O in (d) and C in (e).

The 2D density map in Figure 82b indicates that the oxide shell has a negligible density ( $< 3$  atoms/nm<sup>3</sup>) as compared to the core Si region (between 30 to 180 atoms/nm<sup>3</sup>). Note that, the average tabulated atomic density for crystalline Si is about 50 atoms/nm<sup>3</sup>, in which by considering the detection efficiency (52 % in LEAP 5000XR) an average atomic density of about 26 atoms/nm<sup>3</sup> is typically expected in APT analysis of Si. In our measurement, the core central region of the NW had an average density of about 51 atoms/nm<sup>3</sup> (190 % higher than 26 atoms/nm<sup>3</sup>) and for the oxide shell this density was about 2 atoms/nm<sup>3</sup>. This implies that the core central volume of the reconstructed data was further compressed (compression of about  $51/26 = 1.9$ ) and the oxide shell was much expanded (compression factor of about  $2/23 = 0.17$ , by taking the reference atomic density of oxide shell equal to 23 atoms/nm<sup>3</sup>). As reported in Table 11, by keeping the NW height fixed to the reconstructed value, the compression factor can be calculated also for the diameter/thickness of the Si core and oxide shell (instead of the compression factor for volume).

Table 11: Comparison between the average atomic density obtained from APT 3D data reconstruction of a slice of NW shown in Figure 82a. The standard atomic density of the native oxide is assumed to be equal to thermally grown silicon dioxide ( $2.3 \times 10^{22}$  atoms/cm<sup>3</sup>). The compression factor for the volume was calculated based on the ration between obtained average density and the standard atomic density multiplied by the detection efficiency. For the fixed number of atoms and the NW height, the compression factor for the diameter was calculated as the square root of that of volume. Finally, the dimension of a NW having the standard atomic density and the same number of detected atoms was estimated by multiplying the reconstructed values of diameter/thickness by the calculated compression factor.

parameters	Region of the tip	
	Silicon core	Oxide shell
Obtained average atomic density [atoms/nm <sup>3</sup> ]	51	2
Standard atomic density $\times$ detection efficiency [atoms/nm <sup>3</sup> ]	$50 \times 0.52$	$23 \times 0.52$
Density compression factor calculated for the volume [-]	1.9	0.17
Density compression factor calculated for the diameter/thickness [-]	1.4	0.41
Reconstructed average diameter/thickness [nm]	$\sim 54$	$\sim 13$
Estimated average diameter/thickness according to standard density[nm]	$\sim 75.6$	$\sim 5.3$

Finally, by implementing the obtained compression factors into the core/shell region of the reconstructed APT data, one can approximately estimate the corresponding diameter of a NW having the standard atomic density (keeping the height fixed to the reconstructed value) to be about 75.6 nm and the oxide thickness of about 5.3 nm. Although the estimated thickness of oxide shell is much thicker than that of actual native oxide, our density analysis confirms that the entire NW was in FOV during APT analysis.

To further investigate, the properties of the oxide shell, the 2D concentration map of Si and O were also reported in Figure 82c and d. The concentration maps confirm that the core central region of the reconstructed data consists of about 100% of Si, while the O concentration in the oxide shell varies from 35% to 65 %. This is slightly lower than what is expected from the native oxide, where the first 7 Å of the oxide (in Si side) is known to be SiO<sub>2</sub> layer and the rest consist of SiO<sub>x</sub> layer ( $x < 2$ ) [186]. This underestimation of O content might be due to the

trajectory aberration and partial projection of Si ions evaporated from core Si region toward the outer shell region of the reconstructed data. In addition, the 2D concentration maps of Si and O (Figure 82c and d) indicate that the concentration of O in the oxide increased from 35% to 65 % as a function the radial distance from the reconstruction center. This suggests that a part of the Si ions close to the native oxide might be projected within the oxide shell (trajectory aberration). Such a trajectory aberration could explain why the average density of oxide shell was higher than the expected value, which also resulted in the higher oxide thickness in Table 11. In addition, the 2D concentration map of the C atoms (Figure 82e) indicates that a C reach region (about 10% in concentration) exist at the outer most region of the oxide shell. Since the C is normally located on the outside of the NW on top of the oxide shell, this also confirms the full tip imaging in this APT measurement. The C could originate from ambient contamination and/or etch residues on the NW.

To further investigate the projection of the native oxide of the sidewall in the form of a thick, less dense oxide layer in the reconstructed data (see Figure 81c), finite element analysis of ion trajectories has been carried out with the exact NW and micropost dimensions as analysed in this APT measurement. In our FEA analysis the apex was assumed to have a hemispherical shape and the image compression factor ( $\xi$ ) was calculated at 20 different radial positions across the apex radius. As discussed in the previous section,  $\xi$  can vary also along the analysis depth with a rate which mainly depends on the micropost dimension (see Figure 74). Hence, we repeated the FEA of  $\xi$  for two different heights of NW (340 and 455 nm) corresponding to the initial and the end height of the shank region in the 3D reconstructed APT data and the results are reported in Figure 83.

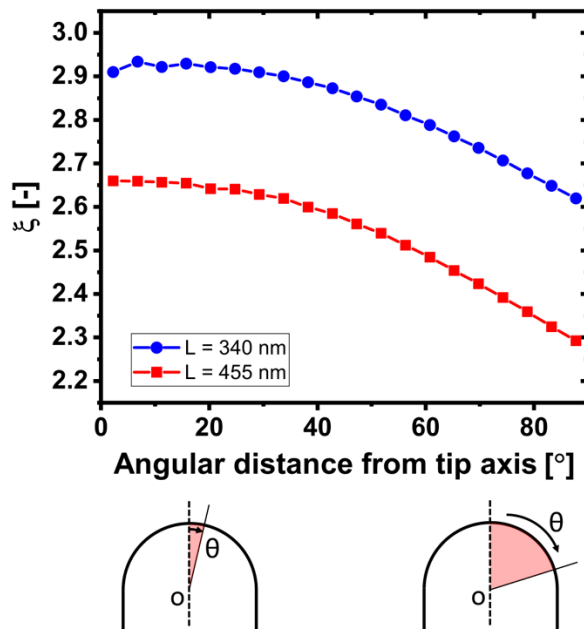


Figure 83: Estimated image compression factor ( $\xi$ ) as a function of angular distance from the specimen axis (launch angle) for two different NW heights corresponding to the initial and the end height of shank region in the 3D reconstructed APT data (height of 344 and 455 nm). The calculation of  $\xi$  was obtained by finite element simulation of ion trajectories.

Our FEA suggests that  $\xi$  drops along the analysis depth, in which the average  $\xi$  (average across different launch angles) drops about 10% as the NW height was reduced from 455 to 320 nm. This can partially explain the observed reduction in the diameter of the dense Si core region along the reconstructed height (see Figure 81c). In addition, since the NW was not prepared exactly at the center of micropost, further compression/distortion in the reconstructed data can be expected due to asymmetric electric field distribution around the specimen.

In addition, the predicted variation of  $\xi$  across different launch angles of a hemispherical apex shape in Figure 83, suggests that the ion trajectories become less compressed as the radial distance from the tip apex increases. This implies that the projection of ions evaporated from a large distance from the specimen axis (large launch angle) will have a higher magnification as compared to those evaporated from the central core area of the apex (small launch angle). Hence the rate of change in  $\xi$  rises sharply at the angular distance of about  $40^\circ$  (see Figure 83).

Although this behavior suggests that reconstructing the APT data using a single  $\xi$  (currently available algorithms) should result in a gradual reduction in the reconstructed density towards the side walls of the NWs and the appearance of native oxide thicker (with lower density) than the actual thickness, the experimentally observed abrupt variation in the density between the Si core and oxide shell cannot be explained by our FEA. A potential explanation lies in the fact that the actual apex shape after APT analysis is far from having hemispheric shape as assumed in our analysis. Such an apex shape after APT measurement is not unusual as for voltage as well as laser mode measurements, whereby typically an ellipsoidal tip shape with a higher curvature towards the specimen edge have been reported [127],[185]. Also TEM images of the analyzed APT tips typically indicated a truncated hemispherical shape confined to  $120^\circ$  rather than  $180^\circ$  corresponding to a hemispherical apex shape [187], [183]. Such a difference between the assumed hemispherical and actual apex shape could potentially influence the variation of  $\xi$  across the different launch angles. Nevertheless, such an experimentally observed thick oxide layer and observed abrupt variation in the density between the Si core and oxide shell cannot be completely explained by the gradual variation of  $\xi$  across different launch angles. This might be partially attributed to the trajectory aberration caused by the differences in the field evaporation of Si and SiO<sub>2</sub>, similarly to what has been reported for SiGe fin embedded in SiO<sub>2</sub> by Melkonyan D., et al. [13].

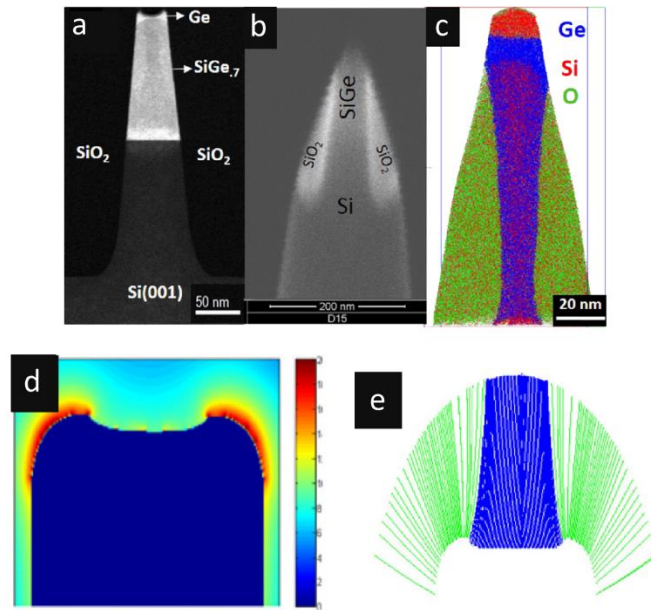


Figure 84: Reconstruction artefact induced due to the differences between the field evaporation of Si (or Ge) and SiO<sub>2</sub>. (a) Cross-sectional dark-field scanning TEM image of the SiGe fin before APT specimen preparation. (b) SEM image of the APT specimen prepared from the SiGe fin. (c) 3D reconstructed APT data, where the Ge, Si and O atoms were represented by blue, red and green dots. The fin width in the reconstructed data is smaller than the actual value. (d) Estimated tip shape and electric field distribution by finite element simulation. (e) Ion trajectories evaporated from one atomic row above the calculated apex shape, where the ion trajectories from the SiO<sub>2</sub> and fin region are shown in green and blue respectively. The figure is reported from reference [13].

As can be seen from Figure 84, due to the lower field evaporation between SiGe fin and SiO<sub>2</sub> region, the apex develops into a shape deviating substantially from the so called hemispherical shape. This results in the distortion of the ion trajectories and the appearance of artefacts in the 3D reconstructed data as this reconstruction is based on a hemispherical tip shape, whereby the ion trajectories originating from the fin region were compressed leading to a fin having a smaller width and higher density with respect to the actual values. In addition, the compression of the fin region increased along the analysis depth, which resulted in a negatively tapered fin versus the actual positively tapered one.

In our full tip imaging of the NW, we have a similar configuration as the embedded fin in oxide. Hence it is not surprising that we observe a similar compression in the core Si NW region and that the reconstructed density of this region was higher than the actual density and diameter of NW (similar to fin width) was reduced along the analysis depth. Since, our experiment is the first full tip imaging in the history of APT, the projection of the native oxide from the specimen side wall is currently unknown in APT analysis. A further numerical investigation including the evaporation field of Si and native oxide is required to better understand the projection of the native oxide of the specimen side wall in APT. In addition, the TEM image of the NW after the APT measurement could provide an insight about the apex shape and possible local variation of apex shape close to the sidewalls.

We also evaluated the degree of agreement between the FEA of the electric field and the observed behavior in the APT experiment. To do so, the FEA analysis has been performed on the exact NW and micropost dimension used in

this APT measurement. As discussed earlier in Section 4.6.1, FEA predicts that field factor ( $k_f$ ) gradually rises along the analysis depth for our NW tip design (see Figure 66). The FEA analysis of the zero degree-shank angle region of the prepared specimen predicted that  $k_f$  gradually rises from 17.7 to 21.4 as the NW height reduces from 455 to 340 nm, corresponding to the initial and end of the 3D reconstructed data in the shank region. To compare the predicted trend of  $k_f$  and the experimentally observed value along the APT analysis, the experimental voltage curve and the predicted trend by the FEA are plotted in Figure 85. Since our FEA only includes the calculation of the electric field and the ion trajectories, the direct estimate of the voltage curve is not available using our model. Hence, to extract the predicted voltage curve in our FEA, the experimental voltage at the ion sequence of 5.7 M atoms (initial part of null-shank angle region) was used to plot the predicted variation of electric potential along the NW height, according to the numerically predicted variation of  $k_f$  along analysis depth.

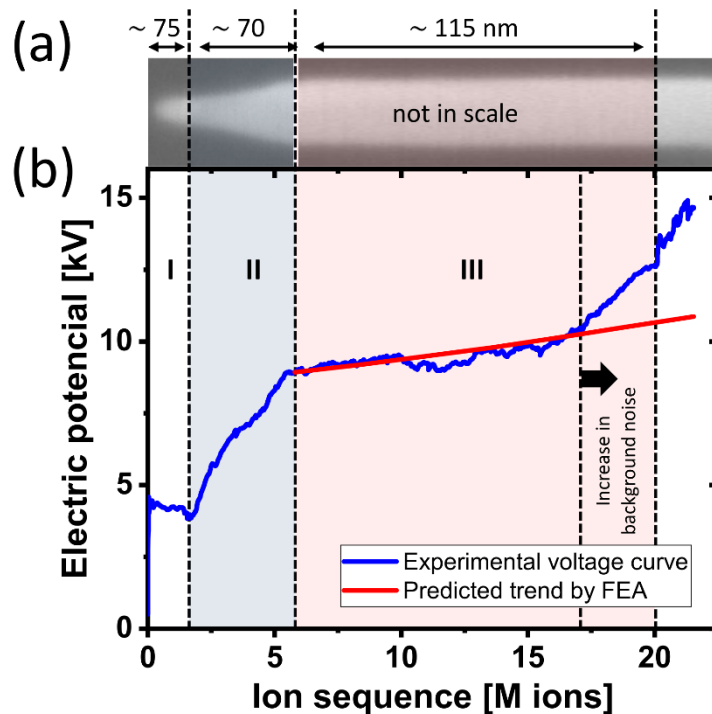


Figure 85: Applied potential during APT analysis. (a) Different regions of the NW heights were used to construct the schematic representation. The height of region I (not reconstructed part) was estimated from the SEM image of the tip, based on the number of ions detected before the complete laser alignment. While, the height of region II (tapered region) and III (null-shank angle) were extracted from the 3D reconstructed data. (b) The experimental voltage curve is plotted in blue and the predicted voltage curve by FEA in red. The trend was only calculated for shank region of the tip (region III) and the calculation was based on the simulated field factor ( $k_f$ ) for NWs having different heights (similar to different sequences of evaporation) and knowing the experimental voltage at the ion sequence of 5.5 M.

The experimental voltage curve and the predicted trend have a reasonable agreement (maximum deviation about 5 %) for ion sequences up to 17 M. Hence, the FEA analysis of electric field matches the experimental values for the majority of NW height in the shank region (about 80 % of the height). For ion sequences  $>$  17 M, the experimental voltage curve diverged rapidly from the predicted trend by FEA. To better understand this experimental result, the detection rate and the collected mass spectrum were further investigated. We observed a linear increase

in the background noise level of the mass spectrum/time-of-flight, for the ion sequences  $> 17$  M. The collected mass spectrum together with the background noise level in the time-of-flight are reported in Figure 86. Since we did not observe any significant change in the detection rate or the CSR along the measurement, such an increase in the background level cannot be attributed to the increase in electric field at the tip apex. Often such an increase in background noise is a precursor to tip rupture and less well understood.

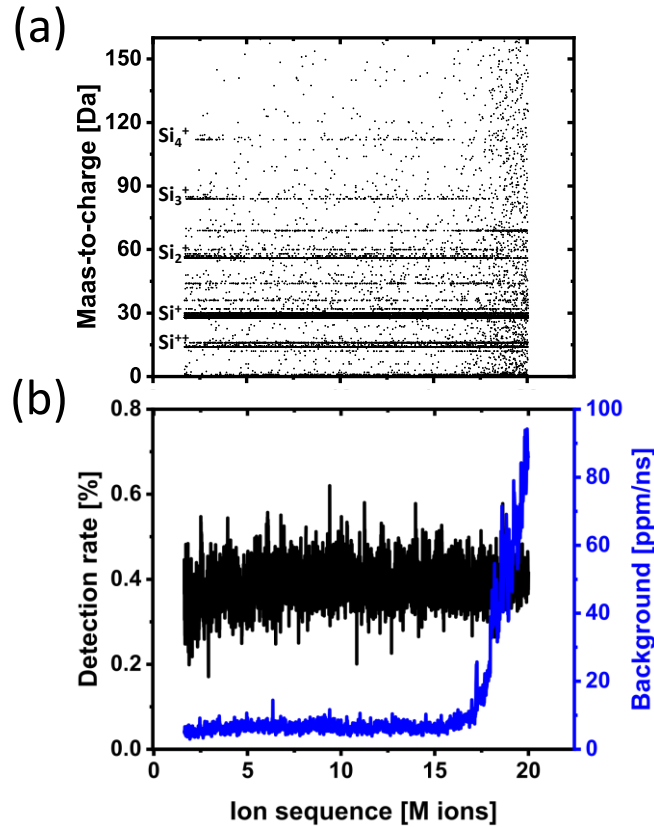


Figure 86: Increase in the background noise for mass spectrum/time-of-flight for ion sequences  $> 17$  M. (a) The collected mass spectrum versus ion sequences. The major Si peaks are also identified on the figure. (b) Detection rate (in black) and background level for time-of-flight (in blue) are plotted versus ion sequence. The background level raised markedly for ion sequences  $> 17$  M, while the detection rate remained unchanged.

## 4.7 Conclusion

In this chapter in order to describe the FOV in APT analysis, the distribution of the electric field in the vicinity of tip apex (near field) and in between the tip and detector (far field) together with ion trajectories have been discussed on the mesoscopic and microscopic scales.

It has been shown that by considering the apex as a smooth hemisphere and neglecting the atomic roughness, the strength of electric field can be estimated using the field factor  $k_f$ . This mesoscopic approach does however underestimate the actual strength of the electric field on the atomic scale. A quantum mechanics-based calculation indicated that there is a local concentration of electric charges at the protruding atoms on the surface, which causes a local field enhancement at these protruding regions. To account for the microscopic atomic roughness, an

additional local field enhancement factor  $\gamma$  (over the average field estimated by  $k_f$ ) has been introduced which has typically a value between 1.5 to 2. Finally, to accurately estimate the distribution of the electric field in the vicinity of the tip surface, one needs to consider both the real tip shape (mesoscopic scale) and the arrangement of surface atoms (atomic scale). In addition, the trajectories of evaporated ions toward the AP detector were discussed in detail. Finite element simulation has been shown to allow the calculation of ion trajectories at both mesoscopic and microscopic scales. Alternative, point-projection model has been introduced as a robust technique to estimate the ion trajectories by image compression factor  $\xi$ .

Finally, 3D data reconstruction in APT was briefly introduced. The main reconstruction parameters and their state-of-the-art calibration technique have been discussed in detail. In addition, some limitations of the currently available protocols to 3D reconstruct back the actual arrangement of the atoms on the original specimen surface and the formation of reconstruction artefacts were also briefly introduced.

The FOV for a hemispheric tip shape was shown to be the core central region of the specimen, which varies from specimen-to-specimen according to the distribution of electric field lines and thus ion trajectories. The FOV for a hemispheric tip shape can be accurately identified from the reconstructed 3D data, provided that the data reconstruction was carried out according to the calibrated reconstruction parameters. Any deviation of the apex shape from an atomically smooth hemispherical shape results in modification of the ideal ion trajectories, which can potentially influence also FOV.

We have studied in detail the FOV for an asymmetric tip shape as induced by UV laser since this is one of the most common examples where the apex shape can strongly deviate from the hemispheric shape. Our study indicates that in UV-assisted APT, the center of the FOV dynamically shifts toward the shadow side of the tip as it projects the ions from the top most region of the specimen always at the detector center. The shift in FOV depends on the degree of asymmetry induced on the apex shape and can be estimated from the distance between the specimen axis and the detector center line on the TEM image. The detector center line can be identified on the specimen TEM image as a vertical line parallel to the tip axis and passing through the local maximum of the specimen.

In order to maximize the FOV and probe the entire specimen volume in APT, we proposed a new design for an APT specimen, which consists of a zero degree-shank angle nanowire prepared on top of a cylindrical micropost. The feasibility of full tip imaging, using our new specimen design, has been proven both numerically and experimentally. Our FEA analysis indicates that the presence of a flat area on micropost below the NW compresses the ion trajectories towards the detector center such that the ions evaporated from the sidewalls of the NW still hit to the detector. We numerically investigated the optimum dimensions (diameter and height) for the preparation of both NW and micropost which allow full tip imaging and create enough electric field enhancement at the apex of the NW.

Such standardized tip shape is also extremely helpful in fundamental studies (i.e. tip-laser interactions) as they allow to eliminate variability contributions in ion-beam damage, retained Ga dose and distribution, tip geometry, heat transfer (shank angle), etc.

In addition, we developed a preparation process, based on standard lithography and etching techniques. The process allows to prepare multiple APT specimens in a reproducible fashion and with minimized tip to tip variations in view of tip radius and shank angle. We fabricated the NW tip shape (zero degree shank angle) on top of a cylindrical micropost according to the exact dimensions suggested from the FEA.

Finally, the APT analysis of the prepared NW tip, proved the full tip imaging feature for such a specimen design, whereby the native oxide of the NW (i.e. side walls) was within the FOV. Our analysis of the number of detected Si atoms versus the estimated number of actual atoms from the SEM image, also confirms the full tip imaging feature in our measurement. We have observed different forms of distortions in the 3D reconstructed data. For instance, the native oxide was projected as a thick layer ( $> 15$  nm) having a very shallow density and the Si as the very dense with a small diameter. By correcting the density to the standard values, we demonstrated that the thickness of Si and the native oxide reached quite close the observed dimensions on the SEM image. Finally, we attributed part of the observed artefacts to the trajectory aberration induced by the high field native oxide shell around the NW.

## Chapter 5

# Atom probe tomography on blanket films

As discussed earlier, the combination of sensitivity ( $<10$  ppm), 3D-spatial resolution and mass identification (isotope selectivity) makes APT a unique competitor for the analysis of 3D nanoscale structures and devices. However, as a recently emerging technique, APT completely lacks standardization, traceability and assessment of its uncertainty budget in view of both quantification and reconstructed 3D morphology. The repeatability and reproducibility in the APT analysis of bulk heterogeneous systems are not well evaluated and they are expected to be worse for more complex heterogeneous systems, including 3D nanostructures or multilayers. In addition, insight in some of the fundamental physics underpinning APT such as laser-tip interaction and preferential detection of one species, are still lacking and need to be investigated.

In order to establish APT as a reliable and traceable metrological technique for quantification and accurate 3D reconstruction of elemental distribution in 3D nanostructured devices and layers, many technical aspects need to be further developed. In view of reliable quantification, several essential steps require further development: development of bulk calibration standards, evaluation of accuracy, repeatability and reproducibility of APT analysis in bulk heterogeneous materials and eventually development of the uncertainty budget for such an analysis.

Regarding the 3D data reconstruction, the traceable calibration of all the reconstruction parameters (with their associated uncertainties), the accurate evaluation of apex shape along the analysis depth (both in mesoscopic and microscopic scale) and the further improvement in the reconstruction protocols (to account for the actual tip shape) are among the required improvements to advance APT towards a reliable and traceable metrological tool for the analysis of 3D heterogeneous nanostructures.

In this study we tried to address and resolve the following issues: the lack of reference material (calibration sample), the evaluation of repeatability and accuracy of APT on bulk heterogeneous system and the unknown reconstruction volume or field-of-view (FOV). The latter has been discussed in Chapter 4, where the zero degree-shank angle nanowire tip shape prepared on top of a cylindrical micropost was introduced to maximize the FOV (full tip imaging). As shown, in this configuration, the sidewalls of the NW can be employed as a reference during the data reconstruction. This eliminates the unknown reconstruction parameters (FOV) and can potentially allow the calibration of detection efficiency by comparing the estimated number of atoms within the NW volume (from TEM) and the atoms detected during the APT analysis.

In this chapter we will discuss APT analysis of B doped SiGe thin films. In Section 5.1, we will introduce a B doped SiGe film sandwiched between Si as the wafer for the development of a potential reference material for APT. We will discuss several complementary analyses to quantify the B and Ge concentration and the corresponding depth profiles. The APT specimen preparation from this well characterized heterogeneous system will be discussed in Section 5.2.

In Section 5.3, we will experimentally evaluate the laser-tip interaction in APT analysis with UV and green laser light. In particular, we will discuss the local distribution of the electric field across the specimen diameter and its variation along the analysis depth for different experimental conditions. Relying on the well-characterized reference system, the accuracy of the APT analysis with UV and green laser light will be evaluated for different experimental conditions (electric field) and the optimum condition will be identified in Section 5.4. In addition, the repeatability of APT analysis in view of the Ge and B quantification will be evaluated in Section 5.5. Finally, in Section 5.6, we will discuss the APT analysis of a thin SiGe multi-layer systems using a combined APT-STEM-EDS analysis and its quantification.[75]

## 5.1 Reference material

Beside scaling device dimensions, the semiconductor industry has already embarked in the use of heterogeneous and advanced functional materials in recent technology nodes. Doped SiGe is among the most used and promising heterogeneous systems for current and future devices. Apparently, the performance of such a device relies also on the concentration and the quality (i.e. vacancies, defects and Ge diffusion) of the SiGe materials [188],[189].

Hence, in this project we developed a B doped SiGe reference material for APT analysis. This allows the evaluation of the APT quantification and the depth profiling capabilities (for B and Ge) in view of accuracy, reproducibility and repeatability. We start from 300 mm Si (100) wafers containing an epitaxially grown B doped  $\text{Si}_{0.78}\text{Ge}_{0.22}$  layer having a thickness of about 110 nm. To protect the region of interest (SiGe layer) from the potential damages induced during the specimen preparation, a 50 nm Si (100) was epitaxially grown on top of the SiGe

layer for one of the wafers. The schematic representation of layer thicknesses and compositions are shown in Figure 87.

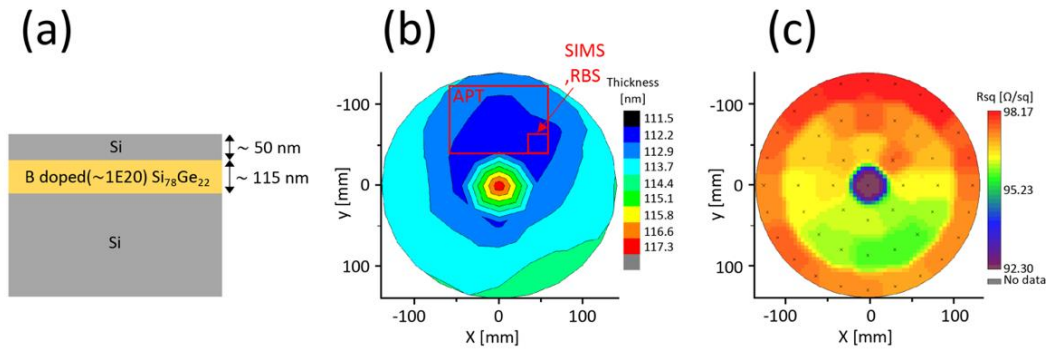


Figure 87: (a) Schematic representation of 300 mm wafer used in our study, where the SiGe (100) and Si (100) have been epitaxially grown on a bulk Si (100) wafer. (b) Distribution of SiGe film thickness across the entire wafer area, measured by spectroscopic ellipsometry (SE). The color bar indicates the thickness values. The region demarcated by red lines was selected for APT, SIMS and RBS analysis (c) Distribution of active B concentration across the entire wafer area, measured by four point probe (4PP) resistive measurement technique. The measurements have been performed at 48 points, indicated by the black dots and the resistance were interpolated elsewhere. Please note that 4pp measurement was performed on the wafer without the Si cap layer.

We have carefully analyzed our wafers using several complementary techniques in view of composition, film thickness and uniformity. These techniques are: grazing incident X-ray fluorescence (GIXRF), secondary ion mass spectroscopy (SIMS), Rutherford backscattering spectrometry (RBS), high resolution X-ray diffraction (HRXRD), scanning ellipsometry and four-point probe (4PP) resistivity measurement. The average Ge concentration, B content and SiGe film thickness obtained from these techniques are compared in Table 12. The uniformity of the SiGe film thickness and the compositions (Ge and B) were estimated from the in-line characterizations (HRXRD, SE and 4PP), where the measurements were repeated several times across the entire wafer area (see Figure 87). The maximum variations of the SiGe film thickness and the sheet resistance across the entire wafer were less than 5% (by SE and HRXRD) and 6% (by 4PP) respectively. By excluding the central region of the wafer (diameter  $\sim 35$  mm), the maximum variation in these parameters becomes less than 1% and 2% respectively. To further minimize the contribution of the homogeneity in our analysis we decide to use only a piece of the wafer ( $-60 \text{ mm} < x < 60 \text{ mm}$ ,  $40 \text{ mm} < y < 120 \text{ mm}$ ) for the further characterization (GIXRF, SIMS and RBS) and APT analysis. The RBS and SIMS analysis were performed on a  $\sim 20 \times 20 \text{ mm}^2$  piece of wafer diced from a region corresponding to:  $40 \text{ mm} < x < 60 \text{ mm}$ ,  $40 \text{ mm} < y < 60 \text{ mm}$ .

Table 12: Average Ge concentration, B content and SiGe film thickness measured on the 300 mm wafer shown in Figure 87. For in-line characterizations techniques (HRXRD, SE and 4PP), the measurements were carried out across the entire wafer. While for GIXRF, SIMS and RBS the measurements were performed on a piece of wafer ( $40 \text{ mm} < x < 60 \text{ mm}$ ,  $40 \text{ mm} < y < 60 \text{ mm}$ ). Please note that the associated uncertainty was only available for GIXRF-XRR and RBS measurements. The reported B content by GIXRF is the preliminary result.

Technique	Ge concentration [%]		B content [atoms/cm <sup>-3</sup> ]		Film thickness [nm]	
	Mean	Uncertainty	Mean	Uncertainty	Mean	Uncertainty
GIXRF-XRR	22.5	± 0.16	1.45 E <sup>20</sup>	± 3.23 E <sup>19</sup>	111.2	± 2.2
RBS	24.0	± 0.61	-	-	-	-
HRXRD	23.1	-	-	-	115.7	-
SE	-	-	-	-	113.1	-
4PP	-	-	9.63 E <sup>19</sup>	-	-	-
SIMS	21.4	-	1.01 E <sup>20</sup>	-	112	-

In our study, since only RBS and GIXRF measurements were traceable and the measurement results were reported with the associated uncertainties, we only used the measured results of these two techniques as a reference for APT analysis. The best estimation ( $\bar{x}$ ) for the reference Ge concentration was evaluated by the weighted mean of these two measurements:

$$\bar{x} = \frac{\sum_{i=1}^n (x_i \sigma_i^{-2})}{\sum_{i=1}^n (\sigma_i^{-2})} \quad 5.1$$

where  $x_i$  and  $\sigma_i$  are the best estimate (or mean value) and the reported uncertainty of each technique respectively (see Table 12). The calculated best estimate for the Ge concentration by weighted mean was 22.8 % which is very close to the mean value reported by GIXRF which has a very small uncertainty.

Finally, the traceable quantification for Ge and B (with associated uncertainty) and their uniformity distribution was planned to be carried by the reference-free GIXRF measurement at PTB (Bessy II synchrotron) according to ISO 35:2017 guide for certified reference material (CRM). The ISO 35:2017 defines reference material (RM) as: “material, sufficiently homogeneous and stable with respect to one or more specified properties, which has been established to be fit for its intended use in a measurement process” whereas a certified reference material (CRM) is defined as: “reference material (RM) characterized by a metrologically valid procedure for one or more specified properties, accompanied by an RM certificate that provides the value of the specified property, its associated uncertainty, and a statement of metrological traceability”. For the assessment of the CRM, the GIXRF measurement was planned to be carried out on four rectangular pieces (width ~ 20 mm) around the ROI of the wafer ( $-110 \text{ mm} < x < 90 \text{ mm}$ ,  $40 \text{ mm} < y < 120 \text{ mm}$ ) and the central region was considered for APT analysis. The detailed description of GIXRF analysis and extraction of the uncertainty can be found in reference [190]. Due to the long beam time required for such an analysis, the complete GIXRF characterization is still ongoing activity at PTB, while the preliminary results are reported in Table 12 (based on two measurements).

Finally, in this PhD project the Ge concentration and the SiGe film thickness measured by GIXRF-XRR was used as a reference value for APT analysis. Since the preliminary reported B content by GIXRF (uncertainty  $\sim 25\%$ ) was not available during this PhD work, we used the measured B content from SIMS, which has also a good agreement with the extracted value from 4PP.

## 5.2 APT specimen preparation

In this study the specimen preparation was carried out by the standard FIB lift-out technique. To minimize the induced FIB damages (i.e. amorphization and Ga implantation), a Ni cap layer ( $\sim 80$  nm thick) was evaporated on top of a  $10 \times 10$  mm<sup>2</sup> piece of wafer. This piece of wafer was cleaved from the previously described ROI ( $-110$  mm  $< x < 90$  mm,  $40$  mm  $< y < 120$  mm). We have prepared several APT specimens which all had quasi-comparable shapes in view of tip diameter in the SiGe layer. To do so, the tip sharpening step was stopped once the tip diameter reached to about 100 nm, then the cleaning step was carried out at 5 keV to remove the entire remaining Pt cap and an apex diameter of about 60 nm was reached. The SEM image of one of the prepared specimens is shown in Figure 88.

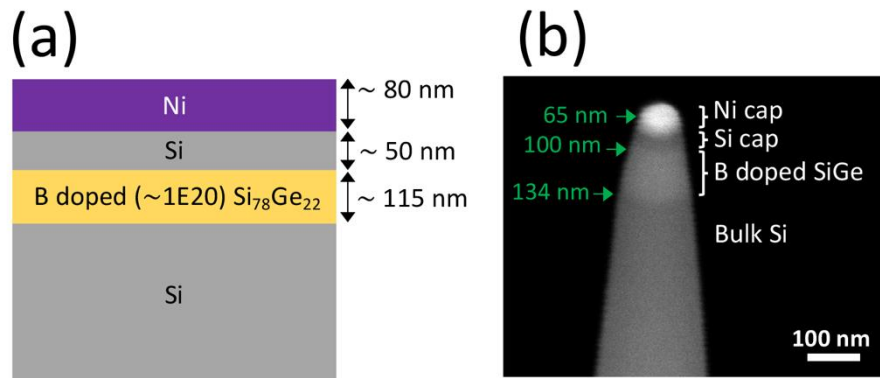


Figure 88: (a) Schematic representation of the wafer used for the preparation of APT specimens. (b) SEM image of one of the prepared APT specimens using the standard FIB lift-out technique. The image was taken after the 5 keV cleaning step. The measured specimen diameters, from the SEM image, at the tip apex, initial of SiGe layer and at the end of SiGe layer are shown on the image.

In the following sections we will discuss APT analysis of the prepared specimens using FIB lift-out technique.

## 5.3 APT analysis

In this project, we have investigated the influence of laser wavelength and electric field (corresponding to different CSRs) on the different aspects of APT analysis, including quantification accuracy and the lateral and depth resolution. The APT measurements were carried out in a LAWATAP tool, using both UV and green laser light. In order to improve the measurement statistics by collecting a large enough number of atoms ( $\sim 8$  millions), several specimens have been analyzed, whereby each measurement was carried out with a fixed laser power and wavelength and other experimental parameters were kept constant during the

entire measurement. The experimental parameters employed in this study are listed in Table 13.

Table 13: The experimental parameters used to study the quantification and depth profiling of B doped SiGe film in LAWATAP APT tool.

Experimental parameter	value
Base temperature [K]	40
Detection rate range [Atom/pulse]	0.004 - 0.006
Pulse rate [kHz]	100
Si <sup>2+</sup> /(Si <sup>+</sup> +Si <sup>2+</sup> ) CSR [%]	From 0.2 to 1
Laser power in UV wavelength [mW]	From 3 to 12
Laser power in green wavelength [mW]	From 5 to 100

According to Kingham theory and the related curves, the CSR is a measure of the electric field at the time of the evaporation event. Typically, at higher laser powers the resulting apex temperature (during evaporation events) increases such that the same evaporation rate can be achieved with a lower electric field or equivalently a lower CSR. By establishing the relation between laser power – CSR value, the estimation of the local apex temperature for metallic [191] and semiconductor [101] specimens become possible. We obtained a quasi-linear relation between the laser power and the observed Si CSR (averaged over the entire SiGe film) for APT analysis in UV laser (see Figure 89). The measurements were carried out in a constant flux mode ( $\sim 0.005$  atom/pulse). Please note that this calibration curve depends on the specimen shape and tool parameters (i.e. laser absorption properties, laser alignment, etc) and may vary from tool-to-tool.

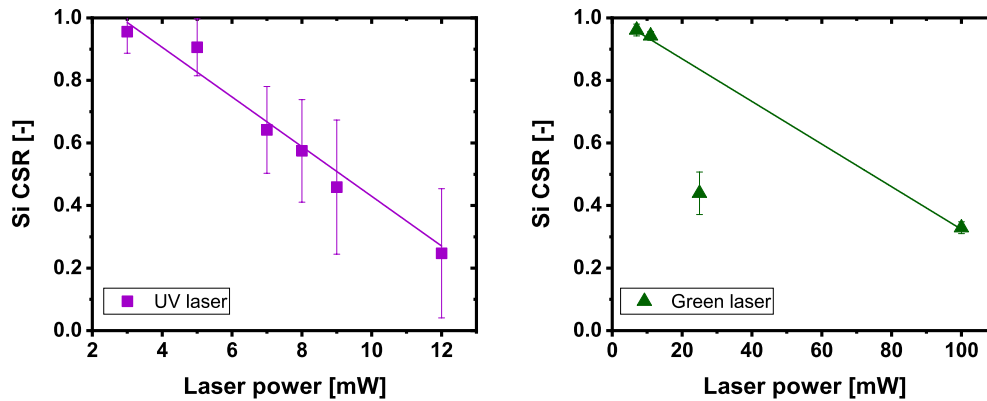


Figure 89: Laser power and the measured Si CSR (Si<sup>2+</sup>/ (Si<sup>2+</sup>+ Si<sup>+</sup>)) for APT analysis in UV (left) and green (right) laser light. Each point on the figures corresponds to one APT specimen measured at a fixed laser power. The error bars have been computed according to the combination of counting statistics and the standard deviation of the Si CSR over a voxel of  $1 \times 1 \times 5 \text{ nm}^3$  in the 3D reconstructed volume. Please note that the measurements were carried out at a fixed detection flux ( $\sim 0.005$  atom/pulse).

Each marker in Figure 89 (for UV laser) corresponds about 8 M collected ions in the SiGe layer. The error bars have been calculated according to the combination of counting statistics and the standard deviation of the CSR over a voxel size of  $1 \times 1 \times 5 \text{ nm}^3$  in the entire reconstructed volume. Please note that the large error bars in the figure do not originated from poor statistics but primarily from the variation of Si CSR over the reconstructed volume. We have further

investigated the possible systematic variation of CSR along the specimen depth as well as across the tip diameter for the APT measurements and the results are discussed in the following sections.

### 5.3.1 Laser absorption with UV laser light

We have analyzed the distribution of the Si and Ge CSRs across the specimen diameter and along the analysis depth for the measurements carried out in constant flux detection mode with a UV laser. We have observed that the Ge and Si CSRs have almost similar values (maximum deviation of the mean value < 6 %) and distributions over the entire volume of the SiGe layer. Hence, in this study we will discuss the distribution of Si CSR over the 3D reconstructed volume (including both SiGe and bulk Si).

The distribution of Si CSR across the specimen diameter for a ~ 50 nm thick section (in z direction) of the specimen in SiGe region, has been calculated for different APT measurements and the results are plotted in Figure 90a. Such a ROI was chosen to exclude the possible local variation of Si CSR in vicinity of interfaces (Si cap/SiGe and SiGe/bulk Si) and maximize the counting statistics. To calculate the distribution of Si CSR across the specimen diameter, the ROI has been divided in 21 slices along the laser illumination direction (x direction) and the Si CSR has been calculated for each slice. Each error bar corresponds to the combination of the counting statistics and the standard deviation for Si CSR /voxel within each slice (voxel size:  $1 \times 1 \times 5 \text{ nm}^3$ ).

Finally, to compare the lateral distribution of the CSRs for specimens having different diameters, the normalized lateral positions with respect to the tip radius are reported in Figure 90a. As can be seen, the Si CSR gradually increased across the tip diameter in the direction of laser illumination (x direction) for all the measurements at different laser powers. The observed large error bars (standard deviations) in Figure 90a, are partially due to the local variation of the CSRs along y direction (see Figure 90b) which might be related to the presence of a crystalline pattern (pole and zone lines) at the center of detector hit map.

For the APT measurements carried out at relatively lower CSRs, we observed that lateral distribution of Si CSRs was extended over a larger range. Whereby, for the APT measurement carried out at 12 mW laser power (average CSR~ 0.22), the Si CSR increased about 600% from the laser side of the tip towards the shadow side, while this variation was negligible (less than 2%) for the measurement at 3 mW laser power (average CSR~ 0.99). This is compatible with the observed tip shape after APT measurement, where a strong asymmetry in the tip shape (different local curvatures) was observed for the APT analysis at lower CSRs.

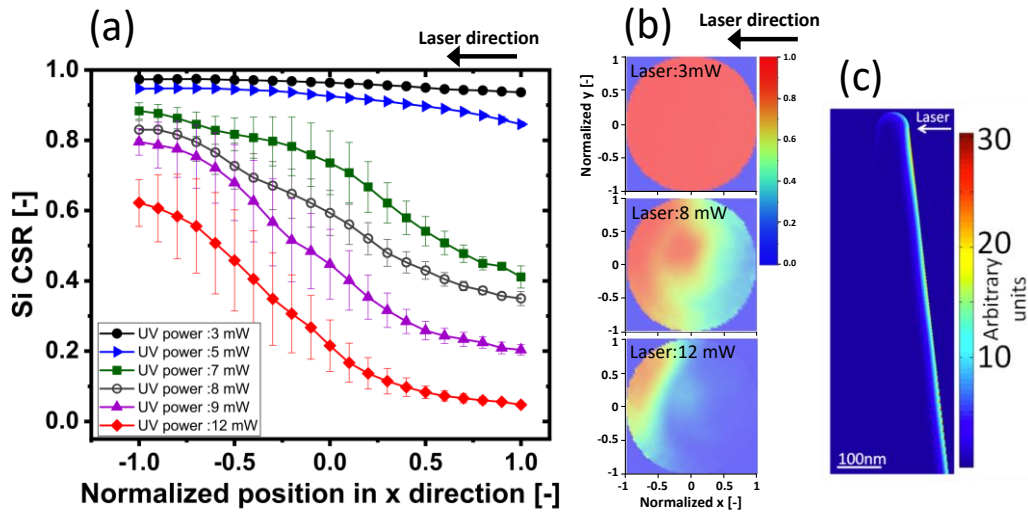


Figure 90: The distribution of Si CSR ( $\text{Si}^{2+}/(\text{Si}^{2+}+\text{Si}^+)$ ) across a 50 nm thick section (in z direction) of the specimen in the SiGe region in the direction of UV laser illumination (a) 1D distribution of Si CSR across x direction (laser illumination) of the reconstructed data for the APT measurements carried out at different laser powers. The horizontal axis shows the normalized lateral positions with respect to the reconstructed tip radius for each measurement. (b) 2D Si CSR map for the same measurement reported in (a) at laser powers equal to 3, 8 and 12 mW. (c) The absorption map computed by finite-difference time domain simulation (reported from [128]) for a silicon tip having an apex radius of 35 nm and a shank angle of  $4^\circ$  illuminated by UV laser light.

Such a lateral distribution of the Si CSR is expected according to the predicted laser absorption map for UV light (see Figure 90b). As discussed in Section 3.4.1, for a Si specimen illuminated by a UV laser, the photon energy is higher than the direct band-gap of the silicon ( $E_{\text{photon}} > E_{\text{gap}}^{\text{direct}}$ ) which leads to a strong absorption of the photon energy (small penetration depth) at the tip surface and sidewalls in the direction of the laser incident light.

We have also investigated the distribution of the Si CSR along the analysis depth for the different APT measurements carried out at several laser powers and the results are reported in Figure 91. Our analysis indicates that the Si CSR gradually drop along the analysis depth for all the specimens analyzed in this study. This drop was negligible for the measurements at relatively high Si CSRs ( $>80\%$ ), while it was maximal (in bulk Si) at midrange values ( $40\% < \text{Si CSR} < 60\%$ ).

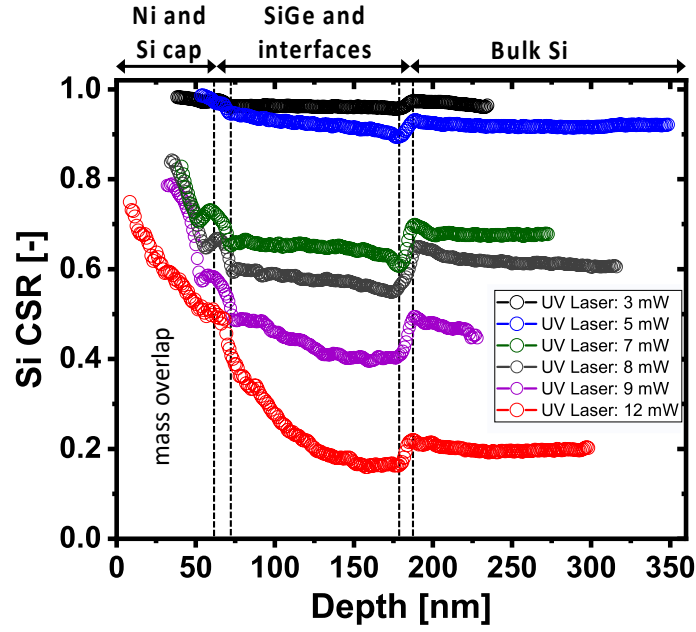


Figure 91: Si CSR ( $\text{Si}^{2+}/(\text{Si}^{2+}+\text{Si}^+)$ ) along the analysis depth for different APT measurements carried out at several UV laser powers. Please note that there was a mass overlap between  $\text{Ni}^{2+}$  and  $\text{Si}^+$ , at the first stage of APT measurement, corresponding to the highlighted region in the gray color, this caused an error in the extraction of Si CSR. Hence this part of the profiles has been partially excluded from the plot. The depth profile of Si CSRs for the different measurements have been aligned based on the Ge depth profile (position of SiGe layer). The initial and end of SiGe interfaces are also indicated by black dash lines on the figure.

We have attributed the reduction in the CSR along the analysis depth to the gradual decrease in the local evaporation rate due to the increase in the FOV along the analysis depth. Indeed, with increasing FOV, the area contributing to the measured evaporation flux increases implying that the local average evaporation rate decreases when working in a constant flux condition. We developed an analytical expression to predict the variation of the electric field along the analysis depth, which is discussed below.

By assuming the same evaporation probability ( $P_{\text{evap}}$ ) for all the surface atoms and a constant pulse frequency ( $f_{\text{pulse}}$ ), the detected flux ( $\Phi_{\text{det}}$ ) in atom/s can be written as:

$$\Phi_{\text{det}} = \frac{\int_{t_1}^{t_2} P_{\text{evap}}(t) S_{\text{FOV}}(t) \rho_{\text{surface}} \epsilon_D f_{\text{pulse}} dt}{(t_2 - t_1)} \quad 5.2$$

Where  $t$  is time in s,  $t_1$  and  $t_2$  are the initial and end time of the analysis in s,  $S_{\text{FOV}}$  is the FOV or equivalently the probed area of the specimen apex at the given sequence of evaporation in  $\text{m}^2$ ,  $\rho_{\text{surface}}$  is average number of atoms on the unit surface area in  $\text{atom}/\text{m}^2$  and  $\epsilon_D$  is the detection efficiency. For a short duration of measurement time ( $t_2 - t_1$ ), we assumed that evaporation probability  $P_{\text{evap}}(t)$  and  $S_{\text{FOV}}(t)$  remain constant and one can write:

$$\Phi_{\text{det}} = \frac{(t_2 - t_1) P_{\text{evap}} S_{\text{FOV}} \rho_{\text{surface}} \epsilon_D f_{\text{pulse}}}{(t_2 - t_1)} \quad 5.3$$

Since our APT analysis was carried out in a constant flux mode and at a fixed pulse frequency,  $\Phi_{\text{det}}$ ,  $f_{\text{pulse}}$  and  $\epsilon_D$  can be assumed to remain constant along each APT measurement. Then, the evaporation probabilities at two different analysis depths, for a fixed infinitesimal duration of time, can be written from the equation as:

$$\frac{P_{\text{evap}_2}}{P_{\text{evap}_1}} = \frac{S_{\text{FOV}_1}}{S_{\text{FOV}_2}} \quad 5.4$$

As shown in Figure 92, the  $S_{\text{FOV}}$  for a hemispherical tip shape having a radius of  $R$  is the cap area of the hemisphere,  $S_{\text{FOV}} = 2\pi R h$ , whereby the plotted trajectory in the figure corresponds to the last detected ion within the FOV. Finally, using a simple triangular relation,  $S_{\text{FOV}}$  can be written as a function of launch angle ( $\theta$ ):  $S_{\text{FOV}} = 2\pi R^2(1 - \cos(\theta))$ .

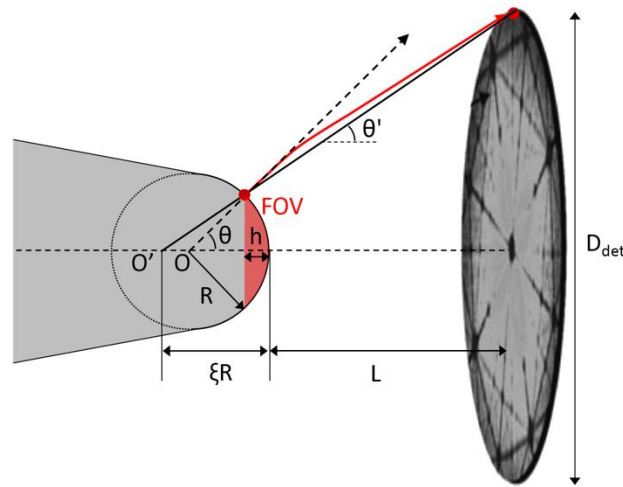


Figure 92: Schematic representation of the FOV for a hemispheric tip shape. Please note that the indicated launch angle corresponds to the last detected atom on the specimen apex within the FOV.

As previously shown in Equation 4.15, the  $\theta$  can be derived as a function of the impact angle of ion trajectory ( $\theta'$ ):  $\theta = \theta' + \arcsin((\xi - 1) \sin(\theta'))$ . We also demonstrated that,  $\theta'$  can be written as a function of detector diameter ( $d$ ), the distance between the detector and the tip ( $L$ ) and the image compression factor ( $\xi$ ):  $\theta' \approx \tan^{-1}\left(\frac{D}{L}\right)$ . By combining these parameters,  $S_{\text{FOV}}$  can be written as:  $S_{\text{FOV}} = 2\pi R^2 g(\xi, D, L)$ , where  $g$  is a function of  $\xi$ ,  $D$  and  $L$ . The two last parameters are fixed for an APT tool, while  $\xi$  can vary according to the electrostatic environment (shank angle, tip height, etc). Nevertheless,  $\xi$  is typically assumed to remain constant during the 3D data reconstruction. Hence, the equation 5.4 can be written as:

$$\frac{P_{\text{evap}_2}}{P_{\text{evap}_1}} = \frac{S_{\text{FOV}_1}}{S_{\text{FOV}_2}} = \left(\frac{R_1}{R_2}\right)^2 \quad 5.5$$

This correlation implies that for a measurement carried out at a constant detection rate, the local evaporation probability varies along the analysis depth as a function of the inverse square of the specimen radius, i.e. the local electric field will slowly decrease. In order to investigate the influence of such a systematic variation of

$P_{\text{evap}}$  on the electric field (F) and finally CSR, we further expand Equation 3.14 by considering that the evaporation probability is proportional to  $P_{\text{evap}} \propto \exp\left(-\frac{Q_b}{k_B T}\right)$ , where  $Q_b$  is evaporation barrier height,  $k_B$  is the Boltzmann constant and T is the apex temperature at the given time of evaporation.

By assuming that the apex temperature is similar at the different sequences of evaporation (i.e. in voltage mode), equation 5.5 can be written as:

$$\frac{\exp\left(-\frac{Q_{b_2}}{k_B T}\right)}{\exp\left(-\frac{Q_{b_1}}{k_B T}\right)} \approx \left(\frac{R_1}{R_2}\right)^2 \quad 5.6$$

According to Image hump model, the barrier height  $Q_b$  can be estimated by:  $Q_b(F) \approx \frac{1}{2} Q_0 \left(1 - \frac{F}{F_{\text{evap}}}\right)$  (see equation 3.7), where  $Q_0$  is the zero-field barrier height for both ionization (first state) and the removal of an atom from the surface and  $F_{\text{evap}}$  is the evaporation field of the material. Hence the above equation can be written as:

$$\frac{\exp\left(-\frac{\frac{1}{2} Q_0 \left(1 - \frac{F_2}{F_{\text{evap}}}\right)}{k_B T}\right)}{\exp\left(-\frac{\frac{1}{2} Q_0 \left(1 - \frac{F_1}{F_{\text{evap}}}\right)}{k_B T}\right)} \approx \left(\frac{R_1}{R_2}\right)^2 \quad 5.7$$

One can simplify the above equation and write the variation of the electric field (F) along the analysis depth as a function of the ratio of the variation of the tip radius ( $R_1$  and  $R_2$ ):

$$\exp\left(\frac{\frac{1}{2} Q_0 (F_2 - F_1)}{F_{\text{evap}} k_B T}\right) \approx \left(\frac{R_1}{R_2}\right)^2 \quad 5.8$$

Finally, by knowing the value of  $k_B$  and  $Q_0$  at first ionization state for Si and by assuming that the evaporation takes place at 300 K, the above relation can be written as:

$$F_2 - F_1 \approx 2.89 \times 10^{-10} \times \ln\left(\left(\frac{R_1}{R_2}\right)^2\right) \quad 5.9$$

This analytical description of the variation of the electric field (F) as a function of tip radius (R) for the Si tip, predicts a drop of  $\sim 0.23$  V/nm in the electric field when the tip radius increases by  $\sim 50$  % due to the shank angle. Such variation of electric field is reflected in a change of the Si CSR according to Kingham curve of Si and can be calculated relative to the initial Si CSR at  $R_1$ .

Since, the extraction of tip radius from SEM image can potentially lead to a large error in the calculation of  $\left(\frac{R_1}{R_2}\right)^2$ , the validity of this derived analytical correlation will be discussed later in Section 5.6 for a combined APT-TEM analysis. Nevertheless, we can roughly estimate this effect for the APT measurement carried out at 8 mW (see Figure 91). According to the SEM image of the specimen before APT analysis, we estimated the increase of the tip radius along the analysis depth from beginning of the SiGe layer up to the end of the analysis, to be ~ 50%. By knowing the initial Si CSR ratio at the end of Si cap (~ 0.65), Equation 4.9 predicts a drop in the Si CSR to ~0.6, which matches the observed variation of the Si CSR along the analysis depth shown in Figure 91.

Please note that although the ratio of the tip radius ( $R_{\text{initial}}/R_{\text{end}}$ ) along the first 250 nm of the specimen depth was approximately comparable ( $40\% < R_{\text{initial}}/R_{\text{end}} < 60\%$ ) for all the specimens, the observed variation of CSRs along the analysis depth were quite different with a pronounced variation of CSRs for mid-range CSRs (see Figure 91). This can be explained according to the Kingham curve of Si and the developed analytical correlation, whereby for the same predicted drop of electric field (i.e. 0.23 V/nm) the apparent variation of Si CSR depends on the initial Si CSR (at  $R_1$ ) or similarly the initial electric field. According to the Kingham curve of Si, the mid-range CSRs ( $35\% < \text{CSR} < 65\%$ ) are highly sensitive to the variation of electric field, while at higher/lower Si CSR regions the curve shows quite insensitive variation of CSR respect to the electric field. This explains well the observed variation of CSRs along the analysis depth with the UV laser.

We have observed that the slopes of the drop in the Si CSRs were higher in SiGe layer with respect to the bulk Si for all the measurements. In particular the maximum drop of the Si CSR was observed for the measurement carried out at highest power. Due to the absence of any correlation between CSR and electric field (Kingham curve) for SiGe, we could not discuss this behavior further.

### **5.3.2 Laser absorption with green laser light**

In contrary, for APT measurements carried out with a green laser, we observed a quite diverse trend for the Si CSR along the analysis depth for the measurements at different laser powers. As shown in Figure 93, the variation of the Si CSRs along the analysis depth had different trend for each laser power. For the APT measurements carried out at 55 and 100 mW (lower average Si CSRs) the specimens were fractured at the very beginning stage of the measurements in the SiGe layer and we reported the rest of the measurement after 400 K events from the fractured position. A possible mechanism for such a fracture at higher laser power will be discussed later in this section.

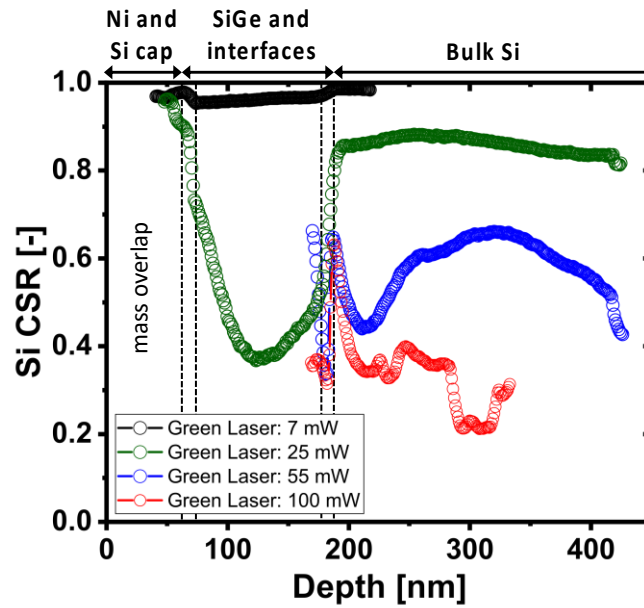


Figure 93: Si CSR ( $\text{Si}^{2+}/(\text{Si}^{2+}+\text{Si}^+)$ ) along the analysis depth for the APT measurement carried out with a green laser using different laser powers. The specimens measured at 55 and 100 mW laser power locally fractured within the SiGe layer, while the measurements were continued successfully after this local fracture. We reported the rest of the measurements, after the fracture events, by excluding about 400 k events from the fractured position. Please note that there was a mass overlap between  $\text{Ni}^{2+}$  and  $\text{Si}^+$ , at the first stage of APT measurement, corresponding to the highlighted region in the gray color, which caused an error in the extraction of the Si CSR. Hence this part of the profiles has been partially excluded from the plot. The Si CSR depth profiles for the different measurements have been aligned based on the Ge depth profile. The initial and end of the SiGe interfaces are also indicated by the black dash lines in figure.

We have observed a successive increase/decrease of the Si CSR along the analysis depth for the APT measurements carried out at relatively higher laser powers (25, 55 and 100 mW). In particular for the measurements carried out at 55 and 100 mW a non-monotonic pattern is seen which will be discussed further.

As discussed in Section 3.4, for a Si specimen illuminated by green laser, the photon energy is in between direct and indirect band-gap energy of Si ( $E_{gap}^{indirect} < E_{photon} < E_{gap}^{direct}$ ) and the photon absorption is assisted by the phonons (to conserve the momentum). Hence, the absorbed energy is weaker as compared to the case for a UV laser and the penetration depth of the green laser can be much deeper than the thickness of the APT tip. In fact, the laser light experiences a series of reflection and refraction events inside the 3D volume of the tip, which can obviously interfere. As a result, a periodic absorption pattern occurs depending on several parameters including tip shape (radius, shank angle, etc). These patterns have been theoretically predicted and are shown in Figure 94a for a Si tip having a tip diameter of 25 nm and a shank angle of  $6^\circ$  [192]. As can be seen, the laser absorption pattern across the specimen diameter (cross-section images) varies along the specimen depth, in which the position of the local maxima of the laser absorption have a fixed distance in z direction equal to the laser wavelength ( $\lambda=515$  nm). Such predicted periodic maxima in the laser absorption map can potentially result in a periodic variation of apex temperature and similarly result in the same periodic variation of the Si CSR along the analysis depth. However, this has not been yet well experimentally evaluated in the literature.

To correlate the experimentally observed variation of Si CSR along the analysis depth to the numerically predicted absorption map in reference [192], we have plotted the observed depth profile of  $\text{Si}^{2+}$  and  $\text{Si}^+$  together with the cross section 2D maps of Si CSRs, at several depth positions, for the APT measurement carried out at 55 mW laser power. This measurement was carried out at an average Si CSR of about 0.5, which according to Kingham curve of Si is the most sensitive CSR to the variation of electric field. This specimen had a comparable average shank angle ( $\sim 6^\circ$ ) and initial radius (30 nm instead of 25 nm) to the tip shape used for the simulation of absorption map shown in Figure 94a.

This comparison clearly indicates that the distance between the maximum-to-maximum of the experimentally observed periodic pattern of Si CSR does not match the predicted period for the local maxima of absorption map ( $\lambda=515$  nm). In addition, the observed lateral distribution of the Si CSR (see 2D Si CSR maps in Figure 94b) indicates a uniform distribution of Si CSRs dominated by the poles and zone lines (see 2D Si density maps in Figure 94b) at different positions in the depth, while the average Si CSR of each section image (2D Si CSR map) was different according to the depth profile of Si CSR. This is compatible to the quasi-hemispherical tip shape observed after all APT measurements using green laser in our study (see Figure 96). However, the numerically calculated absorption maps at different sections of the specimen (see Figure 94a) predicted a number of absorption maxima with a distribution depending on the depth position.

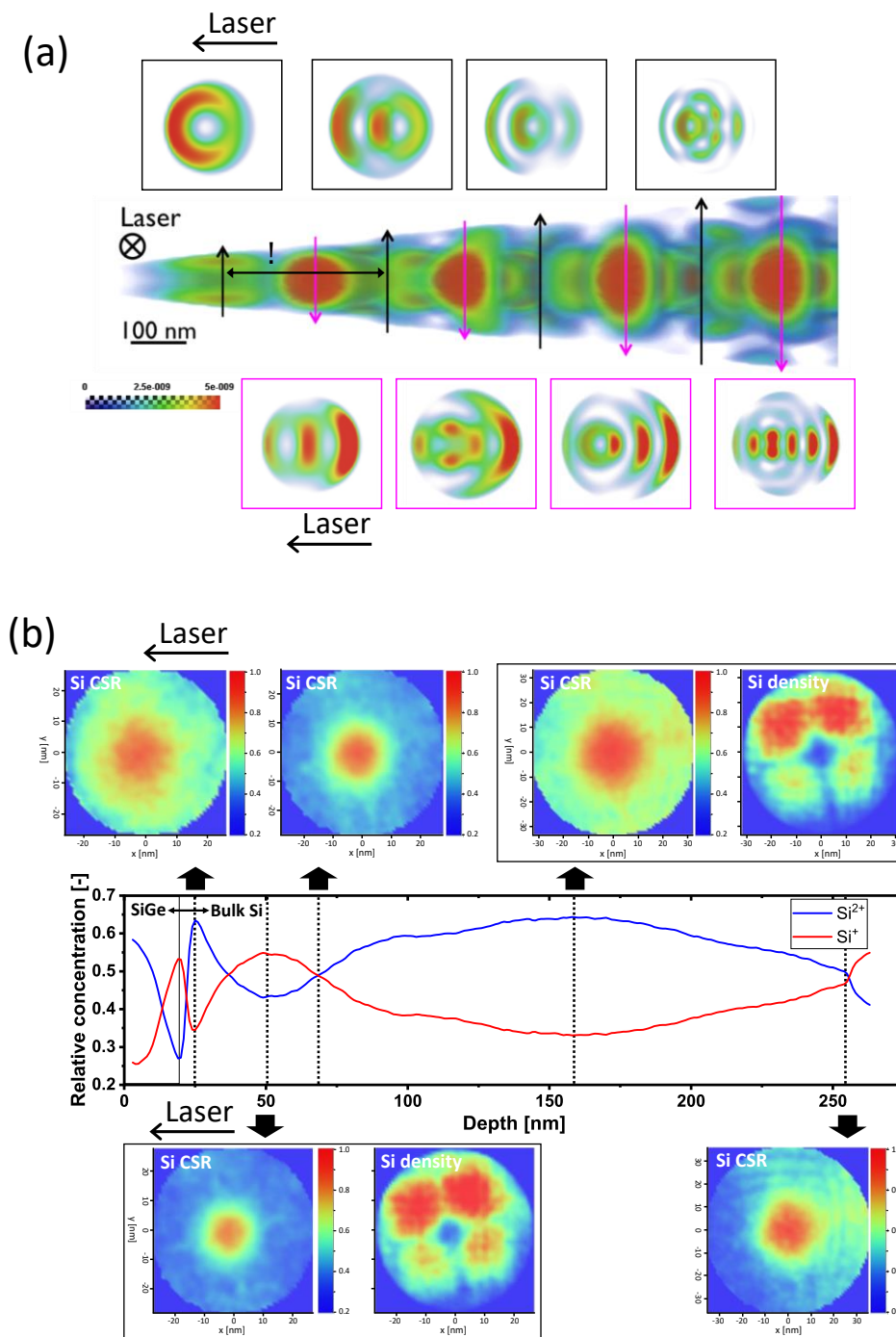


Figure 94: (a) The predicted 3D absorption map computed by finite-difference time domain for a silicon tip having an apex radius of 25 nm and a shank angle of  $6^\circ$ . The image in the center shows the successive absorption maxima along the specimen depth at the laser illuminated side of the tip. The images on the top and the bottom show the laser absorption pattern in the tip cross-section at different positions along the specimen depth. The figure is reported from [192]. (b) The experimentally observed variation of Si CSR for APT measurement carried out at 55 mW green laser power on a SiGe/Si specimen having apex radius of about 30 nm and a shank angle of about  $6^\circ$ . The image in the center shows depth profile of  $\text{Si}^{2+}$  and  $\text{Si}^+$  along the analysis depth, where the marked region up to 19 nm in depth, belongs to SiGe layer and the rest corresponds to bulk Si. The images at the top and the bottom show the 2D Si CSR maps for the specimen cross-section having a 5 nm thin depth. The 2D Si density maps are also shown for two sections of the tip at 50 nm and 160 nm in depth.

To better understand the observed discrepancies between the experimentally observed distribution of Si CSR (both lateral and depth) and the numerically predicted absorption pattern (local maxima), the laser tip interaction has to be

analyzed further in detail. We have described this discrepancy in the following paragraphs.

For a given specimen with a constant shank angle, the finite difference analysis predicts that the absorption map (both in the shank and close to the apex) varies depending on the initial tip radius [113]. This implies that a single simulation cannot be used to predict the absorption map along the analysis depth. Hence, the simulation should be repeated at each apex diameter (along the analysis depth) to estimate the apparent absorption map during the course of evaporation. This has been shown in Figure 95 for a Si tip having a fix shank angle of  $4^\circ$  at four different initial tip diameters (20, 50, 100 and 160 nm) corresponding to evaporation sequences at different depths. As can be seen, the predicted absorption map close to the apex of the tip having an initial diameter of 160 nm (Figure 95 a) is quite different from that of tips with different initial diameters (Figure 95 b to d).

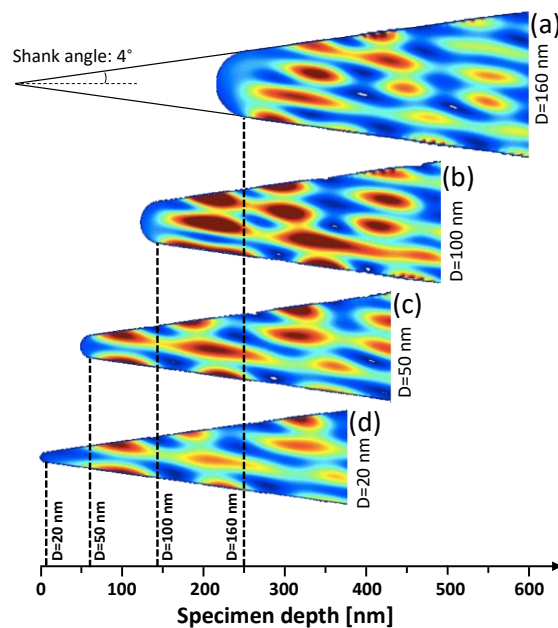


Figure 95: 3D absorption maps computed for a silicon tip having a fixed shank angle of  $4^\circ$  at four different initial tip diameters (a) 20 nm, (b) 50 nm, (c) 100 nm and (d) 160 nm illuminated by green laser. The absorption maps were calculated by finite-difference time domain simulations. Reproduced from [192].

Indeed, to correlate accurately the 3D absorption map to the field evaporation process (at the specimen apex), one should repeat the numerical simulation of absorption map several times along the analysis depth, corresponding to simulations at different initial tip diameters. Hence, the apparent distance between the absorption maxima (obtained from different simulations) may vary from  $\lambda=515$  nm and needs to be studied in detail. In addition, the first absorption maximum in green laser is located in a certain distance from the specimen apex (see Figure 95). This results in the energy absorption and heating by the specimen volume rather than local apex surface, in contrary to what typically observed in UV laser illumination [82]. Hence, the apparent distribution of apex temperature during the course of evaporation may not necessarily follow the predicted lateral pattern of absorption maxima (first cross-section in Figure 94a) at a certain distance from the apex surface. However, experimentally we do observe slightly

higher Si CSR on the laser side of the specimen cross-section for some positions in depth (see 2D Si CSR maps in Figure 94b), which might be interpreted as non-uniform heating of the apex.

In addition, the quasi-symmetric tip shape typically observed after APT analysis in green laser confirms the quasi-uniform heating of the apex. The SEM images of the three specimens after APT measurements at different laser powers are reported in Figure 93. As can be seen the apex shape had a quite symmetric shape for all the specimens while we observed local dips at the sidewalls of specimen shank for the APT analysis at relatively higher laser powers (25 and 100 mW). Such a local dip in the specimen shank was observed also in reference [101], where the author observed multiple dips along the specimen depth having a spacing (in z direction) equal to the  $\lambda=515$  nm. The author attributed the presence of such local dips to laser melting (and enhanced evaporation, not necessarily ablation) at the position of local absorption maxima in the specimen depth. The observed local fracture at the very initial stage of the APT measurements (see Figure 93) at high laser powers (55 and 100 mW) might be also attributed to a similar effect (laser melting). Vice versa, due to the small tip diameter at the beginning of the APT measurement, a possible damage/dip (by laser melting) would cause a complete fracture of the tiny upper part of the specimen.

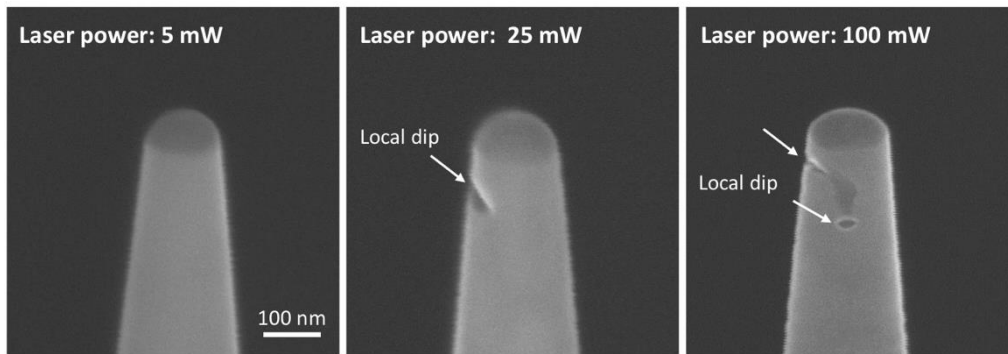


Figure 96: SEM images of APT specimens after analysis at different laser powers.

To summarize, we have discussed the experimentally observed distribution of Si CSR over the reconstructed volume for APT measurements in UV and green laser at different laser powers. The experimentally observed distribution of Si CSR (lateral and depth) was compared to the numerically predicted absorption maps for UV and green laser lights and different aspects of the APT measurement have been explored in detail. In particular we have developed an analytical description for the decrease of the electric field along the analysis depth as a function of tip radius.

Since our APT measurements have been carried out in a constant flux mode, the variation of the CSRs along the analysis depth implies that the apparent electric field or apex temperature was varying during the course of the evaporation. Such a variation of the CSR along the analysis depth is not desirable in APT measurement, since the electrical field is a crucial factor determining the quantification accuracy [193], [194]. But also, the related temperature increase might be detrimental for the accuracy. Gault et al. [195] demonstrated that higher

laser powers lead to a significant surface migration, which degrades the lateral resolution of APT analysis. It has been also reported that CSR has a significant impact on mass resolving power [196] and accuracy of quantification in APT analysis [193], [194]. In the next section we will discuss the impact of different CSRs on the quantification of Ge and B in SiGe film.

## 5.4 Quantification of Ge and B in SiGe

Currently, the accuracy and the uncertainty assessment of APT analysis is not yet available, even for the quantification in bulk specimens. This is mainly due to the absence of any reference material and the complexity in estimating the instrumental uncertainty (type B uncertainty). In this project we will evaluate the accuracy of APT analysis in view of Ge and B quantification in SiGe and its link to the different experimental conditions (electric field) by relying on a sample with a well characterized SiGe composition. In addition, we will evaluate the statistical uncertainty (type A uncertainty) for the measured average Ge concentration and B content in a bulk SiGe film. As discussed in Section 5.1, we have carefully analyzed our reference specimen (SiGe film) by other complementary traceable techniques (RBS and GIXRF). In particular, the accuracy of APT analysis in bulk SiGe will be assessed with reference to the GIXRF results in this section.

For an APT measurement, the standard uncertainty (type A uncertainty) can be calculated according to the counting statistics. In this case for each ranged mass, the counting statistic follows the Poisson distribution and the standard deviation ( $S_c$ ) can be calculated as a function of number of counts  $N_c$  [197]:

$$S_c = \sqrt{N_c} \quad 5.10$$

As we typically are dealing with millions of atoms,  $S_c$  is expected to be small. However, being an inherently 3D characterization technique, the reconstructed specimen volume is usually divided into a number of voxels, each with a much lower counting statistics and thus larger standard deviation. The choice of the voxel size does thus not only have an influence on the extracted mean concentrations but also on the related type A uncertainty per voxel.

On the one hand, the choice for a very large voxel size (up to all the atoms) results in an averaging over a large volume such that the intrinsic resolution is reduced/lost while it does improve the overall standard deviation due to the better counting statistics. This is the case for APT analysis for a bulk specimen where by taking the entire specimen as one voxel (no spatial and depth resolution), the standard deviation of the analysis will become equal to the overall counting statistics (see equation 5.10) which are typically some millions of counts. Hence, the standard deviation for such an analysis becomes very small.

Vice versa, taking a voxel equal to the ultimate resolving power of APT will provide the highest spatial resolution, unfortunately at the price of strongly reduced counting statistics and thus large standard deviation. As a compromise

one aims for a reasonable voxel size such that the best estimate of the measurand  $\bar{x}_i$  (i.e. concentration) can be calculated according to the number of counts within such a voxel and the associated standard deviation ( $S_i$ ). The best estimate (mean value) of the measurand  $\bar{X}$  can be calculated by averaging over the mean values  $\bar{x}_i$  of all the voxels (see equation 5.11). The overall standard deviation  $S_t$  of the measurand can be calculated by the combination of the standard deviation of each voxel  $S_i$  and the standard deviation of the means  $\bar{x}_i$  as:

$$\bar{X} = \frac{\sum_{i=1}^n \bar{x}_i}{n}$$

$$S_t^2 = \frac{\sum_{i=1}^n S_i^2}{n} + \frac{\sum_{i=1}^n (\bar{x}_i - \bar{X})^2}{n - 1} \quad 5.11$$

where  $n$  is the total number of voxels. Please note that this equation relies on the same number of counts over the entire voxels which is valid if the number of counts are comparable for different voxels similar to what suggested by [198]. Otherwise a weighted standard deviation needs to be applied.

This allows local quantification with an associated type A uncertainty calculated over the entire reconstructed volume but with a lateral and depth resolution defined by the voxel size.

For a bulk specimen the calculated overall standard deviation (over the entire voxels) is also the measure of the uniformity of the measurand (i.e. mean concentration) over the reconstructed volume. We will further discuss this concept in this section by evaluating the Ge concentration and its distribution over the specimen volume measured at different experimental conditions.

We have quantified the Ge and B concentrations/distributions for all the APT measurements described in the previous section (different laser powers at both UV and green laser wavelengths). We observed a systematic underestimate of the Ge concentration as a function of average Si CSRs for APT measurements in both UV and green laser lights as shown in Figure 97. Each point in the figure corresponds to one APT measurement carried out at fixed laser power. The error bars in the figures correspond to the overall standard deviation (see equation 5.11) of the Ge concentration and the Si CSR over the specimen volume by taking the voxel size equal to  $1 \times 1 \times 5 \text{ nm}^3$ . As discussed previously, by taking the entire reconstructed volume as a single block (one voxel), the standard deviation becomes determined by the total counting statistics and reduces to less than 0.1% owing to the large number of detected events (about 8 M ions for each measurement).

Hence, the obtained large error bars (overall standard deviation) for APT measurements carried out with a UV laser, and mostly at relatively lower CSRs (high laser power), suggest that a strong variation of the apparent Ge concentration (and Si CSR) exists over the reconstructed volume. The error bars

for the APT measurements in green laser appear much smaller in comparison to the measurements with UV laser.

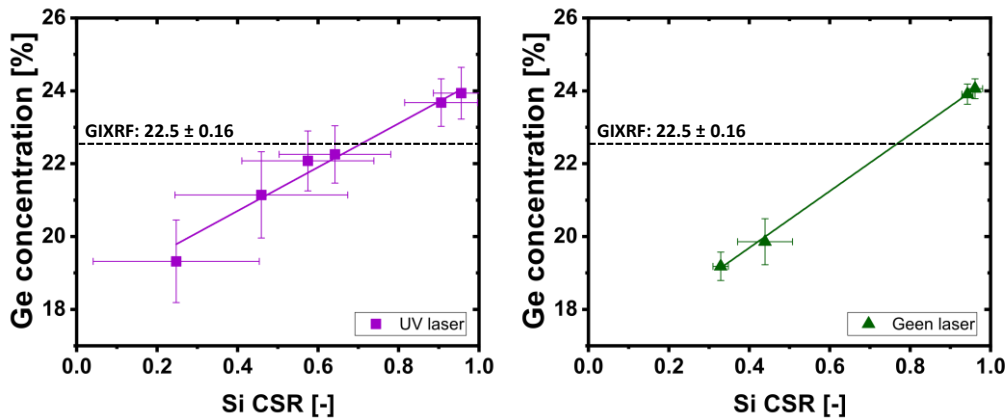


Figure 97: Average Ge concentration versus Si CSR ( $\text{Si}^{2+}/(\text{Si}^{2+} + \text{Si}^+)$ ), ( $\sim$  electric field) for different specimens measured with UV (left) and green (right) laser light. Each point in the figure corresponds to one APT specimen measured at the fixed laser power. The error bars were calculated according to the counting statistics and the standard deviation of the voxel means (see Equation 5.11) by taking the voxel size as  $1 \times 1 \times 5 \text{ nm}^3$ . The linear fit for each data set is also plotted. The dashed black line indicates the reference Ge concentration obtained from the GIXRF measurement.

A systematic underestimation of the Ge content for a C-doped  $\text{Si}_{75}\text{Ge}_{25}$  layer analysed at different electric fields ( $40\% < \text{Si CSR} < 93\%$ ) was also reported by Estivill R., et al [199], [200]. The authors reported that the apparent concentration of Ge increases as a function of the electric field, similar to what has been observed in our study. However, the maximum measured Ge concentration (at Si CSR  $\sim 93\%$ ) reported still underestimates their nominal value (22.5 % versus 24.4 % of the Ge concentration). As the nominal concentration of Ge and the analysis conditions (e.g. detection flux) in our study were comparable to that of ref [200], the discrepancy in the measured Ge concentration at high electric fields might be attributed to the accuracy in defining the reference Ge value. The latter highlights the need for a certified reference material (CRM) usable an interlaboratory comparisons on the quantification of such a system (e.g. ranging protocols, background subtraction, etc) using APT. These authora also mentioned that the observed variation of the apparent Ge concentration with the electric field remained an open question and that further investigation was required to better understand their results. In line with these observations and conclusions, we have studied the Ge quantification in SiGe in more detail.

To better understand the observed variation of the Ge concentration as a function of the average Si CSR (or equivalently the electric field) and its large deviations, we have further investigated the local variation of the Ge concentration over the entire reconstructed volume for the different APT measurements in this study.

In the previous section, the lateral/depth distribution of Si CSR for APT measurement with UV laser was discussed in detail. In particular, we have demonstrated that there was a systematic variation of Si (or similarly Ge) CSR across the specimen diameter in the direction of laser illumination, which is also reported in Figure 98b. We have also observed a systematic variation of the Ge concentration across the specimen diameter for all the specimens measured with

the UV laser. In Figure 98a, the distribution of the Ge concentration across the specimen diameter (in the direction of the laser illumination) is shown for a 50 nm thick section of SiGe film. To compare the trend for different specimens having different tip diameters, the lateral position was normalized to the specimen radius for each measurement. As can be seen, the concentration of Ge was higher on the shadow side for all the specimens. To possibly correlate the local distribution of Ge concentration (see Figure 98a) to the local variation of Si CSR (see Figure 98b) across the specimen diameter, these parameters were plotted versus each other in Figure 98c.

Our analysis clearly demonstrates that the local Ge concentration (across specimen diameter) was relatively increased as a function of the local Si CSR (or electric field) for all the specimens measured at different UV laser powers. However, for the same value of Si CSR, the local Ge concentration showed different values for the specimens measured at different laser powers (see Figure 98c). For instance, at local Si CSR of about 0.4, the local Ge concentrations were about 19.5, 20.5 and 21.5 % for the specimens measured at laser powers equal to 12, 9 and 8 mW respectively. This discrepancy was mostly observed for the measurement carried out at lower average Si CSRs (below 0.6).

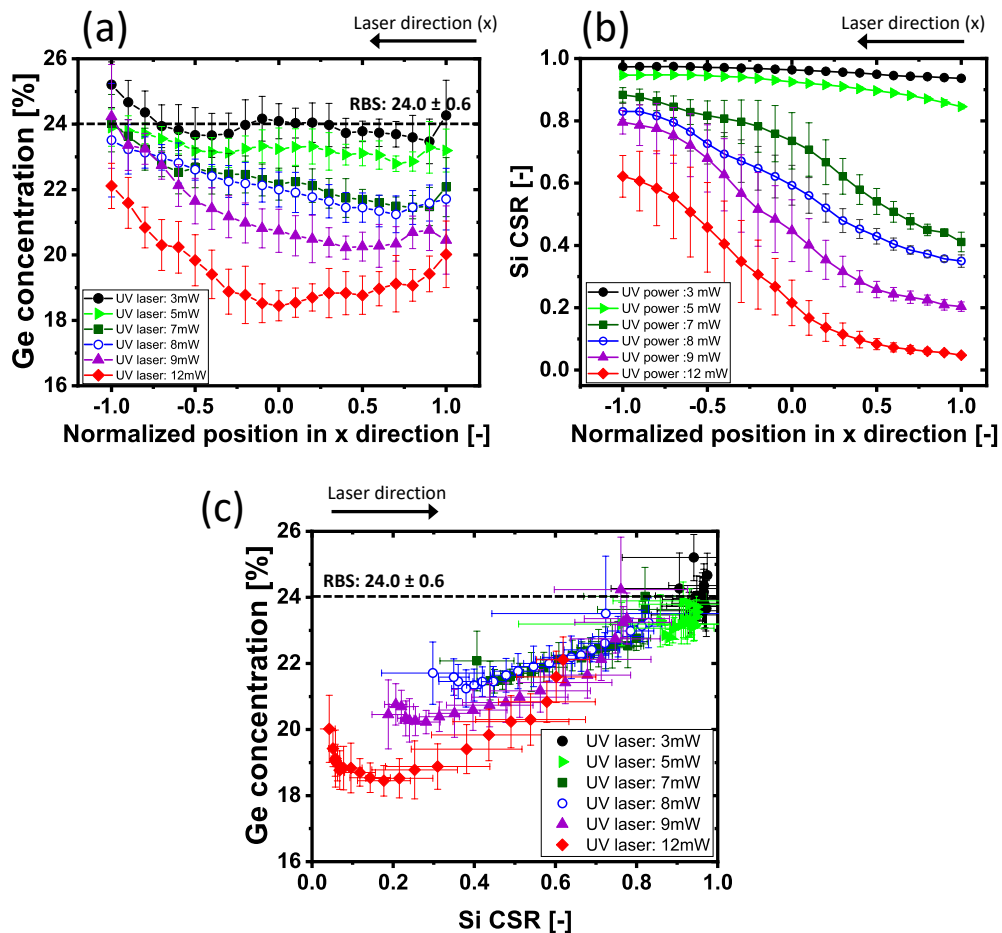


Figure 98: The distribution of local Ge concentration across the specimen diameter for APT measurements carried out with a UV laser at different laser powers. A 50 nm thick section (in z direction) of the reconstructed tip in the SiGe film was used for this analysis. (a) Distribution of local Ge concentration versus lateral position on the specimen in x direction (laser direction). To compare different specimens having different diameters, each position was normalized to the tip radius. (b) Distribution of local Si CSR versus lateral position on the specimen in x direction. (c) Correlation between local Ge concentration and

local Si CSR across the specimen diameters. This figure was obtained by combining the figures (a) and (b). The error bars were calculated according to the weighted standard deviation.

The 1D depth profile of the Ge concentration (averaged over the entire tip diameter) was calculated for different APT measurements with the UV laser and the results are reported in Figure 99. Our analysis suggests that the Ge concentration was increased along the analysis depth for all the measurements at different UV laser powers by  $\sim 1\%$  in the Ge content. The figure also indicates that Si CSR dropped along the analysis depth in the SiGe layer for all the measurements. The latter has been discussed in detail in the previous section. This drop in Si CSR was higher for the measurements at low CSR regions (higher laser power), while for the measurements carried out at 12 mW laser power, the Si CSR was dropped by more than 100 % along the analysis depth. Although it is clear that the average apparent Ge concentration at each position in depth becomes higher as the electric field (Si CSR) increases, the correlation is less pronounced as compared to the lateral variation. Note for instance for the lowest laser power where there is hardly any change in CSR, the local Ge concentration (averaged over the tip diameter) still varies with depth. We have observed a similar increase in Ge concentration along the analysis depth also in the APT measurements in green laser (see Figure 100).

These observations could be real as a small increase in Ge concentration ( $< 1\%$ ) was also observed in the SIMS analysis. Further confirmation in the depth profile of our reference wafer is ongoing using the GIXRF technique.

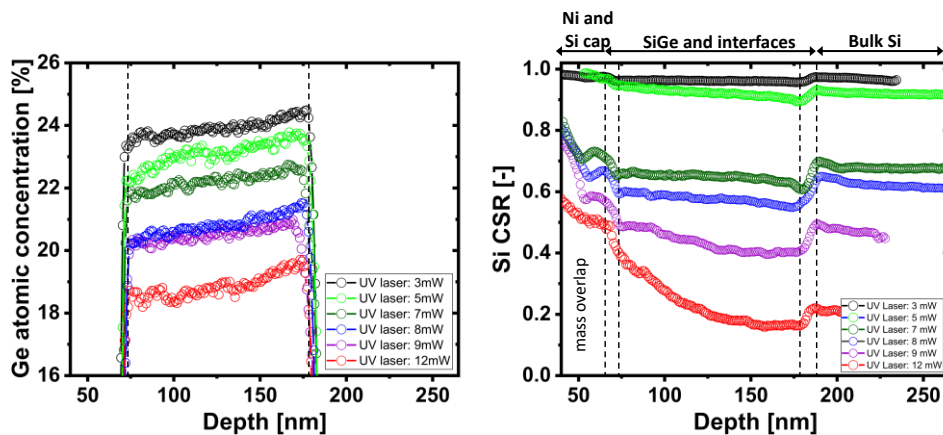


Figure 99: The depth profile of Ge concentration and Si CSR for different APT measurements carried out with UV laser. Each curve corresponds to one specimen measured at a fixed laser power. The interfaces between Si cap/SiGe and SiGe/bulk are indicated by black dashed lines.

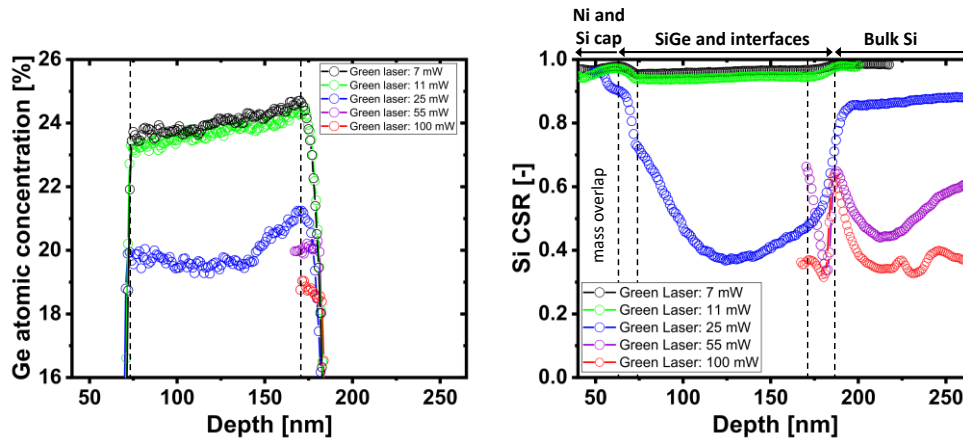


Figure 100: The depth profile of Ge concentration and Si CSR for different APT measurements carried out in green laser. Each curve corresponds one specimen measured at a fixed laser power. The interfaces between Si cap/SiGe and SiGe/bulk are indicated by black dashed line.

To understand the origin of such an underestimation of the Ge content in SiGe at low field region (Si CSR < 0.7) and its over estimation at high field regions (Si CSR > 0.7), we have investigated the potential loss mechanisms including DC evaporation, dissociation of molecular ions into neutrals and detector dead zone.

At high electric fields (high CSR), evaporation in-between laser pulses due to the presence of the high DC voltage may occur. As these are non-timed events, they lead to nonidentifiable species and an increase in the overall background signal. In case of specimens containing species with strongly different field evaporations ( $F_{\text{evap}}$ ), such DC evaporation may cause preferential evaporation of low field species and lead to its detection loss (underestimation). To evaluate such a possible loss mechanism, we calculated the background signals in our mass spectra. We did observe a gradual increase in the back ground level as a function of Si CSR, from 8 ppm/ns (at Si CSR=0.2) up to above 20 ppm/ns (at Si CSR=0.99) for the APT measurement carried out in UV laser. Since Ge has a slightly lower evaporation field compared to Si (29 versus 33 V/nm), the observed higher background level might be attributed to DC evaporation of Ge in the high field region. By ranging the entire background and calculating its concentration for different APT measurements in UV laser (different Si CSRs), we have evaluated the possible modification of SiGe stoichiometry according to the background level.

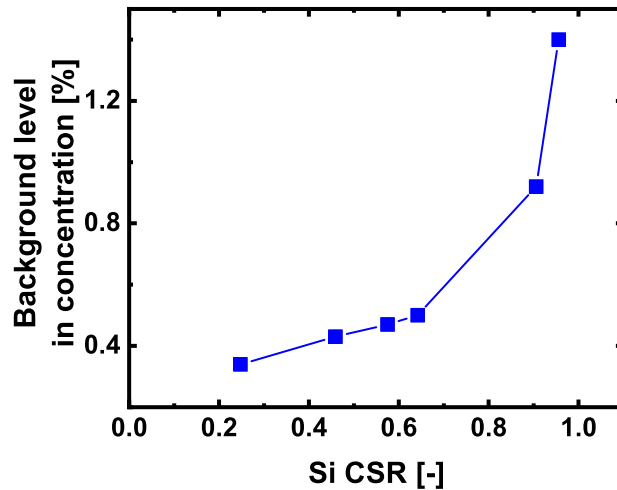


Figure 101: Estimated additional Ge concentration by assigning all background counts to Ge as a function of Si CSR ( $\text{Si}^{2+}/(\text{Si}^{2+} + \text{Si}^+)$ ) for UV. The background level was estimated by ranging the entire non ranged mass-to-charges in the mass spectrum. Each marker corresponds to one specimen measured at a fixed laser power.

As can be seen from Figure 101, the background level increases at higher Si CSR but its actual value ( $< 1\%$ ) cannot explain the observed discrepancies in concentrations. At low electric fields, where the underestimate is the largest, the background is low thus the added concentration as well ( $< 0.5\%$ ). At high fields, the preferential Ge loss would increase to  $1\%$  (causing some underestimate) at variance with the observed overestimate of Ge. Hence whether or not the background reflects a (non)preferential evaporation of Ge, it can never explain the observed errors on the quantification.

Another possible loss mechanism is the dissociation of molecular ions and the generation of neutrals, which was reported to cause underestimation of N in GaN due to formation of  $\text{N}_2$  neutrals [193], [129]. We have evaluated such a possible loss mechanism by analyzing the multi hits and by tracking the possible dissociation patterns, similar to what discussed in Section 6.3.2. We did not observe any significant dissociation pattern for the APT analysis at different electric fields. Hence, the dissociation of molecular ions and the generation of neutrals was also excluded from the possible loss mechanisms in our study.

Another source leading to a possible loss mechanism is the dead zone (or dead volume) of detection system in delay line detectors (DLD). In case two or more ions reach to the detector with the time difference smaller than a certain threshold (2 ns for our system) and a distance between atoms is less than certain limit (2 mm for our system), the DLD system is unable to identify them as two atoms and only assigns one count to the detected event. Obviously, the other atom in the multi-hit is not counted [82]. In particular, some species in APT are known to evaporate more in the form of multi-hit events, such as B in Si [201] and C in SiGe [200], hence these are more prone to such a loss mechanism. However, in our analysis we did not observe any significant number of multi-hit events: they were  $\sim 5\%$  for Si CSR  $\sim 0.2$  and up to  $\sim 9\%$  at Si CSR  $\sim 0.99$ . A similar range of Si and Ge multi-hits events was also reported by Estivill R., et al [200] for a C-doped  $\text{Si}_{75}\text{Ge}_{25}$  layer. In addition, the composition of the detected Ge in double

hits was not much different from that of single-hit events. This implies that there is no preferential evaporation mechanism in the form of multiple events between Si and Ge. Hence, we do not expect any significant impact of the detector dead zone on the compositional analysis of SiGe. However, as expected, the concentration of B in multi hits was much higher than that of single detected events.

Finally, to evaluate other possible sources of preferential evaporation/detection loss for one of our species (Ge or Si) over the other at different electric fields, we have compared the APT analysis of three different  $\text{Si}_x\text{Ge}_{1-x}$  compositions ( $x \sim 22, 50$  and  $72$ ). For instance, in case a systematic preferential evaporation/detection of Si at low electric field exists for  $\text{Si}_{78}\text{Ge}_{22}$ , this may become more significant for a higher Ge content (i.e.  $\text{Si}_{25}\text{Ge}_{75}$ ). The Ge concentrations for three different  $\text{Si}_x\text{Ge}_{1-x}$  stoichiometries ( $x \sim 22, 50$  and  $72$ ) do show however a very similar trends at all different electric fields (see Figure 102.)

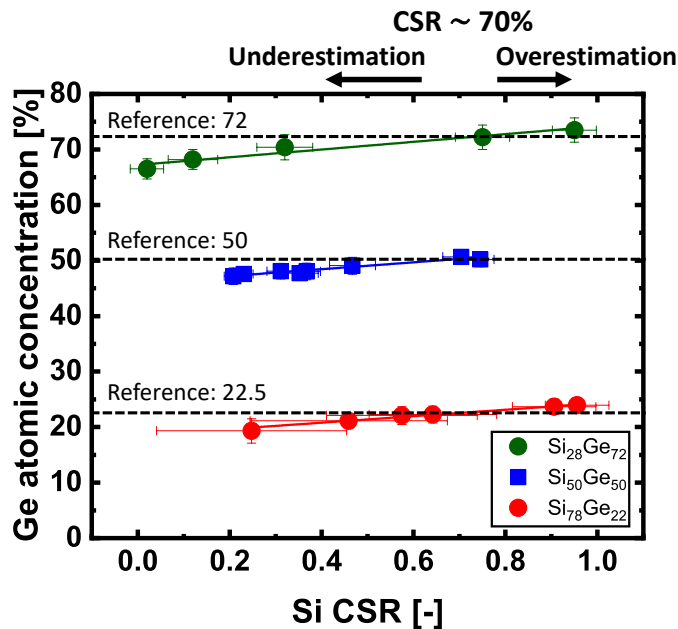


Figure 102: Ge concentration versus electric field (Si CSR) for three different  $\text{Si}_x\text{Ge}_{1-x}$  compositions ( $x \sim 22, 50$  and  $72$ ). The APT measurements for  $\text{Si}_{28}\text{Ge}_{72}$  was carried out in LEAP 5000 XR, while the other measurements were carried out in LAWATAP. Please note that the markers reported for  $\text{Si}_{28}\text{Ge}_{72}$  and  $\text{Si}_{50}\text{Ge}_{50}$  are lateral slices of one and two specimens respectively, while each marker for  $\text{Si}_{78}\text{Ge}_{22}$  corresponds to one tip measured at a fixed laser power. The error bars have been calculated according to the standard deviations.

Our analysis suggests that the APT measurement at average Si CSR of about 0.7, allows the accurate quantification for all three  $\text{Si}_x\text{Ge}_{1-x}$  compositions ( $x \sim 22, 50$  and  $72$ ) while the Ge content is underestimated for APT measurements at Si CSR  $< 0.7$  and overestimated for Si CSR  $> 0.7$ . Despite our detailed investigations of the potential loss mechanisms, we could not find any physical explanation for the observed underestimation/overestimation of Ge content in SiGe at low and high field regions. Potentially surface migration driven by the electric field may be the dominant process which is however hard to prove. At least for B it was reported that at high laser powers B migrates from outside the FOV within the analysis region thereby leading to an overestimate [202].

So far, we identified an optimized condition (electric field), which allows a more accurate stoichiometry for the APT analysis of  $\text{Si}_x\text{Ge}_{1-x}$  compositions ( $x \sim 22, 50$  and  $72$ ) to be obtained regardless of the use of a UV and green laser system. Our developed full tip imaging technique might help better understanding of the observed behavior by probing the entire tip and address a possible preferential trajectory aberration or the migration for one species out of FOV. For instance, a wider FOV can address the migration of B in the high laser powers and it can potentially resolve the inaccuracy in the B quantification.

We looked at the quantified B content for a B doped  $\text{Si}_{78}\text{Ge}_{22}$  at different electric field (Si CSR) for APT measurements in both UV and green laser, a similar underestimate of the B content at low field regions is observed (see Figure 103). At present, the SIMS measurement was used as a reference for the B content ( $1.01 \times 10^{20}$  atom/cm<sup>3</sup>) while the GIXRF analysis is still ongoing to more accurately quantify the reference B content with its traceable uncertainty.

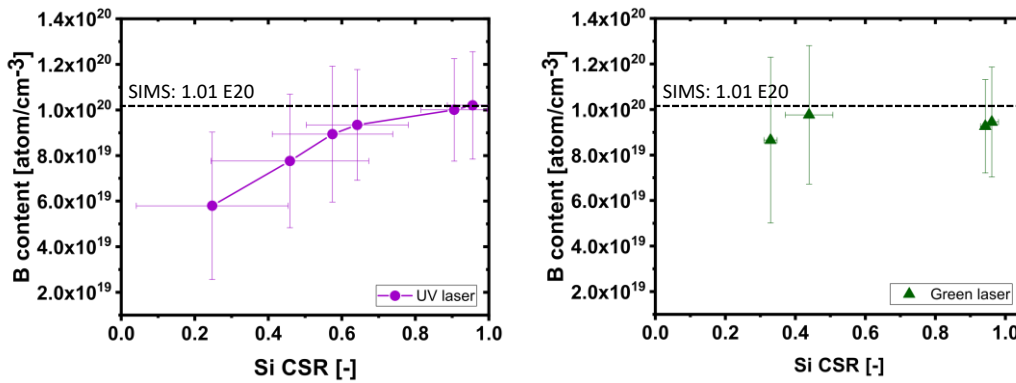


Figure 103: APT quantification of B content in  $\text{Si}_{78}\text{Ge}_{22}$  versus Si CSR (electric field) for measurements carried out at both UV and green laser in LAWATAP tool. The error bars were calculated according to the counting statistics and standard deviation of voxel means (see equation 5.11) for the reported parameters by taking the voxel size as  $1 \times 1 \times 5 \text{ nm}^3$ .

Melkonyan D., et al [201] reported a loss of B in Si was, though a recent results by Kouzminov D., et al [203] shows the opposite as well. The discrepancies could be linked to the fields used (at present not reported in [203]) since also our preliminary analysis also suggests that there is not much underestimation of the B content at high electric field. Obviously more systematic studies are required to clarify the accuracy which can be obtained.

## 5.5 Precision of APT quantification for Ge and B

In the previous section, we investigate the optimum experimental condition (high electric field) which allows a more accurate stoichiometry for the APT analysis of  $\text{Si}_{78}\text{Ge}_{22}$ . This accuracy assessment was carried out using the GIXRF analysis as the traceable reference, which was discussed in Section 5.1.

In order to mimic the repeatability of APT analysis and assess its precision, we carried out several APT measurements on multiple tips under the same optimal experimental conditions. At the time of this analysis, the result of the GIXRF measurement was not yet available and we used the RBS measurement as the

reference value. The APT measurements were repeated on 5 different specimens using UV and 3 specimens using a green laser with the Si CSR > 95%. The results are reported in Figure 104.

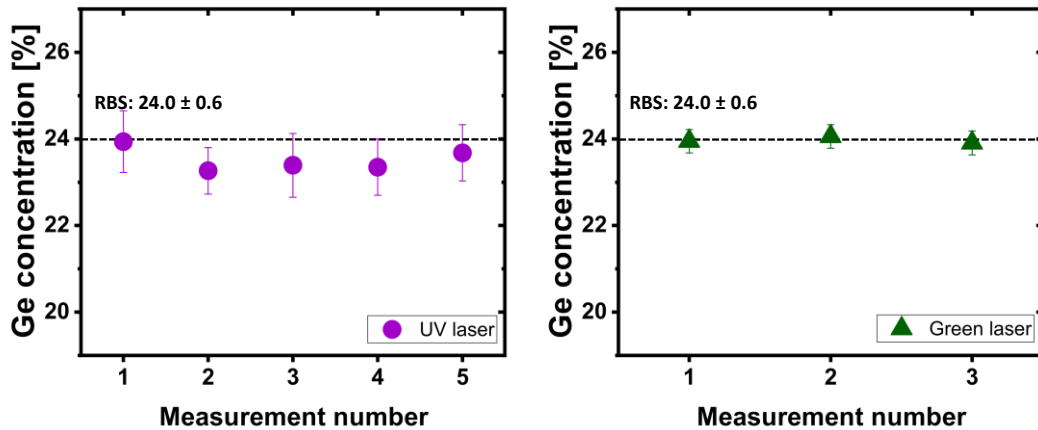


Figure 104: Repeatability of Ge quantification in SiGe by APT using UV (left) and green laser (right). Each marker corresponds on one APT tip measured at a fixed Si CSR > 95 %. The error bars were calculated according to the counting statistics and the standard deviation of the voxel means (see equation 5.11) for a voxel size of  $1 \times 1 \times 5 \text{ nm}^3$ .

Please note that the reported error bars were calculated according to the counting statistics and standard deviation of the voxel means (see equation 5.11) for both Ge concentration and the Si CSR over the reconstructed volume by taking the voxel size as  $1 \times 1 \times 5 \text{ nm}^3$ . Hence, our measurand is the concentration of Ge at each position within the reconstructed volume rather than the average Ge concentration over the entire tip (no lateral/depth information). Although both measurands lead to the same mean value for the overall Ge concentration, the difference is that the latter does not evaluate the possible variation of Ge concentration across the volume and the error bar becomes simply the overall counting statistics. Vice versa, the reported error bars in this study include the degree of homogeneity of the Ge concentration over the reconstructed volume (standard deviation of the mean). We obtained a smaller statistical error bars for all the APT measurements in green laser as compared to the measurements at the same condition and field (Si CSR > 95%) with the UV laser. This implies that APT analysis in green laser allows more accurate quantification of Ge in view of the Ge distribution (lateral and depth) in a reconstructed tip volume. This is most likely because more symmetrical tip shape and the minimal CSR variation across the tip.

Our analysis suggests that the Ge quantification in APT has a quite high repeatability, in which the calculated standard deviation of the mean for different measurements was only  $\sim 0.28 \%$  and  $\sim 0.57 \%$  using UV and green laser respectively. This corresponds to a precision better than  $1.2 \%$  and  $0.2 \%$  for the average quantification of Ge concentration respectively. The measurement data and the associated uncertainties are reported in Table 14.

Table 14: The Ge concentrations and their statistical uncertainties obtained from the APT measurements at a fixed experimental condition and a Si CSR > 0.95. The precision of the APT measurement was also evaluated in view of the average Ge concentration. Please note that the reported statistical uncertainty was calculated according to standard deviation (including the counting statistics) of different voxels using the 68.27 % confidence level.

APT Measurement		Ge concentration [%]		Repeatability		
Laser	Si CSR [%]	Mean value [%]	Statistical uncertainty [%]	Mean value [%]	Standard deviation of means [%]	Precision
UV	0.99	23.9	0.71	23.5	0.28	1.2 %
	0.98	23.3	0.53			
	0.94	23.3	0.73			
	0.96	23.3	0.65			
	0.98	23.7	0.64			
Green	0.99	23.9	0.27	23.9	0.57	0.2 %
	0.98	24.0	0.27			
	0.96	23.9	0.28			

We did a similar analysis for the B quantification in SiGe using both UV and green lasers. As can be seen in Figure 105, the calculated statistical uncertainty for the B quantification showed relatively large values in compare to that of Ge for both analyses in UV and green laser light. Although this is partially due to the poor counting statistics for B (small number of counts), we also observed a quite inhomogeneous distribution of B over the entire reconstructed tip volume (see Figure 106), similar to what observed by [201] for B in Si. Hence, we attributed the high statistical uncertainty to the inhomogeneity of B concentration (though a measurement artefact). Finally, the calculated precision for the B quantification in SiGe (mean value) is better than 1.1% (UV laser) and 2.2 % (green laser).

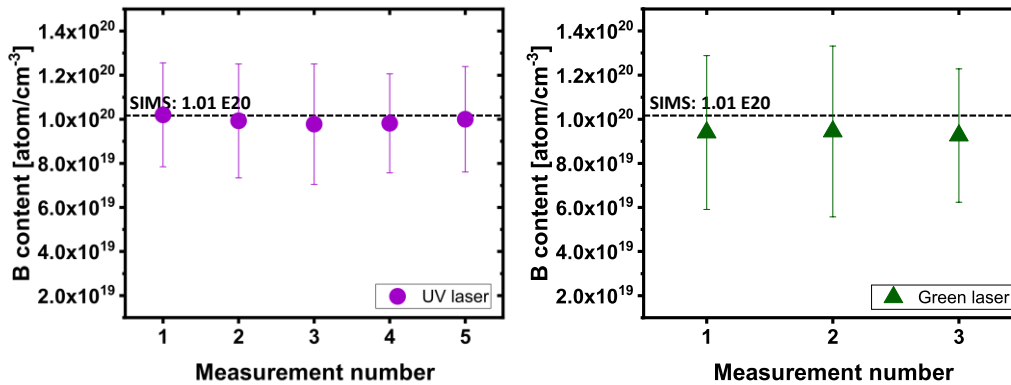


Figure 105: Repeatability of B quantification in SiGe by APT using UV (left) and green (right) laser light. Each marker corresponds on one APT tip measured at a fixed Si CSR > 95 % with all the other experimental conditions kept constant during all the measurements. The error bars were calculated according to the counting statistics and standard deviation of voxel means (see equation 5.11) for the reported parameters over the reconstructed volume by taking the voxel size as  $1 \times 1 \times 5 \text{ nm}^3$ .

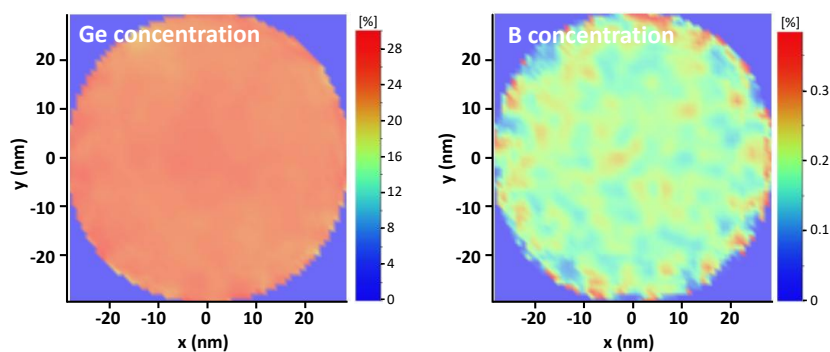


Figure 106: Lateral distribution of Ge (left) and B (right) concentration across the specimen diameter (2D concentration maps) measured at Si CSR~0.99 in UV laser.

## 5.6 APT analysis of multi-layer systems

SiGe multi-layer systems have many applications in the semiconductor industry including quantum wells, superlattices for infrared detectors and resonant tunneling diodes. Since the composition and the thickness of each layer can have a strong influence on the overall performance and properties of the system, these parameters need to be measured accurately. The scanning transmission electron microscopy (STEM in combination with EDS) is commonly used for determining the layer thicknesses, composition and some information on the interdiffusion profiles at the Ge/SiGe/Si interface with sub-Å resolution [10]. Nevertheless, it lacks the sensitivity to probe the dopant distribution for which APT is much more suited as it has a higher sensitivity, even for dopants, and has a comparable resolution to STEM. However, due to the unknown reconstruction parameters, the reconstructed APT data can easily lead to a wrong layer thickness or other morphological parameters.

Therefore, a combined APT-(S)TEM analysis on the same specimen, referred to as correlative microscopy, can address the aforementioned limitations of each technique and generate more reliable information about the specimen. In this context, the STEM microscopy can improve the 3D data reconstruction in APT analysis, whereby the STEM data (e.g. tip shape, layer thicknesses, etc) can be used to guide the data reconstruction in APT through calibrating the reconstruction parameters or even by identifying the local magnifications (i.e. artefacts). In addition, the STEM microscopy can provide crystallographic information which is not typically available in the APT analysis (e.g. defects and dislocations) [82].

The feasibility of such a complex correlative microscopy, focusing on the same sharpened APT specimen, has been demonstrated by several authors [204],[205] and has been identified as pathway towards a more accurate APT data reconstruction for complex systems (e.g. devices) [206] and even atomic-scale tomography, as suggested by Kelly F.T., et al. [207]. Several studies have been reported on the development of suitable hardware (i.e. holders) or protocols for such a complex analysis [206],[132]. Recently, Mouton I., et al. [208] have developed a protocol for accurate reconstruction and the correlation of APT analysis to the STEM data for nanoporous materials.

So far, all correlation microscopy has been done ex-situ i.e. the STEM results are obtained either by interrupting the APT process [172] or at the end of an APT run. In either case one needs to be concerned about the impact of the STEM tomography as it can potentially modify the specimen through electron beam damage (i.e. knock-on displacement) [209] or growth a carbon contamination. Their impact can be minimized by adopting a suitable (low) voltage during the STEM analysis and successive plasma treatment after the image acquisition. A more detailed description regarding the potential electron beam damages to an APT specimen can be found in [82].

In this project, we will demonstrate similarly the use of a combined APT-STEM tomography analysis on the same APT specimen to obtain an accurate quantification and 3D data reconstruction of the SiGe multilayers. In addition, we have exploited the comparison of the depth profiles obtained with EDS analysis and APT, to address several aspects of the Ge quantification in SiGe multilayers. This is in line with the studies of Koelling, S., et al. who reported that based on such comparison the depth resolution and the accuracy of the APT analysis degrades depending on the laser wavelength and laser power used. [210].

The schematic representation of the SiGe multi-layer system in our study together with the developed measurement flow is reported in Figure 107.

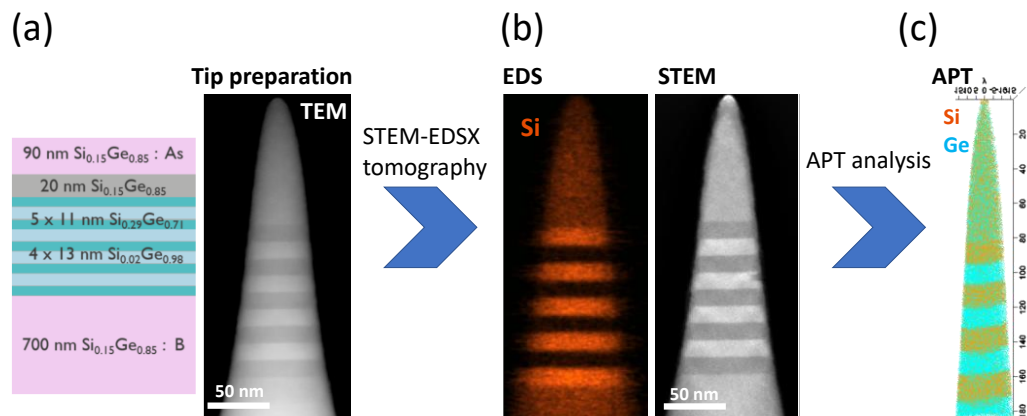


Figure 107: Representation of the measurement flow for the developed combined STEM/EDS tomography-APT analysis. (a) The schematic representation of the SiGe multi-layer system and the TEM image of the prepared sharpened APT specimen by standard FIB lift-out technique. (b) The ortho slices obtained from STEM-EDS tomography on the sharpened APT tip. (c) The 3D reconstructed APT data obtained from the APT measurement on the same sharpened specimen after cleaning by oxygen plasma.

The differences in the field evaporation of Si and Ge and the presence of different layers along the specimen depth, can potentially modify the apex shape and cause reconstruction artefacts at the interface between these layers [211]. To minimize the number of layers involved simultaneously in the field evaporation from the tip apex, the tip shape was prepared in form of a high aspect ratio (small shank angle and initial radius) to ensure a small tip diameter even at 100 nm in depth, where the thin Si<sub>x</sub>Ge<sub>1-x</sub> multi-layers were located. The specimen preparation was carried out by FIB lift-out according to the standard procedures. Then, the specimen was stored in the load lock of the APT tool (high vacuum) before loading to the STEM chamber. The specimen transfer to the STEM chamber was carried out in air. After STEM/EDS analysis, the specimen was cleaned by an isotropic oxygen

plasma for 2 min to eliminate the possible carbon-based materials deposited by the e-beam on the apex and sidewalls of the specimen.

We have measured two APT specimens, according to the described procedures, in the LAWATAP AP tool, while the STEM/EDS tomography was carried out only on one of the specimens. The APT measurements were carried out using UV and green lasers at the optimum experimental condition ( $\text{Si CSR} > 0.95$ ) which allows the accurate quantification of Ge in different  $\text{Si}_x\text{Ge}_{1-x}$  layers. The other experimental conditions were as the follows: base temperature  $\sim 40$  K, detection flux  $\sim 0.005$  atom/pulse and pulse rate  $\sim 100$  kHz.

The tip shape and layer thicknesses measured by TEM/STEM, were used as a reference for the APT data reconstruction. The overlay of the depth profiles for the Si and the Ge concentrations obtained from the APT measurements using UV and green together with EDS analysis is shown in Figure 108. As can be seen the APT measured concentration of Ge/Si for the different layers matched quite well (accuracy better than 5 %) the nominal values reported in Figure 107a, while the EDS was unable to accurately estimate the concentration of  $\text{Si}_{29}\text{Ge}_{71}$ . In addition, the depth profiles obtained by APT indicated a sharper rising and leading edges at the interfaces between the layers. Due to the formation of reconstruction artefacts at the interfaces, we observed a small retention of the core central region of upper layer down to a few nanometer (about 1 to 2 nm) into the lower layer for all the layer structures in our study. This resulted in the appearance of the rising and leading edges of the interfaces in the depth profile with a certain slope (instead of ideal  $90^\circ$ ). The formation of such an artefact at the interface between Si/SiGe was discussed in detail in [211].

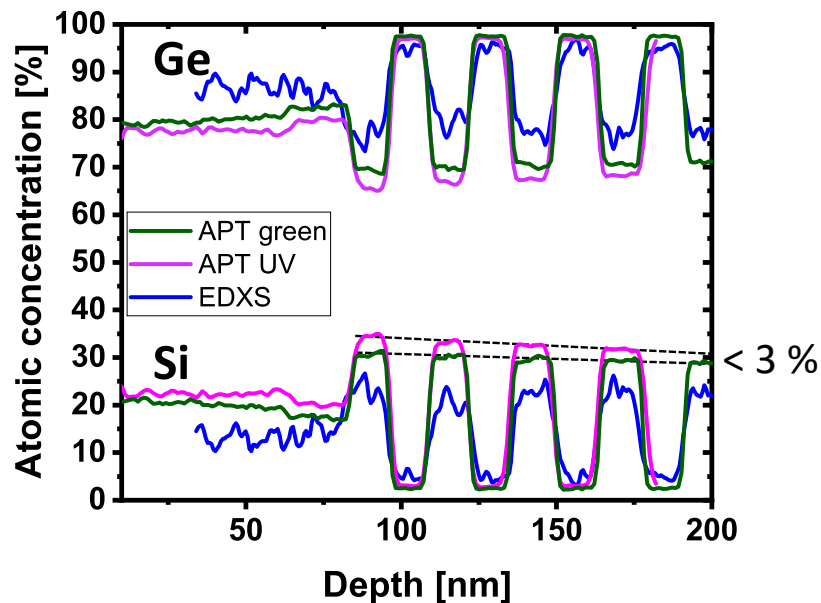


Figure 108: Comparison between the depth profiles obtained by APT measurements (using UV and green laser) and the EDS analysis. The depth profiles for the APT measurements were taken from the  $7 \times 7$  nm<sup>2</sup> core central region of the reconstructed data.

The comparison between the depth profiles of APT measurements using UV and green laser (see Figure 108), indicates that the APT measurement with UV underestimated the Ge concentrations for all the  $\text{Si}_{15}\text{Ge}_{85}$  and  $\text{Si}_{29}\text{Ge}_{71}$  layers by

about 3% (in Ge concentration). In addition, we observe an overall increase in the measured concentration of Ge along the analysis depth by about 2% in green and 3% in UV laser. To better understand these observations, we calculated the variation of electric field (Ge CSR) along the analysis depth for both APT measurements and the results are reported in Figure 109. Our analysis clearly indicates that the overall electric field (Ge CSR) was gradually decreases with analysis depth for both APT measurements, while at the interfaces between the individual layers more pronounced variations occur. This is expected due to the higher field evaporation of Si ( $\sim 33$  V/nm) with respect to Ge ( $\sim 29$  V/nm). Hence, the electric field (Ge CSR) was locally increased by the APT tool (higher supply voltage) at the depth positions corresponding to SiGe layers having higher concentration of Si, to keep the detection rate at a constant level.

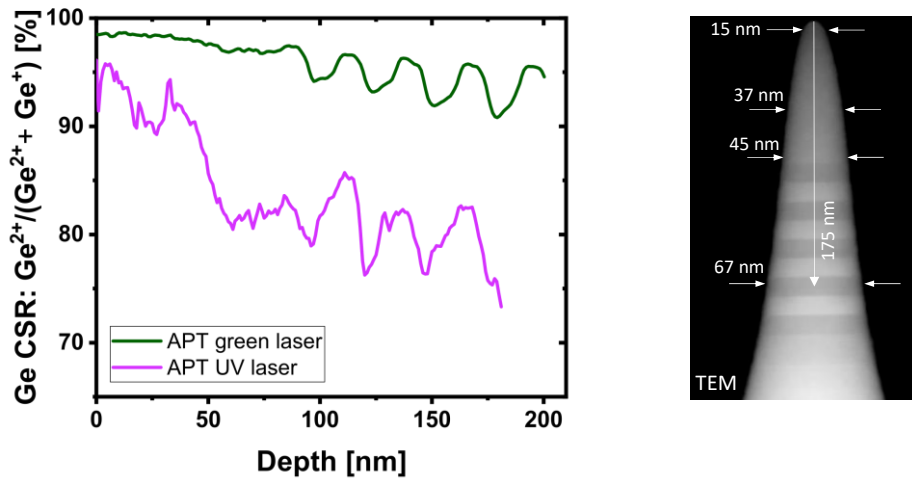


Figure 109: Gradual decrease in the electric field (Ge CSR) along the analysis depth for the APT measurements in UV and green laser (left). The TEM image of the APT specimen before the measurement in UV laser (right).

As discussed in Section 5.3.1, the FOV in APT increases gradually along the analysis depth, as the square function of specimen radius ( $S_{FOV} \approx R^2$ ). In order to maintain the same detection rate along the specimen depth, the evaporation rate has to decrease gradually as the inverse ratio of  $S_{FOV}$  ( $\frac{P_{evap2}}{P_{evap1}} = \frac{S_{FOV1}}{S_{FOV2}} = \left(\frac{R_1}{R_2}\right)^2$ ) as derived in Equation 5.5. Finally, this requires a decrease in the electric field according to Equation 5.8:

$$\exp\left(\frac{\frac{1}{2}Q_0(F_2 - F_1)}{F_{evap}k_B T}\right) \approx \left(\frac{R_1}{R_2}\right)^2 \quad 5.12$$

where  $Q_0$  is the evaporation barrier height at zero electric field,  $F_2$  and  $F_1$  are the electric fields at the tip radius of  $R_2$  and  $R_1$ ,  $F_{evap}$  is the evaporation field of material,  $k_B$  is the Boltzmann constant and  $T$  is the apex temperature.

In the absence of the fundamental material constants to calculate  $Q_0$  and also the value of  $F_{evap}$  for SiGe compounds and even Ge, we have evaluated this equation for a Si specimen having the same tip shape and the initial electric field

(CSR) as the APT measurement in UV laser shown in Figure 109 and using the relation:  $F_2 - F_1 \approx 2.89 \times 10^{-10} \times \ln\left(\left(\frac{R_1}{R_2}\right)^2\right)$ . As can be seen from the TEM image in Figure 109, the initial tip radius ( $R_1$ ) and the radius at 175 nm depth ( $R_2$ ) were about 15 and 67 nm respectively. By knowing the initial Si CSR, the electric field  $F_1$  can be calculated from the Kingham curve of Si to be  $\sim 20.9$  V/nm. Then the  $F_2$  can be calculated from Equation 5.12 to be  $\sim 20.0$  V/nm, which corresponds to a Si CSR of about 75 % according to the Kingham curve of Si. The predicted drop in Si CSR (from 95% to 75 %) is very close to what we have observed experimentally for the drop of Ge CSR along the APT measurement using UV laser (see Figure 109).

The large drop of the electric field (Ge CSR) for the APT measurement using the UV laser can clearly explain the underestimation of the Ge concentration using UV with respect to the same analysis using a green laser. According to the calibration curve described in the previous section (see Figure 102), for a drop of the Ge CSR from 95% to 75%, we expect a reduction in Ge concentration of  $\sim 3\%$ . This matches with the experimentally observed difference between the Ge concentration for APT measurements in UV and green laser light.

We have also observed a gradual increase of the Ge concentration along the analysis depth for both APT measurements while the EDS analysis did not show such a variation. This is very similar to what has been observed for  $\text{Si}_{78}\text{Ge}_{22}$  in the previous section (see Figure 99 and Figure 100).

## 5.7 Conclusion

In this chapter, we have experimentally investigated the distribution of the electric field (or CSR) over the 3D reconstructed specimen volume (lateral and depth) for SiGe/Si tips illuminated by UV and green laser light. As expected, when using a UV laser, the local electric field (Si CSR) gradually increased across the specimen diameter in the direction of laser illumination, whereby at high laser powers (average Si CSR  $< 0.7$ ) we observed a strong gradient in the lateral distribution of electric field while it was negligible at low laser powers (high CSR). In addition, we have observed a gradual decrease in the electric field (Si CSR) along the analysis depth (in SiGe and Si) for all the APT measurements carried out with UV laser (constant flux and laser power). The slope of such a drop in Si was steeper for the analysis using mid-range Si CSR values ( $0.4 < \text{Si CSR} < 0.6$ ).

We attributed the drop in the Si CSR along the analysis depth to the gradual decrease in the evaporation rate linked to the increase in the FOV along the analysis depth. We have developed an analytical expression to predict the variation of electric field ( $F$ ) along the analysis depth correlating it to the variation of the specimen radius  $\left(\frac{1}{R^2}\right)$  along the specimen depth and the initial electric field. This description has been experimentally verified using SEM and TEM.

For APT analysis with a green laser, we have experimentally evaluated the simulated 3D absorption map. Our analysis confirmed the presence of the

predicted non-monotonic variations of the Si CSR along the analysis depth over a wide range of laser powers. However, we observed that the variation of Si CSR along the analysis depth did not follow the predicted periodicity (distance between absorption maxima  $\sim$  laser wavelength).

In the absence of any certified reference material (CRM) for APT, we have developed a concept for a B-doped SiGe reference material (RM) for APT. Such a specimen was carefully analyzed by different complementary techniques to identify the thickness and the composition of the SiGe layer. The traceable quantification for Ge and B (with associated uncertainty) and their uniformity assessment are still ongoing tasks using the reference-free GIXRF technique according to ISO 35:2017 guide for certified reference materials (CRM).

The accuracy of APT analysis in view of Ge quantification over the specimen volume has been evaluated for APT analysis using UV and green laser as well as in different experimental conditions (electric field). We observed a systematic increase in the apparent Ge concentration as a function average electric field (Si CSR). Our analysis indicated that at an average Si CSR  $< 0.6$ , the quantified Ge concentration underestimates the reference concentration. Such an underestimation reached up to about 3% at average Si CSR of about 0.2. In contrary, APT analysis at Si CSR  $> 0.8$  resulted in an overestimation of the Ge content, up to 1.5 %.

We have also investigated the uniformity of the Ge concentration over the reconstructed 3D volume. Our analysis indicates that the Ge concentration varies across the specimen diameter in line with the variation of the electric field (Si CSR) along the laser illumination direction. In particular, for APT analysis with a UV laser, we have observed that Ge concentration increased gradually from the laser side towards the shadow side of the specimen in line with the asymmetric tip shape which is formed under UV laser light.

In order to understand this variation of Ge concentration as a function of electric field (Si CSR), we have investigated several possible loss mechanisms for the Si and Ge atoms, including DC evaporation, dissociation of molecular ions into neutrals and the detector dead zone. However, we did not find any physical explanation for this observed mismatch in the measured stoichiometry of SiGe at low and high field regions. Surface migration might be one factor to be invoked which is however hard to observe. Nevertheless, we identified optimized experimental condition (electric field), which allow more accurate stoichiometry for APT analysis of  $\text{Si}_x\text{Ge}_{1-x}$  compounds ( $x \sim 22, 50$  and  $72$ ) using UV or green lasers.

Our preliminary analysis of the B quantification suggests that there is not much underestimation of the B content in  $\text{Si}_{78}\text{Ge}_{22}$  at high electric field regions, contrary to what was reported for B in Si [201]. Similar to Ge, we have observed an underestimation of the B content at low electric field (Si CSR) for APT analysis using UV and green laser light.

To evaluate the repeatability of APT analysis, in terms of Ge and B quantification and to assess their precisions, we carried out several APT measurements on multiple tips under the same experimental conditions. These

measurements were carried out at the electric field (Si CSR) appropriate for a more accurate quantification in SiGe. Our analysis indicates that the Ge and B quantification in APT has a high repeatability, corresponding to a precision better than 1.2 % and 0.2 % for the average quantification of Ge concentration using a UV or green laser respectively. Similarly, the obtained precision for average B content was better 1.1% (UV) and 2.2 % (green).

Finally, we have demonstrated that the combined STEM/EDS tomography-APT analysis at the optimized APT experimental condition (i.e. electric field) allows for an accurate quantification and 3D data reconstruction of SiGe multi layers. Such an analysis allows the complete 3D geometrical characterization by STEM tomography providing the essential input to reconstruct the APT data with improved 3D composition and layer thicknesses accuracy.

## Chapter 6

# Atom probe tomography on organic/inorganic 3D nanostructures

In this chapter we will discuss the state-of-the-art APT analysis of organic-inorganic systems together with our own results for a polyaniline-porous silicon nano composite. Currently, polymer-porous silicon nano composites are considered as an extremely promising material for a wide range of scientific and engineering applications including: energy storage, optoelectronic devices, photovoltaics, chemical sensors and various emerging biological application such as lab-on-chip and drug delivery [212]. Apparently, the prospective properties of such a 3D composite system vary according to the choice of polymer (i.e. molecular weight), composite morphology and quality of pore filling.

To evaluate these properties for such a complex 3D heterogeneous system, in depth 3D compositional and morphological characterization of such a system is required. Although electron microscopy (i.e. STEM) allows the morphological characterization and an estimate of the pore filling, the compositional analysis remained unsolved (i.e. retention of the solvent in the pores) in this technique. On the other hand, conventional chemical analysis does not have enough lateral resolution to resolve the material within the small pores of such a system. APT is a 3D-analysis method with a high spatial resolution, which might potentially address the required 3D characterization (compositional and morphological) with a high resolution for polymer-porous silicon (PSi) nano composites.

In this project we studied the feasibility of APT analysis of porous silicon (PSi) filled by polyaniline (Pani). The SEM images of this composite system are shown in Figure 110. The thickness of the PSi was about 1  $\mu\text{m}$ , which was achieved by electrochemical etching of a  $n^+$ -doped Si (100). The pore filling was carried out by electrochemical deposition. The SEM image shown in Figure 110c suggests that the Pani was penetrated deeply inside the PSi (1~  $\mu\text{m}$ ),

corresponding to the entire film thickness. Please note that, according to other SEM images, the filling was not uniform across the specimen surface as in some regions the thickness of the filled layer was slightly thinner.

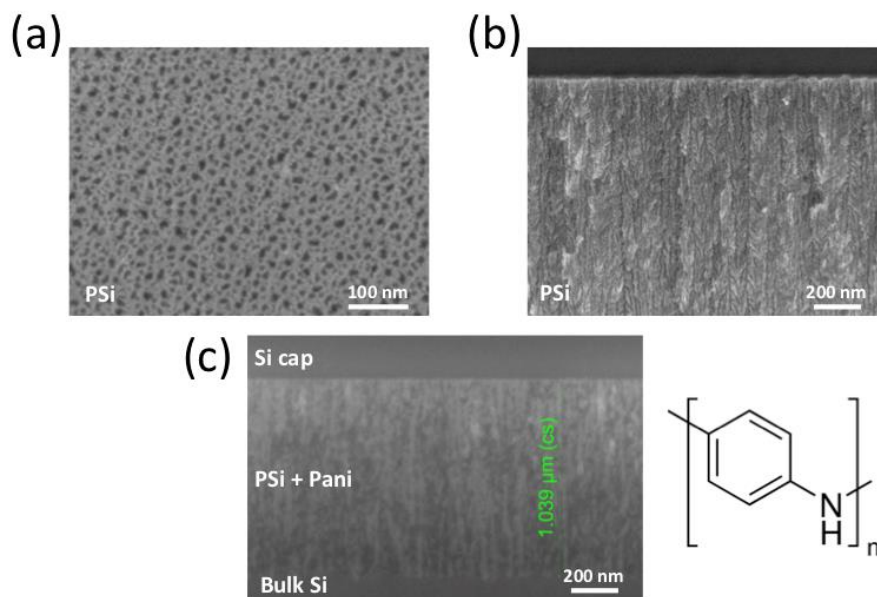


Figure 110: SEM top (a) and cross-section (b) images of porous silicon (PSi) as the inorganic template. (c) SEM cross-section image of PSi filled by polyaniline. The thickness of PSi layer was measured about 1  $\mu\text{m}$ . The schematic representation of the monomer is also shown in the figure. Please note that SEM image shown in (b) were taken from a similar system with a thicker PSi layer.

We also performed a ToFSIMS measurement on the filled structure to ensure the presence of polyaniline within the pore. The measurement clearly indicated peaks at the molecular structure of polyaniline:  $\text{C}_{12}\text{H}_{10}\text{N}_2\text{H}_2^+$ ,  $\text{C}_6\text{H}_8\text{N}^+$  and  $\text{C}_6\text{H}_7\text{N}^+$ .

## 6.1 APT analysis of organics

Traditionally, APT analysis in pulse-voltage was limited to metallurgical specimens, mainly due to their electrical conductivity. By the advent of modern laser-pulse AP instruments such a limitation has been circumvented, in which the application of APT analysis has been extended to semiconductors, non-conductive insulators, ceramics and biological materials [213].

Successful APT analysis has been reported for biominerals and tissues (i.e. bones and teeth). Gordon, L. M., et al. [139] reported a 3D reconstruction of an elephant tusk dentin together with the collected mass spectra. The same author also demonstrated that APT allows the analysis of a buried organic-inorganic interfaces in a chiton tooth [214]. In addition, a FIB specimen preparation technique was reported to be suitable for the preparation of APT specimen from biominerals.

Nevertheless, APT analysis of polymers and organic molecules has not been well explored. Prosa, T. J., et al. [142] reported the mass spectrum from poly(3-alkylthiophene)s thin films, deposited on the Al pre-sharpened APT specimens. The spectrum for the P3AT film deposited by electrospray ionization methodology is shown in Figure 111. This study clearly demonstrated that the

detected fragments were not at the individual atom scale and the fragments varied according to the structural morphology of the polymeric thin film.

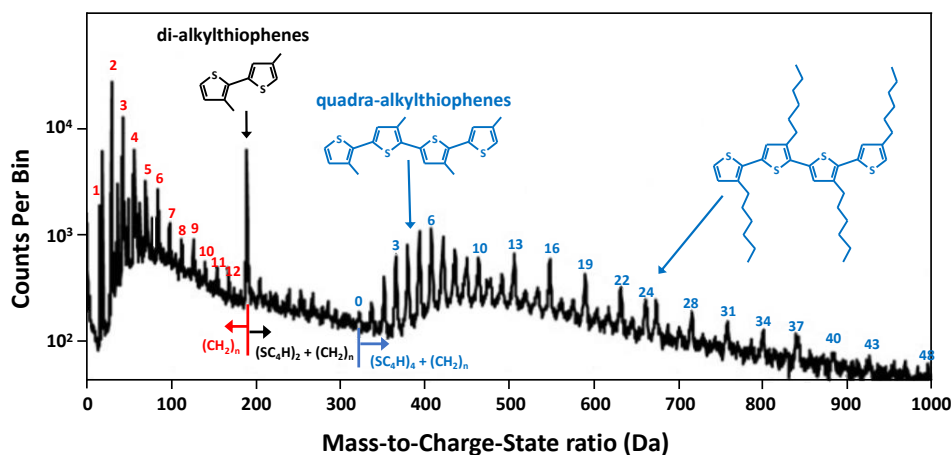


Figure 111: The collected APT mass spectrum from poly(3-alkylthiophene) thin film deposited by electrospray ionization on Al pre-sharpened APT specimen. The labeled peaks on the spectrum ( $15 < m/z < 190$  Da) were identified as single charged alkane fragments:  $C_nH_{-2n}^+$ , with  $n = 1, 2, \dots, 12$ . The peak at 190 Da and its successive peaks at the interval of 12 Da were identified as di-thiophene molecules having different amounts of attached alkane according to the mass/charge ratio. The numbered peaks (0 to 48) after 320 Da are identified as quadra-thiophene molecules with different amounts of alkane attached. Reproduced from [142].

Although, Gault, B., et al. [144] reported a preliminary result for self-assembled monolayers, the 3D distribution (lateral and depth) for the molecular structure of polymers or organic molecules has not yet been reported in literature. This is not surprising, given the currently used specimen preparation technique which is based on thin film deposition (i.e. dip-coating or electrospray ionization) on a pre-sharpened metallic specimen. Indeed, accurate 3D data reconstruction can only be carried out once the apex has been shaped during the first stage of APT analysis, whereby the thin deposited organic film is already consumed. In addition, organic molecules are known to undergo structural phase transitions at much lower temperatures as compared to inorganic material [215]. Hence, they are more sensitive to the choice of the experimental conditions, including laser power and pulse rate. Several recent studies have been focused on the development of specimen preparation techniques for organic molecules and polymers [137], [140], while no significant improvement in terms of the 3D data reconstruction has been observed.

The APT analysis of synthesized organic-inorganic nano composites has not been documented in the literature. We expected that the conductive inorganic template (i.e. PSi in our study) can potentially improve the field enhancement at the tip apex and facilitate the field evaporation process similar to what suggested by Kelly, T. F., et al. [138]. Hence, PSi might potentially be considered as a template for the analysis of non-conductive organics in APT.

To conclude, APT can allow the analysis of organic molecules and polymers whereby large molecular fragments (ions), corresponding to structural morphology of organic molecule, can be identified. So far, the 3D distribution (lateral and depth) of a molecular structure has not been reported in the literature. To evolve APT into an accepted metrology tool in the field of organic molecules

and polymers, still many aspects need to be explored and developed such as: better understanding of the fragmentation variability, study of the possible dissociation of molecular ions and the role of the experimental conditions, the specimen stability and the minimization of the damage to the molecular structure.

## 6.2 APT specimen preparation

In order to prepare APT specimens from  $\sim 1 \mu\text{m}$  thick film of PSi filled by Pani, the standard FIB specimen preparation technique was selected either from the top or in the cross-sectional configurations. In Figure 112, the SEM images of two prepared specimens from top and cross-section configurations are reported.

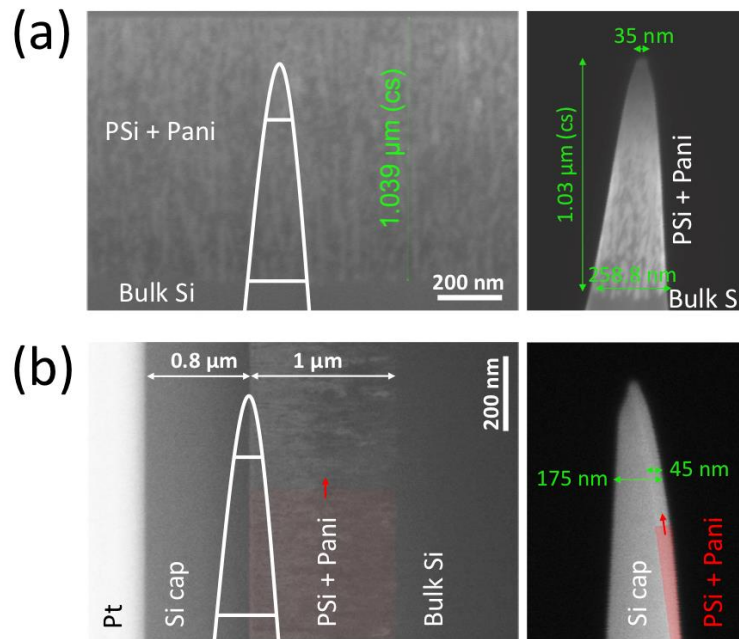


Figure 112: APT specimens prepared from  $\sim 1 \mu\text{m}$  thick film of porous silicon filled by polyaniline. The specimen preparation was carried out according to the standard FIB technique in (a) top configuration (b) cross-section configuration.

To minimize the extent of the Ga induced damage along the specimen depth (in top configuration), a  $\sim 60 \text{ nm}$  thick Cr film was evaporated on top of the substrate. The Cr cap together with the remaining Pt were milled away during the final low ion energy clean. In order to allow lamella lift-out in the cross-section configuration, about  $0.8 \mu\text{m}$  thick Si cap layer was evaporated on top of the substrate. In addition, a thick Pt layer  $\sim 0.6 \mu\text{m}$  was deposited on top of the evaporated Si cap.

We have prepared several APT specimens in both configurations. The prepared specimens in top configuration were quite comparable in view of specimen diameter. In the next section the APT analysis of the prepared specimens will be discussed in detail.

### 6.3 APT analysis of PSi filled with Pani

To analyze the APT specimens made from PSi filled with Pani, we used LEAP 5000XR with UV light. The pulse rate was adjusted to 150 kHz in order to have a large enough mass range in view potentially large fragment formation. After the alignment of the specimen in front of local detector followed by a coarse laser alignment (manual alignment), we have observed a mass spectrum consisting of Si and C peaks. Note that the automatic laser scan did not proceed successfully and we could not start the measurement in the constant detection regime as the detection rate was fluctuating even at a constant applied potential and primarily burst of ions were detected. We have repeated the automatic laser scan several times on different specimens (top and cross-section configurations) and various choices of Si CSRs. None of them gave any improvement in view of reaching a steady state evaporation rate and the automatic laser scan failed in all the cases. This observed evaporation/detection in bursts is not surprising for such a complex non-homogeneous 3D specimen consisting of pores and elements with large differences in the evaporation fields (Si and C).

We have tried this measurement on another APT tool (LAWATAP) where the laser spot has a larger diameter and the fine laser alignment (automatic scan) is not required. In addition, to tackle with previously observed burst evaporation/detection, we defined a wide detection window (0.0015 to 0.005 ion/pulse) for the adjustment of the applied electric potential. This implies that for the different detection rates within this defined window, the measurement was assumed to be at constant detection rate, in which the tool did not adjust the applied voltage for the variation of detection rate within this window.

In order to find the optimum experimental conditions to start the APT measurement in this detection range, we used different laser wavelengths (IR, Green and UV laser) and various laser powers. We observed that the APT measurement was only started with the UV light at relatively high laser powers, corresponding to a Si CSR < 0.5.

The APT measurement started smoothly at 15  $\mu$ W laser power in UV range (Si CSR  $\sim$  0.5), where the other experimental conditions were as the follows: detected flux from 0.0015 to 0.005 ion/pulse, base temperature: 60 K and laser pulse rate of 100 kHz which is fixed on LAWATAP tool. To investigate the possible influence of electric field (or equivalently temperature) on the fragmentation/dissociation of molecular ions, the laser power was gradually increased after every 300,000 detected events by a step of 5  $\mu$ W up to the maximum value of 35  $\mu$ W. The experimental conditions for this measurement are summarized in Table 15.

Table 15: Experimental condition used during APT analysis of the porous silicon filled with polyaniline. The measurement was carried out in LAWATAP instrument, where the pulse rate is fixed to a value of about 100 kHz.

Ion sequences [M ions]	UV laser power [ $\mu$ W]	Detection rate [ion/pulse]	Base temperature [K]
0 to 0.3	15	0.0015 to 0.005	60
0.3 to 0.6	20	0.0015 to 0.005	60
0.6 to 0.9	25	0.0015 to 0.005	60
0.9 to 1.2	30	0.0015 to 0.005	60
1.2 to 7.1	35	0.0015 to 0.005	60

### 6.3.1 APT 3D data reconstruction

The 3D data reconstruction for the described APT measurement was carried out in IVAS software and the results are shown in Figure 113. To visualize the distribution of PSi and Pani, the monoatomic ions of Si (for PSi) and C (for Pani) were used in this study. Please note that the average atomic density of such a complex 3D system, which consists of many voids, is unknown. In addition, the presence of localized regions with different materials having very different field evaporations add more complexity to the 3D data reconstruction. In this study we finely tuned the reconstruction parameters to approximately match the obtained pore diameter to the TEM image as also done by Mouton. I., et al. [208] on a similar PSi specimen filled with an inorganic Ni filler. To better visualize the distribution of Pani within the pores of PSi, the side and cross-section view of a slice of the reconstructed volume having a height from 150 to 210 nm are shown in Figure 113b. As can be seen, the monoatomic C-ions were distributed within the Si pores along the specimen depth. Hence, the distribution of Pani within the pores of PSi can clearly be identified according to the distribution of monoatomic ions of C and Si. In addition, the 2D concentration maps of C ( $C^+$ ,  $C^{++}$ ), Si ( $Si^+$ ,  $Si^{++}$ ) and silicon oxide ( $SiO^+$ ,  $SiO_2^+$ ) were plotted for the same slice of the specimen volume in Figure 113c. This figure indicates the presence of localized Si rich regions (concentration > 95 %) and regions where the concentration of C ions are maximum similar to what reported by Mouton. I., et al. [208] on PSi filled with a Ni filler. We assigned these C rich regions to the pores of PSi.

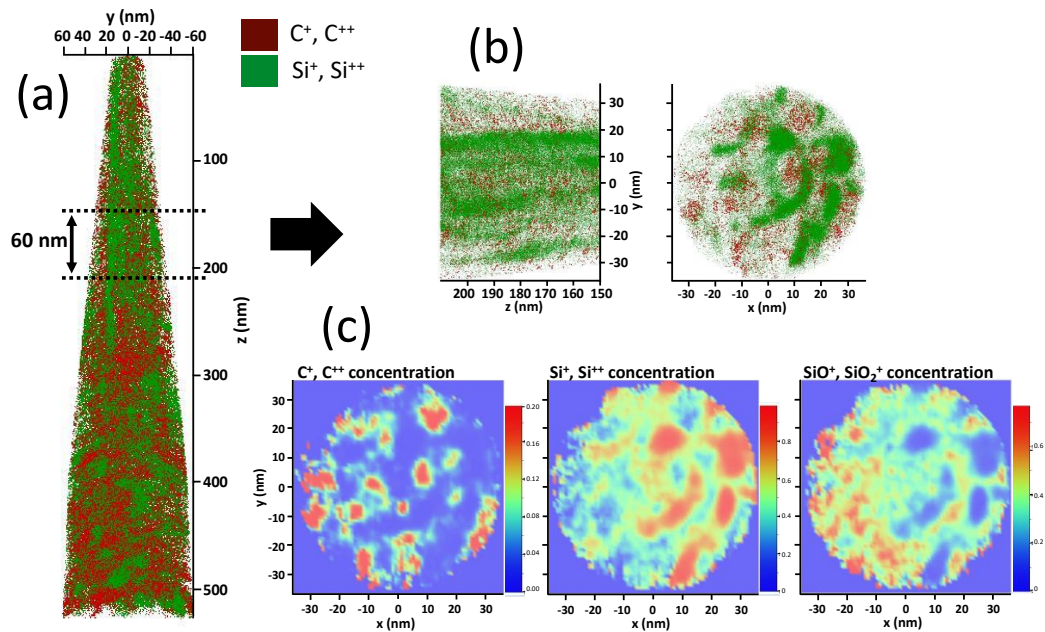


Figure 113: The 3D reconstruction of APT measurement on a specimen prepared from PSi filled with Pani. (a) The 3D reconstructed volume of the specimen according to the monoatomic ions of C (represented by red dots) and Si (represented by green dots). (b) The distribution of C within the pores are shown in a zoomed view (side and cross-section) of a slice of the reconstructed volume having a height from 150 to 210 nm, where the same color code was used to represent the C and Si ions. (c) The 2D concentration maps of C ( $C^+$ ,  $C^{++}$ ), Si ( $Si^+$ ,  $Si^{++}$ ) and silicon oxide ( $SiO^+$ ,  $SiO_2^+$ ) for the same slice of the specimen shown in (b). The color bars show the ionic concentration according to the all ranged peaks on the spectrum.

In addition, the 2D concentration maps of  $SiO^+$  and  $SiO_2^+$  ions were also compared to the C and Si maps. The overall concentration of silicon oxide in the specimen volume was higher as compared to that of bulk Si, probably due to the presence of the large native oxide volume around the pores of PSi. The figure also suggests that the concentration of  $SiO^+$  (and  $SiO_2^+$ ) was higher within the pores. This is similar to what was reported by Mouton, I., et al. [208] on a PSi matrix. Furthermore, a careful comparison between the C and oxide concentration maps indicates that the localized maximum concentrations of C and oxides are not spatially correlated. This might be due to a reconstruction artefact or to the presence of voids (not filled pores). Further investigation of 3D structure/composition of inorganic matrix (PSi) with different fillers by APT and TEM tomography can better understanding of the actual 3D distribution of the silicon oxide.

To summarize, the distribution of Pani within the pores of PSi can be identified according to the distribution of monoatomic ions of C and Si. Nevertheless, due to the presence of 3D structures with different evaporation fields (Si, oxide and Pani), we expect that the apex shape should have deviated from the atomically smooth hemispherical shape which was assumed in the data reconstructed protocols. Hence, we expect several reconstruction artefacts in the reported 3D reconstructed data which hamper the resolution of APT analysis (both depth and spatial) and might induce a compression/extension of the actual 3D structure.

### 6.3.2 Fragmentation of polyaniline

The mass spectra as obtained by APT at different laser powers are shown in Figure 114. To compare the peak heights, only 300,000 detected events were plotted for each spectrum. As can be seen from the spectra, the major peaks are either monoatomic ions of carbon ( $C^{++}$  and  $C^+$ ) or monoatomic/molecular ions from the P*Si* inorganic template ( $Si^{++}$ ,  $Si^+$ ,  $SiO^+$ , etc). In addition, there are several unidentified peaks having minor counts, which due to the lack of clear isotopic ratios for the molecular ions composed from C, N, O and H cannot be identified accurately. Hence, Pani was mainly detected as carbon atomic fragments, whereby the structural morphology of the polymer cannot be identified. The comparison between the spectra obtained at different laser powers, indicates no improvement in view of the organic fragment size (for Pani), while at higher laser powers the Si clusters size became larger ( $Si_2^+$ ,  $Si_3^+$ , up to  $Si_5^+$ ). Hence, regardless of the choice of experimental conditions during APT analysis (field and temperature), the Pani was detected always as mono atomic ions of carbon.

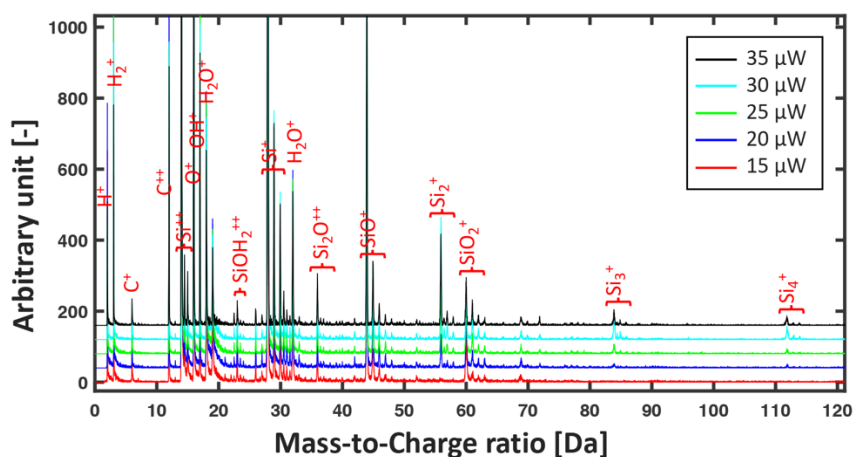


Figure 114: Comparison among the collected mass spectra at different laser powers. Each spectrum corresponds to 300,000 collected events, where the major peaks are also identified on the figure. Please note that the y axis has an arbitrary unit and the figure only compares the position of the peaks (mass-to-charge ratio) rather than the counts.

The observed small organic fragments might be associated to the dissociation of larger clusters during their flight toward the detector. In the presence of intense electric field at the vicinity of specimen apex, metastable molecular ions may decompose into smaller fragments (two or more), which typically occurs during the first stage of their flight. This has been widely studied for inorganic systems. For instance, oxides and nitrides are known to evaporate as molecular ions, whereby some unstable ions were observed to dissociate in the presence of strong electric field in the vicinity of specimen [216], [217]. Typically, the dissociation study in APT can be done either by numerical prediction (molecular dynamics simulation) of unstable molecular ions or by analyzing the multi-hits events detected during APT measurement. In this section the multi-hits events and the corresponding dissociation study are first briefly introduced.

The multi-hits events can be associated either to the co-evaporation (or delayed evaporation) or dissociation of molecular ions into two or more smaller ions/neutrals fragments. Upon the trigger of the laser pulse, each surface atom has a certain evaporation probability. Hence, depending on the arrangement of the surface atoms (local field enhancement) and the required evaporation field of elements, there is also a certain probability for co-evaporation during/soon after the laser pulse. Typically, in diluted systems, elements having higher evaporation fields (i.e. C and B) are predominantly involved in the multi-hits detection events. Such multi-hits are typically closely correlated in space. Alternatively, the dissociation of molecular ions, evaporated from the surface, into two or more ions/neutrals fragments, can lead to detected multiple event.

The statistical analysis of detected pairs in multiple events, can bring many insights on the different aspects of evaporations, including: dissociation, compositional biases, etc. To analyze the multiple events (i.e. double hits), typically the mass-to-charge ratio of the ion pairs are plotted versus each other ( $m_1$  versus  $m_2$ ). Such a plot is known as the ion correlation histogram [218]. Each point in the correlation histogram corresponds to a pair combination observed as a multiple event. In the correlation histogram typically four main characteristic shapes can be identified:

**Dots on the intersection of horizontal/vertical lines:** these ion pairs represent the co-evaporation of two ions, evaporated coincidentally with the laser pulse or shortly after the pulse [219].

**Dots along horizontal/vertical lines:** these ion pairs represent the delayed evaporation of one ion with respect to the other one. Typically, one ion evaporates on the laser pulse or shortly after, while the paired ion evaporates by a delay ( $dt$ ) after the laser pulse within the decay of the specimen temperature [218].

**Diagonal trails with positive slopes:** these ion pairs represent the simultaneous evaporation of both ions from the specimen surface by a delay  $dt$  after the laser pulse. Hence, their times-of-flight are extended by  $dt$  and the pair appears similar to a curved track on the correlation histogram [218], [219].

**Diagonal trails with negative slopes:** these ion pairs represent the molecular dissociation tracks, which occur after field evaporation of metastable molecular ions. In the presence of intense electric fields, the metastable molecular ions may decompose into two or more smaller fragments (ion or neutrals). By assuming that the metastable molecular ion (parent ion) has a mass-to-charge ratio of  $m_p$  and was evaporated at the potential of  $V_e$ , the dissociation can take place at different distances from the specimen surface, where the electric potential  $V$  is smaller than  $V_e$ . Hence the dissociation products or daughter ions  $m_1$  and  $m_2$ ,  $\left(m_p \xrightarrow{\text{dissociation}} m_1 + m_2\right)$  will appear by slightly different mass-to-charge ratios ( $m_1'$  and  $m_2'$ ) depending on the electric potential where the dissociation has been

occurred (or equivalently the distance from the surface) [219]. The dissociation track on the correlation histogram begins by the daughter ion pairs ( $m_1$ ,  $m_2$ ), corresponding to the dissociation at the specimen surface ( $V = V_e$ ) and it follows by a curved path corresponding to the different mass-to-charge ratios ( $m_1'$  and  $m_2'$ ), where the dissociation has occurred at the different distances from the surface ( $V < V_e$ ). Finally, the dissociation track ends at ( $m_1' = m_p$  and  $m_2' = m_p$ ), corresponding to no dissociation or equivalently dissociation at the detector position ( $V = 0$ ).

To investigate the possible dissociation of molecular fragments of Pani into the observed mono atomic ions of C in our APT analysis, we carried out a multi-hit analysis. We observed that less than 5 % of the detected events were in form of multi hits. In Figure 115 the correlation histogram for double-hits ion pairs is shown. As can be seen, the majority of the tracks are associated to co-evaporation and delayed evaporations. We have only observed two minor dissociation tracks in the correlation histogram, which are both associated to the oxides of inorganic template (PSi). The first dissociation track (track #1 in Figure 115) starts at mass-to-charge ratio of ( $m_x=16$  Da,  $m_y=28$  Da) and ended at ( $m_x=22$  Da,  $m_y=22$  Da), while the second shallow track (track #2 in Figure 115) starts at mass-to-charge ratio of ( $m_x=16$  Da,  $m_y=60$  Da) and ends at ( $m_x=44$  Da,  $m_y=44$  Da). Similar to what reported by Zanuttini, D., et al, [216], we attributed this dissociation tracks to  $SiO^{2+} \xrightarrow{\text{dissociation}} Si^+ + O^+$  and  $Si_2O^{2+} \xrightarrow{\text{dissociation}} SiO^{2+} + O$  respectively. Please note that the neutral product of the dissociation (O) had enough velocity to reach the detector [216].

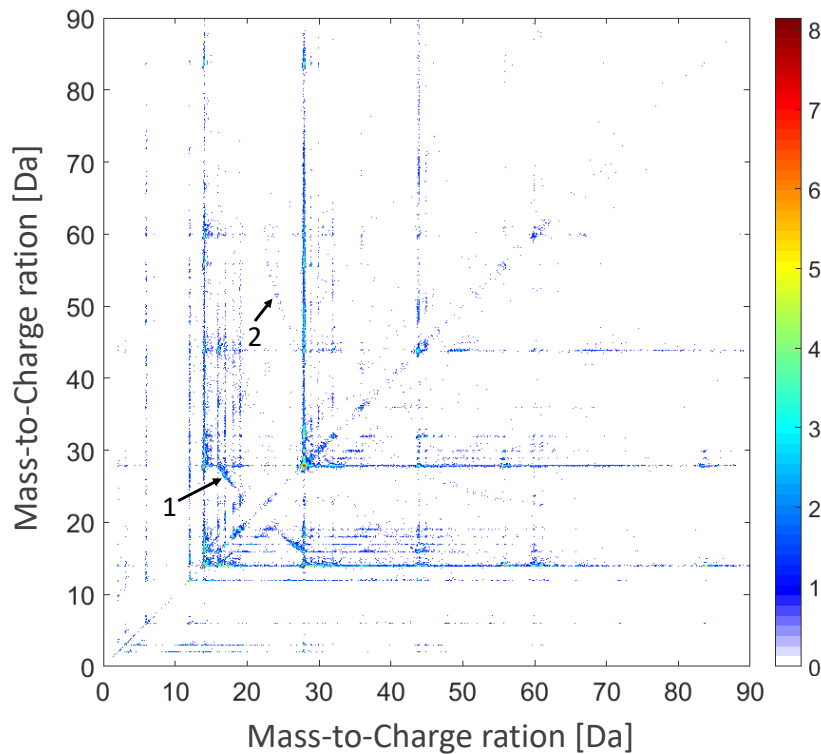


Figure 115: Correlation histogram obtained from the double-hits ion pairs detected in the APT analysis of PSi filled by Pani. The two dissociation tracks in the figure are: 1:  $SiO^{2+} \xrightarrow{\text{diss}} Si^+ + O^+$ . and 2:  $Si_2O^{2+} \xrightarrow{\text{diss}} SiO^{2+} + O$ . The color bar shows the relative counts.

Our analysis reveals that there was no dissociation track associated to the molecular ions of Pani. Hence, the detected mono atomic ions of C ( $C^+$  and  $C^{++}$ ) were evaporated as the small fragments of C. Prosa T. J., et al. [142] has a similar observation on a C60-doped P3HT polymer sandwich between Al contact and Si substrate. They observed that for the specimens prepared by FIB lift-out technique, the mass spectrum only consisted of the mono atomic ions of carbon ( $C^+$ ,  $C^{2+}$ ), without any molecular peaks of the polymer (Figure 116a). While in the same study, the APT spectrum of the same polymer using another sample preparation technique (dip coating) clearly indicated the molecular peaks for the polymer (Figure 116b). A similar observation was also reported for resin, where the monoatomic ions of carbon ( $C^+$ ,  $C^{2+}$ ) were reported to be the most dominant peaks [137].

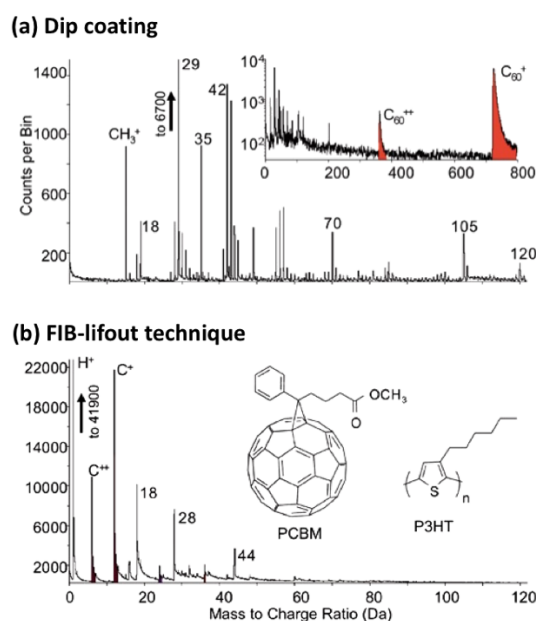


Figure 116: APT mass spectrum for C60-doped P3HT polymer, obtained from an APT tip prepared by dip coating (a) and FIB lift-out technique (b). The molecular peaks for the polymer were absent in case of FIB lift-out sample prep. The spectra are reported from reference [136].

Currently, the extent of FIB-induced damage on the polymers and organic materials is not well understood and little has been documented in this area. Bassim N. D., et al, [135] carried out a study on the extent of electron and Fib damage on polyacrylamide polymer using X-ray absorption near-edge structure (XANES). They reported that electron imaging (at 5 keV) induced a considerable chemical damage to the polymer [135], while a minor damage has been reported by varying the FIB parameter (final ion voltage).

Hence, we attributed the observed monoatomic ions of C to the FIB-induced damages or electron imaging during the specimen preparation and we assumed that the polymer structure was fully dissociated to small fragments prior to APT measurement. A more sophisticated study on the possible impact of the electron imaging and the impact of  $Ga^+$  ions on the dissociation and damage to the molecular structure of polymers during FIB lift-out sample preparation and the successive sharpening step is required. For instance, Cryo FIB specimen preparation might help in minimizing the induced damage to the polymer.

## 6.4 Conclusion

In this section we briefly described the state-of-the-art APT analysis of organic materials. APT has been reported to be successful for the analysis of biominerals and tissues (i.e. bones and teeth), where the mass spectrum and the 3D distribution (lateral and depth) of organic/inorganic fragments can be identified. Vice versa, the work using APT on organic molecules and polymer so far was limited to the collection of mass spectra. The larger molecular fragments, corresponding to structural morphology of the polymer were identified in the spectrum, while the 3D reconstruction (lateral and depth distribution) for a molecular structure has not been reported for organic molecules and polymers.

We studied in detail the APT analysis of an organic-inorganic system based on a polyaniline (Pani)-porous silicon (PSi) nano composite. Our analysis suggests that such a complex system can be analyzed by APT. By tuning the reconstruction parameters, the 3D distribution of polyaniline within the pores of PSi can be identified according to the distribution of monoatomic ions of C (for Pani) and Si ions (PSi). Our analysis indicated that the molecular structure of the polymer was completely damaged during FIB specimen preparation step such that Pani was mainly detected as monoatomic ions of carbon ( $C^{++}$  and  $C^+$ ) and the larger molecular fragments corresponding to structural morphology of the polymer were absent in the spectrum. Our dissociation analysis also confirmed that the Pani was evaporated as monoatomic ions of carbon and no any trace of dissociation has been observed in the spectrum associated with the polymer fragments.

An improvement in specimen preparation technique is clearly required to eliminate/minimize the damage to the polymer as a first step towards a successful APT analysis. A possible solution could be Cryo FIB.

# Chapter 7

## Conclusion and Outline

The aim of this doctoral project was to develop and fabricate different 3D heterogeneous micro and nano structures as potential reference materials for different 3D compositional/chemical analysis techniques: time-of-flight secondary ion mass spectrometry (ToFSIMS), Grazing incidence X-ray fluorescence (GIXRF) and atom probe tomography (APT). The motivation for the preparation of such reference 3D structures was to assess the metrological framework, i.e. accuracy, precision and traceability, for the aforementioned 3D analysis techniques, which is currently hampered due to the absence of any available certified 3D reference material (CRM) and the standard procedures.

In this project we have developed several well-characterized organic-inorganic 3D reference microstructures for 3D ToFSIMS. Three different 3D model-systems composed of a double layered organic system (irganox and polystyrene) confined within a microstructured Si template were developed. The traceable dimensional characterization of the Si templates was carried out by a calibrated optical profilometer and the measurement results are reported with the associated uncertainties followed by a certification from the length department of INRIM (NMI of Italy). Similarly, the morphology of each organic layer was measured by the optical profilometer (no uncertainty assessment at the moment). The design of the reference structure in this project allows the use of the planar organic layers, far from the 3D microstructured region, as a reference for the calibration of the sputter yields and the chemical information.

To prepare the 3D reference nanostructures for GIXRF with structural ordering and dimensions comparable to those industrial applications (i.e. the technology node), we exploit the self-assembly of di-block copolymers (DBC) as a lithography mask. The DBCs in the perpendicularly oriented cylindrical morphology allow the preparation of a well-ordered lithography mask on a large scale (e.g. entire sample area) with the tunable characteristic dimensions at sub 20 nm scale. We have studied in detail, the pattern transfer of such DBC masks (pore diameter from 19 nm down to 13 nm) into the Si substrate, which will be

summarized in Section 7.1. By combining the capabilities of self-assembly of DBCs and the fine control on the pattern transfer, we were able to prepare different 3D nanostructures in the form of holey Si, SiO<sub>2</sub>, Ge and SiGe with characteristic dimensions below 20 nm and with a fine control over the pore diameter, periodicity and the depth of structures. The developed reference 3D structures are suitable as the test vehicle for GIXRF analysis, where the characteristic dimensions (i.e. pore diameter and the periodicity) and their distributions are known over a large area.

In order to develop a potential reference material for APT, we have studied in detail the different metrological aspects of the data reconstruction in APT, i.e. field of view (FOV) and the calibration of the different reconstruction parameters. In Section 7.2, I will summarize our study on the FOV and the developed new specimen design, which maximizes the FOV (full tip imaging) in the APT analysis. In Section 7.3, the accuracy and the precision assessment of the APT analysis in view of the quantification of B and Ge in a B doped Si<sub>78</sub>Ge<sub>22</sub> film will be reported. In Section 7.4, the extent of the APT analysis of organic materials and its challenges will be summarized. Finally, in the last section, I will outline some potential routes to improve the different aspects of APT analysis based on the obtained results in this project.

## 7.1 Feature-dependent RIE etch as sub 20 nm

We have studied in detail the pattern transfer of DBC masks into the Si substrate by reactive-ion etching (RIE) in Chapter 2. We discussed that the Cryogenic mixing mode of SF<sub>6</sub> + O<sub>2</sub> is the most suitable etch process for the direct pattern transfer of nanometric features using a soft mask, owing to the high selectivity (Si with respect to the polymeric mask) which this process can offer. The feature-dependent etch of Si at sub 20 nm scale has been investigated for this process using the polystyrene-block-polymethylmethacrylate (PS-b-PMMA) DBC masks in the cylindrical morphology with different pore diameters ranging from 19 to 13 nm. Our analysis clearly indicates that the etch rate on the bare Si substrate (unmasked substrate) is about 450% higher than that obtained through the narrow pores of DBC masks, which indicates a remarkable drop in the etch selectivity (Si to PS) from 15:1 to less than 1:1. In addition, our analysis suggested that the Si etch rate through the pores of the DBC masks decreases about 14% as the pore diameter reduces from 19 to 13 nm.

Moreover, our analysis revealed that by increasing the thickness of the DBC masks by 33% (from 30 to 40 nm), the etch rate drops about 40%, which implies that a thicker DBC mask cannot improve the maximum achievable etch depth and vice versa it has a negative impact on the etch rate and the maximum achievable etch depth. We attributed the observed etch behavior to the limited transport of fluorine-based neutrals through the narrow pores of the DBC masks/Si nanostructures, which can be described by the Knudsen transport as the mean free path of the fluorine-based neutrals in the plasma are much higher respect to the pore diameter of the DBC masks.

## 7.2 Field-of-view in APT

As discussed in Chapter 4, the field-of-view (FOV) in APT analysis is commonly defined as an area of the apex surface from where the evaporated ions can reach the detector. We discussed that the FOV is governed by those ion trajectories which hit the detector, thus FOV can be determined according to the ion trajectories and the detector dimension. The FOV for a hemispheric tip shape was shown to be the core central region of the specimen, which varies from specimen-to-specimen according to the distribution of ion trajectories. The FOV for a hemispheric tip shape can be accurately identified from the reconstructed data, provided that the data reconstruction was carried out according to the calibrated reconstruction parameters.

Vice versa, as the deviation of the apex shape from an atomically smooth hemispherical shape results in the aberration of the ideal ion trajectories (i.e. that of smooth hemispherical tip shape), the currently available reconstruction protocols are unable to accurately reconstruct the data, thus the FOV must be determined directly from the ion trajectories for such a tip shape.

We discussed that finite element simulations allow the calculation of ion trajectories at both mesoscopic and microscopic scales. We have studied in detail the FOV for an asymmetric tip shape as induced by UV laser since this is one of the most common examples, where the apex shape can strongly deviate from the hemispherical shape. The results of our study are summarized as follows.

### **FOV for UV-induced asymmetric tip shape**

The UV laser induced asymmetric tip shape is one of the typical examples, where the apex shape can strongly deviate from the ideal hemispherical shape. Our study indicates that in the UV-assisted APT, the center of the FOV dynamically shifts toward the shadow side of the tip as it projects the ions from the top most region of the specimen always at the detector center. The shift in FOV depends on the degree of asymmetry induced on the apex shape and can be estimated from the distance between the specimen axis and the detector center line defined on the specimen image (i.e. TEM image). The detector center line can be identified on the TEM image of the specimen as a vertical line parallel to the tip axis which passes through the local maximum of the specimen height. We estimated the shift in FOV (towards the shadow side of the tip) for a Si specimen analyzed at a Si CSR  $\sim 0.2$  to be about 13 nm, where the tip radius was about 75 nm.

### **Full tip imaging in APT**

As the FOV in the APT analysis is determined by the combination of the ion trajectories and the detector dimension, one can improve the FOV either through compressing further the ion trajectories towards the detector or by increasing the

detector dimension. The latter requires further developments in the detection system (hardware) and it is not currently available.

In this project to maximize the FOV and probe the entire specimen volume in APT (full tip imaging), we proposed a new design for an APT specimen, which consists of a zero degree-shank angle nanowire prepared on top of a cylindrical micropost. The feasibility of full tip imaging, using our new specimen design, has been proven both numerically and experimentally. Our FEA analysis indicates that the presence of a flat area on top of the micropost, below the NW, compresses the ion trajectories towards the detector center such that the ions evaporated from the sidewalls of the NW still hit to the detector. We numerically investigated the optimum dimensions (diameter and height) for the preparation of both NW and micropost which allow full tip imaging and create enough electric field enhancement at the apex of the NW.

In order to experimentally evaluate the performance of this new specimen design, we developed a preparation process, based on the standard lithography and etching technique. The process allows to prepare multiple APT specimens in a reproducible fashion and with minimized tip to tip variations in view of tip radius and shank angle. Finally, we fabricated the NW tip shape (zero degree shank angle) on top of a cylindrical micropost according to the exact dimensions suggested from the FEA.

The APT analysis of the prepared NW tip, proved the full tip imaging feature for such a specimen design, whereby the native oxide of the NW side walls was within the FOV. In addition, our analysis of the number of detected Si atoms versus the estimated number of the actual atoms from the SEM image (from the analyzed volume), also confirms the full tip imaging feature in our measurement. As the first full tip imaging in the history of APT analysis (sidewalls within the FOV), we have observed different forms of distortions in the 3D reconstructed data. For instance, the native oxide was projected as a thick layer ( $> 15$  nm) having a very shallow density and the Si as the very dense region with a small diameter. By correcting the density to the standard values, our analysis demonstrated that the thickness of Si and the native oxide reached quite close the observed dimensions on the SEM image. Finally, we attributed a part of the observed artefacts to the trajectory aberrations induced by the high field native oxide shell around the NW.

The impacts of the full tip imaging on different aspects of APT analysis will be discussed in Section 7.5. We will see that full tip imaging (FOV equals the tip size) allows to maximize the statistics and a self-calibration of some reconstruction parameters such as image compression factor and detection efficiency. This can finally pave the way for the assessment of the uncertainty for all the reconstruction parameters and potentially enables a more reliable 3D data reconstruction in APT with a quantifiable uncertainty.

### 7.3 Accuracy and precision in APT analysis

In the absence of any certified reference material (CRM) for APT, we have developed a concept for a B doped SiGe reference material (RM) for APT. Such a specimen (i.e. piece of wafer) was carefully analyzed by different traceable complementary techniques (i.e. reference free GIXRF and RBS) to identify the thickness and the composition of the SiGe layer with the associated uncertainties. In Section 7.5, we will discuss that the combination of such a well characterized wafer with our developed repeatable specimen preparation process (based on lithography and etching) can be considered as a promising route towards a certified reference material (CRM) for the APT.

In order to evaluate the accuracy of the APT analysis at different experimental conditions (i.e. electric field), in Chapter 5 we have experimentally investigated the distribution of the electric field (CSR) over the 3D reconstructed specimen volume (lateral and depth) for SiGe/Si tips illuminated by UV and green laser light. As expected, when using a UV laser, the local electric field (Si CSR) gradually increased across the specimen diameter in the direction of laser illumination. In addition, we have observed a gradual decrease in the electric field (Si CSR) along the analysis depth (in SiGe and Si) for all the APT measurements carried out with a UV laser (constant flux and laser power). We attributed this drop in the Si CSR along the analysis depth to the gradual decrease in the evaporation rate linked to the increase in the FOV along the analysis depth. We have developed an analytical expression to predict the variation of electric field along the analysis depth as a function of the variation of the specimen radius  $\left(\frac{1}{R^2}\right)$  along the specimen depth and the initial electric field. This description has been experimentally verified using SEM and TEM images.

For the APT analysis in green laser light, we observed that at low laser powers the electric field (Si CSR) has a better uniformity across the specimen diameter (better than 1%) as compared to the UV laser, whereby as expected the average electric field (Si CSR) monotonically decreased along the analysis depth (linked to the increase in the FOV). However, for higher laser powers, we observed a non-monotonic variation of electric field (CSR) along the analysis depth quasi in accordance with the predicted absorption maps in the literature.

The accuracy of APT analysis in view of Ge quantification over the specimen volume has been evaluated using UV and green laser lights and in the different experimental conditions (electric field). We observed a systematic increase in the apparent Ge concentration as a function average electric field (Si CSR). Our analysis indicated that at an average Si CSR  $< 0.6$ , the quantified Ge concentration underestimates the reference concentration. This underestimation reached up to about 3% at an average Si CSR about 0.2. In contrary, APT analysis at Si CSR  $> 0.8$  resulted in an overestimation of the Ge content, up to 1.5 %. We have also investigated the uniformity of the Ge concentration over the reconstructed 3D volume. Our analysis indicates that the Ge concentration varies

across the specimen diameter in line with the variation of the electric field (Si CSR) along the laser illumination direction (in UV laser light).

To understand this variation of Ge concentration as a function of electric field (Si CSR), we have investigated several possible loss mechanisms for Si and Ge atoms, including DC evaporation, dissociation of molecular ions into neutrals and the detector dead zone. However, we did not find any physical explanation for this observed mismatch in the measured stoichiometry of SiGe at low and high field regions. Surface migration might be one factor to be invoked which is however hard to observe. Nevertheless, we identified optimized experimental conditions (electric field), which allow more accurate stoichiometry for APT analysis of  $\text{Si}_x\text{Ge}_{1-x}$  compounds ( $x \sim 22, 50$  and  $72$ ) using UV or green laser lights.

Our preliminary analysis of the B quantification suggests that there is not much underestimation of the B content in  $\text{Si}_{78}\text{Ge}_{22}$  at high electric field regions, contrary to what is reported for B in Si [201]. Similar to Ge, we have observed an underestimation of the B content at low electric field (Si CSR) for APT analysis using UV.

Finally, we assessed the precision of the APT analysis by carrying out several APT measurements on multiple tips under the same experimental conditions (Si CSR > 95 %). Our analysis indicates that the Ge and B quantification in APT has a high repeatability, corresponding to a precision better than 1.2 % and 0.2 % for the average quantification of Ge concentration using a UV and green laser respectively. Similarly, the obtained precision for average B content was better 1.1% (UV) and 2.2 % (green).

## 7.4 Analysis of organics in APT

The state-of-the-art APT analysis of organic materials was described in Chapter 6. We discussed that APT had been reported to be successful for the analysis of biominerals and tissues (i.e. bones and teeth), where the mass spectrum and the 3D distribution (lateral and depth) of the organic/inorganic fragments can be identified. In contrary, the extent of APT analysis to polymers and organic molecules so far was only limited to the collection of mass spectra, whereby the large molecular fragments, corresponding to structural morphology of the polymer, were identified in the spectrum. However, the 3D reconstruction (lateral and depth distribution) for a molecular structure has not been yet reported for organic molecules and polymers.

In this project, we studied in detail the APT analysis of an organic-inorganic system based a polyaniline (Pani)-porous silicon (PSi) nano composite. We demonstrated that such a complex system can be analyzed by APT and the 3D distribution of Pani within the pores of PSi (lateral and depth distribution) can be identified according to the distribution of monoatomic ions of C (for Pani) and Si ions (PSi).

However, our analysis suggested that the molecular structure of the polymer was completely damaged during FIB specimen preparation step such that Pani was mainly detected as monoatomic ions of carbon ( $\text{C}^{++}$  and  $\text{C}^+$ ) and the larger

molecular fragments corresponding to structural morphology of the polymer were absent in the spectrum. Our dissociation analysis also confirmed that the Pani was evaporated as the monoatomic ions of carbon and no any trace of dissociation has been observed in the spectrum associated with the polymer fragments.

In the next section, a potential route to minimize such a damage during the specimen preparation will be suggested.

## 7.5 Outline for future developments in APT analysis

In this project we demonstrated a promising route towards the preparation of a certified reference material (CRM) for APT, which is currently not available and hampers the metrological evaluation of the APT analysis. As we discussed, we have developed a well characterized B doped SiGe reference system for APT, whereby different traceable complementary techniques (i.e. reference free GIXRF and RBS) were used to identify the thickness and the composition of the SiGe layer with the associated uncertainties. The traceable quantification for Ge and B (with associated uncertainty) and their uniformity assessment are still ongoing tasks using the reference-free GIXRF technique according to ISO 35:2017 guide for certified reference materials (CRM). By integrating such a well characterized wafer with our developed specimen preparation process (based on standard lithography and etching technique), one can prepare multiple APT specimens in a repeatable fashion having a well-defined composition (followed by it associated uncertainty) with minimized tip to tip variations in view of the tip radius and the shank angle and no retained Ga dose. To develop such a CRM, we optimized the aforementioned specimen preparation process for our well-characterized B doped SiGe system. Implementation of the process in the near future will depend on the availability of adequate etching tools.

Our developed specimen design with the full tip imaging feature (FOV equal to the tip size), allows a potentially route for an accurate self-calibration of all reconstruction parameters, whereby the detection efficiency can be accurately calibrated by comparing the detected number of atoms in the APT analysis to the actual number of atoms in the specimen volume (i.e. estimated from TEM image). Similarly, the image compression factor ( $\xi$ ) can be accurately tuned to match the reconstructed volume to the actual nanowire dimension, owing to the full tip imaging feature where the sidewalls of the tip are also within the FOV.

The full tip imaging paves the way for the uncertainty assessment for all the reconstruction parameters and potentially enables a more reliable 3D data reconstruction in APT with the quantifiable uncertainties. In addition, such a standardized tip shape is also extremely helpful in fundamental studies (i.e. tip-laser interactions) as they allow to eliminate the variability contributions in the tip geometry, ion-beam damage, retained Ga dose and its distribution, heat transfer (shank angle), etc.

In this content, based on the results of this PhD project, the first interlaboratory study on the quantification and reproducibility in APT analysis has been initiated under the VAMAS umbrella [220], with the aim to address the

accuracy, reproducibility and possible uncertainty budget in APT analysis related to the quantification of the Ge and B in SiGe. Such an interlaboratory study can also potentially lead to the development of a standard procedure for the ranging protocol and a reliable background subtraction method, which is not currently well-established.

In this project we have explored the concept of hybrid metrology based on combining STEM tomography-APT analysis, to derive the optimized APT experimental conditions (i.e. electric field) which do lead to an accurate quantification and 3D data reconstruction of SiGe multi layers. In particular the detailed analysis of the discrepancies between both methods has provided insight in the parameters governing the accuracy of APT.

Finally, regarding the APT analysis of organic-inorganic systems (i.e. polyaniline-porous silicon nanocomposite), as the molecular structure of the polymer (polyaniline) was completely damaged during FIB specimen preparation step, an improvement in specimen preparation techniques is clearly required to eliminate/minimize the damage to the polymer during the FIB milling/SEM inspection as a first step towards a successful APT analysis. A possible solution could be the use of Cryo FIB, as it is a well-established technique for the preparation of the lamella in biology from live tissues.

# Appendix A

The RIE etch recipes used for the preparation of microstructured Si templates (see Table 16) and nanostructured Si using DBC masks (see Table 17).

Table 16: Recipe of the Bosch process used to etch the Si templates with a target depth about 2.3  $\mu\text{m}$ .

<b>Deposition step</b>	RF=10 W, ICP=1500 W, C4F8=50 sccm, SF6=1 sccm, p=20 mTorr, T=18 °C and time =4 s
<b>Etch step</b>	RF=12 W, ICP= 1500 W, C4F8= 0 sccm, SF6=120 sccm, p=20 mTorr, T=18 °C and time = 7 s
<b>Number of cycles</b>	7

Table 17: Recipe of Cryogenic etch process used to etch the Si substrate using DBC masks.

<b>Gas flow [sccm]</b>	<b>Temperature °C</b>	<b>Pressure [mTorr]</b>	<b>RF power [W]</b>	<b>ICP power [W]</b>
SF <sub>6</sub> = 28, O <sub>2</sub> =1	-120	20	12	550



**CERTIFICATO DI MISURA**  
N. 16-0632-01 emesso il 2016-07-19

**Oggetto** Campioni in silicio con una matrice di buchi a forma quadrata

**Modello/Tipo** A5-1; A30-2; A50-3

**Identificazione** A5-1; A30-2; A50-3

**Costruttore** INRIM - Divisione Nanotecnologie

**Data delle misurazioni** dal 2016-04-22 al 2016-05-13

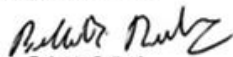
**Procedura applicata**

**Registro di laboratorio** 1199 pag. 11

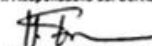
**Committente** INRIM - Divisione Nanotecnologie

**Indirizzo** Sede

**Responsabile attività**

  
Roberto Bellotti

**Firmatario autorizzato**  
Il Responsabile del Servizio

  
Dott. Vito Fericola

Il presente certificato attesta la riferibilità delle misure ai Campioni Nazionali (D.M. n. 591/1992) e alle unità di misura realizzate all'INRIM o in altri Istituti Metrologici Primari ai sensi della Legge n. 273/1991.  
I risultati qui riportati si riferiscono esclusivamente agli oggetti descritti e alle condizioni di misura specificate.  
L'autenticità del presente certificato è attestata dall'apposizione in originale delle firme e del timbro a secco. La riproduzione del presente certificato è ammessa solo in copia conforme integrale; la riproduzione in copia conforme parziale è ammessa solo su autorizzazione scritta rilasciata dall'INRIM, da riportare con il numero di protocollo sulla riproduzione.

Figure 117: Issued certificate from the length department of INRIM (NMI of Italy) for the dimensional characterization of the prepared microstructured Si templates as the potential reference material of 3D ToFSIMS.

# Appendix B

The process flow for the preparation of a potential reference sample for APT is schematically represented in Figure 118. The detailed description of each process step is reported in Table 18.

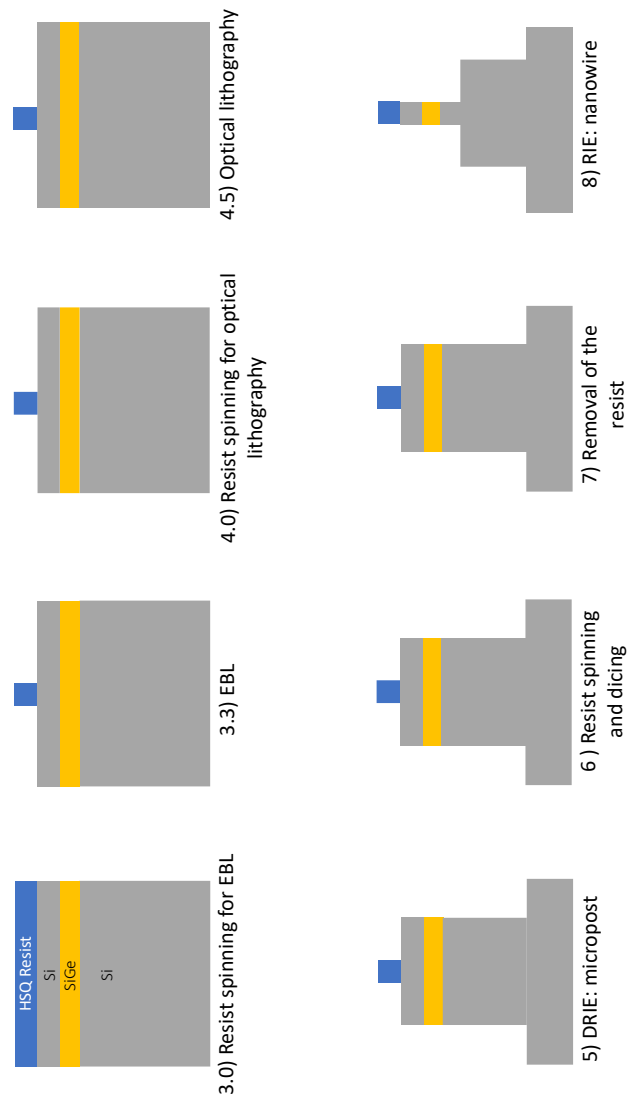


Figure 118: schematic representation of the process flow for the preparation of a potential reference specimen for APT.

Table 18: Brief description of the process steps used for the preparation of the potential reference sample for APT.

Step	Process	Tool	Parameters
1.0	Spinning the photo lithography resist	Spinner	Resist name: S1828 Spinning parameters: 2000 rpm, 30s
1.1	Prebake	Hotplate	At 115 °C for 5 min
1.2	Cleaving	Dicing tool	Die dimension: 86 x 86 mm <sup>2</sup>
2.0	Cleaning	Wet bench	Dirty hot acetone (45 °C): 3min Ultrasonic bath acetone: 5 min Hot acetone (45 °C): 5 min Hot IPA (65 °C): 5 min N <sub>2</sub> dry O <sub>2</sub> stripping 100 W for 20 min
3.0	Spinning the EBL resist	Spinner	Resist name: XR1541_006 Spinning parameters: 600 rpm, 60 min
3.1	Prebake (EBL)	Hotplate	At 90 °C for 5 min
3.2	Exposure (EBL)	Electron beam lithography (EBL)	Dose: NW (d=50, 60, 70 and 80) = 4700 μC Alignment markers= 1100 μC
3.3	Development (EBL)	Wet bench	Immersion in: TMAH 25wt% (Silicon etch): 1 min TMAH 2.38wt% (OPD5262): 10 s Rinse: 1'30" water + rinse in IPA and N <sub>2</sub> DRY
4.0	Spinning	Spinner	TI primer Spinning parameters: 4000 rpm, 30 s
4.1	bake	Hotplate	At 120 °C for 2 min
4.2	Spinning	Spinner	Resist name: S1828 Spinning parameters: 2000 rpm, 30 s
4.3	Prebake	Hotplate	At 115 °C for 5'
4.4	Photo lithography	Karl Suss MA6 Mask aligner	Hard contact, 6'' exposure
4.5	Development	Wet bench	OPD 5262 developer: 70 s, water rinse for 2' and N <sub>2</sub> dry
4.6	Postbake	Hotplate	At 120 °C for 5 min
5.0	Deep etching for micropost	Oxford100 Cobra DRIE	450 cycles for 40 μm tall micropost Recipe is reported in Table 19
5.1	Inspection	SEM	-
6.0	Spinning	spinner	Resist name: S1828 Spinning parameters: 2000 rpm, 30 s
6.1	Prebake	Hotplate	At 115 °C for 5 min
6.2	Dicing	Dicing tool	Dicing the wafer piece to several chips (final APT specimen)

7.0	Cleaning	Wet bench	Dirty hot acetone (45 °C): 5 min Hot acetone (45 °C): 5 min Hot IPA (65 °C): 5 min N <sub>2</sub> dry O <sub>2</sub> stripper at 100 W for 40 min
8.0	Etching for nanowire	Oxford100 RIE tool	Recipe is reported in Table 20
8.1	Inspection	SEM	-

Table 19: DRIE Bosch recipe for etching of micropost using Oxford 100 Cobra DRIE tool.

Parameters	Deposition	Etch
Gas flow [sccm]	SF <sub>6</sub> :10, C <sub>4</sub> F <sub>8</sub> :180	SF <sub>6</sub> :5, C <sub>4</sub> F <sub>8</sub> :200
Pressure [mbar]	0.033	0.053
Temperature [°C]	0	0
ICP power [W]	1500	1800
RF power [W]	5	30
Duration [s]	2	1.5

Table 20: RIE etch recipe for etching of nanowire using Oxford 100 RIE tool.

Parameters	values
Pressure [mTorr]	10
SF <sub>6</sub> flow [sccm]	35
C <sub>4</sub> F <sub>8</sub> flow [sccm]	45
Temperature [°C]	15
ICP power [W]	200
RF power [W]	7

## References

- [1] International technology roadmap for semiconductors (ITRS) 2013 edition
- [2] Kubicek M, Holzlechner G, Opitz A K, Larisegger S, Hutter H and Fleig J 2014 A novel ToF-SIMS operation mode for sub 100 nm lateral resolution: Application and performance *Appl. Surf. Sci.* **289** 407–16
- [3] Sakamoto T, Koizumi M, Kawasaki J and Yamaguchi J 2008 Development of a high lateral resolution TOF-SIMS apparatus for single particle analysis *Appl. Surf. Sci.* **255** 1617–20
- [4] IonTOF Time-of-Flight secondary ion mass spectrometry (TOF-SIMS)
- [5] Vandervorst W, Fleischmann C, Bogdanowicz J, Franquet A, Celano U, Paredis K and Budrevich A 2017 Dopant, composition and carrier profiling for 3D structures *Mater. Sci. Semicond. Process.* **62** 31–48
- [6] Franquet A, Douhard B, Melkonyan D, Favia P, Conard T and Vandervorst W 2016 Self Focusing SIMS: Probing thin film composition in very confined volumes *Appl. Surf. Sci.* **365** 143–52
- [7] Mody J, Duffy R, Eyben P, Goossens J, Moussa A, Polspoel W, Berghmans B, van Dal M J H, Pawlak B J, Kaiser M, Weemaes R G R and Vandervorst W 2010 Experimental studies of dose retention and activation in fin field-effect-transistor-based structures *J. Vac. Sci. Technol. B, Nanotechnol. Microelectron. Mater. Process. Meas. Phenom.* **28** C1H5-C1H13
- [8] Mody J, Zschatzsch G, Kolling S, De Keersgieter A, Eneman G, Kambham A K, Drijbooms C, Schulze A, Chiarella T, Horiguchi N, Hoffmann T-Y, Eyben P and Vandervorst W 2011 3D-carrier profiling in FinFETs using scanning spreading resistance microscopy *2011 International Electron Devices Meeting (IEEE)* pp 6.1.1-6.1.4
- [9] Beckhoff B 2008 Reference-free X-ray spectrometry based on metrology using synchrotron radiation *J. Anal. At. Spectrom.* **23** 845–53
- [10] Pennycook S J and Nellist P D 2011 *Scanning Transmission Electron Microscopy* (New York, NY: Springer New York)
- [11] Lugg N R, Kothleitner G, Shibata N and Ikuhara Y 2015 On the quantitiveness of EDS STEM *Ultramicroscopy* **151** 150–9
- [12] Inoue K, Yano F, Nishida A, Takamizawa H, Tsunomura T, Nagai Y and

- Hasegawa M 2009 Dopant distributions in n-MOSFET structure observed by atom probe tomography *Ultramicroscopy* **109** 1479–84
- [13] Melkonyan D, Fleischmann C, Arnoldi L, Demeulemeester J, Kumar A, Bogdanowicz J, Vurpillot F and Vandervorst W 2017 Atom probe tomography analysis of SiGe fins embedded in SiO<sub>2</sub>: Facts and artefacts *Ultramicroscopy* **179** 100–7
- [14] Bas P, Bostel A, Deconihout B and Blavette D 1995 A general protocol for the reconstruction of 3D atom-probe data *Appl. Surf. Sci.* **87–8** 298–304
- [15] Robinson M A, Graham D J and Castner D G 2012 ToF-SIMS depth profiling of cells: Z-correction, 3D imaging, and sputter rate of individual NIH/3T3 fibroblasts *Anal. Chem.* **84** 4880–5
- [16] Dialameh M, Lupi F F, Imbraguglio D, Zanenga F, Lamperti A, Martella D, Seguni G, Perego M, Rossi A M, De Leo N and Boarino L 2017 Influence of block copolymer feature size on reactive ion etching pattern transfer into silicon *Nanotechnology* **28** 404001
- [17] Dialameh M, Ferrarese Lupi F, Hönicke P, Kayser Y, Beckhoff B, Weimann T, Fleischmann C, Vandervorst W, Dubček P, Pivac B, Perego M, Seguni G, De Leo N and Boarino L 2018 Development and Synchrotron-Based Characterization of Al and Cr Nanostructures as Potential Calibration Samples for 3D Analytical Techniques *Phys. Status Solidi Appl. Mater. Sci.* **215**
- [18] John C. V and Briggs D 2013 *ToF-SIMS: Surface Analysis by Mass Spectrometry* (IM Publications)
- [19] Green F M, Gilmore I S and Seah M P 2006 TOF-SIMS: Accurate mass scale calibration *J. Am. Soc. Mass Spectrom.* **17** 514–23
- [20] Shard A G, Havelund R, Spencer S J, Gilmore I S, Alexander M R, Angerer T B, Aoyagi S, Barnes J P, Benayad A, Bernasik A, Ceccone G, Counsell J D P, Deeks C, Fletcher J S, Graham D J, Heuser C, Lee T G, Marie C, Marzec M M, Mishra G, Rading D, Renault O, Scurr D J, Shon H K, Spampinato V, Tian H, Wang F, Winograd N, Wu K, Wucher A, Zhou Y and Zhu Z 2015 Measuring Compositions in Organic Depth Profiling: Results from a VAMAS Interlaboratory Study *J. Phys. Chem. B* **119** 10784–97
- [21] Lee J L S, Ninomiya S, Matsuo J, Gilmore I S, Seah M P and Shard A G 2010 Organic depth profiling of a nanostructured delta layer reference material using large argon cluster ions *Anal. Chem.* **82** 98–105
- [22] Standard reference material (SRM) for SIMS by NIST
- [23] Terlier T, Lee J, Lee K and Lee Y 2018 Improvement of the Correlative AFM and ToF-SIMS Approach Using an Empirical Sputter Model for 3D Chemical Characterization *Anal. Chem.* **90** 1701–9
- [24] Bernard L, Heier J, Paul W and Hug H J 2014 The SFM/ToF-SIMS combination for advanced chemically-resolved analysis at the nanoscale *Nucl. Instruments Methods Phys. Res. Sect. B Beam Interact. with Mater. Atoms* **339** 85–90
- [25] Jung S, Lee N, Choi M, Lee J, Cho E and Joo M 2018 Methodological development of topographic correction in 2D/3D ToF-SIMS images using AFM images *Appl. Surf. Sci.* **432** 90–6
- [26] Margui E 2013 *X-Ray Fluorescence Spectrometry and Related Techniques* (Momentum Press, New York NY10017)
- [27] Bertin E P 1975 Principles and Practice of X-Ray Spectrometric Analysis *Principles and Practice of X-Ray Spectrometric Analysis* (Boston, MA:

- Springer US) pp 459–500
- [28] Klockenkämper R 1997 *Total reflection X-ray fluorescence analysis* ed R Klockenkämper (Wiley)
- [29] Leenaers A J G, Vrakking J J A M and De Boer D K G 1997 Glancing incidence X-ray analysis: More than just reflectivity! *Spectrochim. Acta - Part B At. Spectrosc.* **52** 805–12
- [30] Compton A H 1923 CXVII. The total reflexion of X-rays *London, Edinburgh, Dublin Philos. Mag. J. Sci.* **45** 1121–31
- [31] Hönicke P, Beckhoff B, Kolbe M, Giubertoni D, Van Den Berg J and Pepponi G 2010 Depth profile characterization of ultra shallow junction implants *Anal. Bioanal. Chem.* **396** 2825–32
- [32] Beckhoff B 2008 Reference-free X-ray spectrometry based on metrology using synchrotron radiation *J. Anal. At. Spectrom.* **23** 845
- [33] Beckhoff B, Fliegau R, Kolbe M, Müller M, Weser J and Ulm G 2007 Reference-Free Total Reflection X-ray Fluorescence Analysis of Semiconductor Surfaces with Synchrotron Radiation *Anal. Chem.* **79** 7873–82
- [34] Hönicke P, Kayser Y, Beckhoff B, Müller M, Dousse J-C, Hoszowska J and Nowak S H 2012 Characterization of ultra-shallow aluminum implants in silicon by grazing incidence and grazing emission X-ray fluorescence spectroscopy *J. Anal. At. Spectrom.* **27** 1432
- [35] Lubeck J, Beckhoff B, Fliegau R, Holfelder I, Hönicke P, Müller M, Pollakowski B, Reinhardt F and Weser J 2013 A novel instrument for quantitative nanoanalytics involving complementary X-ray methodologies *Rev. Sci. Instrum.* **84** 045106
- [36] Windt D L 1998 IMD—Software for modeling the optical properties of multilayer films *Comput. Phys.* **12** 360
- [37] von Bohlen A, Krämer M, Sternemann C and Paulus M 2009 The influence of X-ray coherence length on TXRF and XSW and the characterization of nanoparticles observed under grazing incidence of X-rays *J. Anal. At. Spectrom.* **24** 792
- [38] Tsuji K, Yamada T, Utaoka T and Hirokawa K 1995 The effects of surface roughness on the angle-dependent total-reflection x-ray fluorescence of ultrathin films *J. Appl. Phys.* **78** 969–73
- [39] Reinhardt F, Nowak S H, Beckhoff B, Dousse J-C and Schoengen M 2014 Grazing incidence X-ray fluorescence of periodic structures – a comparison between X-ray standing waves and geometrical optics calculations *J. Anal. At. Spectrom.* **29** 1778–84
- [40] Nowak S H, Reinhardt F, Beckhoff B, Dousse J-C and Szlachetko J 2013 Geometrical optics modelling of grazing incidence X-ray fluorescence of nanoscaled objects *J. Anal. At. Spectrom.* **28** 689
- [41] Nowak S H, Banaś D, Błchucki W, Cao W, Dousse J-C, Hönicke P, Hoszowska J, Jabłoński Ł, Kayser Y, Kubala-Kukuś A, Pajek M, Reinhardt F, Savu A V and Szlachetko J 2014 Grazing angle X-ray fluorescence from periodic structures on silicon and silica surfaces *Spectrochim. Acta Part B At. Spectrosc.* **98** 65–75
- [42] BATES F S 1991 Polymer-Polymer Phase Behavior *Science (80-. )*. **251** 898–905
- [43] Ferrarese Lupi F, Giammaria T J, Seguíni G, Vita F, Francescangeli O, Sparnacci K, Antonioli D, Gianotti V, Laus M and Perego M 2014 Fine tuning of lithographic masks through thin films of PS-b -PMMA with

- different molar mass by rapid thermal processing *ACS Appl. Mater. Interfaces* **6** 7180–8
- [44] Ferrarese Lupi F, Giammaria T J, Seguíni G, Ceresoli M, Perego M, Antonioli D, Gianotti V, Sparnacci K and Laus M 2014 Flash grafting of functional random copolymers for surface neutralization *J. Mater. Chem. C* **2** 4909–17
- [45] Ferrarese Lupi F, Giammaria T J, Seguíni G, Laus M, Dubček P, Pivac B, Bernstorff S and Perego M 2017 GISAXS Analysis of the In-Depth Morphology of Thick PS- b -PMMA Films *ACS Appl. Mater. Interfaces* **9** 11054–63
- [46] Ferrarese Lupi F, Giammaria T J, Ceresoli M, Seguíni G, Sparnacci K, Antonioli D, Gianotti V, Laus M and Perego M 2013 Rapid thermal processing of self-assembling block copolymer thin films *Nanotechnology* **24** 315601–3156
- [47] Seguíni G, Zanenga F, Giammaria T J, Ceresoli M, Sparnacci K, Antonioli D, Gianotti V, Laus M and Perego M 2016 Enhanced Lateral Ordering in Cylinder Forming PS-b-PMMA Block Copolymers Exploiting the Entrapped Solvent *ACS Appl. Mater. Interfaces* **8** 8280–8
- [48] Han E, Stuenkel O, La Y, Nealey P F and Gopalan P 2008 Effect of Composition of Substrate-Modifying Random Copolymers on the Orientation of Symmetric and Asymmetric Diblock Copolymer Domains *Macromolecules* **41** 9090–7
- [49] Andreozzi A, Lamagna L, Seguíni G, Fanciulli M, Schamm-Chardon S, Castro C and Perego M 2011 The fabrication of tunable nanoporous oxide surfaces by block copolymer lithography and atomic layer deposition. *Nanotechnology* **22** 335303
- [50] Liu Z, Gu X, Hwu J and Sassolini S 2014 Low-temperature plasma etching of high aspect-ratio densely packed 15 to sub-10nm silicon features derived from PS-PDMS block copolymer patterns *Nanotechnology* **25** 285301
- [51] Zhang X, Sushkov A B, Metting C J, Fackler S, Drew H D and Briber R M 2012 Silicon patterning using self-assembled PS-b-PAA diblock copolymer masks for black silicon fabrication via plasma etching *Plasma Process. Polym.* **9** 968–74
- [52] Popa A M, Niedermann P, Heinzelmann H, Hubbell J a and Pugin R 2009 Fabrication of nanopore arrays and ultrathin silicon nitride membranes by block-copolymer-assisted lithography. *Nanotechnology* **20** 485303
- [53] Cummins C, Ghoshal T, Holmes J D and Morris M A 2016 Strategies for Inorganic Incorporation using Neat Block Copolymer Thin Films for Etch Mask Function and Nanotechnological Application *Adv. Mater.* **28** 5586–618
- [54] Kamcev J, Germack D S, Nykypanchuk D, Grubbs R B, Nam C Y and Black C T 2013 Chemically enhancing block copolymers for block-selective synthesis of self-assembled metal oxide nanostructures *ACS Nano* **7** 339–46
- [55] Peng Q, Tseng Y C, Darling S B and Elam J W 2010 Nanoscopic patterned materials with tunable dimensions via atomic layer deposition on block copolymers *Adv. Mater.* **22** 5129–33
- [56] Peng Q, Tseng Y, Darling S B and Elam J W 2011 A Route to Nanoscopic Materials via Sequential Infiltration Synthesis on Block Copolymer Templates *ACS Nano* **5** 4600–6
- [57] Kiihamäki J and Franssila S 1999 Pattern shape effects and artefacts in

- deep silicon etching *J. Vac. Sci. Technol. A Vacuum, Surfaces, Film.* **17** 2280–5
- [58] Yeom J, Wu Y, Selby J C and Shannon M A 2005 Maximum achievable aspect ratio in deep reactive ion etching of silicon due to aspect ratio dependent transport and the microloading effect *J. Vac. Sci. Technol. B Microelectron. Nanom. Struct.* **23** 2319
- [59] Wu Y, Olynick D L, Goodyear A, Peroz C, Dhuey S, Liang X and Cabrini S 2011 Cryogenic etching of nano-scale silicon trenches with resist masks *Microelectron. Eng.* **88** 2785–9
- [60] Bourouina T, Masuzawa T and Fujita H 2004 The MEMSNAS Process : Microloading Effect for Micromachining 3-D Structures of Nearly All Shapes **13** 190–9
- [61] Karttunen J, Kiihamäki J and Franssila S 2000 Loading effects in deep silicon etching **4174** 90–7
- [62] Tsai H, Pitera J W, Miyazoe H, Bangsaruntip S, Engelmann S U, Liu C C, Cheng J Y, Bucchignano J J, Klaus D P, Joseph E A, Sanders D P, Colburn M E and Guillorn M A 2014 Two-dimensional pattern formation using graphoepitaxy of PS-b-PMMA block copolymers for advanced FinFET device and circuit fabrication *ACS Nano* **8** 5227–32
- [63] Delalande M, Cunge G, Chevolleau T, Bézard P, Archambault S, Joubert O, Chevalier X and Tiron R 2014 Development of plasma etching processes to pattern sub-15 nm features with PS-b-PMMA block copolymer masks: Application to advanced CMOS technology *J. Vac. Sci. Technol. B, Nanotechnol. Microelectron. Mater. Process. Meas. Phenom.* **32** 051806
- [64] Henry M D, Walavalkar S, Homyk a and Scherer a 2009 Alumina etch masks for fabrication of high-aspect-ratio silicon micropillars and nanopillars. *Nanotechnology* **20** 255305
- [65] Laermer F and Urban A 2005 Milestones in deep reactive ion etching (Solid-State Sensors, Actuators and Microsystems, 2005. Digest of Technical Papers. TRANSDUCERS'05. The 13th International Conference) pp 1118–21
- [66] Wu B, Kumar A and Pamarthy S 2010 High aspect ratio silicon etch: A review *J. Appl. Phys.* **108** 0–20
- [67] Henry M D, Shearn M J, Chhim B and Scherer a 2010 Ga(+) beam lithography for nanoscale silicon reactive ion etching. *Nanotechnology* **21** 245303
- [68] Tachi S, Tsujimoto K, Arai S and Kure T 1991 Low-temperature dry etching *J. Vac. Sci. Technol. A Vacuum, Surfaces, Film.* **9** 796–803
- [69] Jansen H V, de Boer M J, Unnikrishnan S, Louwense M C and Elwenspoek M C 2009 Black silicon method: X. A review on high speed and selective plasma etching of silicon with profile control: an in-depth comparison between Bosch and cryostat DRIE processes as a roadmap to next generation equipment *J. Micromechanics Microengineering* **19** 033001
- [70] Sökmen Ü, Stranz A, Fündling S, Wehmann H-H, Bandalo V, Bora A, Tornow M, Waag A and Peiner E 2009 Capabilities of ICP-RIE cryogenic dry etching of silicon: review of exemplary microstructures *J. Micromechanics Microengineering* **19** 105005
- [71] Gu X, Liu Z, Gunkel I, Chourou S T, Hong S W, Olynick D L and Russell T P 2012 High aspect ratio sub-15 nm Silicon Trenches from Block Copolymer Templates *Adv. Mater.* **24** 5688–94
- [72] Keil D and Anderson E 2001 Characterization of reactive ion etch lag

- scaling *J. Vac. Sci. Technol. B Microelectron. Nanom. Struct.* **19** 2082
- [73] Bakhtazad A, Huo X and Sabarinathan J 2011 Cryogenic shallow reactive ion etch process for profile control on silicon on insulator platform *J. Vac. Sci. Technol. B Microelectron. Nanom. Struct.* **29** 041001
- [74] Gottscho R A 1992 Microscopic uniformity in plasma etching *J. Vac. Sci. Technol. B Microelectron. Nanom. Struct.* **10** 2133
- [75] Frascaroli J, Cianci E, Spiga S, Seguini G and Perego M 2016 Ozone-Based Sequential Infiltration Synthesis of Al<sub>2</sub>O<sub>3</sub> Nanostructures in Symmetric Block Copolymer *ACS Appl. Mater. Interfaces* **8** 33933–42
- [76] Müller K P, Roithner K and Timme H-J 1995 Selectivity and Si-load in deep trench etching *Microelectron. Eng.* **27** 457–62
- [77] Jansen H, de Boer M, Wiegerink R, Tas N, Smulders E, Neagu C and Elwenspoek M 1997 RIE lag in high aspect ratio trench etching of silicon *Microelectron. Eng.* **35** 45–50
- [78] Blauw M A, Van der Drift E, Marcos G and Rhallabi A 2003 Modeling of fluorine-based high-density plasma etching of anisotropic silicon trenches with oxygen sidewall passivation *J. Appl. Phys.* **94** 6311–8
- [79] Müller E W 1956 Field Desorption *Phys. Rev.* **102** 618–24
- [80] Gomer R and Swanson L W 1963 Theory of Field Desorption *J. Chem. Phys.* **38** 1613–29
- [81] Ibach H 2006 *Physics of Surfaces and Interfaces* (Springer Berlin Heidelberg)
- [82] Vurpillot F and Sauvage X 2016 *Atom probe tomography - Put Theory Into Practice* vol 1
- [83] Gault B, Moody M P, Cairney J M and Ringer S P 2012 *Atom Probe Microscopy* vol 160
- [84] Vurpillot F and Oberdorfer C 2015 Modeling Atom Probe Tomography: A review *Ultramicroscopy* **159** 202–16
- [85] Tsong T T 1978 Field ion image formation *Surf. Sci.* **70** 211–33
- [86] Forbes R G 1995 Field evaporation theory: a review of basic ideas *Appl. Surf. Sci.* **87–88** 1–11
- [87] Forbes R G and Chibane K 1986 Derivation of an activation energy formula in the context of charge draining *Le J. Phys. Colloq.* **47** C7-65-C7-70
- [88] McMullen E R and Perdew J P 1987 Theory of field evaporation of the surface layer in jellium and other metals *Phys. Rev. B* **36** 2598–606
- [89] Rolland N, Vurpillot F, Duguay S and Blavette D 2015 A Meshless Algorithm to Model Field Evaporation in Atom Probe Tomography *Microsc. Microanal.* **21** 1649–56
- [90] Sánchez C G, Lozovoi A Y and Alavi A 2004 Field-evaporation from first-principles *Mol. Phys.* **102** 1045–55
- [91] Kreuzer H J and Nath K 1987 Field evaporation *Surf. Sci.* **183** 591–608
- [92] Kellogg G L 1984 Measurement of activation energies for field evaporation of tungsten ions as a function of electric field *Phys. Rev. B* **29** 4304–12
- [93] Haydock R and Kingham D R 1980 Post-ionization of field-evaporated ions *Phys. Rev. Lett.* **44** 1520–3
- [94] Kingham D R 1982 The post-ionization of field evaporated ions: A theoretical explanation of multiple charge states *Surf. Sci.* **116** 273–301
- [95] Kumar A, Bogdanowicz J, Demeulemeester J, Bran J, Melkonyan D, Fleischmann C and Vandervorst W 2018 Measurement of the apex

- temperature of a nanoscale semiconducting field emitter illuminated by a femtosecond pulsed laser *J. Appl. Phys.* **124** 245105
- [96] Brandon D G 1966 On field evaporation *Philos. Mag.* **14** 803–20
- [97] Miller M K 2004 Atom Probe Tomography and the Local Electrode Atom Probe *Microsc. Microanal.* **10** 150–1
- [98] Kingham D R 1982 Model calculations of tunnelling and thermal evaporation rate constants relating to field evaporation *J. Phys. D. Appl. Phys.* **15** 2537–44
- [99] Wada M, Konishi M and Nishikawa O 1980 Binding states of Ga and Sn on W and Mo: Structures, evaporation field and its temperature dependence *Surf. Sci.* **100** 439–52
- [100] MENAND A and BLAVETTE D 1986 Temperature dependence of iridium field evaporation rate *Le J. Phys. Colloq.* **47** C7-17-C7-20
- [101] Arul K 2016 *Qualitative and Quantitative analysis of compound semiconductors using Atom Probe Tomography* (Katholieke Universiteit Leuven (KUL))
- [102] Kellogg G L 1981 Determining the field emitter temperature during laser irradiation in the pulsed laser atom probe *J. Appl. Phys.* **52** 5320–8
- [103] Wada M 1984 On the thermally activated field evaporation of surface atoms *Surf. Sci.* **145** 451–65
- [104] Vurpillot F, Gault B, Vella A, Bouet M and Deconihout B 2006 Estimation of the cooling times for a metallic tip under laser illumination *Appl. Phys. Lett.* **88** 86–9
- [105] Tsong T T, Block J H, Nagasaka M and Viswanathan B 1976 Photon stimulated field ionization *J. Chem. Phys.* **65** 2469–70
- [106] Tsong T T 1990 *Atom-probe field ion microscopy: field ion emission, and surfaces and interfaces at atomic resolution* (Cambridge University Press)
- [107] Kelly T F and Miller M K 2007 Atom probe tomography *Rev. Sci. Instrum.* **78** 031101
- [108] Grenier A, Lardé R, Cadel E, Vurpillot F, Juraszek J, Teillet J and Tiercelin N 2007 Atomic-scale study of TbCo<sub>2.5</sub>/Fe multilayers by laser-assisted tomographic atom probe *J. Appl. Phys.* **102** 033912
- [109] Kelly T F, Vella A, Bunton J H, Houard J, Silaeva E P, Bogdanowicz J and Vandervorst W 2014 Laser pulsing of field evaporation in atom probe tomography *Curr. Opin. Solid State Mater. Sci.* **18** 81–9
- [110] Blaber M G, Arnold M D, Harris N, Ford M J and Cortie M B 2007 Plasmon absorption in nanospheres: A comparison of sodium, potassium, aluminium, silver and gold *Phys. B Condens. Matter* **394** 184–7
- [111] Houard J, Vella A, Vurpillot F and Deconihout B 2010 Optical near-field absorption at a metal tip far from plasmonic resonance *Phys. Rev. B - Condens. Matter Mater. Phys.* **81** 1–5
- [112] Kittel C and Holcomb D F 1967 Introduction to Solid State Physics *Am. J. Phys.* **35** 547–8
- [113] Innocenti N 2010 *Interaction of femtosecond laser pulses with nanoscale Si-tips for atom probe tomography* (University of Liège)
- [114] Sundaram S K and Mazur E 2002 Inducing and probing non-thermal transitions in semiconductors using femtosecond laser pulses *Nat. Mater.* **1** 217–24
- [115] Silaeva E P, Karahka M and Kreuzer H J 2013 Atom Probe Tomography and field evaporation of insulators and semiconductors: Theoretical issues *Curr. Opin. Solid State Mater. Sci.* **17** 211–6

- [116] Silaeva E P, Arnoldi L, Karahka M L, Deconihout B, Menand A, Kreuzer H J and Vella A 2014 Do Dielectric Nanostructures Turn Metallic in High-Electric dc Fields? *Nano Lett.* **14** 6066–72
- [117] Tsong T . 1979 Field penetration and band bending near semiconductor surfaces in high electric fields *Surf. Sci.* **81** 28–42
- [118] Liu H F and Tsong T T 1984 Numerical calculation of the temperature evolution and profile of the field ion emitter in the pulsed-laser time-of-flight atom probe *Rev. Sci. Instrum.* **55** 1779–84
- [119] Bunton J H, Olson J D, Lenz D R and Kelly T F 2007 Advances in pulsed-laser atom probe: Instrument and specimen design for optimum performance *Microsc. Microanal.* **13** 418–27
- [120] Vurpillot F, Houard J, Vella A and Deconihout B 2009 Thermal response of a field emitter subjected to ultra-fast laser illumination *J. Phys. D. Appl. Phys.* **42**
- [121] Tsong T T and Kinkus T J 1984 Energy distributions of pulsed-laser field-desorbed gaseous ions and field-evaporated metal ions: A direct time-of-flight measurement *Phys. Rev. B* **29** 529–42
- [122] Tsong T T 1984 Pulsed-laser-stimulated field ion emission from metal and semiconductor surfaces: A time-of-flight study of the formation of atomic, molecular, and cluster ions *Phys. Rev. B* **30** 4946–61
- [123] Mazumder B, Vella A, Gilbert M, Deconihout B and Schmitz G 2010 Reneutralization time of surface silicon ions on a field emitter *New J. Phys.* **12** 113029
- [124] Gault B, Vurpillot F, Bostel A, Menand A and Deconihout B 2005 Estimation of the tip field enhancement on a field emitter under laser illumination *Appl. Phys. Lett.* **86** 1–3
- [125] Vella A, Vurpillot F, Gault B, Menand A and Deconihout B 2006 Evidence of field evaporation assisted by nonlinear optical rectification induced by ultra fast laser *IVNC IFES 2006 - Tech. Dig. - 19th Int. Vac. Nanoelectron. Conf. 50th Int. F. Emiss. Symp.* 83–4
- [126] Tsong T T 1978 Measurement of the field evaporation rate of several transition metals *J. Phys. F Met. Phys.* **8** 1349–52
- [127] Gerstl S, Geiser B, Kelly T and Larson D 2009 Evaluation of Local Radii of Atom-Probe-Tomography Specimens *Microsc. Microanal.* **15** 248–9
- [128] Koelling S, Innocenti N, Schulze A, Gilbert M, Kambham A K and Vandervorst W 2011 In-situ observation of non-hemispherical tip shape formation during laser-assisted atom probe tomography *Journal of Applied Physics* vol 109 p 104909
- [129] Morris R, Cuduvally R, Melkonyan D, Fleischmann C, Zhao M, Arnoldi L, van der Heide P and Vandervorst W 2018 Toward accurate composition analysis of GaN and AlGaN using atom probe tomography *J. Vac. Sci. Technol. B, Nanotechnol. Microelectron. Mater. Process. Meas. Phenom.* **36** 03F130
- [130] Thompson K, Lawrence D, Larson D J, Olson J D, Kelly T F and Gorman B 2007 In situ site-specific specimen preparation for atom probe tomography *Ultramicroscopy* **107** 131–9
- [131] Pérez-Willard F, Wolde-Giorgis D, Al-Kassab T, López G A, Mittemeijer E J, Kirchheim R and Gerthsen D 2008 Focused ion beam preparation of atom probe specimens containing a single crystallographically well-defined grain boundary *Micron* **39** 45–52
- [132] Gorman B P, Diercks D, Salmon N, Stach E, Amador G and Hartfield C

- 2008 Hardware and Techniques for Cross- Correlative TEM and Atom Probe Analysis *Microsc. Today* **16** 42–7
- [133] Kelly T F and Larson D J 2012 Atom Probe Tomography 2012
- [134] Giannuzzi L A and Stevie F A 1999 A review of focused ion beam milling techniques for TEM specimen preparation *Micron* **30** 197–204
- [135] Bassim N D, De Gregorio B T, Kilcoyne A L D, Scott K, Chou T, Wirick S, Cody G and Stroud R M 2012 Minimizing damage during FIB sample preparation of soft materials *J. Microsc.* **245** 288–301
- [136] Joester D, Hillier A, Zhang Y and Prosa T J 2012 Organic Materials and Organic/Inorganic Heterostructures in Atom Probe Tomography *Microsc. Today* **20** 26–31
- [137] Adineh V R, Marceau R K W, Chen Y, Si K J, Velkov T, Cheng W, Li J and Fu J 2017 Pulsed-voltage atom probe tomography of low conductivity and insulator materials by application of ultrathin metallic coating on nanoscale specimen geometry *Ultramicroscopy* **181** 150–9
- [138] Kelly T F, Nishikawa O, Panitz J A and Prosa T J 2009 P rospects for Nanobiology with Tomography *MRS Bull.* **34**
- [139] Gordon L M, Tran L and Joester D 2012 Atom probe tomography of apatites and bone-type mineralized tissues *ACS Nano* **6** 10667–75
- [140] Hirai Y, Kim Y, Yukawa T and Owari M 2016 Study on a Novel Sample Preparation Method for Organic Materials in Atom Probe Tomography *e-Journal Surf. Sci. Nanotechnol.* **14** 154–7
- [141] Kostrna S L P, Mengelt T J, Ali M, Larson D J, Goodman S L and Kelly T F 2004 Creating Polymer Microtip Specimens for Atom Probe Tomography **10** 5–6
- [142] Prosa T J, Keeney S K and Kelly T F 2010 Atom probe tomography analysis of poly(3-alkylthiophene)s *J. Microsc.* **237** 155–67
- [143] Gault B, Yang W, Ratinac K R, Zheng R, Braet F and Ringer S P 2009 Investigation of self-assembled monolayer by atom probe microscopy *Microsc. Microanal.* **15** 272–3
- [144] Gault B, Yang W, Ratinac K R, Zheng R, Braet F and Ringer S P 2010 Atom Probe Microscopy of Self-Assembled Monolayers: Preliminary Results **15** 5291–4
- [145] Greene M, Prosa T, Panitz J, Larson D and Kelly T 2009 Development of Atom Probe Tomography for Biological Materials *Microsc. Microanal.* **15** 582–3
- [146] Panitz J A and Stintz A 1991 Imaging atom-probe analysis of a vitreous ice interface *Surf. Sci.* **246** 163–8
- [147] McIntosh J R 1989 Summary for Policymakers *Climate Change 2013 - The Physical Science Basis* vol 53, ed Intergovernmental Panel on Climate Change (Cambridge: Cambridge University Press) pp 1–30
- [148] Larson D J, Prosa T J, Ulfing R M, Geiser B P and Kelly T F 2013 *Local Electrode Atom Probe Tomography*
- [149] Robert G 1961 *Field Emission and Field Ionization* (Harvard University Press)
- [150] Schlesiger R and Schmitz G 2009 A quantitative assessment of microelectrodes *Ultramicroscopy* **109** 497–501
- [151] Loi S T, Gault B, Ringer S P, Larson D J and Geiser B P 2013 Electrostatic simulations of a local electrode atom probe: The dependence of tomographic reconstruction parameters on specimen and microscope geometry *Ultramicroscopy* **132** 107–13

- [152] Lozovoi A Y and Alavi A 2003 Reconstruction of charged surfaces: General trends and a case study of Pt(110) and Au(110) *Phys. Rev. B - Condens. Matter Mater. Phys.* **68** 1–18
- [153] Peralta J, Broderick S R and Rajan K 2013 Mapping energetics of atom probe evaporation events through first principles calculations *Ultramicroscopy* **132** 143–51
- [154] Karahka M and Kreuzer H J 2013 Field evaporation of oxides: A theoretical study *Ultramicroscopy* **132** 54–9
- [155] Gipson G S, Yannitell D W and Eaton H C 1979 On the electric field distribution within the field ion microscope and near the surface of field emitters *J. Phys. D. Appl. Phys.* **12** 987–96
- [156] Gipson G S 1980 An improved empirical formula for the electric field near the surface of field emitters *J. Appl. Phys.* **51** 3884–9
- [157] Gault B, Haley D, de Geuser F, Moody M P, Marquis E A, Larson D J and Geiser B P 2011 Advances in the reconstruction of atom probe tomography data *Ultramicroscopy* **111** 448–57
- [158] Vurpillot F, Bostel A, Cadel E and Blavette D 2000 The spatial resolution of 3D atom probe in the investigation of single-phase materials *Ultramicroscopy* **84** 213–24
- [159] Larson D J, Geiser B P, Prosa T J, Gerstl S S A, Reinhard D A and Kelly T F 2011 Improvements in planar feature reconstructions in atom probe tomography *J. Microsc.* **243** 15–30
- [160] Moore A J W 1981 The simulation of FIM desorption patterns *Philos. Mag. A* **43** 803–14
- [161] Vurpillot F, Bostel A and Blavette D 2000 Trajectory overlaps and local magnification in three-dimensional atom probe *Appl. Phys. Lett.* **76** 3127–9
- [162] Haley D, Petersen T, Ringer S P and Smith G D W 2011 Atom probe trajectory mapping using experimental tip shape measurements *J. Microsc.* **244** 170–80
- [163] Gault B, de Geuser F, Stephenson L T, Moody M P, Muddle B C and Ringer S P 2008 Estimation of the Reconstruction Parameters for Atom Probe Tomography *Microsc. Microanal.* **14** 296–305
- [164] Vurpillot F, Gruber M, Da Costa G, Martin I, Renaud L and Bostel A 2011 Pragmatic reconstruction methods in atom probe tomography *Ultramicroscopy* **111** 1286–94
- [165] Gault B, Loi S T, Araullo-Peters V J, Stephenson L T, Moody M P, Shrestha S L, Marceau R K W, Yao L, Cairney J M and Ringer S P 2011 Dynamic reconstruction for atom probe tomography *Ultramicroscopy* **111** 1619–24
- [166] Southworth H N and Walls J M 1978 The projection geometry of the field-ion image *Surf. Sci.* **75** 129–40
- [167] Cerezo A, Warren P J and Smith G D W 1999 Some aspects of image projection in the field-ion microscope *Ultramicroscopy* **79** 251–7
- [168] Fortes M A 1971 General properties of the field-ion image projection *Surf. Sci.* **28** 117–31
- [169] Geiser B, Larson D, Oltman E, Gerstl S, Reinhard D, Kelly T and Prosa T 2009 Wide-Field-of-View Atom Probe Reconstruction *Microsc. Microanal.* **15** 292–3
- [170] Webber R D and Walls J M 1979 The shape of field-ion emitters *J. Phys. D. Appl. Phys.* **12**
- [171] Gault B, Moody M P, De Geuser F, Haley D, Stephenson L T and Ringer

- S P 2009 Origin of the spatial resolution in atom probe microscopy *Appl. Phys. Lett.* **95**
- [172] Marquis E A, Geiser B P, Prosa T J and Larson D J 2011 Evolution of tip shape during field evaporation of complex multilayer structures *J. Microsc.* **241** 225–33
- [173] Chen Y C and Seidman D N 1971 On the atomic resolution of a field ion microscope *Surf. Sci.* **26** 61–84
- [174] Ehrlich G and Stolt K 1980 Surface Diffusion *Annu. Rev. Phys. Chem.* **31** 603–37
- [175] Tsong T T and Kellogg G 1975 Direct observation of the directional walk of single adatoms and the adatom polarizability *Phys. Rev. B* **12** 1343–53
- [176] James M. B 2012 *Surface Physics of Materials* (Elsevier)
- [177] Gault B, Danoix F, Hoummada K, Mangelinck D and Leitner H 2012 Impact of directional walk on atom probe microanalysis *Ultramicroscopy* **113** 182–91
- [178] Yamaguchi Y, Takahashi J and Kawakami K 2009 The study of quantitiveness in atom probe analysis of alloying elements in steel *Ultramicroscopy* **109** 541–4
- [179] Waugh A R, Boyes E D and Southon M J 1976 Investigations of field evaporation with a field-desorption microscope *Surf. Sci.* **61** 109–42
- [180] Vurpillot F, Cerezo A, Blavette D and Larson D J 2004 Modeling Image Distortions in 3DAP *Microsc. Microanal.* **10** 384–90
- [181] Oberdorfer C and Schmitz G 2011 On the field evaporation behavior of dielectric materials in three-dimensional atom probe: A numeric simulation *Microsc. Microanal.* **17** 15–25
- [182] Casey J 1996 *Exploring Curvature* (Wiesbaden: Vieweg+Teubner Verlag)
- [183] Du S, Burgess T, Tjing Loi S, Gault B, Gao Q, Bao P, Li L, Cui X, Kong Yeoh W, Hoe Tan H, Jagadish C, Ringer S P and Zheng R 2013 Full tip imaging in atom probe tomography *Ultramicroscopy* **124** 96–101
- [184] Loi S T, Gault B, Ringer S P, Larson D J and Geiser B P 2013 Electrostatic simulations of a local electrode atom probe: The dependence of tomographic reconstruction parameters on specimen and microscope geometry *Ultramicroscopy* **132** 107–13
- [185] Shariq A, Mutas S, Wedderhoff K, Klein C, Hortenbach H, Teichert S, Kücher P and Gerstl S S A 2009 Investigations of field-evaporated end forms in voltage- and laser-pulsed atom probe tomography *Ultramicroscopy* **109** 472–9
- [186] Al-Bayati A H, Orrman-Rossiter K G, van den Berg J A and Armour D G 1991 Composition and structure of the native Si oxide by high depth resolution medium energy ion scattering *Surf. Sci.* **241** 91–102
- [187] Wilkes T J, Smith G D W and Smith D A 1974 On the quantitative analysis of field-ion micrographs *Metallography* **7** 403–30
- [188] Dutta A, Koley K and Sarkar C K 2014 Impact of underlap and mole-fraction on RF performance of strained-Si/Si<sub>1-x</sub>Ge<sub>x</sub>/strained-Si DG MOSFETs *Superlattices Microstruct.* **75** 634–46
- [189] Zwanenburg F A, Dzurak A S, Morello A, Simmons M Y, Hollenberg L C L, Klimeck G, Rogge S, Coppersmith S N and Eriksson M A 2013 Silicon quantum electronics *Rev. Mod. Phys.* **85** 961–1019
- [190] 3DMetChemIT EMPIR project
- [191] Marquis E A and Gault B 2008 Determination of the tip temperature in laser assisted atom-probe tomography using charge state distributions *J.*

- [192] Koelling S 2011 *Three dimensional compositional analysis of semiconductors with the Atom Probe* (Katholieke Universiteit Leuven (KUL))
- [193] Riley J R, Bernal R A, Li Q, Espinosa H D, Wang G T and Lauhon L J 2012 Atom Probe Tomography of a  $c$ -Axis GaN Nanowires: Analysis of Nonstoichiometric Evaporation Behavior *ACS Nano* **6** 3898–906
- [194] Kumar A, Komalan M P, Lenka H, Kambham A K, Gilbert M, Gencarelli F, Vincent B and Vandervorst W 2013 Atomic insight into Ge $_{1-x}$ Sn $_x$  using atom probe tomography *Ultramicroscopy* **132** 171–8
- [195] Gault B, Müller M, La Fontaine A, Moody M P, Shariq A, Cerezo A, Ringer S P and Smith G D W 2010 Influence of surface migration on the spatial resolution of pulsed laser atom probe tomography *J. Appl. Phys.* **108**
- [196] Bunton J, Olson J, Lenz D and Kelly T 2008 Investigation of Performance-Influencing Factors in Pulsed Laser Atom Probe *Microsc. Microanal.* **14** 1238–9
- [197] Bevington P R and Robinson D K 2003 *data reduction and error analysis for the physical science* (McGraw-Hill Education)
- [198] Hedges L V. and Olkin I 2014 *Statistical Methods for Meta-Analysis* (Elsevier)
- [199] Estivill R, Grenier A, Duguay S, Vurpillot F, Terlier T, Barnes J-P, Hartmann J-M and Blavette D 2015 Quantitative analysis of Si/SiGeC superlattices using atom probe tomography *Ultramicroscopy* **159** 223–31
- [200] Estivill R, Grenier A, Duguay S, Vurpillot F, Terlier T, Barnes J-P, Hartmann J-M and Blavette D 2015 Quantitative investigation of SiGeC layers using atom probe tomography *Ultramicroscopy* **150** 23–9
- [201] Melkonyan D, Fleischmann C, Bogdanowicz J, Morris R and Vandervorst W 2017 Accuracy in APT analysis: The case of boron in silicon (Sardinia Italy: 79th IUVSTA Workshop)
- [202] Tu Y, Takamizawa H, Han B, Shimizu Y, Inoue K, Toyama T, Yano F, Nishida A and Nagai Y 2017 Influence of laser power on atom probe tomographic analysis of boron distribution in silicon *Ultramicroscopy* **173** 58–63
- [203] Kouzminov D 2018 Kouzminov's, Dimitry (Atom Probe Tomography and Microscopy (APT&M))
- [204] Herbig M, Choi P and Raabe D 2015 Combining structural and chemical information at the nanometer scale by correlative transmission electron microscopy and atom probe tomography *Ultramicroscopy* **153** 32–9
- [205] Lefebvre W, Hernandez-Maldonado D, Moyon F, Cuvilly F, Vaudolon C, Shinde D and Vurpillot F 2015 HAADF–STEM atom counting in atom probe tomography specimens: Towards quantitative correlative microscopy *Ultramicroscopy* **159** 403–12
- [206] Arslan I, Marquis E A, Homer M, Hekmaty M A and Bartelt N C 2008 Towards better 3-D reconstructions by combining electron tomography and atom-probe tomography *Ultramicroscopy* **108** 1579–85
- [207] Kelly T F, Miller M K, Rajan K and Ringer S P 2013 Atomic-Scale Tomography: A 2020 Vision *Microsc. Microanal.* **19** 652–64
- [208] Mouton I, Printemps T, Grenier A, Gambacorti N, Pinna E, Tiddia M, Vacca A and Mula G 2017 Toward an accurate quantification in atom probe tomography reconstruction by correlative electron tomography approach on nanoporous materials *Ultramicroscopy* **182** 112–7

- [209] Egerton R F, McLeod R, Wang F and Malac M 2010 Basic questions related to electron-induced sputtering in the TEM *Ultramicroscopy* **110** 991–7
- [210] Koelling S, Gilbert M, Goossens J, Hikavy A, Richard O and Vandervorst W 2009 High depth resolution analysis of Si/SiGe multilayers with the atom probe *Appl. Phys. Lett.* **95** 144106
- [211] Dyck O, Leonard D N, Edge L F, Jackson C A, Pritchett E J, Deelman P W and Poplawsky J D 2017 Accurate Quantification of Si/SiGe Interface Profiles via Atom Probe Tomography *Adv. Mater. Interfaces* **4** 1700622
- [212] Canham L 2014 *Handbook of Porous Silicon* (Cham: Springer International Publishing)
- [213] Amouyal Y and Schmitz G 2016 Atom probe tomography—A cornerstone in materials characterization *MRS Bull.* **41** 13–8
- [214] Gordon L M and Joester D 2011 Nanoscale chemical tomography of buried organic-inorganic interfaces in the chiton tooth *Nature* **469** 194–8
- [215] Kelly T F, Nishikawa O, Panitz J A and Prosa T J 2009 Prospects for Nanobiology with Atom-Probe Tomography *MRS Bull.* **34** 744–50
- [216] Zanuttini D, Blum I, Rigutti L, Vurpillot F, Douady J, Jacquet E, Anglade P-M and Gervais B 2017 Electronic structure and stability of the SiO<sub>2</sub> modifications produced in tomographic atom probe experiments *J. Chem. Phys.* **147** 164301
- [217] Vurpillot F, Parviainen S, Djurabekova F, Zanuttini D and Gervais B 2018 Simulation tools for atom probe tomography: A path for diagnosis and treatment of image degradation *Mater. Charact.* **146** 336–46
- [218] Saxey D W 2011 Correlated ion analysis and the interpretation of atom probe mass spectra *Ultramicroscopy* **111** 473–9
- [219] Peng Z, Vurpillot F, Choi P-P, Li Y, Raabe D and Gault B 2018 On the detection of multiple events in atom probe tomography *Ultramicroscopy* **189** 54–60
- [220] 2018 Versailles Project on Advanced Materials and Standards (VAMAS): A25 Interlaboratory study on atom probe quantification and reproducibility